Forces Controlling the Dynamics of Planetary Interiors

Emma Hunter

Submitted in fulfilment of the requirements
for the Degree of Doctor of Philosophy

School of Mathematics and Statistics
College of Science and Engineering
University of Glasgow

July 2025

Abstract

Convection occurs naturally in the atmospheres of giant planets and within electrically conducting regions of terrestrial planets, such as Earth's outer core. Over time, increasing attention has been given to these conducting fluid regions in astrophysical and geophysical bodies, as they are believed to generate magnetic fields through dynamo action. Therefore, understanding convection and the dynamo process is fundamental to explaining how magnetic fields are sustained in astrophysical and geophysical bodies.

This thesis investigates convective fluid flows under the influence of rotation and magnetic fields. Numerical simulations are conducted using two models: an annulus model with an imposed magnetic field, and a spherical shell model that allows for the self-excitation of magnetic fields. Throughout this thesis, particular attention is given to the forces governing the flow dynamics. The first part presents a literature review of existing work and outlines the methods used in both models.

New results from nonlinear simulations of an annulus model with an imposed magnetic field are presented. The study examines how varying the strength of magnetic field and convection affects the prevailing force balances and flow patterns. Additionally, the characteristics of zonal flows and multiple jets within the annulus model are investigated, with particular emphasis on the influence of magnetic field strength and the force balances required to sustain these flows. Zonal flows and multiple jet solutions are typically found at weak magnetic field strength where a strong inertial force is present, although some cases of zonal flows and multiple jets are found at strong magnetic field strength where a strong Lorentz force is present. Force balances occur that are similar to those found in the main regimes of dynamo action.

Finally, spherical shell simulations are performed to investigate both forces and solenoidal forces, where flow lengthscales in two distinct directions are examined. Dynamically relevant flow lengthscales are identified by introducing a triple balance point involving key forces characteristic of the main dynamo regimes. These dynamically relevant lengthscales are then successfully compared with energetically dominant scales, highlighting how force balances at particular scales set the size of the flow. The forces and solenoidal forces across different regions of the spherical shell are further analysed. Transitions between the main dynamo regimes are examined, where solenoidal forces are used to explain the mechanisms driving these transitions.

Contents

List of Figures

Acknowledgements

I want to take this opportunity to thank everyone who has supported me throughout my PhD. Most of all, I would like to express my sincere gratitude to my supervisor, Rob Teed. You first introduced me to the world of research with my Masters project five years ago. From then, and through to now, you have been unwaveringly supportive of me, incredibly generous with your time, and have provided all the guidance I could possibly ask for. You have made pursuing this PhD an incredibly valuable experience, and I will always be grateful.

I would also like to thank my examiners, Celine Guervilly and Radostin Simitev, and the viva convener, Misha Feigin, for the valuable comments and suggestions provided which have improved this thesis.

Next, I would like to thank all my friends and colleagues in the Mathematics Department at the University of Glasgow for creating such a supportive research environment. I want to thank all the people I have met along the way who have helped make these past four years so rewarding and enjoyable. Thanks also to everyone in the GAFD research group for many helpful discussions and engaging seminars.

I would also like to thank all my friends outside of university for always being there and helping me stay motivated throughout my PhD. A special thanks to everyone at Stefano's Italian, where I worked throughout my time at university. Your support has meant a lot to me and has always provided me with a good laugh when I needed it.

Lastly, I would like to thank my family. Thank you to my mum, dad and brother Mark for their unwavering support throughout everything. Your love and support have meant the world to me. A special thanks to my mum for all her proofreading. Finally, thank you to my partner Tom for all his love and encouragement and for adding most of the commas in this thesis.

Declaration

With the exception of Chapters 1 and 2, which contain introductory material, all work in this thesis was carried out by the author unless otherwise explicitly stated.

Chapter 1

Introduction

Convection driven by thermal and/or compositional gradients occurs naturally in the atmospheres of giant planets and within regions of terrestrial planets such as the outer core of Earth. Such fluids are often electrically conducting and act as the seat of their planet's dynamo, generating the planetary magnetic field. This idea was first introduced by Larmor (1919), where they proposed that electrically conducting fluid generated the magnetic field and provided an explanation for the magnetisation of sunspots. Therefore, an understanding of convection is necessary to provide an explanation for dynamo action in astrophysical and geophysical systems.

Our understanding of planetary magnetic field generation has been made possible through numerical simulations, which are the focus of this thesis, and through observations from satellites and paleomagnetic studies. Magnetic field generation in convecting fluid regions is governed by the Navier-Stokes and Maxwell's equations. Due to their complexity, these equations can only be solved analytically in certain limits. However, over recent decades, advancements in computational power have made it possible to solve these equations numerically. In the first part of this thesis, we investigate magnetoconvection using an annulus model. This is a localised model of spherical geometry, which we use to focus on the force balances controlling the dynamics of the flow (see Section 1.5.2) and zonal flows which are azimuthal large scale flows. The second part centres on a three-dimensional spherical shell model capable of the self-excitation of magnetic fields. Here we analyse globally averaged and lengthscale dependent force balances, by considering the entire shell and specific localised regions.

This chapter discusses the structure of Earth and Jupiter. We introduce the Navier-Stokes and Maxwell's equations and discuss planetary magnetic field generation. A literature review is presented, focusing on studies involving an annulus model and a spherical shell model. We introduce the main regimes of dynamo action which will be essential for interpreting the force dynamics observed in our simulations.

1.1 EARTH'S STRUCTURE

The Earth has a radius of approximately 6370 km and is composed of several distinct layers. At the surface lies the crust, which is relatively thin compared to Earth's total radius. Below the crust is the rocky mantle which extends to approximately 2900 km. Beneath the mantle lies a dense iron rich core. This core is divided into two distinct regions: a solid inner core and a liquid outer core. The outer core, composed of liquid metal, is believed to generate and sustain the Earth's magnetic field due to its electrically conducting nature. The boundary separating the mantle and the core is known as the core-mantle boundary (Fig. 1.1).

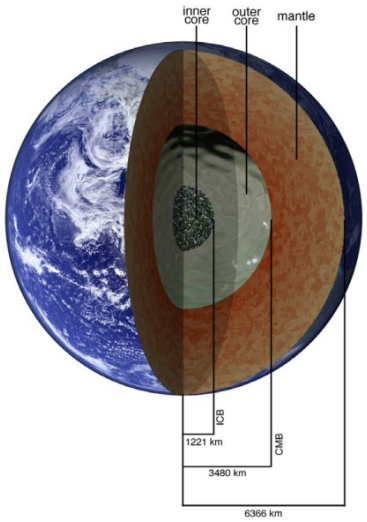

Figure 1.1: Earth's internal structure. Taken from Roberts and King (2013)

Our understanding of Earth's internal structure has largely been shaped through the study of seismology, which is the study of vibrations of waves generated by earthquakes through the interior of Earth. Two types of waves studied in seismology are longitudinal waves (P-waves) and transverse waves (S-waves). These waves reveal the density of the material they pass through, as P-waves can pass through any material, but S-waves can only pass through solids. S-waves are unable to propagate in the outer core, demonstrating that it must be a fluid. The core itself was first identified by Oldham (1906), but it wasn't until 1926 that the liquid state of the outer core was confirmed by Jeffreys (1926), and the solid inner core was discovered a decade later by Lehmann (1936). The iron rich core is convecting and it is believed to be the source of Earth's magnetic field. This is due to the release of heat from Earth's inner core which drives convection in the electrically conducting fluid, generating a magnetic field. While the mantle is also convecting, its weak electrical conductivity and poor electrical properties make it incapable of generating or sustaining the Earth's magnetic field.

Understanding the behaviour of Earth's magnetic field has advanced significantly through paleomagnetic studies, satellite observations, and numerical simulations. Paleomagnetic research provides insights into the geodynamo by analysing the magnetisation preserved in rocks and archaeological artifacts, providing an understanding of the magnetic field's evolution. In contrast, satellite data provides a detailed view of the present day geodynamo, confirming that

Earth's magnetic field is predominantly dipolar. Paleomagnetic evidence has also revealed that the magnetic field undergoes polarity reversals. Numerical simulations complement these approaches by offering valuable insights into the convective processes within Earth's core that cannot be directly observed through satellites.

Paleomagnetic evidence indicates that Earth's magnetic field has existed for at least 3.7 billion years, but the material in Earth's outer core responsible for generating the geodynamo exhibits electrical resistance, leading to energy loss through Ohmic dissipation. Moffatt (1978) demonstrated that in the absence of an energy source to sustain fluid motion, such dissipation would cause the magnetic field to decay on a timescale of approximately $20,000$ years unless there is another source driving the fluid in the outer core. This is likely driven by thermal and compositional convection due to the temperature difference in the core. Thermal convection occurs due to the crystallisation of the inner core releasing latent heat, forming a temperature gradient. Compositional convection occurs as the inner core solidifies and releases light elements into the surrounding fluid. These lighter elements mix with the dense iron rich fluid creating differences in composition that drive the fluid motion. While both types of convection play a significant role in the geodynamo, this thesis focuses on thermal convection.

1.2 Jupiter's structure

Jupiter is the largest planet of the Solar System and is mainly composed of hydrogen and helium. Jupiter is believed to have a rocky core surrounded by hydrogen and helium gas. Deep in the gaseous region of the planet it is very hot and dense, and this pressure causes the release of electrons. This release of electrons creates an electrically conducting metallic hydrogen. Jupiter's magnetic field is driven by dynamo action and it is expected to be generated in the metallic hydrogen region. As Jupiter is rapidly rotating the convection caused by the release of heat from the centre causes the electrically conducting metal to generate the magnetic field. Surrounding the core is an outer layer of molecular hydrogen and helium. This region helps to transport heat from the interior.

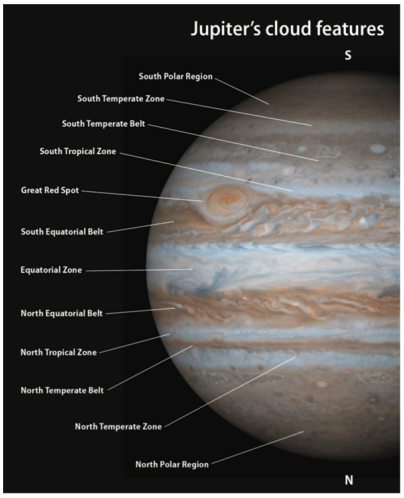

Figure 1.2: Jupiter's surface. Taken from Klesman (2020)

Jupiter's visible atmosphere is dominated by alternating light and dark bands known as zones and belts respectively (Fig. 1.2). The banded structure is made up of zonal flows propagating in either the prograde or retrograde direction and are believed to be driven by the turbulent motion caused by convection. The rapid rotation of Jupiter is key in driving these jets. The depths of the zonal flows have long been unknown but recent evidence using data from the Juno mission suggests that the flows extend 3000 km below the surface (Kaspi et al., 2023). Busse (1976b) introduced a deep model proposing that zonal flows are driven deep in the interior. However, this model is often unable to produce jets, possibly due to the inability to reach sufficiently large rotation rates. Shallow models have also been proposed that assume that zonal flows are confined to a thin layer at the surface and driven by small scale turbulence. However, this model can produce jets but cannot produce the correct equatorial structure. This suggests that a combination of both models is required to reproduce the structures observed in the Jovian atmosphere. High resolution simulations by Heimpel et al. (2005) have produced multiple jets using deep and shallow processes. Other features of Jupiter include large scale vortices like the Great Red Spot (Fig. 1.2). These are not expected to extend deep into Jupiter's atmosphere.

1.3 Governing equations of magnetohydrodynamics

To analyse the behaviour of fluid flow, the basic equations governing the motion need to be defined. We begin by discussing the equations governing fluid dynamics, followed by an introduction to Maxwell's equations, before combining these to form the governing equations of magnetohydrodynamics (MHD).

1.3.1 Equations governing fluid dynamics

The equations governing fluid dynamics can be found in many textbooks, for example Batchelor (2000). The Navier-Stokes equation or the momentum equation is given by

$$\rho\frac{\partial U_i}{\partial t} + \rho U_j\frac{\partial U_i}{\partial x_j} = F_i + \frac{\partial P_{ij}}{\partial x_j} \tag{1.1}$$

where ρ is the density of the fluid, x is the position, U is the velocity, t is time and F is the body force acting on the system. The fluid is assumed to be isotropic and the stress is linearly proportional to the strain so the stress tensor P_{ij} can be written as

$$P_{ij} = -p\delta_{ij} + \gamma\left(\frac{\partial U_i}{\partial x_j} + \frac{\partial U_j}{\partial x_i}\right) - \frac{2}{3}\gamma\frac{\partial U_k}{\partial x_k}\delta_{ij}$$

where p is the isotropic pressure at x_i in the absence of strain and γ is the coefficient of viscosity. The derivation for this form of the stress tensor can be found in Chandrasekhar (1961). Substituting the stress tensor into the Navier-Stokes equation we obtain

$$\rho\frac{\partial U_i}{\partial t} + \rho U_j\frac{\partial U_i}{\partial x_j} = F_i - \frac{\partial p}{\partial x_i} + \frac{\partial}{\partial x_j}\left(\gamma\left(\frac{\partial U_i}{\partial x_j} + \frac{\partial U_j}{\partial x_i}\right) - \frac{2}{3}\gamma\frac{\partial U_k}{\partial x_k}\delta_{ij}\right). \tag{1.2}$$

We also have the continuity equation which is given by

$$\frac{\partial \rho}{\partial t} + \frac{\partial}{\partial x_j}(\rho U_j) = 0 \tag{1.3}$$

which expresses the conservation of mass. Also required is a governing equation for the temperature as we will be looking at the effects of temperature changes, giving rise to thermally driven buoyancy. The equation of heat conduction expresses the conservation of energy and is given by

$$\rho \frac{\partial}{\partial t}(c_V T) + \rho U_j \frac{\partial}{\partial x_j}(c_V T) = \frac{\partial}{\partial x_j}\left(k \frac{\partial T}{\partial x_j}\right) - p\frac{\partial U_j}{\partial x_j} + \Phi \tag{1.4}$$

where c_V is the specific heat at constant volume, T is the temperature, k is the coefficient of heat conduction and Φ is the rate at which energy is dissipated and is given by

$$\Phi = \frac{\gamma}{2}\left(\frac{\partial U_i}{\partial x_j} + \frac{\partial U_j}{\partial x_i}\right)^2 - \frac{2}{3}\gamma\left(\frac{\partial U_j}{\partial x_j}\right)^2.$$

An equation of state is also required which can be expressed as

$$\rho = \rho_0\left[1 - \alpha\left(T - \tilde{T}\right)\right] \tag{1.5}$$

where α is the coefficient of volume expansion, ρ_0 is a reference density and $\tilde{T}$ is the temperature at which $\rho = \rho_0$.

1.3.1.1 Boussinesq approximation

In the previous section no assumptions were made regarding the variables α, c_V, γ or k. We can use the Boussinesq approximation, developed by Boussinesq (1903), where it was highlighted that the density can be neglected when we have variations in the temperature of small amounts. We follow a similar method to Chandrasekhar (1961). Fluids of interest in this thesis usually have $10^{-4}K^{-1} < \alpha < 10^{-3}K^{-1}$, which means that the density varies by small amounts provided the variation in temperature is small. This allows variations in density to be ignored and ρ can be treated as a constant. The only exception to this is when the density is coupled with gravity. This occurs in the F_i term in the Navier-Stokes equation where we have a buoyancy force given by ρg_i acting on the system. Under the Boussinesq approximation we can also assume that α, c_V, γ and k are constant. Under the Boussinesq approximation (1.3) becomes

$$\frac{\partial U_j}{\partial x_j} = 0 \tag{1.6}$$

meaning the fluid is incompressible. Equation (1.2) becomes

$$\frac{\partial U_i}{\partial t} + U_j\frac{\partial U_i}{\partial x_j} = -\frac{1}{\rho_0}\frac{\partial p}{\partial x_i} + \frac{\rho g_i}{\rho_0} + \nu\nabla^2 U_i \tag{1.7}$$

where $\nu = \gamma/\rho_0$ is the kinematic viscosity. We can substitute in ρ given by (1.5) and rewrite $T - \tilde{T}$ as T to obtain (1.7) in vector form as

$$\frac{\partial \mathbf{U}}{\partial t} + (\mathbf{U} \cdot \nabla)\,\mathbf{U} = -\frac{1}{\rho_0}\nabla p - \alpha T \mathbf{g} + \nu \nabla^2 \mathbf{U}. \tag{1.8}$$

The heat conduction equation (1.4) becomes

$$\frac{\partial T}{\partial t} + U_j \frac{\partial T}{\partial x_j} = \kappa \nabla^2 T \tag{1.9}$$

where $\kappa = k/\rho_0 c_V$ is the coefficient of thermal diffusivity and we have ignored the dissipation term Φ as it is smaller than the convecting terms. The heat equation can be written in vector form which gives

$$\frac{\partial T}{\partial t} + (\mathbf{U} \cdot \nabla)\, T = \kappa \nabla^2 T. \tag{1.10}$$

1.3.1.2 The effects of rotation on the hydrodynamic equations

As our work considers a rotating system we need to include the effects of rotation on the governing equations. The only equation affected by rotation is the Navier-Stokes equation. Suppose our fluid is rotating about a fixed axis with constant angular velocity $\mathbf{\Omega}$. The motion is described by an observer at rest in a frame rotating about the same axis with the same angular velocity. In this rotating frame the velocities and accelerations will differ from the velocities and accelerations observed in an inertial frame. This gives the rotational terms in the Navier-Stokes equation. The Coriolis force given by $2\rho\mathbf{\Omega} \times \mathbf{U}$ and the centrifugal force is given by $\frac{1}{2}\rho\frac{\partial}{\partial x_i}\left(|\mathbf{\Omega} \times \mathbf{x}|^2\right)$ (Chandrasekhar, 1961). We assume the Boussinesq approximation also applies to these terms. The Euler force is also important but this involves a time derivative and we have constant $\mathbf{\Omega}$ so it can be neglected. Hence the Navier Stokes equation given by (1.7) becomes

$$\frac{\partial U_i}{\partial t} + U_j \frac{\partial U_i}{\partial x_j} + 2\epsilon_{ijk}\Omega_j U_k = -\frac{1}{\rho_0}\frac{\partial p}{\partial x_i} + \frac{1}{2}\frac{\partial}{\partial x_i}\left(|\epsilon_{jkl}\Omega_k x_l|^2\right) + \frac{F_i}{\rho_0} + \nu \frac{\partial^2 U_i}{\partial x_j^2}. \tag{1.11}$$

Expressing (1.11) in vector form we obtain

$$\frac{\partial \mathbf{U}}{\partial t} + (\mathbf{U} \cdot \nabla)\,\mathbf{U} + 2\mathbf{\Omega} \times \mathbf{U} = -\frac{1}{\rho_0}\nabla p_m + \frac{\mathbf{F}}{\rho_0} + \nu \nabla^2 \mathbf{U} \tag{1.12}$$

where $p_m = p + \frac{1}{2}\rho_0 |\mathbf{\Omega} \times \mathbf{x}|^2$. The effects of rotation play an important role as two new terms have been introduced to the momentum equation.

1.3.2 MAXWELL'S EQUATIONS

Maxwell's equations underpin electromagnetism and they describe how electric charges and currents form electric and magnetic fields. Maxwell's equations are

$$\text{Gauss' law: } \nabla \cdot \mathbf{E} = \frac{\rho_c}{\epsilon} \tag{1.13}$$

$$\text{Faraday's law: } \nabla \times \mathbf{E} = -\frac{\partial \mathbf{B}}{\partial t} \tag{1.14}$$

$$\text{Gauss' law for magnetism: } \nabla \cdot \mathbf{B} = 0 \tag{1.15}$$

$$\text{Ampere's law: } \nabla \times \mathbf{B} = \mu \mathbf{j} + \mu\epsilon \frac{\partial \mathbf{E}}{\partial t} \tag{1.16}$$

where $\mathbf{E}$ is the electric field, $\mathbf{B}$ is the magnetic field, ρ_c is the charge density, $\mathbf{j}$ is the current density, μ is the magnetic permeability and ϵ is the permittivity. These can be found in many textbooks, for example Davidson (2017). The current density can be expressed with Ohm's law, $\mathbf{j} = \sigma \mathbf{E}$, where σ is the electrical conductivity. We take $\epsilon = \epsilon_0$ and $\mu = \mu_0$ which are the permittivity and magnetic permeability in free space.

In (1.16) the last term was introduced by Maxwell as a correction to Ampere's law and is known as the displacement current. If we take the divergence of Ampere's law we obtain

$$\nabla \cdot (\nabla \times \mathbf{B}) = \mu_0 \left(\nabla \cdot \mathbf{j} + \epsilon_0 \frac{\partial}{\partial t} \nabla \cdot \mathbf{E} \right) = 0$$

$$\implies \nabla \cdot \mathbf{j} = -\epsilon_0 \frac{\partial}{\partial t} \nabla \cdot \mathbf{E} = -\frac{\partial \rho_c}{\partial t}$$

using the conservation of charge which states that

$$\nabla \cdot \mathbf{j} = -\frac{\partial \rho_c}{\partial t}.$$

In MHD, $\partial \rho_c / \partial t$ is negligible which suggests that $\epsilon_0 \partial \mathbf{E} / \partial t$ is small. We have

$$\epsilon_0 \frac{\partial \mathbf{E}}{\partial t} \sim \frac{\epsilon_0}{\sigma} \frac{\partial \mathbf{j}}{\partial t} \ll \mathbf{j}.$$

Therefore Ampere's law reduces to

$$\nabla \times \mathbf{B} = \mu_0 \mathbf{j} \tag{1.17}$$

and taking the divergence of this gives

$$\nabla \cdot \mathbf{j} = 0.$$

Using (1.15) the magnetic field can be expressed in terms of a vector potential $\mathbf{A}$ which is divergence-free so

$$\mathbf{B} = \nabla \times \mathbf{A} \implies \nabla \cdot \nabla \times \mathbf{A} = 0$$

which guarantees that $\mathbf{B}$ is solenoidal.

1.3.2.1 The Lorentz force

The force per unit volume on a fluid with charge density ρ_c and current density $\mathbf{j}$ is

$$\mathbf{F} = \rho_c \mathbf{E} + \mathbf{j} \times \mathbf{B} \tag{1.18}$$

where the first term is the electric force and the second term is the magnetic force (Davidson, 2017). In MHD we are interested in the case where $|\mathbf{u}| \ll c$ where c is the speed of light. We can show that the first term in Equation (1.18) can be ignored as it is much smaller than the Lorentz force. Let U be a typical speed, T a typical time scale, L a typical length scale, B a typical magnetic field strength and E a typical electric field strength. From (1.13) and (1.17)

$$|\rho_c| \sim \epsilon_0 \frac{E}{L} \text{ and } |\mathbf{j}| \sim \frac{B}{\mu_0 L}$$

and from Faraday's law given by (1.14) we have

$$\frac{E}{L} \sim \frac{B}{T} \implies \frac{E}{B} \sim \frac{L}{T} = U. \tag{1.19}$$

Then considering the terms in (1.18) we have

$$\frac{|\rho_c \mathbf{E}|}{|\mathbf{j} \times \mathbf{B}|} \sim \mu_0 \epsilon_0 \frac{E^2}{B^2} \sim \frac{U^2}{c^2} \ll 1$$

where we have used (1.19) and the fact that $c = 1/\sqrt{\epsilon_0 \mu_0}$. Therefore $\rho_c \mathbf{E}$ is small in comparison with $\mathbf{j} \times \mathbf{B}$ so we can neglect it. Hence, from here on in, the Lorentz force will take the form

$$\mathbf{F} = \mathbf{j} \times \mathbf{B}.$$

The Lorentz force can be rewritten so that it is made up of magnetic tension and magnetic pressure. Taking the reduced form of Ampere's law given in (1.17) we can express $\mathbf{j}$ as

$$\mathbf{j} = \frac{1}{\mu_0} \nabla \times \mathbf{B}$$

so that

$$\mathbf{F} = \mathbf{j} \times \mathbf{B} = \frac{1}{\mu_0} (\nabla \times \mathbf{B}) \times \mathbf{B}.$$

We can then use the vector identity

$$\nabla (\mathbf{A} \cdot \mathbf{B}) = (\mathbf{B} \cdot \nabla) \mathbf{A} + (\mathbf{A} \cdot \nabla) \mathbf{B} + \mathbf{B} \times (\nabla \times \mathbf{A}) + \mathbf{A} \times (\nabla \times \mathbf{B})$$

and noting that $(\nabla \times \mathbf{B}) \times \mathbf{B} = -\mathbf{B} \times (\nabla \times \mathbf{B})$ to obtain

$$\mathbf{F} = \mathbf{j} \times \mathbf{B} = \frac{1}{\mu_0} (\mathbf{B} \cdot \nabla) \mathbf{B} - \frac{1}{2\mu_0} \nabla B^2. \tag{1.20}$$

When considering magnetised terms, the Lorentz force is included in the external force term given by $\mathbf{F}$ in the Navier-Stokes equation.

1.3.2.2 The induction equation

We now obtain the induction equation, which is the evolution equation for $\mathbf{B}$ relating the magnetic field and velocity of the electrically conducting fluid. To do this we start with Ohm's law (Davidson, 2017) which is given by

$$\mathbf{j} = \sigma\left(\mathbf{E} + \mathbf{U} \times \mathbf{B}\right) \implies \mathbf{E} = \sigma^{-1}\mathbf{j} - \mathbf{U} \times \mathbf{B}.$$

Taking the curl of this, and making use of (1.14) and (1.17), gives

$$\begin{aligned} \nabla \times \mathbf{E} = -\frac{\partial \mathbf{B}}{\partial t} &= \nabla \times \sigma^{-1}\mathbf{j} - \nabla \times (\mathbf{U} \times \mathbf{B}) \\ \implies \frac{\partial \mathbf{B}}{\partial t} &= \nabla \times (\mathbf{U} \times \mathbf{B}) - \nabla \times \left(\sigma^{-1}\mu_0^{-1}\nabla \times \mathbf{B}\right) \\ \implies \frac{\partial \mathbf{B}}{\partial t} &= \nabla \times (\mathbf{U} \times \mathbf{B}) - \nabla \times (\lambda \nabla \times \mathbf{B}) \end{aligned}$$

where $\lambda = 1/\sigma\mu_0$ is the magnetic diffusivity. Assuming λ is a constant and using the identity $\nabla \times (\nabla \times \mathbf{B}) = \nabla(\nabla \cdot \mathbf{B}) - \nabla^2\mathbf{B}$ and (1.15) gives

$$\frac{\partial \mathbf{B}}{\partial t} = \nabla \times (\mathbf{U} \times \mathbf{B}) + \lambda \nabla^2 \mathbf{B} \tag{1.21}$$

which is the transport equation for the magnetic field, known as the induction equation or the advection-diffusion equation for the magnetic field. On the left-hand side we have the rate of change of the magnetic field. The first term on the right-hand side is the advection or induction term and the second term is the magnetic diffusion.

1.3.3 Full system of equations

In the previous sections we have derived the set of equations that will govern the models used in this thesis. For clarity, these are restated here. The full set of equations governing MHD are

$$\frac{\partial \mathbf{U}}{\partial t} + (\mathbf{U} \cdot \nabla)\,\mathbf{U} + 2\boldsymbol{\Omega} \times \mathbf{U} = -\frac{1}{\rho_0}\nabla P_m - \alpha T \mathbf{g} + \frac{1}{\rho_0 \mu_0}(\nabla \times \mathbf{B}) \times \mathbf{B} + \nu \nabla^2 \mathbf{U} \tag{1.22}$$

$$\frac{\partial T}{\partial t} + (\mathbf{U} \cdot \nabla)\,T = \kappa \nabla^2 T \tag{1.23}$$

$$\frac{\partial \mathbf{B}}{\partial t} = \nabla \times (\mathbf{U} \times \mathbf{B}) + \lambda \nabla^2 \mathbf{B} \tag{1.24}$$

$$\nabla \cdot \mathbf{U} = 0 \tag{1.25}$$

$$\nabla \cdot \mathbf{B} = 0. \tag{1.26}$$

1.3.4 TAYLOR-PROUDMAN THEOREM

An important result occurring in rapidly rotating systems where the Rossby number is small is given by the Taylor-Proudman theorem. Suppose we have a slow-moving, inviscid, incompressible, homogeneous fluid with constant density and steady velocity. Based on these assumptions (1.12) becomes

$$2\boldsymbol{\Omega} \times \mathbf{U} = -\nabla \left(\frac{P_m}{\rho_0} \right).$$

This balance between the Coriolis force and the pressure gradient is known as a geostrophic balance. Taking the curl of this gives

$$\nabla \times (\boldsymbol{\Omega} \times \mathbf{U}) = 0. \tag{1.27}$$

Expanding the left hand side we have

$$\nabla \times (\boldsymbol{\Omega} \times \mathbf{U}) = (\mathbf{U} \cdot \nabla)\, \boldsymbol{\Omega} - \mathbf{U}\, (\nabla \cdot \boldsymbol{\Omega}) - (\boldsymbol{\Omega} \cdot \nabla)\, \mathbf{U} + \boldsymbol{\Omega}\, (\nabla \cdot \mathbf{U}).$$

Using the continuity equation $\nabla \cdot \mathbf{U} = 0$ and assuming a constant rotation rate, (1.27) becomes

$$(\boldsymbol{\Omega} \cdot \nabla)\, \mathbf{U} = 0. \tag{1.28}$$

This is known as the Taylor-Proudman theorem (Proudman, 1916; Taylor, 1922). Physically this means that the velocity of a rotating fluid is invariant in the direction of the rotation axis. Therefore the fluid must move in columns that are independent of the rotation axis (aligned with the axis of rotation), which means the motion of the fluid must be two-dimensional.

1.4 MAGNETIC FIELD GENERATION

The phenomenon of magnetism has been recognised since ancient times, when the Chinese used lodestones to demonstrate magnetic properties. Gilbert (1600) was the first to propose that Earth itself behaves like a giant magnet. He demonstrated how Earth's magnetic field could be modelled using a spherical lodestone. Gauss (1839) introduced the first mathematical description of Earth's magnetic field using spherical harmonics. Gauss was able to distinguish between internal and external sources of magnetic fields leading to the conclusion that the dominant part of Earth's magnetic field originates from within the planet. In the early 1900s, Larmor (1919) first proposed that the electrically conducting fluid generated and maintained the magnetic field, known as dynamo action. Cowling (1933) introduced his anti-dynamo theorem where he stated that no steady axisymmetric magnetic field can be maintained by a steady axisymmetric flow. Despite this anti-dynamo theorem Elsasser (Elsasser, 1946a,b, 1947) demonstrated how electrically conducting fluid motions in Earth's outer core could produce a dynamo. The geomagnetic field (and other planetary magnetic fields) is not axisymmetric. Cowling's theorem only applies to a steady axisymmetric field, so a dynamo can produce a field

that is not axisymmetric.

Cowling's theorem led researchers to focus on alternative flows that could generate a self-sustaining magnetic field. Cowling's antidynamo theorem only ruled out steady axisymmetric fields. This moved the focus toward more realistic flows, resulting in a focus on kinematic dynamos. These models simplify the system as the flow is prescribed and does not consider the distortion to the flow by the magnetic field. By prescribing the flow, only the induction equation needs to be solved. Bullard and Gellman (1954) introduced a spectral decomposition of the flow and field which is still used today to investigate dynamo action. They claimed to obtain dynamo action for a chosen fluid motion. However, analysis by Lilley (1970) and Gubbins (1973) disproved this, and showed that the dynamo action was caused by insufficient resolution. They truncated the spherical harmonics at a low degree without any justification for this. Backus (1958) and Herzenberg (1958) found flows that produced dynamo action and were able to provide justification for the truncation of the spherical harmonics. Although the flows were geophysically unrealistic, the results were important as they demonstrated that fluid flow can maintain a magnetic field.

Kinematic dynamos consider a prescribed flow so only the induction equation is required to be solved. However the magnetic field is expected to be strong enough to alter the fluid motions, meaning the velocity field is affected by the Lorentz force. The Lorentz force enters the system through the momentum equation, leading to a complex system of equations to be solved. This moved the focus to models where the flow is dynamically determined. Convectively-driven dynamos were studied early on in a plane layer by Childress and Soward (1972) and Soward (1974) and in spherical geometry by Zhang and Busse (1989, 1990). The advancement of computing power led to numerical studies of convectively-driven dynamos in spherical shells. This allowed the complex system to be solved numerically. The first simulation of this was performed by Glatzmaier and Roberts (1995) where they demonstrated a polarity reversal. Since 1995, a large number of studies of numerical dynamos in spherical shells have been performed studying various aspects such as parametric studies, diffusivity profiles and effects of different boundary conditions. These have been discussed in a review paper by Roberts and King (2013). Despite these results, challenges in dynamo modelling still remain, and we discuss this further in the next section.

1.5 MODELS

Various models are employed to better understand magnetic field generation in planetary interiors. Spherical geometry is the most suitable model as this can completely capture the effects of the geometry on the dynamics of the flow. However, simplified models, such as a Cartesian box or cylindrical geometry, can often be more useful when the aim is to isolate and study specific physical processes without the added complexity of spherical geometry. This thesis explores two models. Chapters 3 and 4 focus on a cylindrical annulus model and Chapters 5 and 6 focus on a spherical dynamo model. A literature review on the annulus model is given

in Section 1.5.1 and a review of spherical dynamo models is discussed in Section 1.5.2, where concepts relevant to the work in this thesis are discussed.

1.5.1 ANNULUS MODEL

Often, simplified models are used to examine different aspects of planetary magnetic field generation. Chapters 3 and 4 examine simulations in an annulus model with an imposed magnetic field. In order to understand where in Earth's core the annulus model is most relevant, we can define a hypothetical tangent cylinder (TC). This runs from pole to pole and touches the inner core boundary, as shown in Figure 1.3. In the annulus model, rotation acts vertically upwards in the z-direction and gravity acts inwards so these are orthogonal to each other. This model is most relevant outside the tangent cylinder (OTC) near the equator where gravity and rotation are orthogonal to each other. A plane layer model with gravity and rotation parallel to one another in the z-direction is most relevant inside the tangent cylinder (ITC) at the poles.

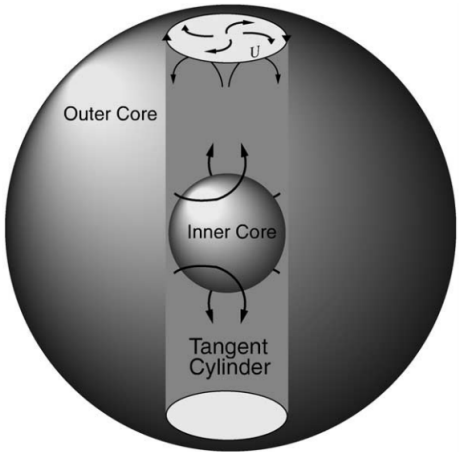

Figure 1.3: Hypothetical tangent cylinder shown within Earth's core. Taken from Aurnou et al. (2003)

Three-dimensional spherical simulations are the most suitable models for understanding magnetic field generation in planetary interiors as they capture the full dynamics of the flow. However, these can be computationally expensive to run and it is impossible to explore such extreme parameter values relevant to the physical systems in question. For example, rotation rates cannot as easily be made as extreme in spherical models compared to simplified geometry models. This means spherical models are often unable to produce some of the more detailed features such as multiple jet structures generated by zonal flows, as very large rotation rates are necessary for these features to appear. The annulus model is a simplified model of spherical geometry and the setup of the model is discussed in detail in Section 2.1. The non-magnetic case has successfully reproduced some key features of planetary convection that are often difficult to capture in full spherical shell simulations (e.g., Jones et al., 2003; Rotvig and Jones, 2006; Teed et al., 2012). The simplicity and reduced numerical complexity of the model make it possible to explore a wider range of parameter space than is typically feasible in three-dimensional spherical simulations. This allows us to investigate phenomena such as multiple jets and zonal flows,

like those observed on Jupiter, which are often challenging to capture in spherical simulations.

The annulus model was first developed by Busse (1970) where the linear theory of non-magnetic convection was explored in a collection of papers (Busse, 1970; Busse and Or, 1986; Or and Busse, 1987; Schnaubelt and Busse, 1992). Non-linear theory of convection in the non-magnetic case has been discussed in depth by Brummell and Hart (1993), Jones et al. (2003), Rotvig and Jones (2006) and Teed et al. (2012) through numerical simulations. These studies have produced bursts of convection and multiple jet solutions. Bursts of convection are a competition between convection and zonal flows. During a burst, the convection drives the zonal flow but eventually the zonal flow becomes large enough to disturb the convection which can no longer maintain the zonal flow. The zonal flow dies away and allows convection to occur again. This process repeats in a quasi-periodic fashion. Multiple jet are zonal flows which display a banded structure, similar to the jets on Jupiter's surface (Fig. 1.2).

Work in this thesis examines non-linear numerical magnetoconvection simulations in an annulus model. Linear and weakly non-linear studies of an annulus with an imposed magnetic field have previously been carried out (e.g., Busse, 1976a; Hori et al., 2014; Hutcheson and Fearn, 1995). The main control parameters involved in these studies are the Rayleigh number Ra which determines the strength of convection, η^* which controls the rotation rate, the Prandtl number Pr measuring viscous to thermal diffusivities, the magnetic Prandtl number Pm measuring viscous to magnetic diffusivities, and the Chandrasekhar number Q which controls the strength of the magnetic field. In a system subject to convective instability, there is a critical Rayleigh number Ra_c which needs to be exceeded for convection to onset. Rotating convective flows without a magnetic field can hinder convection due to the Taylor-Proudman theorem (see Section 1.3.1). Magnetic fields in a convective fluid without rotation can also hinder convection. However, rotation and magnetic effects combined can promote convection (Chandrasekhar, 1961). If the magnetic field is strong enough when combined with rotation, it can relax the Taylor-Proudman constraint and aid convection, by accessing 'magnetostrophic modes'. The rotation and magnetic field form a balance allowing convection to onset at lower Ra_c. Details of magnetoconvection can be found in Chandrasekhar (1961) and more recently by Weiss and Proctor (2014). A recent study by Horn and Aurnou (2022) demonstrated the co-existence of both geostrophic and magnetostrophic modes, for an interval of Q-space. Without a magnetic field only geostrophic modes are present but for large enough magnetic field and a sufficiently supercritical value of Ra, magnetostrophic and geostrophic modes appear together but the geostrophic modes are no longer the preferred mode.

Busse (1976a) discussed the effects of magnetic diffusion in the annulus, finding the dispersion relation for modes modified by weak magnetic diffusion. Busse and Finocchi (1993) examined the system in the limit of strong magnetic diffusion, where the marginal curves are examined for different magnetic field strengths. A linear stability analysis by Hori et al. (2014) found a variety of different waves depending on the parameter space. They found that strong magnetic diffusion (small Pm) suppressed MHD waves, but when magnetic diffusion was weak (large

Pm) they obtained MHD waves. They also considered both fixed temperature and heat flux conditions and found that these had an effect on the critical Rayleigh number. Weakly non-linear studies of an annulus model with a magnetic field have also been studied, for example by Hutcheson and Fearn (1995) and Kurt et al. (2004). The setup for the weakly non-linear studies differ to the setup in our work as we consider sloped top and bottom boundaries, in keeping with the classical model of Busse (1970). Previous work has used a variety of setups including through different boundary conditions, boundary geometry, and morphology of the imposed magnetic field. This work extends previous work on the subject by exploring the non-linear regimes of magnetoconvection in an annulus with a particular focus on how the magnetic field changes the known results of non-magnetic convection in the same model.

Although non-linear magnetoconvection simulations in an annulus model have not been explored, other geometries have been used to explore magnetoconvection. This has been explored in detail in spherical geometry, for example by Cardin and Olson (1995), Gillet et al. (2007) and Teed et al. (2015). Most recently Mason et al. (2022) examined magnetoconvection in a spherical shell where the effect of an imposed magnetic field on the flow dynamics, force balances, and zonal flow generation is examined.

1.5.2 Spherical dynamo model

The first geodynamo simulation was carried out by Glatzmaier and Roberts (1995) where they demonstrated a polarity reversal of the magnetic field. Since then there have been numerous studies examining dynamo simulations which aim to better understand magnetic field generation. Some of the key findings which are relevant to the work carried out in this thesis are highlighted below.

In convectively-driven dynamos, the four main non-dimensional input parameters are the Rayleigh number, the Ekman number, Prandtl number and the magnetic Prandtl number. The Ekman number measures the rotation rate with smaller Ekman number meaning a larger rotation rate.

The behaviour of the flow and magnetic field can be categorised by the Elsasser number Λ which measures the strength of the magnetic field, the Reynolds number Re which determines the ratio of inertial to viscous forces, the magnetic Reynolds number Rm which measures magnetic induction to diffusion and the Rossby number Ro which measures the ratio of inertial to Coriolis forces. We can relate Rm, Re and Pm by $Rm = PmRe$. Larger Re means the flow becomes more turbulent which means Rm must exceed some value for dynamo action to commence. This means Rm must be large enough and the flow complex enough for a magnetic field to be generated.

As we are unable to directly observe the flow in planetary cores, numerical dynamo simulations aim to provide a better understanding of core dynamics and the generation of planetary magnetic fields. Numerical simulations are able to provide good approximations for core dynamics

Parameter	Core	Simulations
E	10^{-15}	$10^{-6} - 10^{-3}$
Ra	10^{10}	$10 - 10^{4}$
Pr	0.1	$0.1 - 10$
Pm	10^{-6}	$0.1 - 10$

Table 1.1: Table of (approximate) parameter values for Earth's core and input parameter values used in (typical) simulations.

but the input parameters achievable in these models differ vastly from the realistic values expected in the core. The differences between the input parameters in typical simulations and approximate values for Earth's core are shown in Table 1.1. The most well known example is the Ekman number which is $O\left(10^{-15}\right)$ in Earth's core but this is usually set at $10^{-6} \leq E \leq 10^{-3}$ in numerical simulations. This causes the viscous forces to have an unrealistically large role in the simulation and may impact on the large scale dynamics in numerical simulations which is not expected to be the case in Earth's core.

Despite simulations being unable to run at the expected core values, there has been significant advancement in numerical dynamo simulations since the first geodynamo simulation by Glatzmaier and Roberts (1995). Several studies followed this, where they demonstrated that geodynamo simulations were able to produce a dipole dominated magnetic field similar to Earth (Kageyama and Sato, 1997; Kuang and Bloxham, 1997). As computing resources expanded, simulations pushed towards lower Ekman number and larger Rayleigh number. However in doing this, studies commonly found a non-dipolar field (Kageyama et al., 2008) or a weak dipolar field that is unrealistic for Earth (Takahashi et al., 2008). These studies managed to reach values of $E = 10^{-6}$ and $E = 10^{-7}$ but were unable to produce Earth-like results. Therefore, other options need to be considered in order to reach an Earth-like solution.

1.5.2.1 Dynamo regimes

Parameter space studies were carried out (Christensen et al., 1999; Christensen and Aubert, 2006; Christensen et al., 2001) which resulted in phase diagrams showing regions of parameter space where dipolar and non-dipolar dynamos were present and areas where no dynamo occurred. This led to the identification of two branches by Kutzner and Christensen (2000). These two branches of solutions showed either a dipolar solution or a multipolar solution. Oruba and Dormy (2014) demonstrated the transition between these two branches is controlled by the inertial term entering the main balance with viscous and Coriolis forces found in the dipolar solution. Bistability between these branches occurs. This was demonstrated using stress-free boundary conditions by Simitev and Busse (2009) and later shown using no-slip conditions by Petitdemange (2018).

The parameter space study carried out by Christensen and Aubert (2006) produced regime diagrams as shown in Figure 1.4. These regime diagrams considered the different types of solutions found for 6 different Ekman numbers, when Pm and Ra are varied. For moderate E,

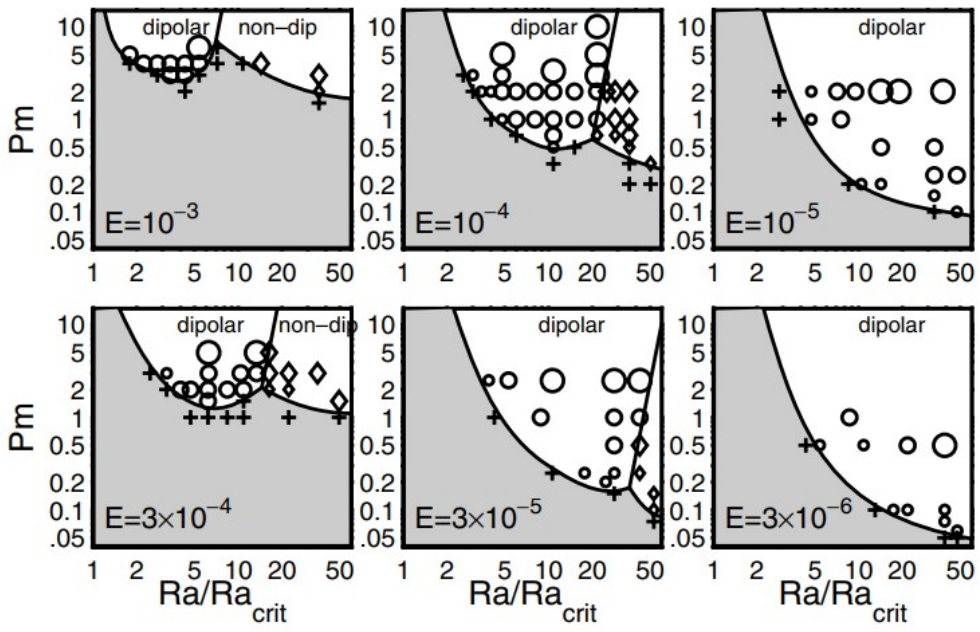

Figure 1.4: Regime diagrams at $Pr = 1$ for six different Ekman numbers, taken from Christensen and Aubert (2006). Circles show dipolar solutions, diamonds are non-dipolar solutions and crosses are failed dynamos. The size of the symbol represents the magnitude of Λ.

both dipolar and multipolar solutions are obtained. However, as E is decreased, only dipolar solutions are found for the values of Pm and Ra explored. This is due to computational limitations where it is hard to run at large enough Ra at low E where the multipolar regime manifests at larger Ra. These regime diagrams also show that the minimum Pm required for dynamos to exist decreases as E is decreased. The size of the shapes represents the magnitude of the Elsasser number Λ. These plots show evidence of dynamos with larger magnetic field strengths as Pm is increased for all E. This led to the identification of the strong field (SD) and weak field (WD) dipolar branches in numerical simulations by Dormy (2016). The WD and SD branches were first suggested by Roberts (1978), as shown in the bifurcation diagram in Figure 1.5. Convection onsets at Ra_c and increasing Ra to Ra_m generates a magnetic field. However, the magnetic field is weak and does not have a significant effect on the dynamics so this can be termed a weak field branch of solutions. Ra can be increased further to Ra_r at which point a runaway growth occurs and the magnetic field becomes strong enough to affect the flow dynamics, and solutions now lie on the strong field branch.

The possible behaviour of the weak and strong field branches has been illustrated by Dormy (2025) in a three-dimensional bifurcation diagram for a fixed value of E (Fig. 1.6). The value E_m is the magnetic Ekman number and can be related to E and Pm by $E_m = E/Pm$. For fixed E, E_m can be can be interpreted as inversely proportional to Pm. The blue circle represents a weak field solution, where two distinct paths can be followed to reach the strong field solution, given by the red circle. The Rayleigh number can be increased until the runaway growth is reached, beyond which the system undergoes a transition to the strong field branch. This path is analogous to the bifurcation diagram proposed by Roberts (1978) and is shown by the dotted green curve. Alternatively, the magnetic Ekman number can be increased and then Ra can

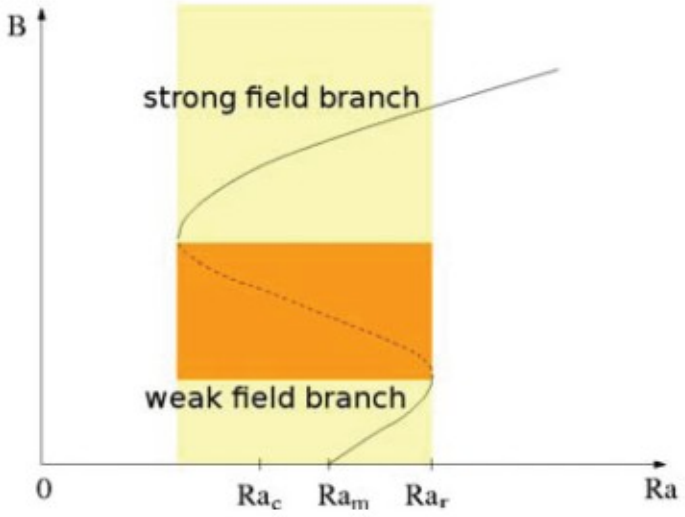

Figure 1.5: Theorised bifurcation diagram applicable to the geodynamo as suggested by Roberts (1988). The yellow region represents the space where bistability occurs and the orange region separates the two types of magnetic fields identified. This was taken from Morin et al. (2011).

be increased in order to reach the strong field solution. This is represented by the dotted red curve. The lower projection of the diagram highlights regions of bistability in parameter space, where both weak and strong field solutions can coexist. The different possible bifurcations can be explained by considering three different cases of E_m. Firstly for large E_m and low Ra only the hydrodynamical solution is found. As Ra is increased, dynamo action onsets on the weak field branch and remains there for larger Ra (until onset of the multipolar solution, which is not shown in the figure). Secondly for moderate E_m at low Ra, we lie in parameter space where only the hydrodynamical solution is possible. As Ra is increased, dynamo action onsets on the weak field branch. Then, at even larger Ra, bistability occurs where both weak and strong field solutions are found and increasing Ra further destabilises the weak field branch leading to only strong field solutions. Finally, at small enough E_m we again obtain only the hydrodynamical case at low Ra. However, there is now a region of Ra-space which allows us to obtain the hydrodynamical solution and the subcritical strong field solution. Then as we increase Ra further, we again obtain bistability between the weak field and strong field solution. Pushing Ra even further loses the bistability and only strong dipolar solutions are obtained.

The three main branches of dynamo action are the SD branch, the WD branch and the fluctuating multipolar (FM) branch. The SD branch is primarily controlled by contributions from the Lorentz, buoyancy and Coriolis forces (MAC balance) and is considered to be the most relevant to Earth's core. The WD branch contains solutions where the Lorentz force does not enter the main balance and is primarily controlled by viscous, buoyancy and Coriolis forces (VAC balance) although in some cases on this branch the inertial force might enter the main balance instead of or together with the viscous force. The FM branch contains solutions which are primarily controlled by contributions from the Coriolis, buoyancy and inertial forces (CIA balance). Rather than pushing input parameters to match Earth's core values, it has been proposed that numerical simulations of the geodynamo focus on the SD regime, which can

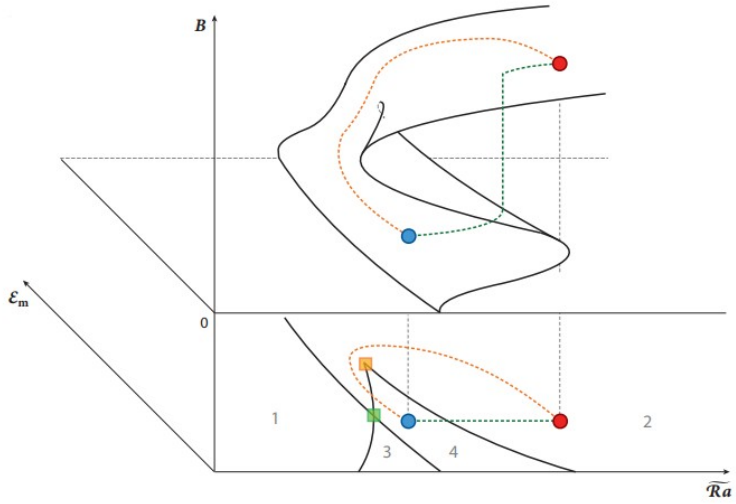

Figure 1.6: Bifurcation diagram expected for transition between weak and strong field branches. The blue circle represents the weak field solution and red circle represents the strong field solution. The dotted green curve represents the runaway field growth and the dotted red curve represents a continuous path from the weak to the strong field branch. This was taken from Dormy (2025).

be achieved using moderate input parameters. One way to assess whether simulations have successfully reached the SD regime without relying on bifurcation diagrams is to examine the force balances in the system. This is discussed in more detail in the next section.

1.5.2.2 Force balances

Force balance studies are used to assess which regime a simulation lies in and are usually guided by bifurcation diagrams. Studies by Soderlund et al. (2015) and Yadav et al. (2016) have examined globally averaged force balances which allowed them to study the interaction of Lorentz and Coriolis forces. Aubert et al. (2017) extended this by studying the lengthscale dependence of the forces controlling the dynamics of the flow. In this analysis they found a leading order geostrophic balance, at least at large scales. However, the pressure gradient is not important as it does not impact the dynamics of the flow (Hughes and Cattaneo, 2019). This is because when solving the system of equations we take the curl and double curl of the momentum equation (Equation 1.1). In order to recover the important first order balance, they formed the ageostrophic Coriolis force by subtracting the pressure gradient from the Coriolis force. It is the first order balance which is most important as this controls the dynamics of the flow. Therefore, from now on, we refer to the forces controlling the dynamics as the first order balance and the unimportant balance involving the pressure gradient at leading order will be referred to as the zeroth order balance.

The ageostrophic Coriolis force is formed based on the assumption that only the gradient parts of the Coriolis force balance the pressure gradient. However, all forces may have gradient parts that balance with the pressure gradient. An alternative approach to deal with the gradient parts of forces was discussed in a recent study by Teed and Dormy (2023) where balances of forces and

solenoidal forces are examined. Solenoidal forces are a way to represent forces without gradient parts. One way of forming the solenoidal forces is by taking the curl of each force, allowing for the removal of the pressure gradient and gradient parts of other forces which do not impact the dynamics of the flow. In forming these they found that this removed the geostrophic balance at zeroth order and instead recovered the important force balance found at leading order. This thesis will use this approach for forming solenoidal forces. Force balances in rotating spherical shell convection has been studied by Naskar et al. (2025), where forces and curls of forces were discussed. At low Ra, they found the VAC balance to be important and as Ra was increased the inertial force also entered the VAC balance. Guervilly and Dormy (2025) also examined rapidly rotating convection in both spherical and planar geometries. Their results show that, regardless of geometry, the dominant flow length scale is determined by either viscous or inertial scale depending on the flow speed.

Studies of the lengthscale dependent forces in dynamo simulations have been examined in great detail by Schwaiger et al. (2019) and Schwaiger et al. (2021), where they focused on relating energetically relevant lengthscales to dynamically relevant lengthscales. In order to do this, they examined crossover points of the relevant forces in the lengthscale dependence plots. This was done by considering crossing points of the Lorentz and buoyancy forces and inertia and buoyancy forces which were compared with the peaks in the poloidal kinetic energy spectrum. For magnetically dominated results they argued that the crossing points of Lorentz and buoyancy forces determine the peak lengthscale in the poloidal kinetic energy spectrum, and for hydrodynamical runs with sufficient driving they argued that the crossing between inertial and buoyancy forces determines the peak lengthscale in the poloidal kinetic energy spectrum. Another relevant balance in simulations is the VAC balance. However, they did not consider the crossing between viscous and buoyancy forces. In Chapter 5 we examine simulations by comparing the kinetic energy spectra with crossings examined by Schwaiger et al. (2019) and Schwaiger et al. (2021) and also consider crossing points between viscous and buoyancy forces. These studies by Schwaiger et al. (2019) and Schwaiger et al. (2021) only considered two of the three forces usually involved in the main balance. In all three cases, the Coriolis force is also important. Naskar et al. (2025) showed that curls of forces in rotating spherical convection did not have clear crossing points when examining the lengthscale dependence of curls of forces. In Chapter 5 we expand on this work by forming a triple balance point between the three relevant forces and compare these to the peak lengthscale in the kinetic energy spectra. This allows us to include the relevant Coriolis force and analyse simulations which do not have crossing points of relevant forces.

1.5.2.3 Convection inside and outside the tangent cylinder

As discussed earlier, a hypothetical tangent cylinder can be defined which runs from pole to pole and touches the inner core boundary (Fig. 1.3). This helps to improve our understanding of convection in the spherical shell. Busse and Cuong (1977) conducted an analytical study of rotating spherical shell convection in the limit of rapid rotation and demonstrated that

convective behaviour differs significantly inside and outside the tangent cylinder with convection OTC onsetting at lower Ra and convection ITC developing only when the temperature gradient is sufficiently large. Subsequent studies have investigated these dynamics in more detail where Gillet and Jones (2006) demonstrated the behaviour outside the tangent cylinder and studies by Sreenivasan and Jones (2005) and Cao et al. (2018) demonstrated the behaviour inside the tangent cylinder using spherical dynamo simulations. Most recently, Gastine and Aurnou (2023) performed spherical shell simulations to analyse heat transfer properties inside and outside the tangent cylinder. They found that the dynamics in a spherical shell at the polar regions exhibit good agreement with Cartesian simulations. Furthermore, they showed that although convection ITC onsets at a higher Ra than OTC, once it does so it becomes more turbulent and is able to transport heat more efficiently as Ra is increased further. Since the flow patterns and development of flows ITC and OTC might differ as Ra is varied, it is reasonable to speculate that the hierarchy of forces ITC and OTC may also differ. Chapter 6 discusses the force balances ITC and OTC.

1.6 THESIS OUTLINE

This thesis explores convective fluid flows under the influence of rotation and magnetic fields. Simulations are performed using two models: in an annulus model with an imposed magnetic field and a spherical shell model capable of the self-excitation of magnetic fields. Chapter 2 discusses the mathematical setup, numerical methods and output parameters of both models and Chapter 7 concludes the work in this thesis and outlines potential future work. The main research chapters are as follows:

- **Chapter 3** examines force balances in the annulus model by performing a wide parameter sweep. Non-magnetic results are discussed and compared with known previous work. Globally averaged quantities and lengthscale dependence of the curls of forces are examined as the magnetic field strength, magnetic diffusion and Rayleigh number are varied. We examine how these compare with force balances found in the main regimes of dynamo action and summarise our findings in a regime diagram.

- **Chapter 4** discusses multiple jet solutions with a focus on the effect of varying magnetic field strength on the multiple jet structures known to exist in the non-magnetic case. The forces required to produce multiple jet solutions are discussed. This chapter has been published in Geophysical and Astrophysical Fluid Dynamics (Hunter and Teed, 2024).

- **Chapter 5** examines force balances in spherical dynamo simulations. We focus on two different lengthscales for forces and curls of forces, discussing the types of force balance, flow pattern and magnetic field morphology that occur in the main regimes of dynamo action. A triple force balance point (dynamic lengthscale) is introduced and this is compared with peaks in the energy (energetic lengthscale), with the aim of finding a correlation between dynamically relevant lengthscales and energetically relevant lengthscales for forces

and curls of forces. This triple balance point extends work by Schwaiger et al. (2021) where triple balance points are formed instead of crossovers for two different lengthscales and the forces and solenoidal forces are presented, rather than only the forces.

- **Chapter 6** compares balances of forces and solenoidal forces ITC and OTC. Firstly, the balances ITC and OTC for the main regimes of dynamo action are examined. Secondly, solenoidal forces are presented as transitions occur between dynamo regimes, in order to compare similarities and differences between the regions ITC and OTC.

Chapter 2

Methods

This thesis explores convective fluid flows under the influence of rotation and magnetic fields. Simulations are performed using two models: an annulus model with an imposed magnetic field and a spherical shell model capable of the self-excitation of magnetic fields. This chapter discusses the mathematical setup, numerical method and various input and output parameters of each model.

2.1 Busse annulus model with an imposed magnetic field

In Chapters 3 and 4 we consider a cylindrical annulus filled with fluid as shown in Figure 2.1. We have sloped top and bottom boundaries which have angle χ with the horizontal. The gap between the two cylinders is of width D, the height of the outer walls of the annulus is L, and the mean radius is given by r_o. The annulus rotates about the axial direction with the rotation rate given by Ω. We have a temperature gradient β which acts between the outer and inner side walls of the annulus. In our model gravity acts inwards so that the gravity and rotation axes are orthogonal to each other. We impose a uniform azimuthal magnetic field of strength B_0. The obvious choice for a coordinate system would be to use cylindrical coordinates. However, we can make the small gap approximation which means we assume the distance D between the cylindrical side walls is small compared with the mean radius r_o, allowing us to ignore the effects of curvature and use a Cartesian coordinate system. We have coordinates x which is the azimuthal coordinate, y is the radial coordinate with $0 \leq y \leq D$ and z is the axial coordinate with $-L/2 \leq z \leq L/2$. Then the annulus rotates with angular velocity $\mathbf{\Omega} = \Omega\hat{\mathbf{z}}$, gravity is given by $\mathbf{g} = g_0\hat{\mathbf{y}}$ and the imposed magnetic field has the form $\mathbf{B_0} = B_0\hat{\mathbf{x}}$. In the context of the geodynamo this corresponds to a toroidal magnetic field. The fluid is contained within the annulus so we require a no-penetration condition on all boundaries. This means that

$$\mathbf{U} \cdot \mathbf{n} = 0$$

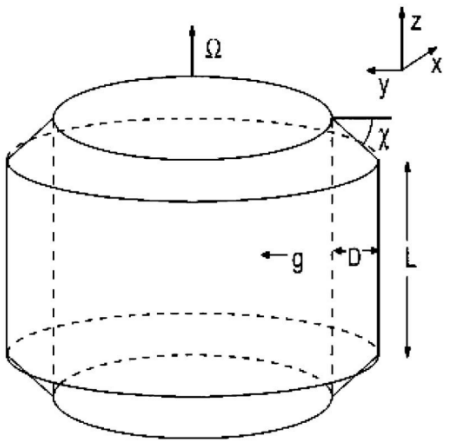

Figure 2.1: Diagram showing the setup of the annulus model. Taken from Jones (2007).

where $\mathbf{n}$ is a normal vector at the boundary. At the annulus lids, this condition depends on the angle χ between the sloped walls and the horizontal where we obtain

$$\cos(\chi)\, u_z \mp \sin(\chi)\, u_y = 0 \tag{2.1}$$

on $z = \pm L/2$.

2.1.1 Governing equations

2.1.1.1 Momentum equation

To derive a set of equations we start from the Navier-Stokes equation given by Equation (1.22) and take the curl to obtain

$$\frac{\partial \mathbf{Z}}{\partial t} + (\mathbf{U}\cdot\nabla)\,\mathbf{Z} - ((2\boldsymbol{\Omega}+\mathbf{Z})\,.\nabla)\,\mathbf{U} = -\alpha\mathbf{g}\times\nabla T + \nu\nabla^2\mathbf{Z} + \frac{1}{\mu_0\rho_0}\nabla\times((\mathbf{B}\cdot\nabla)\,\mathbf{B}) \tag{2.2}$$

where $\mathbf{Z} = \nabla\times\mathbf{U}$ and is the vorticity. We can then take the z-component of (2.2) and substitute in the forms of $\mathbf{g}$ and $\boldsymbol{\Omega}$ to obtain

$$\frac{\partial Z}{\partial t} + \mathbf{U}\cdot\nabla Z - 2\Omega\hat{\mathbf{z}}\cdot\frac{\partial \mathbf{U}}{\partial z} = -g_0\alpha\frac{\partial T}{\partial x} + \nu\nabla^2 Z + \frac{1}{\mu_0\rho_0}\hat{\mathbf{z}}\cdot[\nabla\times((\mathbf{B}\cdot\nabla)\,\mathbf{B})] \tag{2.3}$$

where Z is the z-component of the vorticity. We have neglected the $(\mathbf{Z}\cdot\nabla)\,\mathbf{U}$ term when taking the curl of the Navier-Stokes equation as we are interested in the case where we have rapid planetary rotation. This means $|2\boldsymbol{\Omega}| \gg |\mathbf{Z}|$ as the planetary rotation dominates over the fluid vorticity. The term which involves $\nabla\times((\mathbf{B}\cdot\nabla)\,\mathbf{B})$ is made up of two terms. One of these is $(\mathbf{B}\cdot\nabla)\,\nabla\times\mathbf{B}$ and another term which contains no z-components. Therefore we can rewrite the last term in (2.3) as $\hat{\mathbf{z}}\cdot[(\mathbf{B}\cdot\nabla)\,\nabla\times\mathbf{B}]$.

The basic state is given by $\mathbf{U} = \mathbf{U}_0 = \mathbf{0}$, $Z = \zeta_0 = 0$, $\mathbf{B} = \mathbf{B}_0$, $T = T_0 = \beta y$ and we perturb

around this by setting

$$\begin{aligned} \mathbf{U} &= \mathbf{u} \\ Z &= \zeta \\ \mathbf{B} &= \mathbf{B_0} + \mathbf{b} \\ T &= T_0 + \theta. \end{aligned} \tag{2.4}$$

In the rapidly rotating limit, we assume the sloped boundaries are nearly flat so $\chi \ll 1$, the flow can be assumed to be quasi-geostrophic meaning the z-component of the velocity $\mathbf{u}$ is small compared with the x and y-components. This allows us to make the ansatz

$$\mathbf{u} = \nabla \times \psi\,(x, y)\,\hat{\mathbf{z}} = \frac{\partial \psi}{\partial y}\hat{\mathbf{x}} - \frac{\partial \psi}{\partial x}\hat{\mathbf{y}}, \tag{2.5}$$

for the velocity where the vertical component, $u_z \ll u_x, u_y$. Following Hori et al. (2014), and for convenience, we choose an equivalent form for the magnetic field:

$$\mathbf{b} = \nabla \times g\,(x, y)\,\hat{\mathbf{z}} = \frac{\partial g}{\partial y}\hat{\mathbf{x}} - \frac{\partial g}{\partial x}\hat{\mathbf{y}}. \tag{2.6}$$

We can obtain ζ by considering

$$\begin{aligned} \boldsymbol{\zeta} &= \nabla \times \mathbf{u} \\ &= \nabla \times \nabla \times \psi\hat{\mathbf{z}} \\ &= \nabla\,(\nabla \cdot \psi\hat{\mathbf{z}}) - \nabla^2\psi\hat{\mathbf{z}} \\ &= -\nabla^2\psi\hat{\mathbf{z}} \\ \implies \zeta &= -\nabla^2\psi. \end{aligned} \tag{2.7}$$

Similarly, taking the curl of (2.6) gives

$$\begin{aligned} \nabla \times \mathbf{b} &= \nabla \times \nabla \times g\hat{\mathbf{z}} \\ &= \nabla\,(\nabla \cdot g\hat{\mathbf{z}}) - \nabla^2 g\hat{\mathbf{z}} \\ &= -\nabla^2 g\hat{\mathbf{z}}. \end{aligned} \tag{2.8}$$

Since χ is small, the end wall boundary conditions given by Equation (2.1) become

$$\begin{aligned} u_z &= \pm\chi u_y \\ \implies u_z &= \mp\chi\frac{\partial \psi}{\partial x} \end{aligned}$$

on $z = \pm L/2$. In our model we are also interested in studying multiple jet solutions which are more readily produced through the addition of a bottom friction term in the equations (Rotvig

and Jones, 2006; Teed et al., 2012). We add this term to u_z at the boundary to obtain

$$u_z = \mp\chi\frac{\partial\psi}{\partial x} + U_E. \tag{2.9}$$

In the equation above U_E is the optional Ekman suction term derived using a method by Greenspan (1968) and is given by

$$U_E = \mp\frac{1}{2}\left(\frac{\nu}{\Omega}\right)^{1/2}\hat{\mathbf{n}}\cdot\nabla\times\left(\frac{1}{|\hat{\mathbf{n}}\cdot\hat{\mathbf{z}}|^{1/2}}\left(\hat{\mathbf{n}}\times\mathbf{u}+\mathbf{u}\right)\right). \tag{2.10}$$

The Ekman suction term has been used in quasi-geostrophic models, for example Jones et al. (2003), and Rotvig and Jones (2006), and is added to replicate the effects of an Ekman boundary layer when rigid top and bottom boundaries are implemented. This is absent in the case of stress-free top and bottom boundaries. This term dampens the zonal flow in the system, but increases the possibility of multiple jets. Taking $\hat{\mathbf{n}} = \hat{\mathbf{z}}$, Equation (2.10) becomes

$$U_E = \mp\frac{1}{2}\left(\frac{\nu}{\Omega}\right)^{1/2}\zeta.$$

Substituting this into (2.9) gives

$$u_z = \mp\chi\frac{\partial\psi}{\partial x} \mp \frac{1}{2}\left(\frac{\nu}{\Omega}\right)^{1/2}\zeta \tag{2.11}$$

on $z = \pm L/2$.

We can then substitute the perturbed forms given by (2.4) into (2.3) to obtain

$$\begin{aligned}
&\frac{\partial\zeta}{\partial t} + u_x\frac{\partial\zeta}{\partial x} + u_y\frac{\partial\zeta}{\partial y} - 2\Omega\frac{\partial u_z}{\partial z} = -g_0\alpha\frac{\partial\theta}{\partial x} + \nu\nabla^2\zeta \\
&\quad - \frac{1}{\mu_0\rho_0}B_0\frac{\partial\nabla^2 g}{\partial x} + \frac{1}{\mu_0\rho_0}\left(\frac{\partial g}{\partial x}\frac{\partial\nabla^2 g}{\partial y} - \frac{\partial\nabla^2 g}{\partial x}\frac{\partial g}{\partial y}\right) \\
\implies &\frac{\partial\zeta}{\partial t} + \frac{\partial\psi}{\partial y}\frac{\partial\zeta}{\partial x} - \frac{\partial\psi}{\partial x}\frac{\partial\zeta}{\partial y} - 2\Omega\frac{\partial u_z}{\partial z} = -g_0\alpha\frac{\partial\theta}{\partial x} + \nu\nabla^2\zeta \\
&\quad - \frac{1}{\mu_0\rho_0}B_0\frac{\partial\nabla^2 g}{\partial x} + \frac{1}{\mu_0\rho_0}\left(\frac{\partial g}{\partial x}\frac{\partial\nabla^2 g}{\partial y} - \frac{\partial\nabla^2 g}{\partial x}\frac{\partial g}{\partial y}\right) \\
\implies &\frac{\partial\zeta}{\partial t} + +\frac{\partial(\zeta,\psi)}{\partial(x,y)} - 2\Omega\frac{\partial u_z}{\partial z} = -g_0\alpha\frac{\partial\theta}{\partial x} + \nu\nabla^2\zeta \\
&\quad - \frac{1}{\mu_0\rho_0}B_0\frac{\partial\nabla^2 g}{\partial x} + \frac{1}{\mu_0\rho_0}\frac{\partial(g,\nabla^2 g)}{\partial(x,y)}
\end{aligned} \tag{2.12}$$

where we have substituted for $\mathbf{u}$ using (2.7) and for $\mathbf{b}$ using (2.8) and have used the Jacobian defined by

$$\frac{\partial(f_1,f_2)}{\partial(x,y)} = \frac{\partial f_1}{\partial x}\frac{\partial f_2}{\partial y} - \frac{\partial f_2}{\partial x}\frac{\partial f_1}{\partial y}$$

for some functions f_1 and f_2.

We now aim to remove the u_z term in (2.12). To do this we integrate over z between $-L/2$ and $L/2$ to obtain

$$\begin{aligned} &L\frac{\partial\zeta}{\partial t}+L\frac{\partial\left(\zeta,\psi\right)}{\partial\left(x,y\right)}-2\Omega\left[u_z\right]_{-L/2}^{L/2}=-Lg_0\alpha\frac{\partial\theta}{\partial x}+L\nu\nabla^2\zeta\\ &-\frac{L}{\mu_0\rho_0}B_0\frac{\partial\nabla^2 g}{\partial x}+\frac{L}{\mu_0\rho_0}\frac{\partial\left(g,\nabla^2 g\right)}{\partial\left(x,y\right)}. \end{aligned} \tag{2.13}$$

Using (2.11) we obtain

$$\begin{aligned} &\frac{\partial\zeta}{\partial t}+\frac{\partial\left(\zeta,\psi\right)}{\partial\left(x,y\right)}+\frac{4\Omega\chi}{L}\frac{\partial\psi}{\partial x}+\frac{2\Omega}{L}\left(\frac{\nu}{\Omega}\right)^{1/2}\zeta=-g_0\alpha\frac{\partial\theta}{\partial x}+\nu\nabla^2\zeta\\ &-\frac{1}{\mu_0\rho_0}B_0\frac{\partial\nabla^2 g}{\partial x}+\frac{1}{\mu_0\rho_0}\frac{\partial\left(g,\nabla^2 g\right)}{\partial\left(x,y\right)}. \end{aligned} \tag{2.14}$$

Using (2.7), Equation (2.14) becomes

$$\begin{aligned} &-\frac{\partial\nabla^2\psi}{\partial t}-\frac{\partial\left(\nabla^2\psi,\psi\right)}{\partial\left(x,y\right)}+\frac{4\Omega\chi}{L}\frac{\partial\psi}{\partial x}-\frac{2\Omega}{L}\left(\frac{\nu}{\Omega}\right)^{1/2}\nabla^2\psi\\ &=-g_0\alpha\frac{\partial\theta}{\partial x}-\nu\nabla^4\psi-\frac{1}{\mu_0\rho_0}B_0\frac{\partial\nabla^2 g}{\partial x}+\frac{1}{\mu_0\rho_0}\frac{\partial\left(g,\nabla^2 g\right)}{\partial\left(x,y\right)}\\ \implies &\frac{\partial\nabla^2\psi}{\partial t}+\frac{\partial\left(\nabla^2\psi,\psi\right)}{\partial\left(x,y\right)}-\frac{4\Omega\chi}{L}\frac{\partial\psi}{\partial x}+\frac{2\Omega}{L}\left(\frac{\nu}{\Omega}\right)^{1/2}\nabla^2\psi\\ &=g_0\alpha\frac{\partial\theta}{\partial x}+\nu\nabla^4\psi+\frac{1}{\mu_0\rho_0}B_0\frac{\partial\nabla^2 g}{\partial x}-\frac{1}{\mu_0\rho_0}\frac{\partial\left(g,\nabla^2 g\right)}{\partial\left(x,y\right)}. \end{aligned} \tag{2.15}$$

2.1.1.2 HEAT EQUATION

We now consider the heat equation given by Equation (1.23) and substitute in the perturbed forms given by (2.4) to obtain

$$\begin{aligned} &\frac{\partial\theta}{\partial t}+\left(u_x\frac{\partial}{\partial x}+u_y\frac{\partial}{\partial y}\right)\left(T_0+\theta\right)=\kappa\nabla^2\theta\\ \implies &\frac{\partial\theta}{\partial t}+u_y\frac{\partial T_0}{\partial y}+u_x\frac{\partial\theta}{\partial x}+u_y\frac{\partial\theta}{\partial y}=\kappa\nabla^2\theta\\ \implies &\frac{\partial\theta}{\partial t}-\beta\frac{\partial\psi}{\partial x}+\frac{\partial\psi}{\partial y}\frac{\partial\theta}{\partial x}-\frac{\partial\psi}{\partial x}\frac{\partial\theta}{\partial y}=\kappa\nabla^2\theta\\ \implies &\frac{\partial\theta}{\partial t}-\beta\frac{\partial\psi}{\partial x}+\frac{\partial\left(\theta,\psi\right)}{\partial\left(x,y\right)}=\kappa\nabla^2\theta \end{aligned} \tag{2.16}$$

where we have substituted in u_x and u_y and have used $T_0=\beta y$.

2.1.1.3 INDUCTION EQUATION

We consider the induction equation given by (1.24), taking the curl and substituting in the perturbed forms given by (2.4) we have

$$\begin{aligned}
&\frac{\partial \nabla \times \mathbf{B}}{\partial t} = \nabla \times (\nabla \times (\mathbf{U} \times \mathbf{B})) + \lambda \nabla^2 \nabla \times \mathbf{B} \\
\implies &\frac{\partial \nabla \times \mathbf{b}}{\partial t} = \nabla \times \nabla \times (\mathbf{u} \times (\mathbf{B_0} + \mathbf{b})) + \lambda \nabla^2 \nabla \times (\mathbf{B_0} + \mathbf{b}) \\
\implies &-\frac{\partial \nabla^2 g \hat{\mathbf{z}}}{\partial t} = \nabla \times \nabla \times (\mathbf{u} \times (\mathbf{B_0} + \mathbf{b})) - \lambda \nabla^4 g \hat{\mathbf{z}}.
\end{aligned} \tag{2.17}$$

The first term on the right-hand side can be expanded to obtain

$$\nabla \times \nabla \times (\mathbf{u} \times (\mathbf{B_0} + \mathbf{b})) = \nabla \times \nabla \times (\mathbf{u} \times \mathbf{B_0}) + \nabla \times \nabla \times (\mathbf{u} \times \mathbf{b}) .$$

Considering both terms individually, for the first term we have

$$\mathbf{u} \times \mathbf{B_0} = B_0 \frac{\partial \psi}{\partial x} \hat{\mathbf{z}}$$

and hence

$$\begin{aligned}
\nabla \times \nabla \times (\mathbf{u} \times \mathbf{B_0}) &= \nabla \left(\nabla \cdot B_0 \frac{\partial \psi}{\partial x} \hat{\mathbf{z}} \right) - \nabla^2 \left(B_0 \frac{\partial \psi}{\partial x} \hat{\mathbf{z}} \right) \\
&= -B_0 \frac{\partial \nabla^2 \psi}{\partial x} \hat{\mathbf{z}}.
\end{aligned} \tag{2.18}$$

We now consider the second term. First, we calculate

$$\begin{aligned}
\mathbf{u} \times \mathbf{b} &= (\nabla \times \psi \hat{\mathbf{z}}) \times (\nabla \times g \hat{\mathbf{z}}) \\
&= \left(\frac{\partial \psi}{\partial y} \hat{\mathbf{x}} - \frac{\partial \psi}{\partial x} \hat{\mathbf{y}} \right) \times \left(\frac{\partial g}{\partial y} \hat{\mathbf{x}} - \frac{\partial g}{\partial x} \hat{\mathbf{y}} \right) \\
&= \frac{\partial (\psi, g)}{\partial (x, y)} \hat{\mathbf{z}}.
\end{aligned}$$

Then we have

$$\begin{aligned}
\nabla \times \nabla \times (\mathbf{u} \times \mathbf{b}) &= \nabla \left(\nabla \cdot \frac{\partial (\psi, g)}{\partial (x, y)} \hat{\mathbf{z}} \right) - \nabla^2 \frac{\partial (\psi, g)}{\partial (x, y)} \hat{\mathbf{z}} \\
&= -\nabla^2 \frac{\partial (\psi, g)}{\partial (x, y)} \hat{\mathbf{z}}.
\end{aligned} \tag{2.19}$$

Substituting equations (2.18) and (2.19) into (2.17) and taking the z-component we obtain the

induction equation in the non-linearised form given as

$$\frac{\partial \nabla^2 g}{\partial t} = B_0 \frac{\partial \nabla^2 \psi}{\partial x} + \nabla^2 \frac{\partial (\psi, g)}{\partial (x, y)} + \lambda \nabla^4 g. \tag{2.20}$$

2.1.1.4 NON-DIMENSIONALISATION

We now non-dimensionalise using a length scale D, a temperature scale βD, a viscous timescale D^2/ν and a magnetic scale B_0. This means that $x \to D\tilde{x}$, $y \to D\tilde{y}$, $\psi \to \tilde{\psi}\nu$, $\theta \to \tilde{\theta}\beta D$, $t \to \tilde{t}D^2/\nu$, $B_0 \to \tilde{B}_0$ and $g \to \tilde{g}B_0 D$. Then the momentum equation (2.15) becomes

$$\begin{aligned}
&\frac{\nu^2}{D^4}\frac{\partial \nabla^2 \tilde{\psi}}{\partial \tilde{t}} + \frac{\nu^2}{D^4}\frac{\partial \left(\nabla^2 \tilde{\psi}, \tilde{\psi}\right)}{\partial (\tilde{x}, \tilde{y})} - \frac{4\chi\Omega\nu}{DL}\frac{\partial \tilde{\psi}}{\partial \tilde{x}} + \frac{2\Omega\nu}{LD^2}\left(\frac{\nu}{\Omega}\right)^{1/2}\tilde{\nabla}^2\tilde{\psi} \\
&= g_0\alpha\beta\frac{\partial \tilde{\theta}}{\partial \tilde{x}} + \frac{\nu^2}{D^4}\nabla^4\tilde{\psi} + \frac{1}{\mu_0\rho_0}\frac{B_0\tilde{B}_0}{D^2}\frac{\partial \nabla^2 \tilde{g}}{\partial \tilde{x}} - \frac{1}{\mu_0\rho_0}\frac{B_0^2}{D^2}\frac{\partial (\tilde{g}, \nabla^2\tilde{g})}{\partial (\tilde{x}, \tilde{y})} \\
\implies &\frac{\partial \nabla^2 \tilde{\psi}}{\partial \tilde{t}} + \frac{\partial \left(\nabla^2 \tilde{\psi}, \tilde{\psi}\right)}{\partial (\tilde{x}, \tilde{y})} - \frac{4\chi\Omega D^3}{\nu L}\frac{\partial \tilde{\psi}}{\partial \tilde{x}} + \frac{2\Omega D^2}{L\nu}\left(\frac{\nu}{\Omega}\right)^{1/2}\tilde{\nabla}^2\tilde{\psi} \\
&= \frac{g_0\alpha\beta D^4}{\nu^2}\frac{\partial \tilde{\theta}}{\partial \tilde{x}} + \nabla^4\tilde{\psi} + \frac{1}{\mu_0\rho_0}\frac{B_0 D^2}{\nu^2}\tilde{B}_0\frac{\partial \nabla^2 \tilde{g}}{\partial \tilde{x}} - \frac{B_0^2 D^2}{\mu_0\rho_0\nu^2}\frac{\partial (\tilde{g}, \nabla^2\tilde{g})}{\partial (\tilde{x}, \tilde{y})}.
\end{aligned}$$

The temperature equation (2.16) becomes

$$\begin{aligned}
&\frac{\beta\nu}{D}\frac{\partial \tilde{\theta}}{\partial \tilde{t}} - \frac{\beta\nu}{D}\frac{\partial \tilde{\psi}}{\partial \tilde{x}} + \frac{\beta\nu}{D}\frac{\partial \left(\tilde{\theta}, \tilde{\psi}\right)}{\partial (\tilde{x}, \tilde{y})} = \frac{\kappa\beta}{D}\nabla^2\tilde{\theta} \\
\implies &\frac{\partial \tilde{\theta}}{\partial \tilde{t}} - \frac{\partial \tilde{\psi}}{\partial \tilde{x}} + \frac{\partial \left(\tilde{\theta}, \tilde{\psi}\right)}{\partial (\tilde{x}, \tilde{y})} = \frac{\kappa}{\nu}\nabla^2\tilde{\theta}.
\end{aligned}$$

The induction equation (2.20) becomes

$$\begin{aligned}
&\frac{B_0\nu}{D^3}\frac{\partial \nabla^2 \tilde{g}}{\partial \tilde{t}} = \frac{\tilde{B}_0\nu}{D^3}\frac{\partial \tilde{\nabla}^2 \tilde{\psi}}{\partial \tilde{x}} + \frac{B_0\nu}{D^3}\tilde{\nabla}^2\frac{\partial \left(\tilde{\psi}, \tilde{g}\right)}{\partial (\tilde{x}, \tilde{y})} + \frac{B_0\lambda}{D^3}\tilde{\nabla}^4\tilde{g} \\
\implies &\frac{\partial \nabla^2 \tilde{g}}{\partial \tilde{t}} = \frac{\partial \tilde{\nabla}^2 \tilde{\psi}}{\partial \tilde{x}} + \tilde{\nabla}^2\frac{\partial \left(\tilde{\psi}, \tilde{g}\right)}{\partial (\tilde{x}, \tilde{y})} + \frac{\lambda}{\nu}\tilde{\nabla}^4\tilde{g}.
\end{aligned}$$

We now introduce dimensionless parameters and drop the tildes (for convenience) to obtain the momentum equation as

$$\begin{aligned}
&\frac{\partial \nabla^2 \psi}{\partial t} + \frac{\partial (\nabla^2\psi, \psi)}{\partial (x, y)} - \eta^*\frac{\partial \psi}{\partial x} + B_f\left|\eta^*\right|^{1/2}\nabla^2\psi \\
&= \frac{Ra}{Pr}\frac{\partial \theta}{\partial x} + \nabla^4\psi + \frac{Q}{Pm}\frac{\partial \nabla^2 g}{\partial x} - \frac{Q}{Pm}\frac{\partial (g, \nabla^2 g)}{\partial (x, y)},
\end{aligned} \tag{2.21}$$

the temperature equation as

$$\frac{\partial\theta}{\partial t} - \frac{\partial\psi}{\partial x} + \frac{\partial\left(\theta,\psi\right)}{\partial\left(x,y\right)} = \frac{1}{Pr}\nabla^2\theta, \tag{2.22}$$

and the induction equation as

$$\frac{\partial\nabla^2 g}{\partial t} = \frac{\partial\nabla^2\psi}{\partial x} + \nabla^2\frac{\partial\left(\psi,g\right)}{\partial\left(x,y\right)} + \frac{1}{Pm}\nabla^4 g, \tag{2.23}$$

where

$$\eta^* = \frac{4\chi\Omega D^3}{\nu L},\ Pr = \frac{\nu}{\kappa},\ Pm = \frac{\nu}{\lambda},\ Ra = \frac{g_0\alpha\beta D^4}{\nu\kappa},\ Q = \frac{B_0^2 D^2}{\rho_0\mu_0\nu\lambda} \text{ and } B_f = \left(\frac{D}{L\chi}\right)^{1/2}.$$

The rotation rate is given by η^*, Pr is the Prandtl number, Pm the magnetic Prandtl number, Ra is the Rayleigh number determining the strength of convection, Q measures the magnetic field strength and B_f is a parameter controlling the strength of the effect of the bottom friction. In the annulus model η^* is inversely related to the Ekman number through $E = \left(2D\chi\right)/\left(L\eta^*\right)$ and therefore in the limit of rapid rotation η^* is large. The Prandtl number measures the strength of viscous to thermal diffusivities, magnetic Prandtl number measures the strength of viscous to magnetic diffusivities. The Rayleigh number is essential for convection problems. This was introduced by Rayleigh (1916) and determines whether a system is convecting or not. For a given system there exists a critical Rayleigh number Ra_c. If Ra exceeds Ra_c then convective instabilities will grow. However if Ra is less than Ra_c then the instabilities will decay. The magnetic field strength Q is similar to the Chandrasekhar number introduced by Chandrasekhar (1961). The parameter B_f has been found to be important in previous non-magnetic studies, as this promotes the creation of multiple jets in the solution. If we are considering stress-free boundaries then $B_f = 0$ and for rigid boundaries we require $B_f \neq 0$.

On the inner and outer annular walls, we assume stress-free, electrically conducting, constant temperature boundaries. Hence the boundary conditions are

$$u_y = 0 \implies \frac{\partial\psi}{\partial x} = 0, \tag{2.24}$$

$$\frac{\partial u_x}{\partial y} = 0 \implies \frac{\partial^2\psi}{\partial y^2} = 0, \tag{2.25}$$

$$\theta = 0, \tag{2.26}$$

$$b_y = 0 \implies \frac{\partial g}{\partial x} = 0, \tag{2.27}$$

on $y = 0, 1$. Equations (2.24) and (2.27) implies that ψ and g are constant at the boundary.

2.1.1.5 OBTAINING A CRITICAL RAYLEIGH NUMBER

Equations (2.21)-(2.23) can be solved linearly in the non-magnetic and magnetic case. In the non-magnetic case the magnetic and non-linear terms in (2.21) are dropped and the induction equation given by (2.23) is ignored. The system can then be solved to obtain a critical Rayleigh number in the hydrodynamical case denoted by Ra_c^{HD}. In the magnetic case, the non-linear terms are dropped and the system can be solved for a critical Rayleigh number in the magnetic case denoted by Ra_c^{MC}. In our simulations, we set the Rayleigh number Ra by considering Ra/Ra_c^{HD}, as this allows for a more direct comparison between runs instead of using the magnetic critical Rayleigh number Ra_c^{MC}. In order to obtain an expression for a critical Rayleigh number Ra_c we consider the linear form of equations (2.21)-(2.23), which are

$$\frac{\partial \nabla^2 \psi}{\partial t} - \eta^* \frac{\partial \psi}{\partial x} = \frac{Ra}{Pr}\frac{\partial \theta}{\partial x} + \nabla^4 \psi + \frac{Q}{Pm}\frac{\partial \nabla^2 g}{\partial x} \tag{2.28}$$

$$\frac{\partial \theta}{\partial t} - \frac{\partial \psi}{\partial x} = \frac{1}{Pr}\nabla^2 \theta \tag{2.29}$$

$$\frac{\partial \nabla^2 g}{\partial t} = \frac{\partial \nabla^2 \psi}{\partial x} + \frac{1}{Pm}\nabla^4 g \tag{2.30}$$

where non-linear terms have been dropped and $B_f = 0$. We can expand ψ, θ and g as

$$\{\psi, \theta, g\} = \sum_{n=1}^{N} \{\psi_n, \theta_n, g_n\} \sin(n\pi y) \exp(i(kx + \omega t)) \tag{2.31}$$

where k is the wavenumber and ω is the frequency, following a similar method to Hori et al. (2014). Substituting (2.31) into (2.28)-(2.30) gives a dispersion relation of the form

$$\left(\frac{K^2}{Pr} + i\omega\right)\left(K^2\left(K^2 + i\omega\right) + ik\eta^*\right) - \frac{Ra}{Pr}k^2 + \frac{Q}{Pm}k^2K^2\frac{\left(\frac{K^2}{Pr} + i\omega\right)\left(\frac{K^2}{Pm} - i\omega\right)}{\frac{K^4}{Pm^2} + \omega^2} = 0 \tag{2.32}$$

where $K^2 = k^2 + (n\pi)^2$. We set $n = 1$ as we solve for the fundamental mode. This means that $K^2 = k^2 + \pi^2$. We can take the real part to obtain an expression for the critical Rayleigh number for each wavenumber given by

$$Ra_c(k) = \frac{K^6}{k^2} - \frac{Pr}{k^2}\left(K^2\omega_c + \eta^* k\right)\omega_c + \frac{Pr}{Pm}QK^2\left(\frac{\frac{K^4}{PrPm} + \omega_c^2}{\frac{K^4}{Pm^2} + \omega_c^2}\right) \tag{2.33}$$

and taking the imaginary part gives an expression for the critical frequency ω_c as

$$K^4\omega_c\left(1 + \frac{1}{Pr}\right) + \eta^* k\frac{K^2}{Pr} + \frac{Q}{Pm}k^2\omega_c K^4\frac{\left(\frac{1}{Pm} - \frac{1}{Pr}\right)}{\frac{K^4}{Pm^2} + \omega_c^2} = 0. \tag{2.34}$$

in the magnetic case, Equations (2.33) and (2.34) can be solved and minimised over k to find Ra_c and ω_c for different values of Pr, Pm, η^* and Q. This has been discussed in detail by Hori et al. (2014).

In the non-magnetic case (2.33) becomes

$$Ra_c = \frac{K^6}{k^2} - \frac{Pr}{k^2}\left(K^2\omega_c + \eta^* k\right)\omega_c \tag{2.35}$$

and (2.34) becomes

$$\omega_c = \frac{-\eta^* k}{K^2\left(Pr+1\right)}. \tag{2.36}$$

Substituting ω_c given by (2.36) into (2.35), minimising over k and taking $\eta^* \to \infty$ we obtain an expression for the non-magnetic critical Rayleigh number Ra_c^{HD} as

$$Ra_c^{HD} = 3\left(\frac{\eta^* Pr}{\sqrt{2}\left(1+Pr\right)}\right)^{4/3}. \tag{2.37}$$

We could instead solve (2.33)-(2.34) for Ra_c^{MC} but this value would change for each η^*, Pr, Pm and Q, making it difficult for direct comparisons between simulations. Hence we measure our level of supercriticality against Ra_c^{HD} given by (2.37) as this depends on η^* and Pr, both of which are fixed in our simulations.

2.1.2 NUMERICAL METHOD

Equations (2.21)-(2.23) have been solved analytically in the linear case by Hori et al. (2014) and weakly non-linear solutions have also been examined by Hutcheson and Fearn (1995). However, the full non-linear system of equations are complex and cannot be solved analytically. We solve the full non-linear system by integrating forward in time using a collocation method written in Fortran. We expand our fields ψ, θ and g using a Fourier expansion in x and a sine expansion in y, similar to the method used in previous non-magnetic simulations (e.g. Rotvig and Jones (2006), Teed et al. (2012)). Therefore we have

$$\psi\left(x,y,t\right) = \frac{1}{2}\sum_{l=-(N_x-1)}^{N_x-1}\sum_{m=1}^{N_y-1}\hat{\psi}_{lm}\left(t\right)\sin\left(m\pi y\right)e^{-ilx(2\pi/L_x)} \tag{2.38}$$

$$\theta\left(x,y,t\right) = \frac{1}{2}\sum_{l=-(N_x-1)}^{N_x-1}\sum_{m=1}^{N_y-1}\hat{\theta}_{lm}\left(t\right)\sin\left(m\pi y\right)e^{-ilx(2\pi/L_x)} \tag{2.39}$$

$$g\left(x,y,t\right) = \frac{1}{2}\sum_{l=-(N_x-1)}^{N_x-1}\sum_{m=1}^{N_y-1}\hat{g}_{lm}\left(t\right)\sin\left(m\pi y\right)e^{-ilx(2\pi/L_x)} \tag{2.40}$$

where N_x is the x resolution, N_y is the y resolution and $L_x = 2\pi$ is the length of the x domain. We apply a semi-implicit scheme by treating the linear terms implicitly using the Crank-Nicolson method and we treat the non-linear terms explicitly using the second order Adams-Bashforth method. Suppose we have an equation of the form $\mathrm{d}u/\mathrm{d}t = F\left(u,t\right)$. Then

the Crank-Nicolson method rewrites the equation as

$$\frac{u^{n+1}-u^n}{\Delta t}=\frac{F\left(u^{n+1},t^{n+1}\right)+F\left(u^n,t^n\right)}{2}$$

and similarly, the second order Adams-Bashforth method rewrites the equation as

$$\frac{u^{n+1}-u^n}{\Delta t}=\frac{3}{2}F\left(u^n,t^n\right)-\frac{1}{2}F\left(u^{n-1},t^{n-1}\right)$$

where Δt is the size of the timestep, n is the timestep index, t^k is the time at the k^{th} timestep and $u^k=u\left(t^k\right)$.

We rewrite the equations given by (2.21)-(2.23) as

$$\frac{\partial\nabla^2\psi}{\partial t}-\eta^*\frac{\partial\psi}{\partial x}+B_f\left|\eta^*\right|^{1/2}\nabla^2\psi-\frac{Ra}{Pr}\frac{\partial\theta}{\partial x}-\nabla^4\psi-\frac{Q}{Pm}\frac{\partial\nabla^2 g}{\partial x}=F \tag{2.41}$$

$$\frac{\partial\theta}{\partial t}-\frac{\partial\psi}{\partial x}-\frac{1}{Pr}\nabla^2\theta=G \tag{2.42}$$

$$\frac{\partial\nabla^2 g}{\partial t}-\frac{\partial\nabla^2\psi}{\partial x}-\frac{1}{Pm}\nabla^4 g=H \tag{2.43}$$

where we have introduced F, G and H to represent the non-linear terms on the right hand side of the equations and are given by

$$F=\frac{\partial\left(\psi,\nabla^2\psi\right)}{\partial\left(x,y\right)}-\frac{Q}{Pm}\frac{\partial\left(g,\nabla^2 g\right)}{\partial\left(x,y\right)}$$

$$G=\frac{\partial\left(\psi,\theta\right)}{\partial\left(x,y\right)}$$

$$H=\nabla^2\frac{\partial\left(\psi,g\right)}{\partial\left(x,y\right)}.$$

We can substitute in the fields for ψ, θ and g given by equations (2.38)-(2.40) and apply the methods above to (2.41)-(2.43) to obtain

$$\begin{aligned}
&\left(-\frac{1}{2}\left(l^2+m^2\pi^2\right)+\frac{\Delta t}{4}\left(il\eta^*-B_f\left|\eta^*\right|^{1/2}\left(l^2+m^2\pi^2\right)-\left(l^2+m^2\pi^2\right)^2\right)\right)\hat{\psi}_{lm}^{n+1}\sin\left(m\pi y_j\right)\\
&+\frac{ilRa\Delta t}{4Pr}\hat{\theta}_{lm}^{n+1}\sin\left(m\pi y_j\right)-\frac{Q\Delta til\left(l^2+m^2\pi^2\right)}{4Pm}\hat{g}_{lm}^{n+1}\sin\left(m\pi y_j\right)\\
&=\left(-\frac{1}{2}\left(l^2+m^2\pi^2\right)-\frac{\Delta t}{4}\left(il\eta^*-B_f\left|\eta^*\right|^{1/2}\left(l^2+m^2\pi^2\right)-\left(l^2+m^2\pi^2\right)^2\right)\right)\hat{\psi}_{lm}^{n}\sin\left(m\pi y_j\right)\\
&-\frac{ilRa\Delta t}{4Pr}\hat{\theta}_{lm}^{n}\sin\left(m\pi y_j\right)+\frac{Q\Delta til\left(l^2+m^2\pi^2\right)}{4Pm}\hat{g}_{lm}^{n}\sin\left(m\pi y_j\right)\\
&+\frac{\Delta t}{2}\left(3\hat{F}_{lm}^{n}-\hat{F}_{lm}^{n-1}\right)\sin\left(m\pi y_j\right),
\end{aligned} \tag{2.44}$$

$$\left(\frac{1}{2}+\frac{\Delta t\left(l^2+m^2\pi^2\right)}{4Pr}\right)\hat{\theta}_{lm}^{n+1}\sin\left(m\pi y_j\right)+\frac{il\Delta t}{4}\hat{\psi}_{lm}^{n+1}\sin\left(m\pi y_j\right)$$
$$=\left(\frac{1}{2}-\frac{\Delta t\left(l^2+m^2\pi^2\right)}{4Pr}\right)\hat{\theta}_{lm}^{n}\sin\left(m\pi y_j\right)-\frac{il\Delta t}{4}\hat{\psi}_{lm}^{n}\sin\left(m\pi y_j\right)$$
$$+\frac{\Delta t}{2}\left(3\hat{G}_{lm}^{n}-\hat{G}_{lm}^{n-1}\right)\sin\left(m\pi y_j\right), \tag{2.45}$$

$$\left(-\frac{1}{2}\left(l^2+m^2\pi^2\right)-\frac{\Delta t}{4Pm}\left(l^2+m^2\pi^2\right)^2\right)\hat{g}_{lm}^{n+1}\sin\left(m\pi y_j\right)-\frac{il\Delta t\left(l^2+m^2\pi^2\right)}{4}\hat{\psi}_{lm}^{n+1}\sin\left(m\pi y_j\right)$$
$$=\left(-\frac{1}{2}\left(l^2+m^2\pi^2\right)+\frac{\Delta t}{4Pm}\left(l^2+m^2\pi^2\right)^2\right)\hat{g}_{lm}^{n}\sin\left(m\pi y_j\right)+\frac{il\Delta t\left(l^2+m^2\pi^2\right)}{4}\hat{\psi}_{lm}^{n}\sin\left(m\pi y_j\right)$$
$$+\frac{\Delta t}{2}\left(3\hat{H}_{lm}^{n}-\hat{H}_{lm}^{n-1}\right)\sin\left(m\pi y_j\right) \tag{2.46}$$

where we have dropped the summation signs and $\hat{F}$, $\hat{G}$ and $\hat{H}$ are the Fourier coefficients of the functions F, G and H respectively. The system of equations needs to be solved for each l. In order to do this, we can rewrite the system of equations as

$$\mathbf{A}\mathbf{X}_l^{n+1}=\mathbf{B}\mathbf{X}_l^{n}+\frac{\Delta t}{2}\left(3\hat{\mathbf{F}}_l^{n}-\hat{\mathbf{F}}_l^{n-1}\right) \tag{2.47}$$

where

$$\mathbf{X}_l^n=\left[\hat{\psi}_{l1}^n\ldots\hat{\psi}_{l(N_y-1)}^n,\hat{\theta}_{l1}^n\ldots\hat{\theta}_{l(N_y-1)}^n,\hat{g}_{l1}^n\ldots\hat{g}_{l(N_y-1)}^n\right]^T,$$
$$\mathbf{F}_l^n=\left[\hat{F}_{l1}^n\ldots\hat{F}_{l(N_y-1)}^n,\hat{G}_{l1}^n\ldots\hat{G}_{l(N_y-1)}^n,\hat{H}_{l1}^n\ldots\hat{H}_{l(N_y-1)}^n\right]^T.$$

The matrix $\mathbf{A}$ contains the coefficients of $\hat{\psi}_{lm}^{n+1}$, $\hat{\theta}_{lm}^{n+1}$ and $\hat{g}_{lm}^{n+1}$ and $\mathbf{B}$ contains the coefficients of $\hat{\psi}_{lm}^{n}$, $\hat{\theta}_{lm}^{n}$ and $\hat{g}_{lm}^{n}$. The rows and columns of $\mathbf{A}$ and $\mathbf{B}$ correspond to the collocation points and the sine expansion respectively.

Linear terms and their derivatives can be calculated directly in spectral space. However, the terms in the non-linear Jacobian terms must be evaluated in real space. Multiplication of these non-linear terms are carried out in real space and are then transformed back to spectral space to use in $\mathbf{F}_l^n$. The vector $\mathbf{X}_l^{n+1}$ can be found by multiplying equation (2.47) through on the left by $\mathbf{A}^{-1}$. The vector $\mathbf{X}_l^{n+1}$ then contains $\hat{\psi}_{lm}$, $\hat{\theta}_{lm}$ and $\hat{g}_{lm}$ for $1\leq m\leq N_y-1$ at the new timestep for any l. At any timestep the real fields ψ, θ and g can be calculated using equations (2.38)-(2.40).

This numerical method is similar to that used by Rotvig and Jones (2006), Jones et al. (2003) and Teed et al. (2012) in the non-magnetic case. We have validated our code by reproducing some of these previous results and are discussed in Chapters 3 and 4.

2.1.3 Output parameters

Various output parameters are computed in our system. We calculate the kinetic, magnetic and zonal energy in our simulations. We also output the zonal flow and the various forces involved in the system.

2.1.3.1 Calculating kinetic and magnetic energy

The kinetic energy density is defined by

$$E_K = \frac{1}{2L_xL_y}\int \rho \mathbf{u}^2 \mathrm{d}S.$$

The dimensions of energy are $[E] = ML^2T^{-2}$, which means we have

$$\begin{aligned} E_K &= \rho D^2 D^2 \left(\frac{D^2}{\nu}\right)^{-2} \tilde{E}_K \\ &= \rho \nu^2 \tilde{E}_K \end{aligned}$$

where tildes represent non-dimensionalised quantities. We can non-dimensionalise E_K to get

$$\begin{aligned} E_K = \frac{1}{2L_xL_y}\rho\left(\frac{\nu}{D}\right)^2 D^2 \int \tilde{\mathbf{u}}^2 \mathrm{d}\tilde{S} = \frac{1}{2L_xL_y}\rho\nu^2 \int \tilde{\mathbf{u}}^2 \mathrm{d}\tilde{S} \\ \implies \tilde{E}_K = \frac{1}{L_xL_y}\int \tilde{\mathbf{u}}^2 \mathrm{d}\tilde{S} = \frac{1}{2L_xL_y}\int \left(\tilde{\nabla}\tilde{\psi}\right)^2 \mathrm{d}\tilde{S} \end{aligned}$$

since $\tilde{\mathbf{u}} = \tilde{\nabla}\times\tilde{\psi}\hat{\mathbf{z}} = \frac{\partial\tilde{\psi}}{\partial\tilde{y}}\hat{\mathbf{x}} - \frac{\partial\tilde{\psi}}{\partial\tilde{x}}\hat{\mathbf{y}} \implies \tilde{\mathbf{u}}^2 = \left(\frac{\partial\tilde{\psi}}{\partial\tilde{y}}\right)^2 + \left(\frac{\partial\tilde{\psi}}{\partial\tilde{x}}\right)^2 = \left(\nabla\tilde{\psi}\right)^2$. Dropping the tildes we obtain

$$E_K = \frac{1}{2L_xL_y}\int (\nabla\psi)^2 \,\mathrm{d}S. \tag{2.48}$$

The magnetic energy is defined by

$$E_M = \frac{1}{2L_xL_y\mu_0}\int \mathbf{B}^2 \mathrm{d}S,$$

and using the dimensions of energy above we get

$$E_M = \rho\nu^2\tilde{E}_M.$$

Then, non-dimensionalising E_M, we have

$$\begin{aligned} E_M = \frac{1}{2L_xL_y\mu_0}B_0^2D^2\int \tilde{\mathbf{B}}^2\mathrm{d}\tilde{S} = \frac{1}{2L_xL_y}Q\rho\nu\eta\int \tilde{\mathbf{B}}^2\mathrm{d}\tilde{S} \\ \implies \tilde{E}_M = \frac{Q}{2PmL_xL_y}\int \tilde{\mathbf{B}}^2\mathrm{d}\tilde{S} = \frac{Q}{2PmL_xL_y}\int \left(\tilde{\nabla}\tilde{g}\right)^2\mathrm{d}\tilde{S}, \end{aligned}$$

where we have used $Q = \frac{B_0^2 D^2}{\rho_0 \nu \mu_0 \lambda} \implies Q\nu\rho_0\lambda = \frac{B_0^2 D^2}{\mu_0}$. Then dropping the tildes we obtain

$$E_M = \frac{Q}{2PmL_xL_y} \int (\nabla g)^2 \, \mathrm{d}S. \tag{2.49}$$

We wish to calculate these quantities in the numeric code. In order to do this we use the expansions given in (2.38) and (2.40). First considering the equation for the kinetic energy given by (2.48) with $L_x = 2\pi$ and $L_y = 1$ we have

$$E_K = \frac{1}{4\pi} \int (\nabla \psi)^2 \, \mathrm{d}S = -\frac{1}{4\pi} \int \psi \nabla^2 \psi \mathrm{d}S$$
$$= \frac{1}{16\pi} \sum_{l=-(N_x-1)}^{N_x-1} \sum_{m=1}^{N_y-1} \sum_{l'=-(N_x-1)}^{N_x-1} \sum_{m'=1}^{N_y-1} \hat{\psi}_{l'm'} \hat{\psi}_{lm} \left(l^2 + m^2\pi^2\right) \int_0^{2\pi} \int_0^1 \sin\left(m'\pi y\right) \sin\left(m\pi y\right) e^{-i(l+l')x} \mathrm{d}y \mathrm{d}x$$

using integration by parts. We find

$$\begin{aligned} &\int_0^1 \sin\left(m'\pi y\right) \sin\left(m\pi y\right) \mathrm{d}y \\ &= \frac{1}{2} \int_0^1 \cos\left(m'\pi y - m\pi y\right) + \cos\left(m'\pi y + m\pi y\right) \mathrm{d}y \\ &= \frac{1}{2} \left[\frac{\sin\left((m' - m\,\pi y\right)}{(m' - m)\,\pi} \right]_0^1 + \frac{1}{2} \left[\frac{\sin\left((m' + m\,\pi y\right)}{(m' + m)} \right]_0^1 = 0 \end{aligned}$$

unless $m = m'$. Conversely, when $m = m'$, we find

$$\begin{aligned} \int_0^1 \sin^2\left(m\pi y\right) \mathrm{d}y &= \frac{1}{2} \int_0^1 1 - \cos\left(2m\pi y\right) \mathrm{d}y \\ &= \frac{1}{2} \left[y - \frac{\sin\left(2m\pi y\right)}{2m\pi} \right]_0^1 = \frac{1}{2}. \end{aligned}$$

Similarly, considering

$$\int_0^{2\pi} e^{-i(l+l')x} \mathrm{d}x = 0$$

unless $l' = -l$. Conversely, when $l = -l'$ we have $\int_0^{2\pi} \mathrm{d}x = 2\pi$. Combining these results yields

$$\begin{aligned} E_K &= \frac{1}{16\pi} \hat{\psi}_{-lm} \hat{\psi}_{lm} \left(l^2 + m^2\pi^2\right) (2\pi) \left(\frac{1}{2}\right) \\ &= \frac{1}{16} \sum_{l=-(N_x-1)}^{N_x-1} \sum_{m=1}^{N_y-1} \mid \hat{\psi}_{lm} \mid^2 \left(l^2 + m^2\pi^2\right) \end{aligned} \tag{2.50}$$

since $\hat{\psi}_{-lm} = \hat{\psi}_{lm}^*$. We follow a similar process to obtain the magnetic energy given by

$$E_M = \frac{Q}{16Pm} \sum_{l=-(N_x-1)}^{N_x-1} \sum_{m=1}^{N_y-1} \mid \hat{g}_{lm} \mid^2 \left(l^2 + m^2\pi^2\right). \tag{2.51}$$

2.1.3.2 CALCULATING ZONAL FLOW AND ZONAL ENERGY

In Chapters 3 and 4 we study zonal flows and multiple jet solutions. The zonal flow is the azimuthal average (i.e. x-average) of the azimuthal component of the velocity. Therefore the zonal flow, $\bar{\mathbf{U}}$, is given by

$$\bar{\mathbf{U}} = \bar{U}\hat{\mathbf{x}} = \langle u_x \rangle_x \hat{\mathbf{x}} = -\frac{\partial \langle \psi \rangle_x}{\partial y}\hat{\mathbf{x}} \tag{2.52}$$

where

$$\langle \psi \rangle_x = \frac{1}{L_x}\int_0^{L_x} \psi \, \mathrm{d}x.$$

Using this and $L_x = 2\pi$, Equation (2.52) becomes

$$\begin{aligned}\bar{U} &= -\frac{1}{2\pi}\int_0^{2\pi} \frac{\partial \psi}{\partial y}\mathrm{d}x \\ &= -\frac{1}{2\pi}\int_0^{2\pi} \sum_{l=-(N_x-1)}^{N_x-1}\sum_{m=1}^{N_y-1} m\pi\hat{\psi}_{lm}e^{-ilx}\cos(m\pi y)\,\mathrm{d}x.\end{aligned}$$

Then clearly $\int_0^{2\pi} e^{-ilx}\mathrm{d}x = 0$ unless $l = 0$. Therefore there is no contribution to the zonal flow from the modes where $l \neq 0$. With $l = 0$, we have $\int_0^{2\pi} e^{-ilx}\mathrm{d}x = 2\pi$ and hence

$$\bar{U} = -\sum_{m=1}^{N_y-1} m\pi\hat{\psi}_{0m}\cos(m\pi y)\,. \tag{2.53}$$

The zonal energy is the contribution to the total energy from the zonal flow defined by

$$E_Z = \frac{1}{2\pi}\int \left(\langle \nabla\psi \rangle_x\right)^2 \mathrm{d}S.$$

This can be calculated in a similar way to the zonal flow $\bar{U}$ which gives

$$E_Z = \frac{1}{8}\sum_{m=1}^{N_y-1} m^2\pi^2\psi_{0m}^2. \tag{2.54}$$

2.1.3.3 CALCULATING FORCES

In Chapter 3 we perform a force balance study in the annulus model. To do this we consider the curl of each force by starting from the vorticity equation given by

$$\underbrace{\frac{\partial \nabla^2\psi}{\partial t} + \frac{\partial(\nabla^2\psi,\psi)}{\partial(x,y)}}_{\text{Inertia}} - \underbrace{\eta^*\frac{\partial\psi}{\partial x}}_{\text{Coriolis}} + \underbrace{B_f\left|\eta^*\right|^{1/2}\nabla^2\psi}_{\text{bottom friction}} = \underbrace{\frac{Ra}{Pr}\frac{\partial\theta}{\partial x}}_{\text{Buoyancy}} + \underbrace{\nabla^4\psi}_{\text{Viscosity}} + \underbrace{\frac{Q}{Pm}\frac{\partial\nabla^2 g}{\partial x} + \frac{Q}{Pm}\frac{\partial(\nabla^2 g, g)}{\partial(x,y)}}_{\text{Lorentz}}.$$

This approach, where the curl of forces have been used, was examined by Teed and Dormy (2023) where they show that the curl of forces provides an alternative option for exploring the

force balances in the system. We use this approach as we solve the curl of the Navier-Stokes equation (i.e. the vorticity equation) rather than the Navier-Stokes equation itself. Also, if we were to consider the forces using the Navier-Stokes equation a few complications arise; one of these being that we do not obtain the same input parameters. Instead of η^* which measures the rotation rate we would obtain the Ekman number E, but this is not involved in our system when solving numerically. Therefore, it makes sense to form the forces from the vorticity equation allowing us to consider the curl of each force.

For a given curl of a force, $\mathbf{C}$, we compute

$$C^2 = \frac{1}{L_x}\int \mathbf{C}^2 \mathrm{d}S = \sum_{l=0}^{N_x}\sum_{m=1}^{N_y} C_{lm}^2$$

allowing us to form a spectrum of the curl of each force in l or m. Taking each force and substituting in the forms for ψ, θ and g from Equations (2.38)-(2.40) we have

$$\begin{aligned}
\mathbf{C}_C &= -\eta^* il\hat{\psi}_{lm}\sin(m\pi y)\, e^{-ilx}\hat{\mathbf{z}} \\
\mathbf{C}_A &= -\frac{ilRa}{Pr}\hat{\theta}_{lm}\sin(m\pi y)\, e^{-ilx}\hat{\mathbf{z}} \\
\mathbf{C}_V &= \left(l^2+m^2\pi^2\right)^2\hat{\psi}_{lm}\sin(m\pi y)\, e^{-ilx}\hat{\mathbf{z}} \\
\mathbf{C}_L &= \frac{Q}{Pm}A_{lm}\sin(m\pi y)\, e^{-ilx}\hat{\mathbf{z}} \\
\mathbf{C}_I &= B_{lm}\sin(m\pi y)\, e^{-ilx}\hat{\mathbf{z}} \\
\mathbf{C}_{bf} &= B_f|\eta^*|^{1/2}\left(l^2+m^2\pi^2\right)\hat{\psi}_{lm}\sin(m\pi y)\, e^{-ilx}\hat{\mathbf{z}}
\end{aligned}$$

where C_C is the Coriolis force, C_A is the buoyancy force, C_V is the viscous force, C_L is the Lorentz force, C_I is the inertial force and C_{bf} is the force resultant from the bottom friction. The terms A_{lm} and B_{lm} denote the non-linear terms in the curl of the Lorentz and inertial force respectively. These are calculated in a similar manner to the energy integrals. We have dropped the time derivative in the inertial force and the x derivative in the Lorentz force as these are very small compared to the non-linear terms. Then considering C^2 for each we have

$$C_C^2 = \frac{\eta^{*2}}{8}\sum_{l=-(N_x-1)}^{N_x-1}\sum_{m=1}^{N_y-1} l^2|\hat{\psi}_{lm}|^2 \tag{2.55}$$

$$C_A^2 = \frac{Ra^2}{8Pr^2}\sum_{l=-(N_x-1)}^{N_x-1}\sum_{m=1}^{N_y-1} l^2|\hat{\theta}_{lm}|^2 \tag{2.56}$$

$$C_V^2 = \frac{1}{8}\sum_{l=-(N_x-1)}^{N_x-1}\sum_{m=1}^{N_y-1}\left(l^2+m^2\pi^2\right)^4|\hat{\psi}_{lm}|^2 \tag{2.57}$$

$$C_{bf}^2 = \frac{B_f^2\eta^*}{8}\sum_{l=-(N_x-1)}^{N_x-1}\sum_{m=1}^{N_y-1}\left(l^2+m^2\pi^2\right)^2|\hat{\psi}_{lm}|^2 \tag{2.58}$$

$$C_L^2 = \frac{Q^2}{2Pm^2} \sum_{l=-(N_x-1)}^{N_x-1} \sum_{m=1}^{N_y-1} |A_{lm}|^2 \tag{2.59}$$

$$C_I^2 = \frac{1}{2} \sum_{l=-(N_x-1)}^{N_x-1} \sum_{m=1}^{N_y-1} |B_{lm}|^2. \tag{2.60}$$

We study both the lengthscale dependence of forces in l and globally averaged quantities. To form the l spectrum for Equations (2.55)-(2.97) we perform the summation over m, we compensate by dividing by l and take the square root of these quantities. For example, the spectrum over l of the curl of the Coriolis force can be obtained by

$$C_l^2 = \frac{\eta^{*2}}{8} \sum_{m=1}^{N_y-1} l^2 |\hat{\psi}_{lm}|^2 \tag{2.61}$$

and the compensated curl of this is calculated by

$$\hat{C}_l^2 = \frac{C_l^2}{l}. \tag{2.62}$$

This method is used similarly for other forces. To form globally averaged quantities, the sum over l and m is carried out for each force, allowing us to obtain a value for the globally averaged force.

2.2 SPHERICAL DYNAMO MODEL

In Chapters 5 and 6 we consider a rotating spherical shell filled with an electrically conducting fluid in the Boussinesq approximation using a spherical coordinate system (r, θ, ϕ). The fluid is contained between $r = r_i$ and $r = r_o$ where r_i and r_o are the inner and outer radius respectively with $r_o > r_i$. The rotation rate is given by $\mathbf{\Omega} = \Omega\hat{\mathbf{z}}$, gravity acts inwards given by $\mathbf{g} = -g\mathbf{r}$ and we assume the fluid has constant density except in the buoyancy term. We have a temperature gradient between the top and bottom boundaries so that $T_0(r_i) = T_i$ and $T_0(r_o) = T_o$. We apply only differential heating so we have no source term in the heat equation. The basic state temperature is $\nabla^2 T_0 = 0$ and solving this using $T_0(r_i) = T_i$ and $T_0(r_o) = T_o$ we obtain a differential heating profile given by

$$T_0(r) = \frac{r_i r_o \Delta T}{r_o - r_i} r^{-1} + \frac{r_o T_o - r_i T_i}{r_o - r_i}$$

where $\Delta T = T_i - T_o$. For convenience, since T_i and T_o are arbitrary reference temperatures, we set $T_o = 0$ so that $\Delta T = T_i$. The basic state for the velocity and magnetic field is $\mathbf{U}_0 = \mathbf{B}_0 = \mathbf{0}$. In the equations that follow $\mathbf{u}$ and $\mathbf{B}$ are used for the total flow and field.

2.2.1 GOVERNING EQUATIONS

To obtain a set of equations we start from the Navier Stokes, heat and induction equations given by Equations (1.22)-(1.26). We non-dimensionalise these equations using a lengthscale $d = r_o - r_i$, a timescale d^2/λ, a temperature scale ΔT and a magnetic scale $\sqrt{\rho_0\mu_0\lambda\Omega}$. This gives

$$\frac{\lambda^2}{d^3}\frac{\partial\tilde{\mathbf{u}}}{\partial\tilde{t}} + \frac{\lambda^2}{d^3}\left(\tilde{\mathbf{u}}\cdot\tilde{\nabla}\right)\tilde{\mathbf{u}} + \frac{2\lambda\Omega}{d}\hat{\mathbf{z}}\times\tilde{\mathbf{u}} = -\frac{1}{\rho_0}\frac{\rho_0\lambda^2}{d^3}\tilde{\nabla}\tilde{P} \tag{2.63}$$

$$+\alpha\Delta T\tilde{T}g\mathbf{r} + \frac{\rho_0\mu_0\lambda\Omega}{\rho_0\mu_0 d}\left(\tilde{\nabla}\times\tilde{\mathbf{B}}\right)\times\tilde{\mathbf{B}} + \frac{\nu\lambda}{d^3}\tilde{\nabla}^2\tilde{\mathbf{u}}, \tag{2.64}$$

$$\Delta T\frac{\lambda}{d^2}\frac{\partial\tilde{T}}{\partial\tilde{t}} + \frac{\lambda}{d^2}\Delta T\left(\tilde{\mathbf{u}}\cdot\tilde{\nabla}\right)\tilde{T} = \frac{\kappa\Delta T}{d^2}\tilde{\nabla}^2\tilde{T}, \tag{2.65}$$

$$\frac{\lambda\sqrt{\rho_0\mu_0\lambda\Omega}}{d^2}\frac{\partial\tilde{\mathbf{B}}}{\partial\tilde{t}} - \frac{\lambda\sqrt{\rho_0\mu_0\lambda\Omega}}{d^2}\tilde{\nabla}\times\left(\tilde{\mathbf{u}}\times\tilde{\mathbf{B}}\right) = \frac{\lambda\sqrt{\rho_0\mu_0\lambda\Omega}}{d^2}\tilde{\nabla}^2\tilde{\mathbf{B}}, \tag{2.66}$$

$$\frac{\lambda^2}{d^3}\tilde{\nabla}\cdot\tilde{\mathbf{u}} = 0 \tag{2.67}$$

$$\frac{\sqrt{\rho_0\mu_0\lambda\Omega}}{d}\tilde{\nabla}\cdot\tilde{\mathbf{B}} = 0. \tag{2.68}$$

We can then rearrange and drop the tildes to obtain a set of non-dimensionalised equations given by

$$\frac{\partial\mathbf{u}}{\partial t} + (\mathbf{u}\cdot\nabla)\,\mathbf{u} + \frac{2Pm}{E}\hat{\mathbf{z}}\times\mathbf{u} = -\nabla P + \frac{RaPm^2}{Pr}T\mathbf{r} + \frac{Pm}{E}(\nabla\times\mathbf{B})\times\mathbf{B} + Pm\nabla^2\mathbf{u}, \tag{2.69}$$

$$\frac{\partial T}{\partial t} + (\mathbf{u}\cdot\nabla)\,T = \frac{Pm}{Pr}\nabla^2 T, \tag{2.70}$$

$$\frac{\partial\mathbf{B}}{\partial t} - \nabla\times(\mathbf{u}\times\mathbf{B}) = \nabla^2\mathbf{B}, \tag{2.71}$$

$$\nabla\cdot\mathbf{u} = 0, \tag{2.72}$$

$$\nabla\cdot\mathbf{B} = 0, \tag{2.73}$$

where the non-dimensional parameters are the Ekman number E, the Rayleigh number Ra, the Prandtl number Pr and the magnetic Prandtl number Pm which are defined as

$$E = \frac{\nu}{\Omega d^2},\ Ra = \frac{\alpha g\Delta T d^3}{\nu\kappa},\ Pm = \frac{\nu}{\lambda}\text{ and }Pr = \frac{\nu}{\kappa}.$$

2.2.2 NUMERICAL METHOD

In order to solve the equations above we apply a poloidal-toroidal decomposition, where the velocity and magnetic fields are decomposed into poloidal and toroidal scalars as

$$\mathbf{u} = \nabla\times(T\mathbf{r}) + \nabla\times\nabla\times(P\mathbf{r}) \tag{2.74}$$

$$\mathbf{B} = \nabla\times(\mathcal{T}\mathbf{r}) + \nabla\times\nabla\times(\mathcal{P}\mathbf{r}) \tag{2.75}$$

where $\mathcal{P}$, $\mathcal{T}$, P and T are the poloidal and toroidal scalar fields of the magnetic field and velocity and are functions of space and time. This form is chosen as it reduces the number of scalars to solve for. For each of $\mathbf{u}$ and $\mathbf{B}$, we are required to solve for the three components of the vector. There is a degree of freedom in both vector fields because each is subject to a solenoidal constraint. The poloidal-toroidal decompositions automatically satisfy these constraints and utilise the degree of freedom by using only two scalars. The poloidal and toroidal parts are then expanded in terms of spherical harmonics so that each take a similar form given by

$$A = \sum_{l=0}^{l_{max}} \sum_{m=-l}^{l} A_{lm}(t,r)\, Y_l^m(\theta,\phi) \tag{2.76}$$

for some scalar field, A, and where A_{lm} are the set of coefficients and l_{max} is the truncation of the spherical harmonic degree. The spherical harmonic function of degree l and order m are of the form

$$Y_l^m(\theta,\phi) = P_l^{|m|}(\cos\theta)\, e^{im\phi}$$

where $P_l^{|m|}$ are the associated Legendre functions. This expansion deals with the angular decomposition. We discuss the radial formulation in the numerical method section below.

In order to obtain equations for the poloidal and toroidal parts of the velocity and magnetic field, the curl and double curl of these have to be computed. For any $b\mathbf{r}$ we have

$$\nabla \times (b\mathbf{r}) = \frac{1}{\sin\theta}\frac{\partial b}{\partial \phi}\hat{\boldsymbol{\theta}} - \frac{\partial b}{\partial \theta}\hat{\boldsymbol{\phi}},$$

and taking the $\hat{\mathbf{r}}$ component gives

$$\hat{\mathbf{r}} \cdot (\nabla \times b\mathbf{r}) = 0. \tag{2.77}$$

Calculating

$$\begin{aligned}\nabla \times \nabla \times (b\mathbf{r}) &= -\left(\frac{1}{r\sin\theta}\frac{\partial}{\partial\theta}\left(\frac{\partial b}{\partial\theta}\sin\theta\right) - \frac{1}{r\sin^2\theta}\frac{\partial^2 b}{\partial\phi^2}\right)\hat{\mathbf{r}} + \frac{1}{r}\frac{\partial}{\partial r}\left(r\frac{\partial b}{\partial\theta}\right)\hat{\boldsymbol{\theta}} + \frac{1}{r\sin\theta}\frac{\partial}{\partial r}\left(r\frac{\partial b}{\partial\phi}\right)\hat{\boldsymbol{\phi}} \\ &= -\frac{1}{r}L^2 b\hat{\mathbf{r}} + \frac{1}{r}\frac{\partial}{\partial r}\left(r\frac{\partial b}{\partial\theta}\right)\hat{\boldsymbol{\theta}} + \frac{1}{r\sin\theta}\frac{\partial}{\partial r}\left(r\frac{\partial b}{\partial\phi}\right)\hat{\boldsymbol{\phi}},\end{aligned}$$

and taking the $\hat{\mathbf{r}}$ component of this gives

$$\hat{\mathbf{r}} \cdot \nabla \times \nabla \times (b\mathbf{r}) = -\frac{1}{r}L^2 b, \tag{2.78}$$

where

$$L^2 = \frac{1}{\sin\theta}\frac{\partial}{\partial\theta}\left(\sin\theta\frac{\partial}{\partial\theta}\right) + \frac{1}{\sin^2\theta}\frac{\partial^2}{\partial\phi^2}.$$

We can then calculate

$$\nabla \times \nabla \times \nabla \times b\mathbf{r} = \nabla \times \left(\nabla(\nabla \cdot b\mathbf{r}) - \nabla^2 b\mathbf{r}\right)$$

$$= -\nabla \times \nabla^2 b\mathbf{r} = -\nabla \times \tilde{b}\mathbf{r}$$

where $\tilde{b} = \nabla^2 b$ and have used the identity $\nabla \times \nabla \times \mathbf{A} = \nabla(\nabla \cdot \mathbf{A}) - \nabla^2 \mathbf{A}$. We can take the $\hat{\mathbf{r}}$ component of this which gives $\hat{\mathbf{r}} \cdot \left(-\nabla \times \tilde{b}\mathbf{r}\right) = 0$ using (2.77). We also consider

$$\begin{aligned}\nabla \times \nabla \times \nabla \times \nabla \times b\mathbf{r} &= \nabla \times \nabla \times \left(\left(\nabla(\nabla \cdot b\mathbf{r}) - \nabla^2 b\mathbf{r}\right)\right) \\ &= -\nabla \times \nabla \times \left(\nabla^2 b\mathbf{r}\right) \\ &= -\nabla \times \nabla \times \tilde{b}\mathbf{r}\end{aligned}$$

and taking the $\hat{\mathbf{r}}$ component we obtain

$$\hat{\mathbf{r}} \cdot \left(-\nabla \times \nabla \times \tilde{b}\mathbf{r}\right) = \frac{1}{r} L^2 \tilde{b} = \frac{1}{r} L^2 \nabla^2 b$$

using equation (2.78).

Then expressing the momentum equation, given by Equation (2.69), as

$$\frac{\partial \mathbf{u}}{\partial t} + (\mathbf{u} \cdot \nabla)\mathbf{u} = \mathbf{N_u}$$

where

$$\mathbf{N_u} = -\nabla P - \frac{2Pm}{E}\hat{\mathbf{z}} \times \mathbf{u} + \frac{RaPm^2}{Pr} T\mathbf{r} + \frac{Pm}{E}(\nabla \times \mathbf{B}) \times \mathbf{B} + Pm\nabla^2 \mathbf{u},$$

equations for the poloidal and toroidal parts of the velocity can be found by considering $\hat{\mathbf{r}} \cdot \nabla \times$ and $\hat{\mathbf{r}} \cdot \nabla \times \nabla \times$ of the momentum equation and using $[L^2 A]_l^m = -l(l+1) A_l^m$ from the properties of spherical harmonics for the expansion given by equation (2.76) we obtain

$$\left[\left(\frac{\partial}{\partial t} - Pm\nabla^2\right) T\right]_l^m = \frac{r}{l(l+1)} \hat{\mathbf{r}} \cdot \nabla \times \mathbf{N_u} \tag{2.79}$$

$$\left[\left(\frac{\partial \nabla^2}{\partial t} - Pm\nabla^4\right) P\right]_l^m = -\frac{r}{l(l+1)} \hat{\mathbf{r}} \cdot \nabla \times \nabla \times \mathbf{N_u}. \tag{2.80}$$

The induction equation can be expressed as

$$\frac{\partial \mathbf{B}}{\partial t} - \nabla^2 \mathbf{B} = \mathbf{N_B}$$

where $\mathbf{N_B} = \nabla \times (\mathbf{u} \times \mathbf{B})$. Taking $\hat{\mathbf{r}} \cdot$ and $\hat{\mathbf{r}} \cdot \nabla \times$ of the induction equation, we obtain evolution equations for the poloidal and toroidal parts of the magnetic field as

$$\left[\left(\frac{\partial}{\partial t} - \nabla^2\right) \mathcal{P}\right]_l^m = \frac{r}{l(l+1)} \hat{\mathbf{r}} \cdot \mathbf{N_B}, \tag{2.81}$$

$$\left[\left(\frac{\partial}{\partial t} - \nabla^2\right) \mathcal{T}\right]_l^m = \frac{r}{l(l+1)} \hat{\mathbf{r}} \cdot \nabla \times \mathbf{N_B}. \tag{2.82}$$

Equations (2.79)-(2.82) are solved alongside the temperature equation given by (2.70).

Our simulations are carried out using the Leeds Spherical dynamo code (Willis et al., 2007). This is written in Fortran which solves the equations given by (2.70) and (2.79) - (2.82) in 3D spherical geometry. The code uses a predictor-corrector method to integrate the equations forward in time. Each evolution equation is of the form

$$\left(a\frac{\partial}{\partial t} - b\nabla^2\right) f = N,$$

where the non-linear terms N have been evaluated in real space at each radial point and then transformed back to spectral space. The code starts by computing a predictor at time t_q with implicitness c. The predictor at j is given by

$$\left(a\frac{1}{\Delta t} - bc\nabla^2\right) f_j^{q+1} = \left(a\frac{1}{\Delta t} + b\left(1-c\right)\nabla^2\right) f^q + cN_{j-1}^{q+1} + \left(1-c\right)N^q,$$

and the corrector at $j+1$ is given by

$$\left(a\frac{1}{\Delta t} - bc\nabla^2\right) f_{j+1}^{q+1} = \left(a\frac{1}{\Delta t} + b\left(1-c\right)\nabla^2\right) f^q + cN_{j}^{q+1} + \left(1-c\right)N^q,$$

and an equation for the corrector f_{corr} can be obtained by subtracting the predictor iteration from the corrector iteration to obtain

$$\left(a\frac{1}{\Delta t} - bc\nabla^2\right) f_{corr} = cN_j^{q+1} - cN^q$$

where $f_{corr} = f_{j+1}^{q+1} - f_j^{q+1}$. The timestep is set through the Courant number C where $0.01 < C < 0.1$. The timstep is dynamically controlled to ensure that it remains small enough so that f_{corr} is satisfactorily small.

The code is parallelised in both the r and θ direction. First the data is split into N_r sections in radius. Then within each of these sections a transpose is performed between radial points and modes, resulting in all modes being present at each r_n. The summation over l at each θ_j is performed on each core which gives data for all θ_j being present for each m. The data within each radial section is then split into N_{th} sections in θ. A transpose between the m modes and θ points is carried out resulting in data for all m being present for each (r, θ) section. The sum over m then takes place to obtain data for all ϕ_i in each (r, θ) section. In the radial direction, a finite difference method is applied using a 7 point stencil which takes a grid point and the three neighbouring points at each side of the grid point.

2.2.2.1 Boundary conditions

We solve using no-slip, rigid and impenetrable boundary conditions. This is equivalent to

$$T = 0,\ P = 0,\ \partial_r P = 0$$

at $r = r_i, r_o$. For the magnetic boundary conditions we decompose the electric current density $\mathbf{j}$ into poloidal and toroidal components by writing

$$\mathbf{j} = \nabla \times (j_t \mathbf{r}) + \nabla \times \nabla \times (j_p \mathbf{r}) .$$

The poloidal and toroidal parts of $\mathbf{j}$ are related to $\mathbf{B}$ as

$$j_p = \mathcal{T}, \; j_t = -\nabla^2 \mathcal{P}.$$

Outside the spherical shell the electric current density is zero so $\mathbf{j} = \mathbf{0}$. Therefore the exterior magnetic field must satisfy

$$\mathcal{T} = \nabla^2 \mathcal{P} = 0$$

which gives

$$\begin{aligned} &\mathcal{T} = 0, \\ &\left[r^2 \frac{\mathrm{d}^2}{\mathrm{d}r^2} + 2r \frac{\mathrm{d}}{\mathrm{d}r} - l\,(l+1) \right] \mathcal{P}_{lm} = 0. \end{aligned} \tag{2.83}$$

Solutions to (2.83) are of the form $\mathcal{P}_{lm} \sim r^\alpha$. Substituting this into (2.83) gives $\alpha\,(\alpha+1) = l\,(l+1)$ which has solution $\alpha = l$ (for external sources) and $\alpha = -l-1$ (for internal sources). For insulating boundary conditions we require there to be no external sources so the exterior magnetic field is $\mathcal{P}_{lm} = A r^{-l-1}$ for some constant A. This gives boundary conditions on the magnetic field as

$$\mathcal{T} = 0, \quad \left(\partial_r - \frac{l}{r} \right) \mathcal{P} = 0 \text{ on } r_i, \tag{2.84}$$

$$\mathcal{T} = 0, \quad \left(\partial_r + \frac{l+1}{r} \right) \mathcal{P} = 0 \text{ on } r_o. \tag{2.85}$$

We have a temperature difference of ΔT maintained between boundaries so $T = 1$ at r_i and $T = 0$ at r_o.

2.2.3 Output parameters

2.2.3.1 Kinetic and magnetic energy

The kinetic energy is defined by

$$E_K = \frac{1}{2} \int \rho \mathbf{u} \mathrm{d}V$$

and the dimensions of energy are $[E] = ML^2T^{-2}$ so we have

$$E_K = \rho d^3 d^2 \left(\frac{d^2}{\nu} \right)^{-2} \tilde{E}_K = \rho \nu^2 d \tilde{E}_K.$$

Non-dimensionalising E_K gives

$$\begin{aligned} E_K &= \frac{1}{2}\rho\left(\frac{\nu}{d}\right)^2 d^3 \int \tilde{\mathbf{u}}^2 \mathrm{d}\tilde{V} \\ &= \frac{1}{2}\rho\nu^2 d \int \tilde{\mathbf{u}}^2 \mathrm{d}\tilde{V} \\ \implies \tilde{E}_K &= \frac{1}{2}\int \tilde{\mathbf{u}}^2 \mathrm{d}\tilde{V}. \end{aligned}$$

Dropping the tildes we obtain E_K in non-dimensionalised form as

$$E_K = \frac{1}{2}\int \mathbf{u}^2 \mathrm{d}V.$$

To calculate the magnetic energy we have

$$E_M = \frac{1}{2\mu_0}\int \mathbf{B}^2 \mathrm{d}V$$

and non-dimensionalising we have

$$\begin{aligned} E_M &= \frac{1}{2\mu_0}\rho_0\mu\lambda\Omega d^3 \int \tilde{\mathbf{B}}^2 \mathrm{d}\tilde{V} \\ &= \frac{\rho_0\lambda\Omega d^3}{2} \int \tilde{\mathbf{B}}^2 \mathrm{d}\tilde{V} \end{aligned}$$

and using $E_M = \rho_0\lambda^2 d\tilde{E}_M$ we get

$$E_M = \frac{Pm}{2E}\int \mathbf{B}^2 \mathrm{d}V.$$

2.2.3.2 Calculating energy integrals

The energy integrals both take a similar form. For any vector $\mathbf{A}$ we can express this as a combination of scalar potentials $\mathcal{R}$, $\mathcal{S}$, and $\mathcal{T}$ as

$$\mathbf{A} = \mathcal{R}\hat{\mathbf{r}} + r\nabla\mathcal{S} + \mathbf{r}\times\nabla\mathcal{T}, \tag{2.86}$$

where $\mathcal{R}$, $\mathcal{S}$ and $\mathcal{T}$ represent the radial, spheroidal and toroidal fields respectively. We can expand these scalar potentials using spherical harmonics such that

$$\mathcal{R} = \sum_{l=0}^{l_{max}} \sum_{m=-l}^{l} \mathcal{R}_l^m(r)\, Y_l^m(\theta,\phi) \tag{2.87}$$

$$\mathcal{S} = \sum_{l=0}^{l_{max}} \sum_{m=-l}^{l} \mathcal{S}_l^m(r)\, Y_l^m(\theta,\phi) \tag{2.88}$$

$$\mathcal{T} = \sum_{l=0}^{l_{max}} \sum_{m=-l}^{l} \mathcal{T}_l^m(r)\, Y_l^m(\theta,\phi) \tag{2.89}$$

where Y_l^m are spherical harmonic functions. We can then substitute Equations (2.87)-(2.89) into Equation (2.86) which gives

$$\begin{aligned}\mathbf{A} &= \sum_{l=0}^{l_{max}} \sum_{m=-l}^{l} \mathcal{R}_l^m Y_l^m \hat{\mathbf{r}} + r\mathcal{S}_l^m \nabla Y_l^m + \mathcal{T}_l^m \mathbf{r} \times \nabla Y_l^m \\ &= \sum_{l=0}^{l_{max}} \sum_{m=-l}^{l} \mathcal{R}_l^m \mathbf{Y}_l^m + \mathcal{S}_l^m \mathbf{\Psi}_l^m + \mathcal{T}_l^m \mathbf{\Phi}_l^m,\end{aligned}$$

where $\mathbf{Y}_m^l = Y_l^m \hat{\mathbf{r}}$, $\mathbf{\Psi}_l^m = r\nabla Y_l^m$ and $\mathbf{\Phi}_l^m = \mathbf{r} \times \nabla Y_l^m$ are the vector spherical harmonics and l_{max} is the truncation of the spherical harmonic degree. The energy of the vector $\mathbf{A}$ is given by

$$\begin{aligned}A^2 &= \int \mathbf{A}^2 \mathrm{d}V \\ &= \sum_{l=0}^{l_{max}} \sum_{m=-l}^{l} \int_0^{2\pi} \int_0^{\pi} \int_{r_i+b}^{r_o-b} \left[\mathcal{R}_l^m \mathcal{R}_{l'}^{m'} \mathbf{Y}_l^m \cdot \mathbf{Y}_{l'}^{m'} + \mathcal{S}_l^m \mathcal{S}_{l'}^{m'} \mathbf{\Psi}_l^m \cdot \mathbf{\Psi}_{l'}^{m'} + \mathcal{T}_l^m \mathcal{T}_{l'}^{m'} \mathbf{\Phi}_l^m \cdot \mathbf{\Phi}_{l'}^{m'}\right] r^2 \sin\theta \mathrm{d}r\mathrm{d}\theta\mathrm{d}\phi \\ &= \sum_{l=0}^{l_{max}} \sum_{m=-l}^{l} \int_{r_i+b}^{r_o-b} \left[\mathcal{R}_l^m \mathcal{R}_{l'}^{m'} \delta_{ll'}\delta_{mm'} + l(l+1)\mathcal{S}_l^m \mathcal{S}_{l'}^{m'} \delta_{ll'}\delta_{mm'} + l(l+1)\mathcal{T}_l^m \mathcal{T}_{l'}^{m'} \delta_{ll'}\delta_{mm'}\right] r^2 \mathrm{d}r \\ &= \sum_{l=0}^{l_{max}} \int_{r_i+b}^{r_o-b} \left[\left|\mathcal{R}_l^0\right|^2 + l(l+1)\left(\left|\mathcal{S}_l^0\right|^2 + \left|\mathcal{T}_l^0\right|^2\right)\right] r^2 \mathrm{d}r \\ &+ 2\sum_{l=0}^{l_{max}} \sum_{m=1}^{l} \int_{r_i+b}^{r_o-b} \left[|\mathcal{R}_l^m|^2 + l(l+1)\left(|\mathcal{S}_l^m|^2 + |\mathcal{T}_l^m|^2\right)\right] r^2 \mathrm{d}r \\ &= 2\sum_{l=0}^{l_{max}} {\sum_{m=0}^{l}}' \int_{r_i+b}^{r_o-b} \left[|\mathcal{R}_l^m|^2 + l(l+1)\left(|\mathcal{S}_l^m|^2 + |\mathcal{T}_l^m|^2\right)\right] r^2 \mathrm{d}r.\end{aligned} \tag{2.90}$$

where b is the boundary layer thickness and the primed sum denotes a halving of the $m = 0$ term. We have made use of the orthonormal properties of vector spherical harmonics given by

$$\begin{aligned}\int_0^{2\pi} \int_0^{\pi} \mathbf{Y}_l^m \cdot \mathbf{Y}_{l'}^{m'} \sin\theta \mathrm{d}\theta\mathrm{d}\phi &= \delta_{ll'}\delta_{mm'} \\ \int_0^{2\pi} \int_0^{\pi} \mathbf{\Psi}_l^m \cdot \mathbf{\Psi}_{l'}^{m'} \sin\theta \mathrm{d}\theta\mathrm{d}\phi &= l(l+1)\delta_{ll'}\delta_{mm'} \\ \int_0^{2\pi} \int_0^{\pi} \mathbf{\Phi}_l^m \cdot \mathbf{\Phi}_{l'}^{m'} \sin\theta \mathrm{d}\theta\mathrm{d}\phi &= l(l+1)\delta_{ll'}\delta_{mm'}.\end{aligned}$$

In Chapter 6, the poloidal and toroidal parts of the kinetic energy are considered. The poloidal energy is the sum of the energy in the radial and spheroidal parts and the toroidal energy is obtained from the energy in the toroidal part. The total energy is obtained by summing the radial, spheroidal and toroidal parts. We set $b = 0$ when calculating the energy integrals but

this can be non-zero if boundary layers are to be removed from the radial integration.

2.2.3.3 STRENGTH AND DIPOLARITY OF THE MAGNETIC FIELD

We output the dipolarity of the field which is defined by

$$f_{dip} = \sqrt{\frac{E_M^{(1,0)}(r_o)}{\sum_{l=1}^{12}\sum_{m=0}^{l} E_M^{(l,m)}(r_o)}} \tag{2.91}$$

where $E_M^{(l,m)}(r)$ is the magnetic energy in the (l,m) harmonic at radius r. The parameter f_{dip} is such that $f_{dip} \in [0,1]$ with a value close to 1 being dipolar and a value close to 0 being multipolar.

The Elsasser number denoted by Λ is a measure of the Lorentz to Coriolis force. Different assumptions can lead to different definitions Λ. The classical definition is given by

$$\Lambda = \frac{|B|^2}{\rho\mu\lambda\Omega} \tag{2.92}$$

and the dynamic Elsasser number is given by (Dormy, 2016; Soderlund et al., 2015)

$$\Lambda' = \frac{\Lambda d}{Rml_B} = \frac{|B|^2}{\rho\mu\lambda\Omega U l_B} \tag{2.93}$$

are both computed. The value l_B measures the typical magnetic dissipation lengthscale and is defined as

$$l_B^2 = \frac{\int_V \mathbf{B}^2 \mathrm{d}V}{\int_V (\nabla\times\mathbf{B})^2 \mathrm{d}V} \tag{2.94}$$

and Rm is the magnetic Reynolds number, which measures the ratio of magnetic induction to diffusion and is given by

$$Rm = \frac{Ud}{\lambda}. \tag{2.95}$$

The Gauss coefficients are also important for determining the dipolarity of the magnetic field. We can find these as the magnetic field can be given by a vector potential as $\mathbf{B} = -\nabla V$. The potential field V can be written as a multipole expansion given by

$$V = a\sum_l \sum_{m=0}^{l} \left(\frac{a}{r}\right)^{l+1} P_l^m(\cos\theta)\left(g_{lm}\cos m\phi + h_{lm}\sin m\phi\right)$$

where g_{lm} and h_{lm} are the Gauss coefficients (Lowes, 1974). From this we can obtain the axial dipole component g_{10} and the axial quadrupole component g_{20} as

$$g_{10} = \frac{\mathcal{P}_1^0(r_o)}{r_o} \text{ and } g_{20} = \frac{2\mathcal{P}_2^0(r_o)}{r_o} \tag{2.96}$$

respectively, where $\mathcal{P}_l^m$ is defined using Equation (2.76) for the poloidal field.

2.2.3.4 CALCULATING FORCES

We examine the forces by considering the Navier Stokes equation given by Equation (2.69). We define the forces as

$$\mathbf{F}_I = \frac{\partial \mathbf{u}}{\partial t} + (\mathbf{u} \cdot \nabla)\,\mathbf{u}, \tag{2.97}$$

$$\mathbf{F}_P = -\nabla P, \tag{2.98}$$

$$\mathbf{F}_C = -\frac{2Pm}{E}\hat{\mathbf{z}} \times \mathbf{u}, \tag{2.99}$$

$$\mathbf{F}_L = \frac{Pm}{E}\,(\nabla \times \mathbf{B}) \times \mathbf{B}, \tag{2.100}$$

$$\mathbf{F}_A = \frac{RaPm^2}{Pr} T\mathbf{r}, \tag{2.101}$$

$$\mathbf{F}_V = Pm\nabla^2\mathbf{u}, \tag{2.102}$$

where $\mathbf{F}_I$, $\mathbf{F}_P$, $\mathbf{F}_C$, $\mathbf{F}_L$, $\mathbf{F}_A$, and $\mathbf{F}_V$ are the inertial, pressure, Coriolis, Lorentz, buoyancy and viscous forces respectively. An individual force can be calculated by considering the energy of a force vector. We can express $\mathbf{F}$ as a combination of scalar potentials similar to Equation (2.86) and using Equation (2.90) gives

$$\begin{aligned} F^2 &= \int \mathbf{F}^2 \mathrm{d}V \\ &= 2\sum_{l=0}^{l_{max}} {\sum_{m=0}^{l}}' \int_{r_i+b}^{r_o-b} \left[|\mathcal{R}_l^m|^2 + l\,(l+1)\left(|\mathcal{S}_l^m|^2 + |\mathcal{T}_l^m|^2\right)\right] r^2 \mathrm{d}r. \end{aligned} \tag{2.103}$$

The curl of each force can be calculated using the same method as the forces. The curl of each force can be written as

$$C\,(\mathbf{F}) = \nabla \times \mathbf{F} = \hat{\mathcal{R}}\hat{\mathbf{r}} + r\nabla\hat{\mathcal{S}} + \mathbf{r} \times \nabla\hat{\mathcal{T}}$$

for some different scalars $\hat{\mathcal{R}}$, $\hat{\mathcal{S}}$ and $\hat{\mathcal{T}}$. Using the same method as the forces we obtain

$$\begin{aligned} C^2 &= \int (\nabla \times \mathbf{F})^2 \,\mathrm{d}V \\ &= 2\sum_{l=0}^{l_{max}} {\sum_{m=0}^{l}}' \int_{r_i+b}^{r_o-b} \left[\left|\hat{\mathcal{R}}_l^m\right|^2 + l\,(l+1)\left(\left|\hat{\mathcal{S}}_l^m\right|^2 + \left|\hat{\mathcal{T}}_l^m\right|^2\right)\right] r^2 \mathrm{d}r. \end{aligned} \tag{2.104}$$

The focus of Chapter 5 is to examine the lengthscale dependence of forces and curls of forces in our simulations. The lengthscale dependence in both l and m are examined. We can form

the power spectrum of an individual force as a function of spherical harmonic degree l as

$$F_l^2 = 2\sum_{m=0}^{l}{}' \int_{r_i+b}^{r_o-b} \left[|\mathcal{R}_l^m|^2 + l\,(l+1)\left(|\mathcal{S}_l^m|^2 + |\mathcal{T}_l^m|^2\right)\right] r^2 \mathrm{d}r \tag{2.105}$$

and similarly we can form the power spectrum as a function of spherical harmonic order m as

$$F_m^2 = 2\sum_{l=0}^{l_{max}} \int_{r_i+b}^{r_o-b} \left[|\mathcal{R}_l^m|^2 + l\,(l+1)\left(|\mathcal{S}_l^m|^2 + |\mathcal{T}_l^m|^2\right)\right] r^2 \mathrm{d}r. \tag{2.106}$$

For the curl of force spectra we can form a similar power spectra for l as

$$C_l^2 = 2\sum_{m=0}^{l}{}' \int_{r_i+b}^{r_o-b} \left[\left|\hat{\mathcal{R}}_l^m\right|^2 + l\,(l+1)\left(\left|\hat{\mathcal{S}}_l^m\right|^2 + \left|\hat{\mathcal{T}}_l^m\right|^2\right)\right] r^2 \mathrm{d}r \tag{2.107}$$

and for m we have

$$C_m^2 = 2\sum_{l=0}^{l_{max}} \int_{r_i+b}^{r_o-b} \left[\left|\hat{\mathcal{R}}_l^m\right|^2 + l\,(l+1)\left(\left|\hat{\mathcal{S}}_l^m\right|^2 + \left|\hat{\mathcal{T}}_l^m\right|^2\right)\right] r^2 \mathrm{d}r. \tag{2.108}$$

In the integrals above for forces and curls of forces we remove the boundary layers in our simulations, where b is set sufficiently large to ensure the boundary layers are removed completely. By excluding the boundary layers, we obtain the balance which is relevant to the bulk flow. The spectra for the curls of forces tend to peak at smaller scales due to the extra derivative involved. Hence to compensate for this we define the spectrum over l as

$$\hat{C}_l^2 = \frac{C_l^2}{l\,(l+1)} \tag{2.109}$$

and the spectrum over m as

$$\hat{C}_m^2 = \frac{C_m^2}{m}. \tag{2.110}$$

2.2.3.5 Spherical to cylindrical grid

The focus of Chapter 6 is to examine the lengthscale dependence of forces and curls of forces ITC and OTC. In order to do this we form a power spectra in m. This is chosen since the dissection of the domain at the TC occurs along a cylindrical surface. The only coordinate in spherical geometry that does not cross this surface is the ϕ coordinate. Hence the m-dependence of quantities can be naturally split and compared ITC and OTC.

In the previous section, each force can be expressed as a combination of scalar potentials given by Equation (2.86). These are then expanded in terms of spherical harmonics which gives data points in the θ and ϕ direction in spectral space and data points in the r direction in physical space. However, to obtain the power spectra of forces and curls of forces ITC and OTC we want to transform data points in the ϕ direction to spectral space but keep data points in the

r and θ direction in physical space. Therefore we consider a Fourier decomposition in the ϕ direction only, which means for an individual force we obtain

$$F = \sum_{m=0}^{M} F_m(r,\theta)\, e^{im\phi}. \tag{2.111}$$

Then, the energy of the force vector is given by

$$\begin{aligned} F^2 &= \int \mathbf{F}^2 \mathrm{d}V \\ &= \sum_{m=0}^{M}\sum_{m'=0}^{M} \int_0^{2\pi}\int_0^{\pi}\int_{r_i+b}^{r_o-b} F_m(r,\theta)\, F'_m(r,\theta)\, e^{im\phi} e^{im'\phi} r^2 \sin\theta \mathrm{d}r\mathrm{d}\theta\mathrm{d}\phi \\ &= \sum_{m=0}^{M} 2\pi \int_0^{\pi}\int_{r_i+b}^{r_o-b} F_m^2(r,\theta)\, r^2 \sin\theta \mathrm{d}r\mathrm{d}\theta \end{aligned} \tag{2.112}$$

Equation (2.112) gives a scalar which is a function of three variables, where data points in (r,θ) are in physical space and ϕ points are in spectral space, represented by m. At each m, we take the grid of points in (r,θ) and convert these to a cylindrical (s,z) grid, meaning we are converting the double integral in r and θ in Equation (2.112) to s and z.

In order to do this, a four point interpolation method is used. For each value of (s,z) on the cylindrical grid we can define a target point (r_t,θ_t) using

$$r_t = \sqrt{s^2+z^2} \text{ and } \theta_t = \tan^{-1}\left(\frac{s}{z}\right).$$

We then find the closest four neighbouring points of (r_t,θ_t), given by (r_1,θ_1), (r_2,θ_1), (r_1,θ_2) and (r_2,θ_2). This allows us to form a rectangle around the target point. From this we compute the weighted interpolation at each of the 4 points as

$$\begin{aligned} w_1 &= (r_2-r_t)(\theta_2-\theta_t) f(r_1,\theta_1) \\ w_2 &= (r_t-r_1)(\theta_2-\theta_t) f(r_2,\theta_1) \\ w_3 &= (r_2-r_t)(\theta_t-\theta_1) f(r_1,\theta_2) \\ w_4 &= (r_t-r_1)(\theta_t-\theta_1) f(r_2,\theta_2). \end{aligned}$$

The interpolated value on the (s,z) grid is given by

$$f(s,z) = \frac{w_1+w_2+w_3+w_4}{(r_2-r_1)(\theta_2-\theta_1)}.$$

This allows us to obtain the energy of a force of the form $F^2(s,z,m)$. The (s,z) grid allows the spherical shell to be split up into the regions ITC and OTC. We can then integrate over s and z in physical space to form a lengthscale dependence for each force in m either globally, ITC or OTC. For lengthscale dependent forces we consider the lengthscale dependent force densities.

These are given by

$$F^2_{OTC} = \frac{1}{V_{OTC}} \sum_{m=0}^{M} \int_{-\sqrt{r_o^2-s^2}}^{\sqrt{r_o^2-s^2}} \int_{r_i}^{r_o} F_m^2(s,z)\,\mathrm{d}s\mathrm{d}z \tag{2.113}$$

$$F^2_{ITCN} = \frac{1}{V_{ITCN}} \sum_{m=0}^{M} \int_{\sqrt{r_i^2-s^2}}^{\sqrt{r_o^2-s^2}} \int_{0}^{r_i} F_m^2(s,z)\,\mathrm{d}s\mathrm{d}z \tag{2.114}$$

$$F^2_{ITCS} = \frac{1}{V_{ITCS}} \sum_{m=0}^{M} \int_{-\sqrt{r_o^2-s^2}}^{-\sqrt{r_i^2-s^2}} \int_{0}^{r_i} F_m^2(s,z)\,\mathrm{d}s\mathrm{d}z \tag{2.115}$$

where F_{OTC}, F_{ITCN} and F_{ITCS} denotes the forces outside the tangent cylinder, inside the tangent cylinder north and inside the tangent cylinder south and V_{OTC}, V_{ITCN} and V_{ITCS} denotes the volume outside the tangent cylinder, inside the tangent cylinder north and inside the tangent cylinder south respectively. The force density ITC can be calculated by $F_{ITC} = F_{ITCN} + F_{ITCS}$. The curls of forces are formed using the same method and are given by

$$C^2_{OTC} = \frac{1}{V_{OTC}} \sum_{m=0}^{M} \int_{-\sqrt{r_o^2-s^2}}^{\sqrt{r_o^2-s^2}} \int_{r_i}^{r_o} C_m^2(s,z)\,\mathrm{d}s\mathrm{d}z \tag{2.116}$$

$$C^2_{ITCN} = \frac{1}{V_{ITCN}} \sum_{m=0}^{M} \int_{\sqrt{r_i^2-s^2}}^{\sqrt{r_o^2-s^2}} \int_{0}^{r_i} C_m^2(s,z)\,\mathrm{d}s\mathrm{d}z \tag{2.117}$$

$$C^2_{ITCS} = \frac{1}{V_{ITCS}} \sum_{m=0}^{M} \int_{-\sqrt{r_o^2-s^2}}^{-\sqrt{r_i^2-s^2}} \int_{0}^{r_i} C_m^2(s,z)\,\mathrm{d}s\mathrm{d}z. \tag{2.118}$$

The boundary layers in these integrals were removed before transforming from a spherical to cylindrical grid where data points where $r < r_i + b$ and $r > r_o + b$ on the spherical grid were set to zero before moving to a cylindrical grid. The curls of forces are compensated by dividing by m. This gives

$$\hat{C}^2_{OTC} = \frac{C^2_{OTC}}{m} \tag{2.119}$$

$$\hat{C}^2_{ITCN} = \frac{C^2_{ITCN}}{m} \tag{2.120}$$

$$\hat{C}^2_{ITCS} = \frac{C^2_{ITCS}}{m}. \tag{2.121}$$

The global lengthscale dependence produced using this method should match the lengthscale dependence produced using Equation (2.106). Unlike the calculation of forces explained in the previous section, the calculation of forces and curls of forces ITC and OTC is performed outwith the main part of the code. The method described above is applied in post-processing after the simulations have finished.

2.3 SUMMARY

The annulus model and the spherical dynamo model have been described. The Boussinesq approximation is applied to both models. The annulus model is a simplified model of spherical geometry and has an imposed magnetic field. The spherical shell model is more representative of Earth's core as it uses spherical geometry and is capable of the self-excitation of magnetic fields. The simplified nature of the annulus model means it is less computationally intensive, whereas the spherical dynamo model, though more representative of Earth's core, requires significantly more computing power. The governing equations and numerical methods for both models are explained, and the output parameters are also discussed. The methods described in Section 2.1 are used in Chapters 3 and 4, and the methods described in Section 2.2 are used in Chapters 5 and 6.

Chapter 3

Force balances in an annulus model

Convection occurring in planetary cores and atmospheres is strongly affected by magnetic fields generated through dynamo action. It is therefore of interest to consider the effect of magnetic fields on convection in planetary interiors in isolation to the dynamo process. Three-dimensional spherical simulations are the most suitable models as they capture the full dynamics of the flow. However, these can be computationally expensive to run. An alternative is to use a simplified model to explore the parameter space more cheaply. The Busse annulus model (Busse, 1970) is a simplified model of spherical geometry, which has been shown to produce features found in planetary cores and atmospheres in the non-magnetic case by Jones et al. (2003), Rotvig and Jones (2006) and Teed et al. (2012). A review of non-magnetic and magnetic work in an annulus model is discussed in Section 1.5.1.

This chapter examines forces balances in an annulus model with an imposed magnetic field. We extend previous non-magnetic work by carrying out non-linear simulations of Boussinesq convection within the annulus model, but additionally subject to an imposed azimuthal magnetic field. The mathematical setup, numerical method, and various output parameters were discussed in Chapter 2. We consider $Pr = 1$, $B_f = 0$, $\eta^* = 5 \times 10^5$, $0.01 \leq Pm \leq 5$ and $10^3 \leq Q \leq 5 \times 10^5$ for varying Ra which is presented in terms of its supercriticality (Ra/Ra_c^{HD}). We solve using stress-free, electrically conducting, constant temperature boundaries. The key features of bursts of convection and multiple jet solutions are discussed before presenting 4 different cases for Pm. The importance of the magnetic field can be determined by considering the Elsasser number, $\Lambda = Q/\eta^*$. The forces controlling the dynamics of the flow are discussed where we examine the force balances required for multiple jets, bursts of convection and other solutions in an annulus model. The force balances and types of solution are summarised in a regime diagram, which allows us to classify which area of parameter space is required in order to produce bursts of convection or multiple jets.

In Section 3.1 and 3.2 we discuss some possible regimes that occur in the model to form the basis for the regime diagrams presented in Section 3.4. A wider parameter sweep is performed upon discussion of the forces in Section 3.3. The properties of multiple jet solutions are explored

in greater detail in Chapter 4.

3.1 BURSTS OF CONVECTION

In a system with bursts of convection, periods of convection will occur which drives a zonal flow through the Reynolds stresses. Once the zonal flow becomes large enough, its shearing effect inhibits the convection causing it to weaken. In turn, this removes the source of generation of the zonal flow, so these also weaken allowing the convection to restart. This process keeps repeating in a quasi-periodic fashion. Bursts of convection have been demonstrated in the annulus model (e.g., Rotvig and Jones, 2006; Teed et al., 2012) and in spherical convection (e.g., Grote and Busse, 2001; Simitev and Busse, 2003). A non-magnetic and a magnetic case are discussed, highlighting the similarities and differences between them.

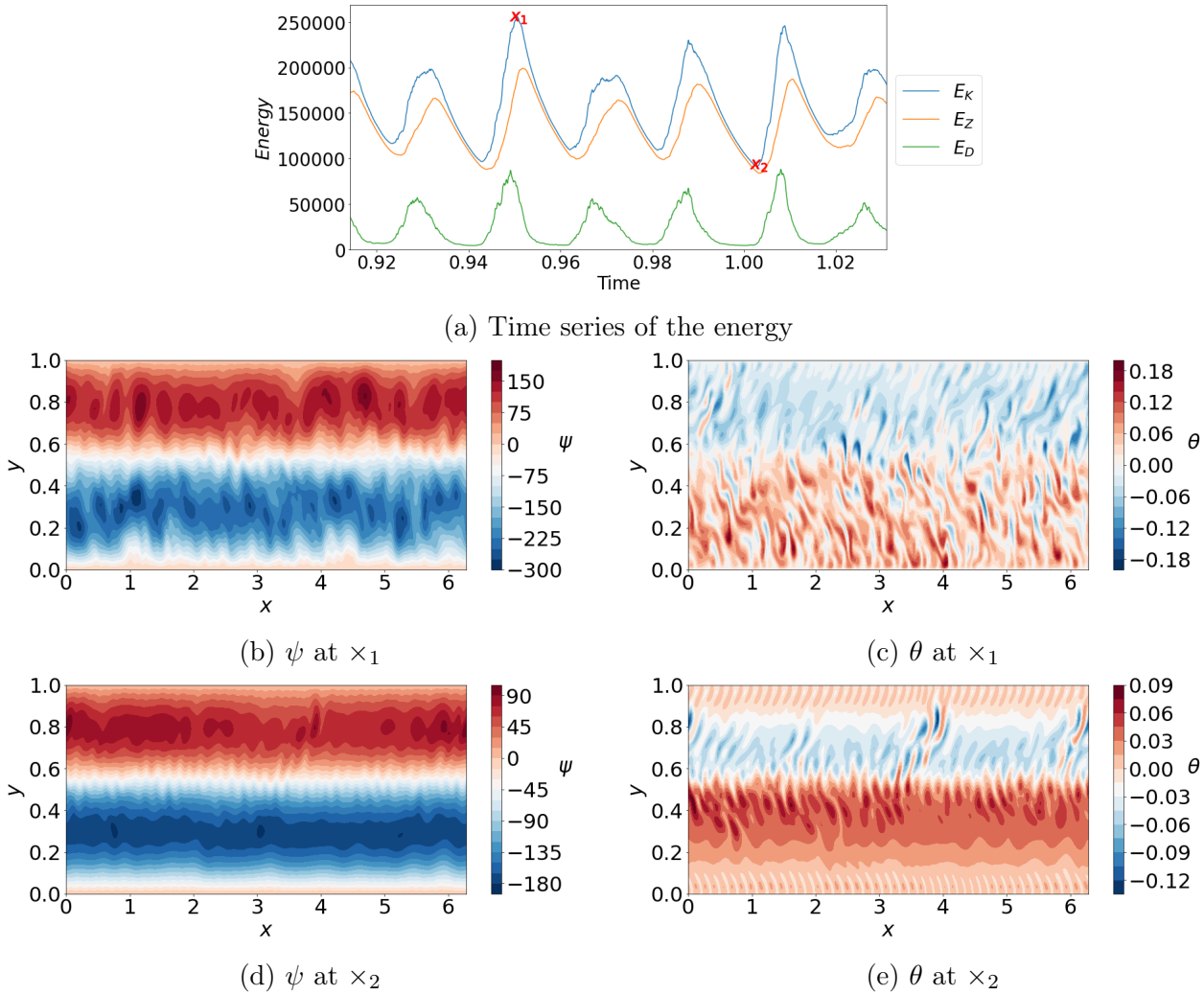

(a) Time series of the energy

(b) ψ at $\times_1$

(c) θ at $\times_1$

(d) ψ at $\times_2$

(e) θ at $\times_2$

Figure 3.1: Non-magnetic run showing bursts of convection for $Pr = 1$, $\eta^* = 5 \times 10^5$, $B_f = 0$ and $Ra/Ra_c^{HD} = 3$.

Oscillatory behaviour has been found in the kinetic energy profile for some of our magnetic runs, similar to bursts of convection found in the non-magnetic case by Teed et al. (2012). Two cases of bursts of convection are presented starting with a case from non-magnetic results by Teed et al. (2012) where it is known that bursts of convection occur, and then we discuss a

magnetic case where bursts of convection are found. In both cases the kinetic energy E_K given by (2.50), the zonal energy E_Z given by (2.54) and the difference between the two denoted by E_D are plotted. The value E_D is the convective energy. The flow patterns for each are also shown and in the magnetic case the magnetic energy given by (2.51) is plotted.

Figure 3.1 shows an example of bursts of convection in the non-magnetic case. The peak in zonal flow energy is just after the peak in convective energy (Fig. 3.1a). The convective energy performs a slow decay during which the zonal energy also decays and the trough in the convective energy occurs near to where the trough in zonal energy occurs (Fig. 3.1a). This is the point where the zonal flow has weakened enough for convection to fire up in another burst. Figures 3.1b-3.1e shows plots of the fields at the peaks and troughs of the kinetic energy which are marked by the points $\times_1$ and $\times_2$. The zonal energy is always larger than the convection but at $\times_1$ the convection is more prominent (Figs 3.1b, 3.1c) compared to the more zonal period at $\times_2$ (Figs 3.1d, 3.1e).

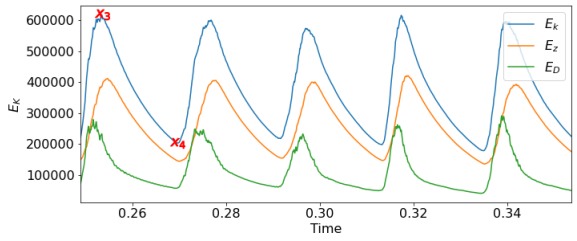

(a) Time series of the energy

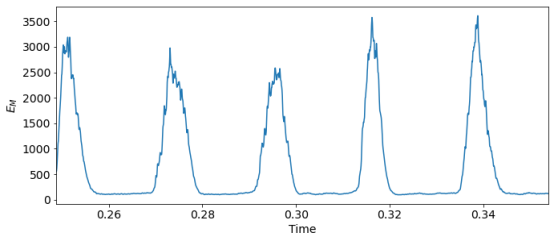

(b) Time series of the magnetic energy

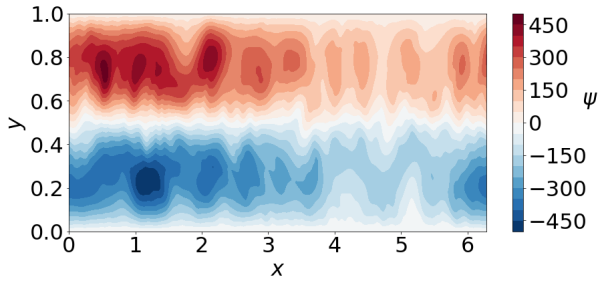

(c) ψ at $\times_3$

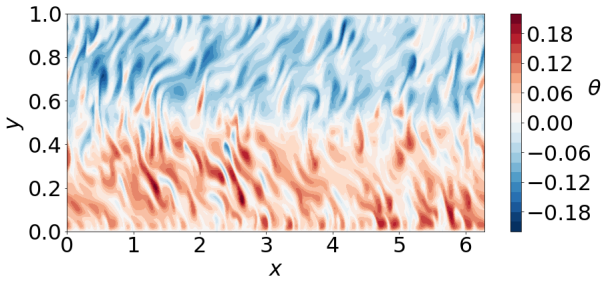

(d) θ at $\times_3$

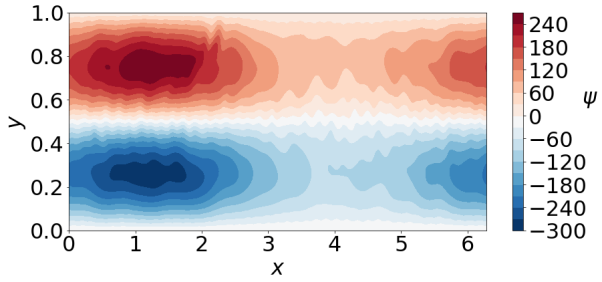

(e) ψ at $\times_4$

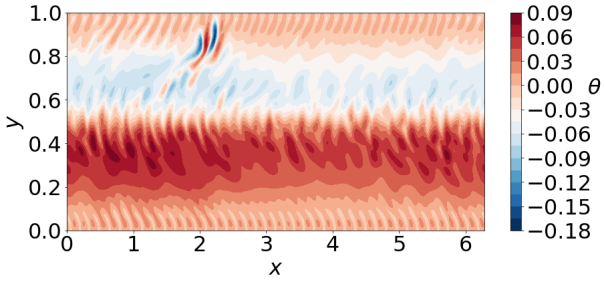

(f) θ at $\times_4$

Figure 3.2: Magnetic run showing bursts of convection for $Pr = 1$, $\eta^* = 5 \times 10^5$, $B_f = 0$, $Pm = 0.5$, $Q = 10^3$ and $Ra/Ra_c^{HD} = 4$.

Figure 3.2 shows a magnetic run with bursts of convection. The behaviour is similar to the non-magnetic case where the peak in zonal flow energy is just after the peak in convective energy (Fig. 3.2a). The convective energy slowly decays as does the zonal energy. The troughs

in both occur at roughly the same time at which point the zonal energy has diminished and the convection starts again in another burst. The magnetic energy is plotted where we observe peaks in the magnetic energy but with a very flat nature for extended periods of time (Fig. 3.2b). The magnetic energy is much smaller than the kinetic energy and thus does not play a role in the bursting nature observed in the kinetic energy. Figures 3.2c-3.2f show plots of ψ and θ at the peaks and troughs of the kinetic energy marked by $\times_3$ and $\times_4$. These plots are very similar to the plots for the non-magnetic case shown in Figure 3.1. In both cases a zonal chaotic behaviour occurs in ψ at the peak in kinetic energy. At the trough, zonal behaviour also occurs in both cases but the flow pattern is less chaotic. In both the magnetic and non-magnetic case, the magnitudes of ψ and θ are larger at the peak in kinetic energy than the trough. These runs behave as magnetically adjusted hydrodynamical runs. The bursts of convection observed in the magnetic case are only found at low values of Q, where the magnetic field does not play an important role on the convection in our system. As Q is increased, we lose the oscillatory behaviour in the kinetic energy and end up with a more chaotic system.

3.2 Multiple jet solutions

Multiple jet solutions have mainly been found in the non-magnetic case when rigid boundaries have been considered, meaning when $B_f \neq 0$. This has been shown by Jones et al. (2003), Rotvig and Jones (2006) and by Teed et al. (2012), where multiple jet solutions are explored as the bottom friction parameter B_f is varied. There is also evidence of multiple jet solutions for stress-free boundary conditions, but these are limited. This has been discussed in Jones et al. (2003) where multiple jet solutions have been found for stress-free conditions in a small window of parameter space. We also find multiple jet solutions for $B_f = 0$ in a small window of parameter space. We mainly find these where Q is small compared to η^* and close to critical Ra. However, we have found a few cases of multiple jet solutions for $Pm = 5$ at larger Q and small Ra with $B_f = 0$.

Previous studies require two conditions to be satisfied for a solution to be described as 'multiple jets'. First, the dominant (time-averaged) mode $\hat{m}$ of the $l = 0$ component should satisfy $\hat{m} \geq 3$. Second, the (time-averaged) ratio of zonal to kinetic energy should satisfy $E_Z/E_K > 0.05$. We follow these criteria but with an additional condition. We also require the $l = 0$ mode to be the dominant azimuthal mode. This extra condition is added because the magnetic field is found to be capable of breaking the axisymmetry of the flow pattern, which is always axisymmetric in the non-magnetic case. We denote the number of jets found in a simulation by $M = \hat{m} + 1$ meaning a 'multiple jet' solution has at least 4 jets.

Four jet solutions are found at low Q (i.e. $Q = 10^3$, $Q = 5 \times 10^3$ and $Q = 10^4$) and low Ra for $Pm = 0.01$, $Pm = 0.1$, $Pm = 0.5$ and $Pm = 5$. At $Q = 5 \times 10^5$ and $Pm = 5$, 4 jet solutions have been found at low Ra. We have also found a 5 jet solution for $Pm = 0.1$. In Figure 3.3 we show an example of a 4 jet solution. This is observed in the plot of ψ as shown in Figure 3.3a, where we observe a banded structure. We also plot the zonal flow given by (2.53) as shown in

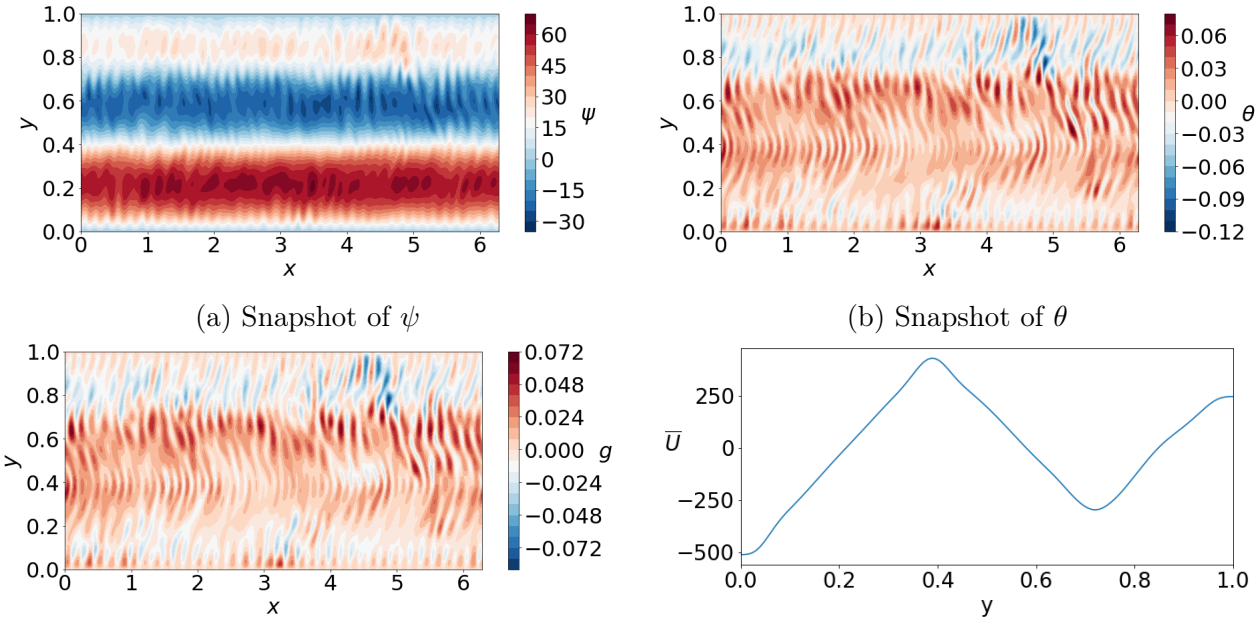

(a) Snapshot of ψ

(b) Snapshot of θ

(c) Snapshot of g

(d) $\bar{U}$

Figure 3.3: Multiple jet solution for $Pr = 1$, $\eta^* = 5 \times 10^5$, $B_f = 0$, $Pm = 0.5$, $Q = 10^3$ and $Ra/Ra_c^{HD} = 2$.

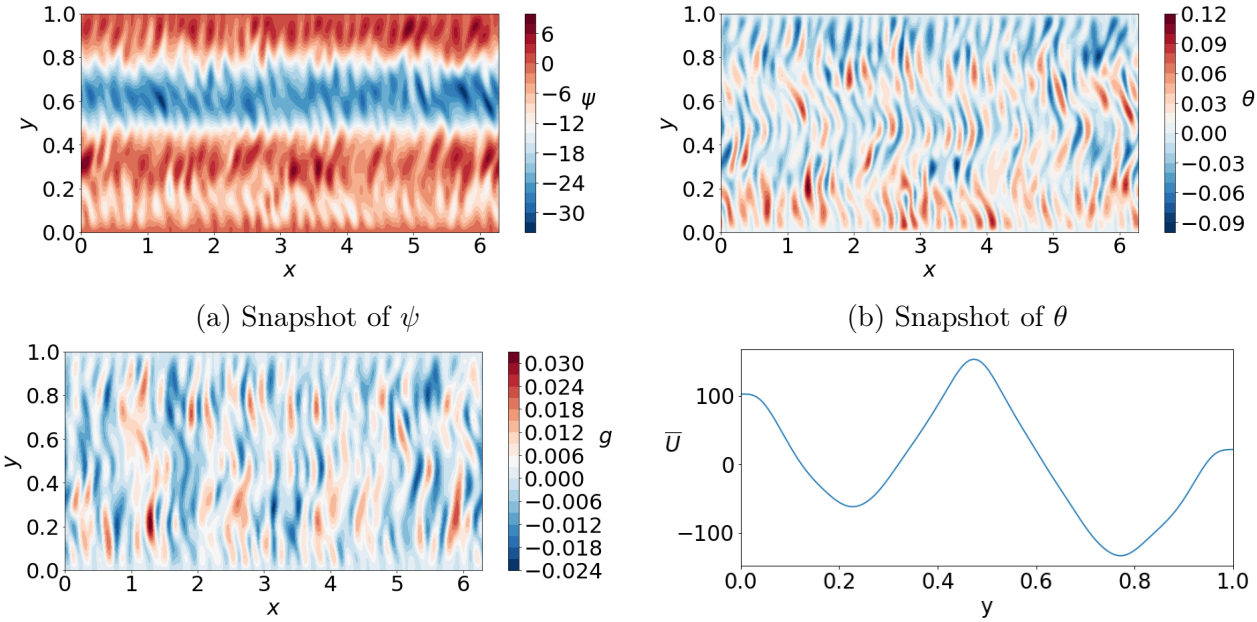

(a) Snapshot of ψ

(b) Snapshot of θ

(c) Snapshot of g

(d) $\bar{U}$

Figure 3.4: Multiple jet solution for $Pr = 1$, $\eta^* = 5 \times 10^5$, $B_f = 0$, $Pm = 0.1$, $Q = 10^4$ and $Ra/Ra_c^{HD} = 2$.

Figure 3.3d where we observe a 4 jet structure. In Figure 3.4 we present a 5 jet solution. We also observe a banded structure in the plot of ψ as shown in Figure 3.4a and we observe a 5 jet structure in the zonal flow as shown in Figure 3.4*d*. The plots of θ and g as shown in Figures 3.3b-3.3c and 3.4b-3.4c are very similar in both cases. These multiple jet solutions are similar to those found in the hydrodynamical case (see for example Figure 2(a) in Teed et al. (2012)).

For each case the energy spectra in m is considered (Fig. 3.5). In Figure 3.5a we have a peak in

the kinetic energy at $m = 3$. This matches the plot of ψ where we observe an $m = 3$ structure in y, confirming an $m = 3$ dominant mode. Figure 3.5b shows a peak in the kinetic energy at $m = 4$ matching the plot of ψ and confirms an $m = 4$ dominant mode. The magnetic energy is smaller than the kinetic energy in these cases as Q is small. If the magnetic field is larger, this would likely inhibit the formation of zonal flows including multiple jets.

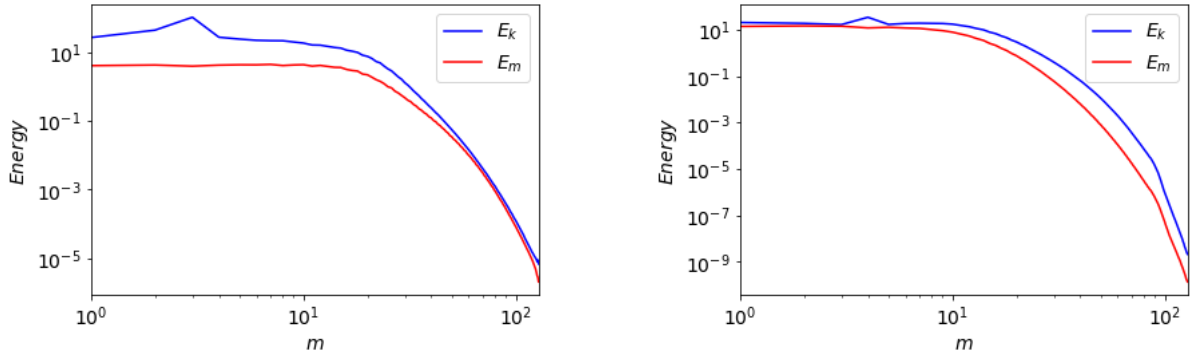

(a) 4 jet solution

(b) 5 jet solution

Figure 3.5: Energy spectra in m.

These multiple jet solutions only appear in a small window of parameter space and vanish as we increase Ra and Q, at least for small Pm. This is similar to the non-magnetic case where the multiple jets appear close to critical Ra when the rotation rate is large and vanish as Ra is increased. We discuss multiple jet solutions in greater detail in Chapter 4, where solutions with $B_f \neq 0$ are examined.

3.3 FORCE BALANCES

We now discuss force balances in the system by varying Q and Ra for four different values of Pm retaining $Pr = 1$, $\eta^* = 5 \times 10^5$ and $B_f = 0$. Each parameter regime produces a particular force balance that can be used to aid identification of bursts of convection, multiple jets and other solutions. Although we refer to forces, the analysis that follows presents the curls of forces.

3.3.1 $Pm = 0.01$

Figure 3.6 shows the lengthscale dependent forces for $Pr = 1$, $\eta = 5 \times 10^5$, $B_f = 0$, $Pm = 0.01$ and $Ra/Ra_c^{HD} = 5$ for different values of Q. These are constructed by considering Equations (2.55)-(2.60) where we have summed over each m forming a spectrum of each force in l. At $Q = 10^3$ a strong inertial force and a weak Lorentz force is observed (Fig. 3.6a). At this value of Q we obtain a multiple jet solution. At $Q = 10^4$ we observe similar behaviour but multiple jet solutions are no longer obtained. This is most likely due to the increase in all other forces. As Q is increased the system transitions to a new balance. The Lorentz force starts to grow with the inertial force remaining strong and we see contributions from the Coriolis and buoyancy (Archimedean) forces in the force balance at larger scales, as shown in Figure 3.6c. Figure 3.6d

shows the forces at $Q = 5 \times 10^5$, where the rotation rate and input magnetic field strength are equal. At these parameter values, the inertial and Lorentz forces swap positions and we now have a strong balance between Lorentz and buoyancy forces with contributions from the Coriolis force at large scales.

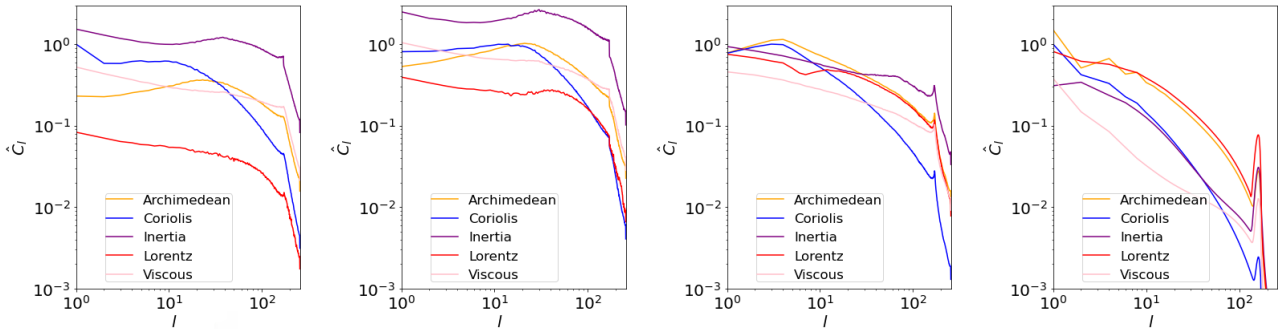

(a) $Q = 10^3$ (b) $Q = 10^4$ (c) $Q = 10^5$ (d) $Q = 5 \times 10^5$

Figure 3.6: Curl of forces for $Pr = 1$, $\eta^* = 5 \times 10^5$, $B_f = 0$, $Pm = 0.01$ and $Ra/Ra_c^{HD} = 5$ for different values of Q.

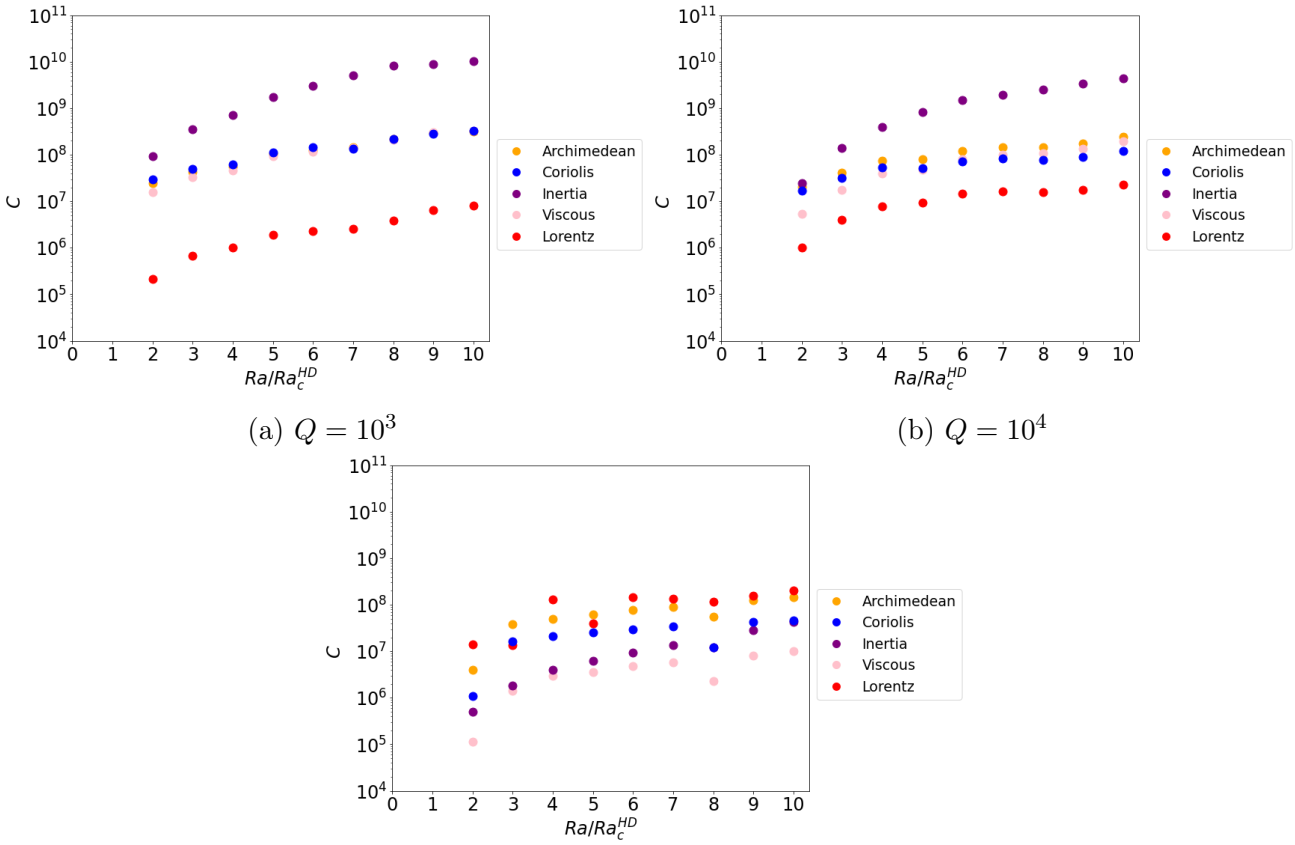

(a) $Q = 10^3$ (b) $Q = 10^4$

(c) $Q = 5 \times 10^5$

Figure 3.7: Globally averaged curl of forces against Ra/Ra_c^{HD} for $Pr = 1$, $\eta^* = 5 \times 10^5$, $B_f = 0$, $Pm = 0.01$ for different values of Q.

In Figure 3.7 the different force balances are shown by summing over l and m for each force as given by Equations (2.55)-(2.60), forming globally averaged quantities of each force. For $Q = 10^3$ and $Q = 10^4$ a strong inertial force with a weak Lorentz force occurs which remains

the case as the Rayleigh number increases (Figs 3.7a-3.7b). At $Q = 10^4$ the buoyancy force has increased, but remains in the secondary balance with Coriolis and viscous forces (Fig. 3.7b). The Lorentz force remains weak but has increased slightly compared with $Q = 10^3$ (Fig. 3.7a). At $Q = 5 \times 10^5$ a balance between Lorentz and buoyancy forces occurs, which persists as we increase the Rayleigh number (Fig. 3.7c).

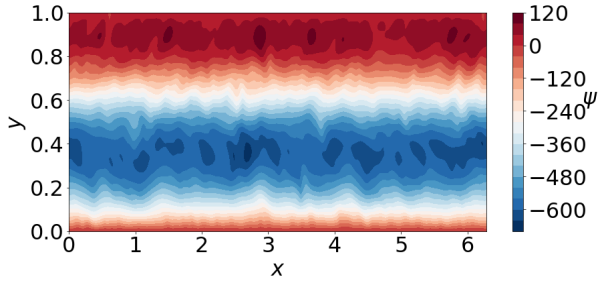

(a) Snapshot of ψ

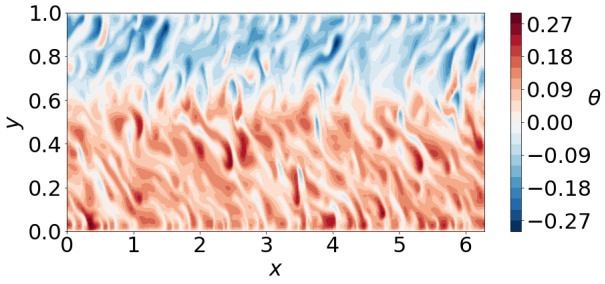

(b) Snapshot of θ

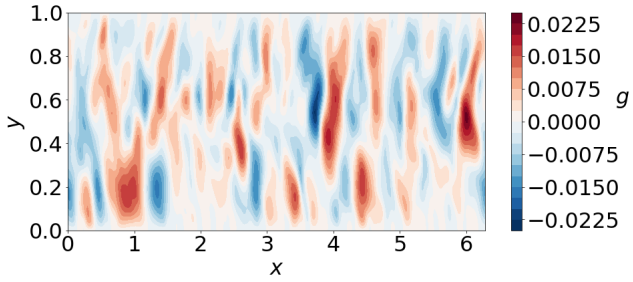

(c) Snapshot of g

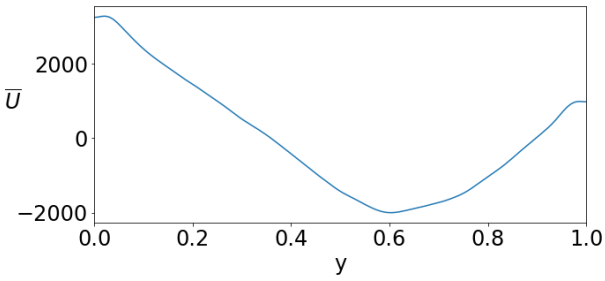

(d) $\bar{U}$

Figure 3.8: Plots of the fields for $Pr = 1$, $\eta^* = 5 \times 10^5$, $B_f = 0$, $Pm = 0.01$, $Q = 10^4$ and $Ra/Ra_c^{HD} = 5$.

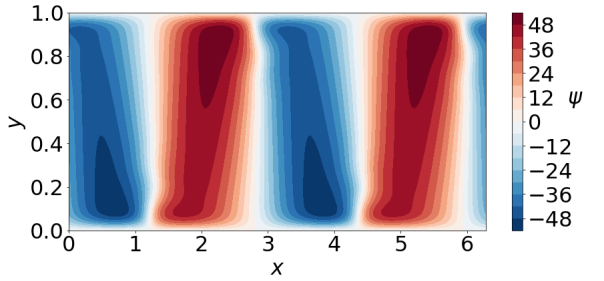

(a) Snapshot of ψ

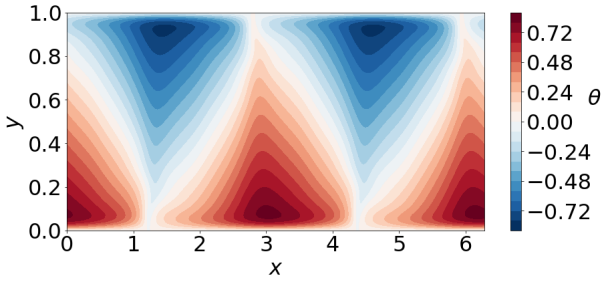

(b) Snapshot of θ

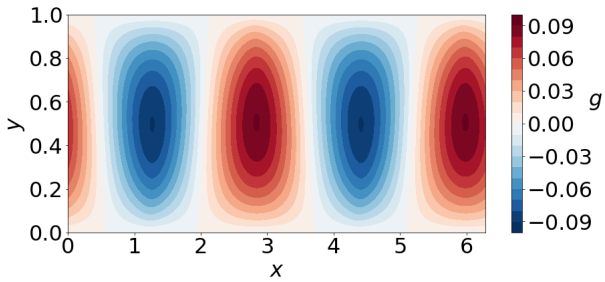

(c) Snapshot of g

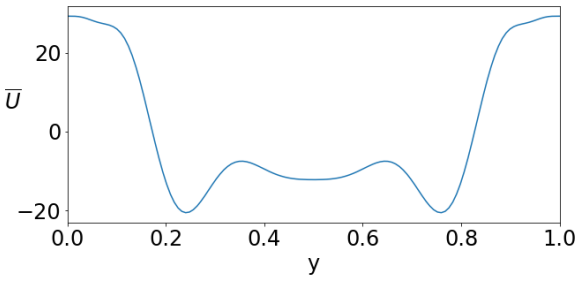

(d) $\bar{U}$

Figure 3.9: Plots of the fields for $Pr = 1$, $\eta^* = 5 \times 10^5$, $B_f = 0$, $Pm = 0.01$, $Q = 5 \times 10^5$ and $Ra/Ra_c^{HD} = 5$.

Different flow patterns are observed between the inertially dominated regime and the regime

where buoyancy and Lorentz forces are in balance. In the inertially dominated regime a turbulent flow pattern is observed (Fig. 3.8). For all cases where the inertial force is strong, similar flow patterns to Figure 3.8 are observed where all have zonal flows in the form of multiple jets at low Ra and bursts of convection as Ra is increased. In the area of parameter space between $Q = 10^5$ and $Q = 5 \times 10^5$ we observe a transition from an inertially dominant regime to a balance between the buoyancy and Lorentz forces. In this regime, the inertial force becomes weaker and no longer plays a role in the main force balance. The flow patterns in this regime show that the magnetic field has a stabilising effect on the flow (Fig. 3.9). The magnitude of ψ has decreased and g has increased between Figures 3.8 and 3.9. Here we observe a flow pattern which is very similar to onset. Considering the plot for g we see that the convection cells fill the entire column which matches convection at onset. The plot of ψ has been stretched in the y direction and θ has been changed in the x direction but they still look very similar to onset where the convection cells fill the entire radial direction. This is the only value of Pm where the magnetic field has a stabilising effect on the flow and the only value of Pm where a balance between the Lorentz and buoyancy forces occur.

3.3.2 $Pm = 0.1$

For $Pm = 0.1$ we find similar results to $Pm = 0.01$. Multiple jet solutions are observed at low Q and close to onset. As we increase Ra at low Q we observe bursts of convection. Figure 3.10 shows the lengthscale dependent forces found for $Pr = 1$, $\eta^* = 5 \times 10^5$, $B_f = 0$, $Pm = 0.1$ and $Ra/Ra_c^{HD} = 7$ for different values of Q. For low Q a strong inertial force and a weak Lorentz force occurs across all lengthscales (Figs 3.10a, 3.10b), similar to $Pm = 0.01$. As we increase Q the Lorentz force gradually increases (Figs 3.10c, 3.10d). However, in contrast with the case presented for $Pm = 0.01$ we never observe a balance between the Lorentz and buoyancy force. If $Q > 5 \times 10^5$ was considered then it might be possible to reach a leading order balance involving the buoyancy and Lorentz force similar to $Pm = 0.01$. For all values of Q, a turbulent flow pattern is observed similar to that shown for $Pm = 0.01$ (Fig. 3.8).

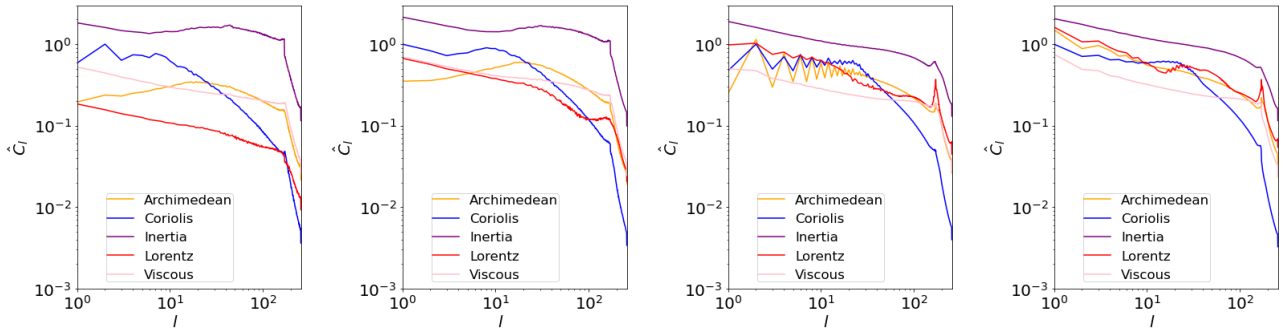

(a) $Q = 10^3$ (b) $Q = 10^4$ (c) $Q = 10^5$ (d) $Q = 5 \times 10^5$

Figure 3.10: Curls of forces for $Pr = 1$, $\eta^* = 5 \times 10^5$, $B_f = 0$, $Pm = 0.1$ and $Ra/Ra_c^{HD} = 7$ for different values of Q.

Figure 3.11 shows the global average of each force. At $Q = 10^3$ we observe a strong inertial

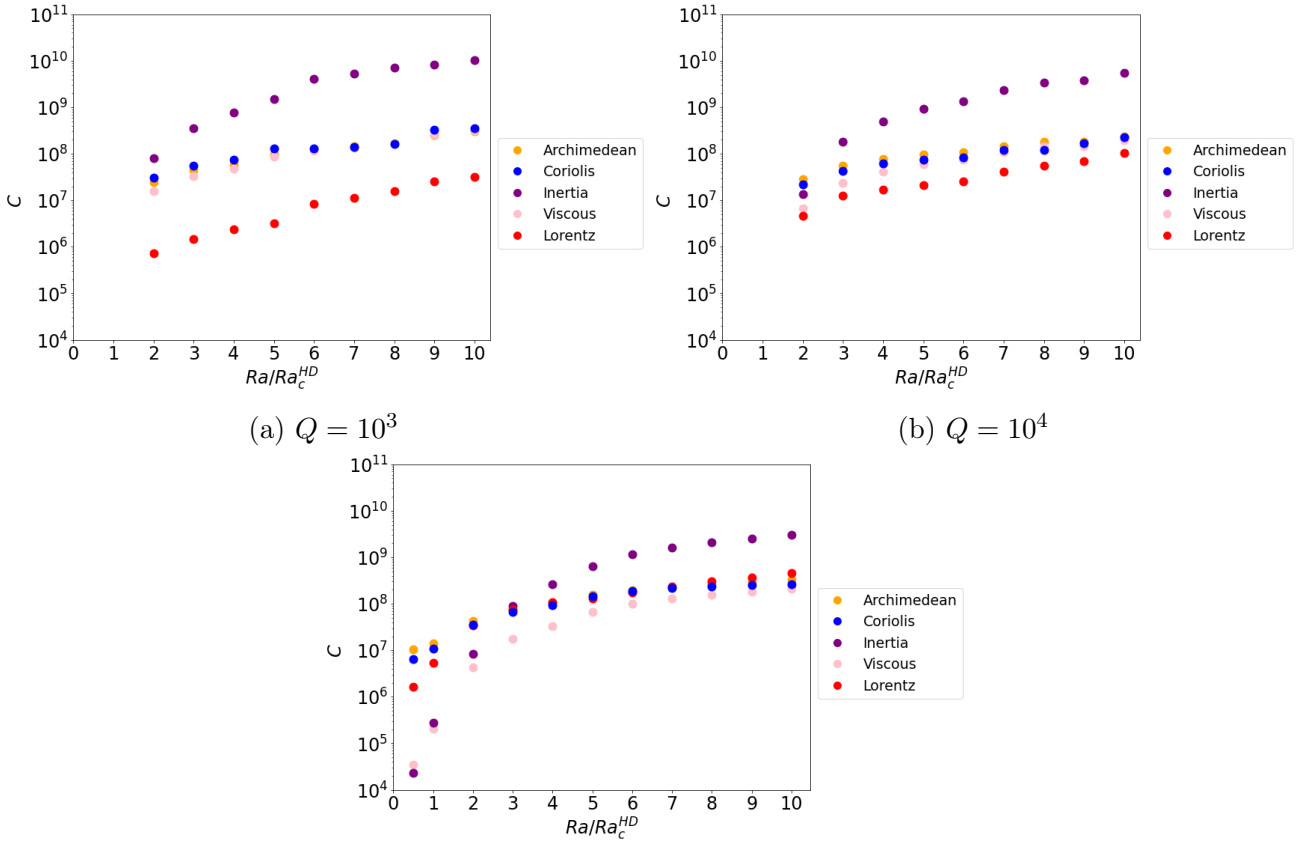

(a) $Q = 10^3$

(b) $Q = 10^4$

(c) $Q = 10^5$

Figure 3.11: Globally averaged curl of forces against Ra/Ra_c^{HD} for $Pr = 1$, $\eta^* = 5 \times 10^5$, $B_f = 0$, $Pm = 0.1$ for different values of Q.

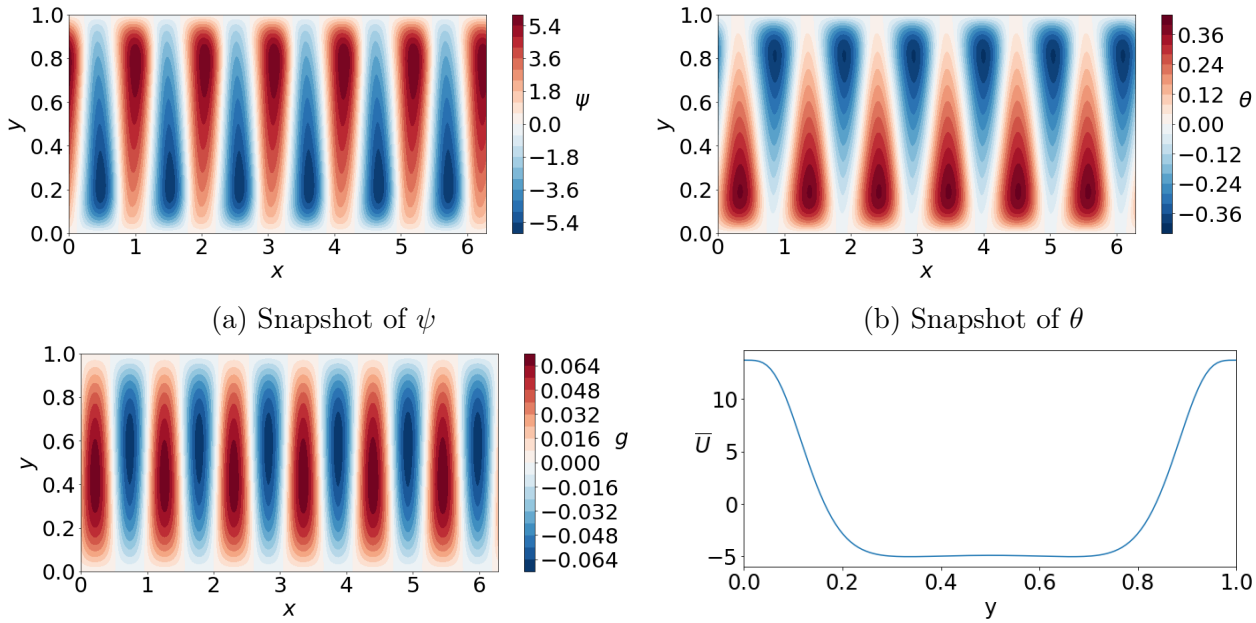

(a) Snapshot of ψ

(b) Snapshot of θ

(c) Snapshot of g

(d) $\bar{U}$

Figure 3.12: Plots of the fields for $Pr = 1$, $\eta^* = 5 \times 10^5$, $B_f = 0$, $Pm = 0.1$, $Q = 10^5$ and $Ra/Ra_c^{HD} = 0.5$.

force and weak Lorentz force, similar to that found for $Pm = 0.01$. At $Q = 10^4$ we still have a strong inertial force but a slight increase in the Lorentz force is observed. At $Q = 10^5$ we

observe a MAC balance close to critical with a weak inertial force, where the flow pattern looks similar to onset as we are only just supercritical (Fig. 3.12). The MAC balance is found for $Ra < Ra_c^{HD}$ because at $Pm = 0.1$ and $Q = 10^5$, the magnetic critical Rayleigh number is smaller than Ra_c^{HD}. As Ra is increased the MAC balance is lost and the system transitions to an inertially dominant regime.

3.3.3 $Pm = 0.5$

For $Pm = 0.5$ we observe three different force balances as we vary Q and Ra. At low Q and close to critical we observe multiple jet solutions and as Ra is increased we observe bursts of convection, similar to results found for $Pm = 0.01$ and $Pm = 0.1$. Figure 3.13 shows the forces for $Pr = 1$, $\eta^* = 5 \times 10^5$, $B_f = 0$, $Pm = 0.5$ and $Q = 10^3$ for two different values of Ra/Ra_c^{HD}. At $Ra/Ra_c^{HD} = 2$ where multiple jets occur (Fig. 3.13a) and at $Ra/Ra_c^{HD} = 5$ where bursts of convection occur (Fig. 3.13b) we observe a strong inertial force and weak Lorentz force at all lengthscales. In Figure 3.13a we see a peak occurring in the inertial force but in Figure 3.13b we do not observe an obvious sharp peak in the force spectra.

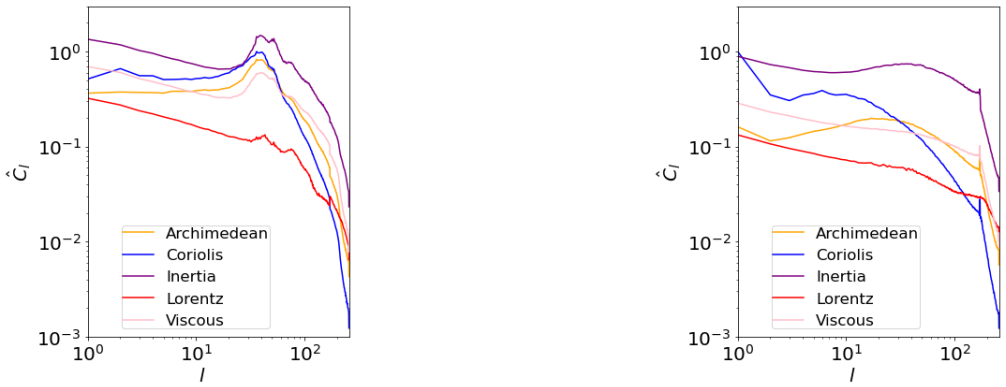

(a) $Ra/Ra_c^{HD} = 2$ where multiple jets occur (b) $Ra/Ra_c^{HD} = 5$ where bursts occur

Figure 3.13: Curl of forces for $Pr = 1$, $\eta^* = 5 \times 10^5$, $B_f = 0$, $Pm = 0.5$ and $Q = 10^3$.

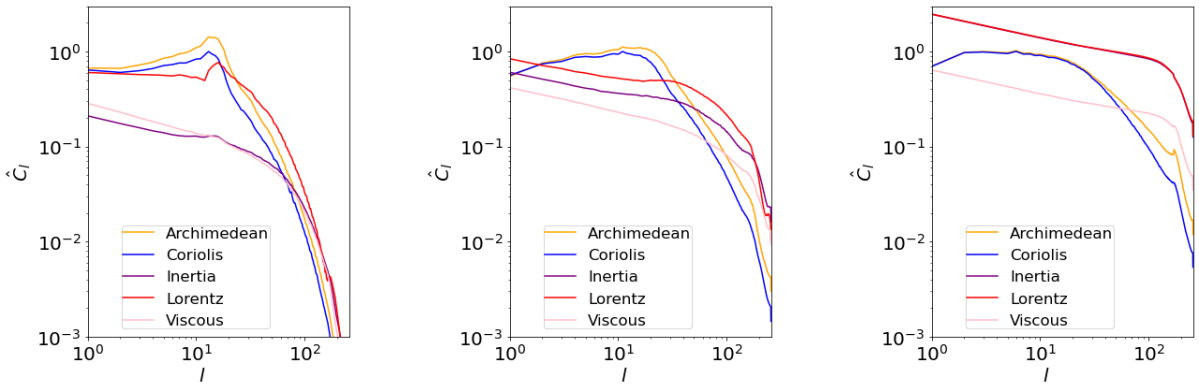

(a) $Ra/Ra_c^{HD} = 2$ (b) $Ra/Ra_c^{HD} = 5$ (c) $Ra/Ra_c^{HD} = 7$

Figure 3.14: Curl of forces for $Pr = 1$, $\eta^* = 5 \times 10^5$, $B_f = 0$, $Pm = 0.5$ and $Q = 10^5$.

Figure 3.14 shows the lengthscale dependent forces for $Pr = 1$, $\eta^* = 5 \times 10^5$, $B_f = 0$, $Pm = 0.5$ and $Q = 10^5$ for different values of Ra/Ra_c^{HD}. A MAC balance occurs at low Ra with a weak

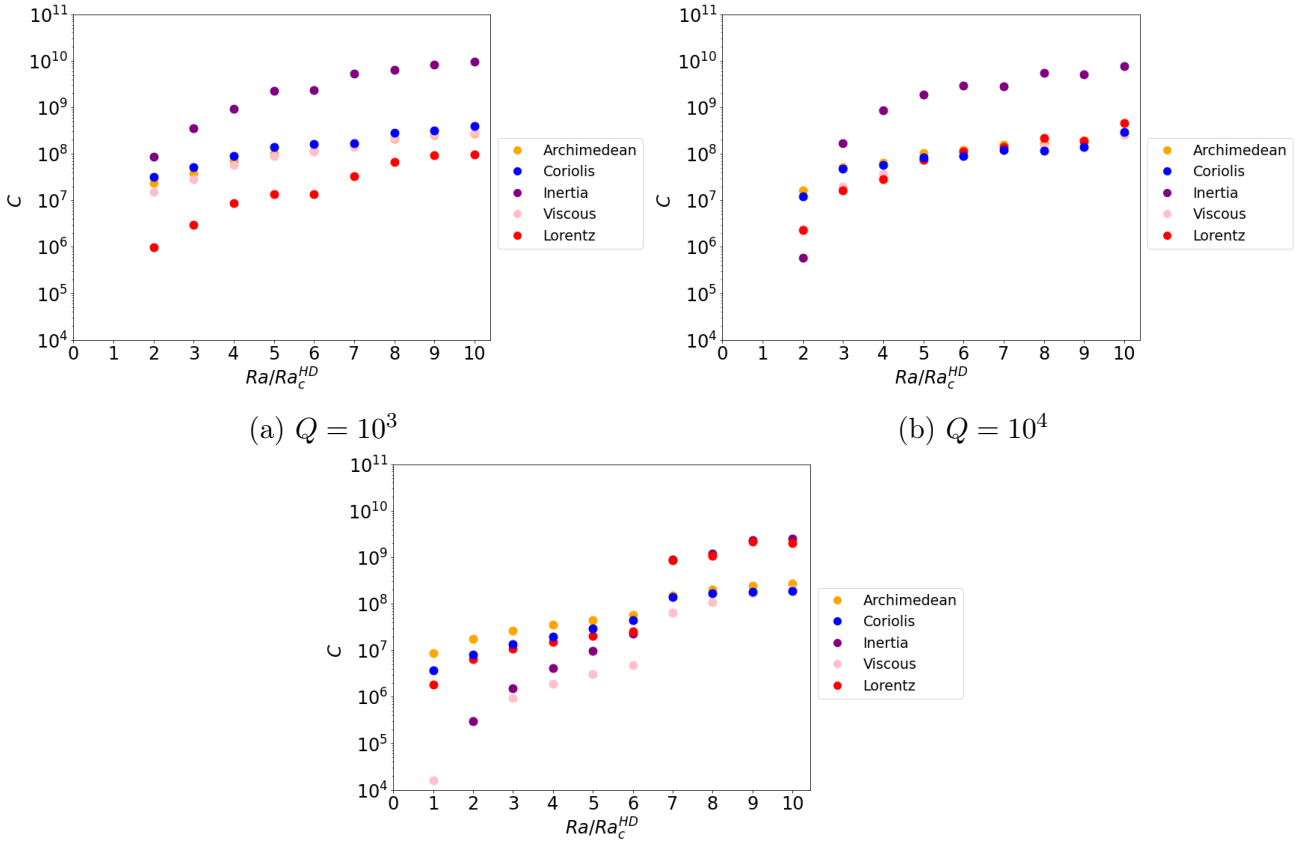

(a) $Q = 10^3$

(b) $Q = 10^4$

(c) $Q = 10^5$

Figure 3.15: Globally averaged curls of forces against Ra/Ra_c^{HD} for $Pr = 1$, $\eta^* = 5 \times 10^5$, $B_f = 0$, $Pm = 0.5$ for different values of Q.

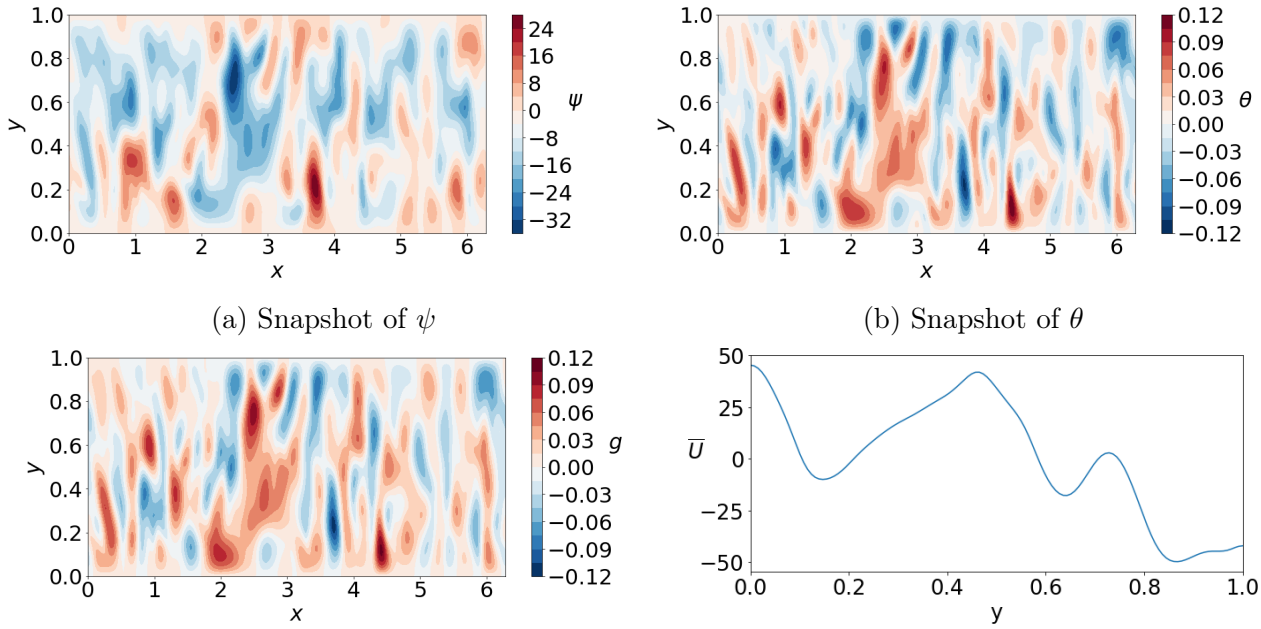

(a) Snapshot of ψ

(b) Snapshot of θ

(c) Snapshot of g

(d) $\bar{U}$

Figure 3.16: Plots of the fields for $Pr = 1$, $\eta^* = 5 \times 10^5$, $B_f = 0$, $Pm = 0.5$, $Q = 10^5$ and $Ra/Ra_c^{HD} = 5$.

inertial force (Fig. 3.14a). As we increase Ra a leading order balance is observed between

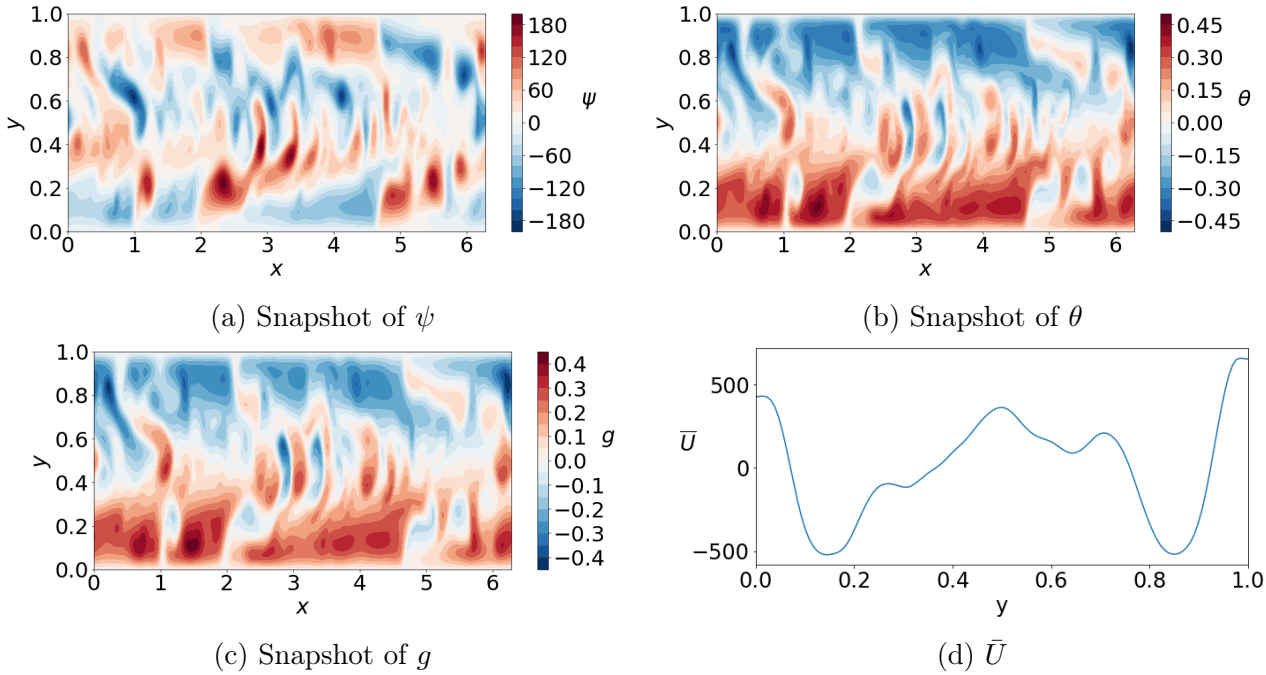

(a) Snapshot of ψ

(b) Snapshot of θ

(c) Snapshot of g

(d) $\bar{U}$

Figure 3.17: Plots of the fields for $Pr = 1$, $\eta^* = 5 \times 10^5$, $B_f = 0$, $Pm = 0.5$, $Q = 10^5$ and $Ra/Ra_c^{HD} = 8$.

the Coriolis and buoyancy force with the Lorentz force also involved in the leading order force balance at some scales (Fig. 3.14b). As we increase Ra further we see a transition from the MAC balance to a balance between Lorentz and inertial forces (Fig. 3.14c). This balance dominates at all lengthscales. In all cases the viscous force remains weak. The flow pattern for this type of force balance are discussed later (Fig. 3.17).

As considered for the previous cases, we plot the globally averaged quantities of each force. For $Q = 10^3$ we observe a strong inertial force and weak Lorentz force at all values of Ra (Fig. 3.15a). This is similar to $Pm = 0.01$ and $Pm = 0.1$ although comparing with Figures 3.7a and 3.11a we see an increase in the other forces. For $Q = 10^4$, at low Ra we observe a balance between the Coriolis and buoyancy force and a secondary balance between Lorentz and viscous forces with a weak inertial force. As we increase Ra, we observe a transition to the case where the inertial force dominates (Fig. 3.15b). Figure 3.15c shows a MAC balance with a weak inertial and viscous force for $Ra/Ra_c^{HD} \leq 6$. We then clearly see the jump between 6 and 7 times critical, where we lose the MAC balance and now have a balance between inertial and Lorentz forces. Also, as we increase Ra the inertial force gradually increases before we reach the transition between force balances. The flow patterns found for the inertially dominated regimes are similar to those at $Pm = 0.01$ (Fig. 3.8). For runs where a MAC balance occurs at low Ra and $Q = 10^5$ (see 3.14b), we observe no zonal flows and the scale of convection is smaller compared to the cases with zonal flows (Fig. 3.16). This differs to the runs with a MAC balance at $Pm = 0.01$ where the magnetic field had a stabilising effect on the flow (Fig. 3.9). For runs where the Lorentz and inertial force are in balance (see 3.14b) we no longer observe zonal flows (Fig. 3.17).

3.3.4 $Pm = 5$

Similar force balances are found at $Pm = 5$ to the other values of Pm considered. However, at $Q = 5 \times 10^5$ we find a dominant Lorentz force for some runs that has not been observed for any other Pm explored (Figs 3.18a and 3.18b). In this area of parameter space we find multiple jet solutions, similar to those found at low Q (Fig. 3.3, 3.4). Plots of a 5-jet solution found at $Q = 5 \times 10^5$ and $Ra = 3Ra_c^{HD}$ is shown in Figure 3.19. However unlike at low Q where a dominant inertial force was required for multiple jets, the system now has a dominant Lorentz force. It is clear from this balance that the magnetic field plays a role in producing the multiple jets. As we increase Ra, we no longer obtain multiple solutions and the system transitions to a dominant balance between Lorentz and inertial forces (Fig. 3.18c).

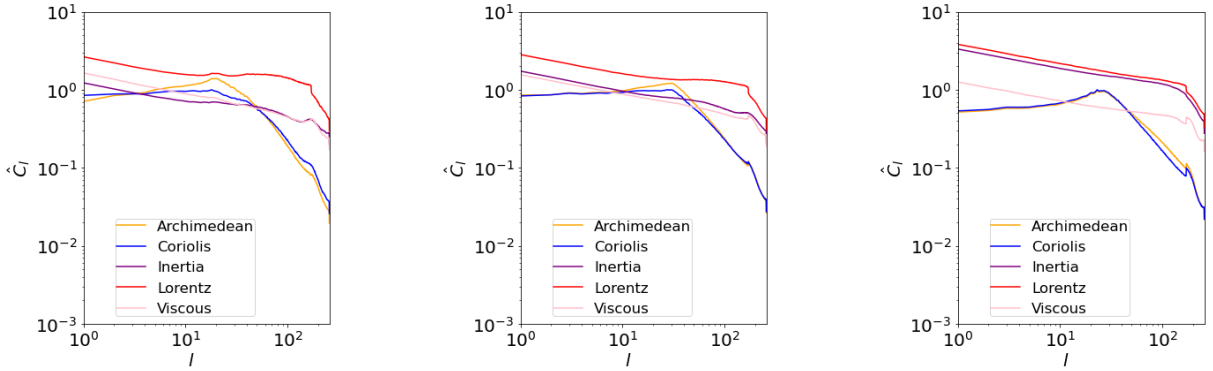

(a) $Ra = 3Ra_c$ (b) $Ra = 5Ra_c$ (c) $Ra = 6Ra_c$

Figure 3.18: Curls of forces for $Pr = 1$, $\eta^* = 5 \times 10^5$, $B_f = 0$, $Pm = 5$ and $Q = 5 \times 10^5$ for different values of Ra.

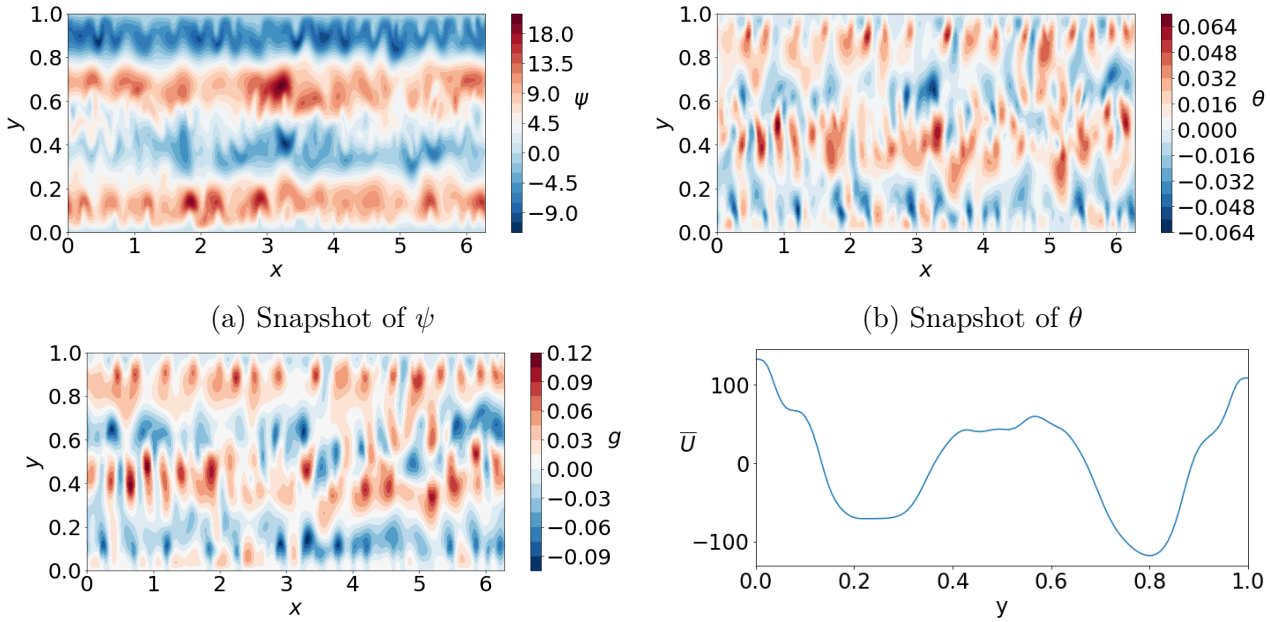

(a) Snapshot of ψ (b) Snapshot of θ

(c) Snapshot of g (d) $\bar{U}$

Figure 3.19: Plots of the fields for $Pr = 1$, $\eta^* = 5 \times 10^5$, $B_f = 0$, $Pm = 5$, $Q = 5 \times 10^5$ and $Ra/Ra_c^{HD} = 3$.

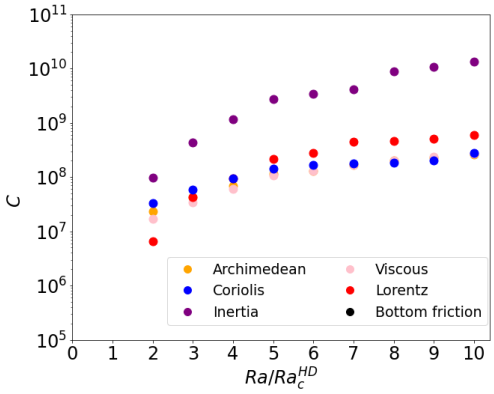

(a) $Q = 10^3$

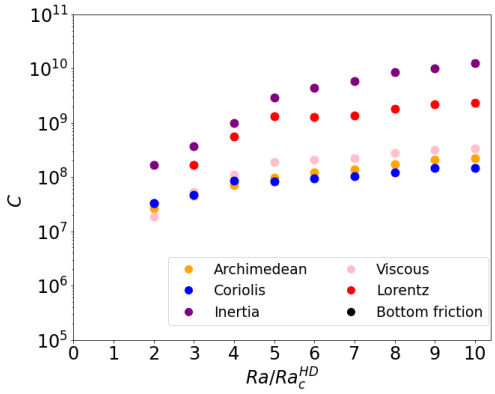

(b) $Q = 10^4$

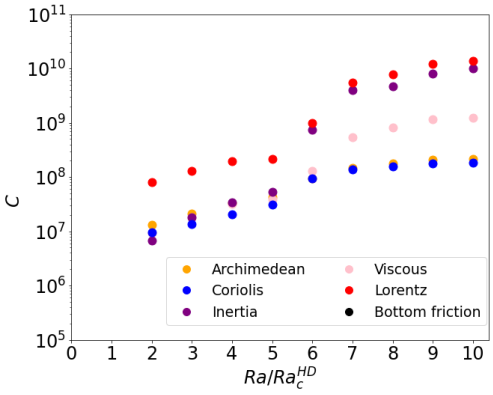

(c) $Q = 5 \times 10^5$

Figure 3.20: Globally averaged curls of forces against Ra/Ra_c^{HD} for $Pr = 1$, $\eta^* = 5 \times 10^5$, $B_f = 0$, $Pm = 5$ for different values of Q.

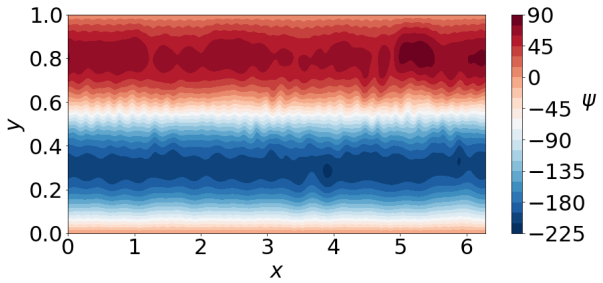

(a) Snapshot of ψ

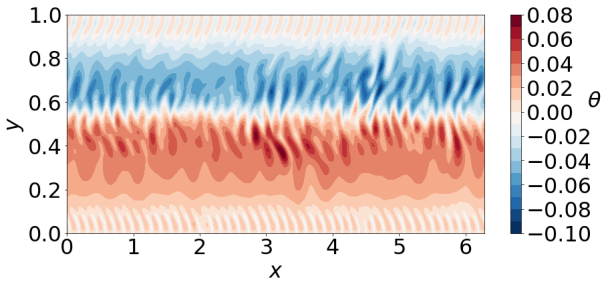

(b) Snapshot of θ

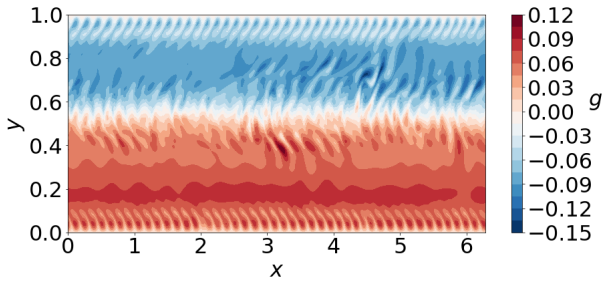

(c) Snapshot of g

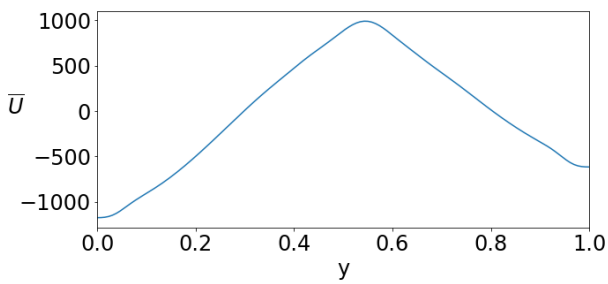

(d) $\bar{U}$

Figure 3.21: Plots of the fields for $Pr = 1$, $\eta^* = 5 \times 10^5$, $B_f = 0$, $Pm = 5$, $Q = 10^3$ and $Ra/Ra_c^{HD} = 3$.

We plot the globally averaged quantity of each force in order to summarise the balances found. A strong inertial force occurs throughout at $Q = 10^3$ and $Q = 10^4$ (Figs 3.20a and 3.20b). The

flow patterns for these runs are shown in Figure 3.21 and are similar to those at smaller Pm and low Q (Fig. 3.8) where zonal flows occur as either jets or bursting. At $Q = 5 \times 10^5$ we obtain a strong Lorentz force at smaller Ra which then transitions to a balance between Lorentz and inertial forces at higher Ra (Fig. 3.20c). This is similar to $Q = 5 \times 10^5$ for $Pm = 0.5$ although instead of a MAC balance occurring before the transition to dominant Lorentz and inertial forces, only the Lorentz force is dominant. In the regime where inertial and Lorentz forces are in balance, the flow patterns are similar to those in Figure 3.16.

3.4 Regime diagrams

We summarise our findings in different regime diagrams for each value of Pm (Figs 3.22a - 3.22d). We have plotted Q against Ra/Ra_c^{HD} where the colour of each run is determined by the total Lorentz term over the total inertial term denoted by C_L/C_I. We focus on this ratio because every run that has been considered either has the inertial term, Lorentz term or both involved in the leading order force balance. Each run is marked by a square if multiple jets are present, a triangle if we have bursts of convection, or a circle to represent convection without bursting or multiple jets. We mark runs where convection does not occur with a cross. We have also plotted the critical curve of Ra_c^{MC}/Ra_c^{HD} to highlight that in some cases convection occurs for $Ra < Ra_c^{HD}$. This is because we have measured the level of supercriticality using the non-magnetic critical Rayleigh number. The magnetic critical Rayleigh number varies for each value of Q and each value of Pm. Therefore, in some cases convection will onset below Ra_c^{HD} and in other cases it will onset above Ra_c^{HD}.

The behaviour is similar for the cases at the 3 lowest values of Pm tested (Figs 3.22a - 3.22c). Multiple jets only appear in a small area of parameter space as discussed earlier. These appear close to critical Ra when Q is small, where the inertial force is strong. Bursts of convection occur for small Q and persist as we increase Ra. In all cases where bursts of convection occur, a strong inertial force and weak Lorentz force is obtained as shown by the blue colour for each run. As Q is increased the inertial force weakens and the Lorentz force takes over, losing bursts of convection. This is the case for most values of Q even as Ra is increased and the inertial term becomes larger. This occurs in the trough of the Ra_c^{MC}/Ra_c^{HD} curve. This suggests that when magnetostrophic modes become important at onset, as was demonstrated by Horn and Aurnou (2022), bursts of convection are not possible. These runs still have strong zonal flows, which tells us that bursts are reliant on weak magnetic fields and/or pre-eminent geostrophic modes. Outside of the trough (i.e. at lower Q) it is possible to retrieve bursts of convection at large enough Ra even if they were not present at onset (i.e. at lower Ra). This is the case for all values of Pm for $Q = 10^3$, $Q = 5 \times 10^3$ and $Q = 10^4$. This behaviour extends to $Q = 5 \times 10^4$ for $Pm = 5$. For the case with strongest magnetic diffusion ($Pm = 0.01$), the Lorentz force impacts at a larger value of Q compared with $Pm = 0.1$ and $Pm = 0.5$. In all three cases there is a clear transition from an inertially dominated regime to a magnetically dominated regime as Q is increased. At $Pm = 0.1$ and $Pm = 0.5$, a strong Lorentz force appears at large Q and

small Ra. As we increase Ra the system transitions back to an inertially dominated regime. For $Pm = 0.01$ and $Pm = 0.5$ at $Q = 5 \times 10^5$ the solutions stay in the magnetically dominated regime for all Ra explored. It might be possible to reach the regime where the inertial force dominates if we considered runs at $Q = 5 \times 10^5$ for $Ra/Ra_c^{HD} > 10$.

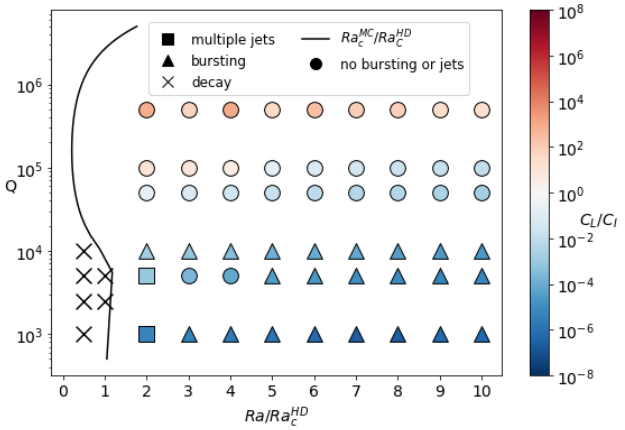

(a) $Pr = 1$, $\eta^* = 5 \times 10^5$, $B_f = 0$ and $Pm = 0.01$

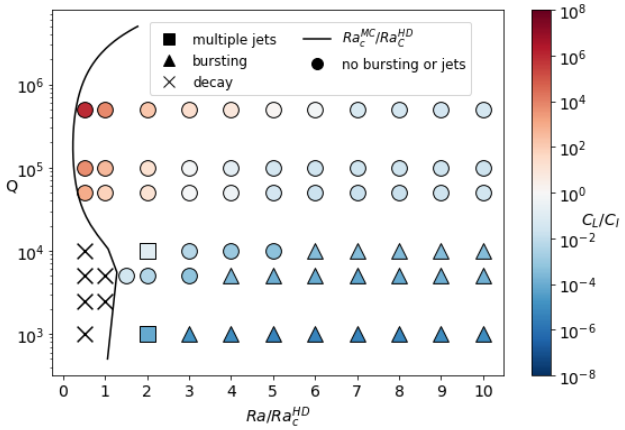

(b) $Pr = 1$, $\eta^* = 5 \times 10^5$, $B_f = 0$ and $Pm = 0.1$

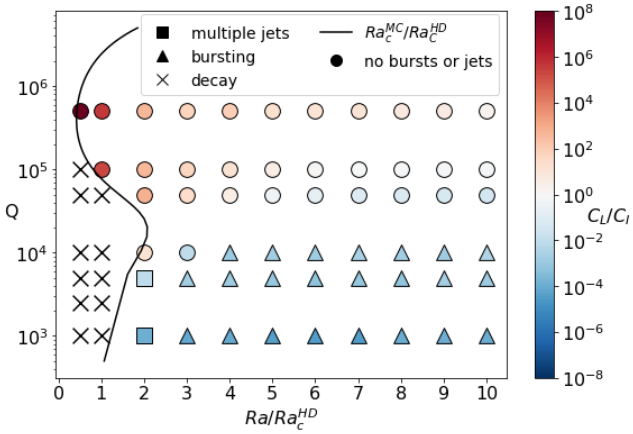

(c) $Pr = 1$, $\eta^* = 5 \times 10^5$, $B_f = 0$ and $Pm = 0.5$

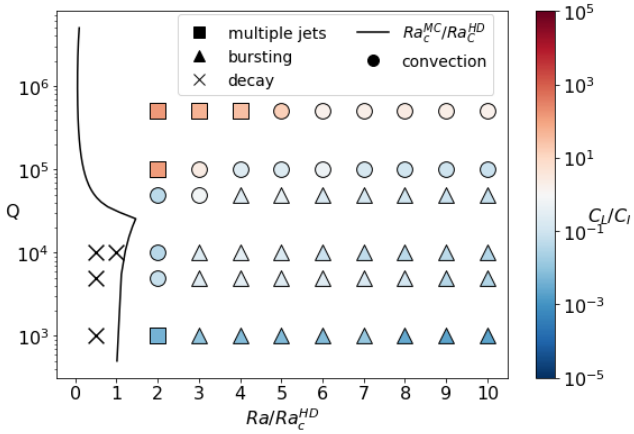

(d) $Pr = 1$, $\eta^* = 5 \times 10^5$, $B_f = 0$ and $Pm = 5$

Figure 3.22: Regime diagrams for varying Pm.

For large Pm ($Pm = 5$) the system behaves slightly differently. We obtain bursts of convection at low Q which persist as Ra is increased, similar to the other values of Pm explored. The bursting behaviour of the solutions persist for larger Q than cases with strong magnetic diffusion. At low Q and small Ra, where the inertial force is strong we find one solution with multiple jets. As Q is increased the system transitions to a regime dominated by the Lorentz force, where we now find jets at large Q and small Ra. It is clear that the magnetic field is playing a role in producing these multiple jets as the Lorentz force is controlling the system. This differs to previous multiple jet solutions at low Q where the system behaved like a magnetically adjusted hydrodynamical run.

The destruction of multiple jets does not depend greatly on Pm. At the three lowest values of Pm a similar pattern is observed, where multiple jet solutions are destroyed at approximately $Q \approx 10^4$. Tobias et al. (2007) investigated magnetohydrodynamic turbulence using a β-plane model and identified a threshold magnetic field strength above which zonal flows were

completely suppressed. They also reported a scaling between this threshold magnetic field and magnetic diffusivity. To obtain a comparison with their results, a wider range of Pm values would need to be explored.

3.5 SUMMARY

The work in this chapter extended previous non-magnetic work by imposing an azimuthal magnetic field. The force balances were considered as the magnetic field strength was varied. We also discussed bursts of convection and multiple jet solutions found in our magnetic work, similar to those found in the non-magnetic case by Rotvig and Jones (2006) and Teed et al. (2012). Similar to the non-magnetic case without bottom friction, we found multiple jets in a small window of parameter space. For strong magnetic diffusion these occurred at low Q and small Ra. In this case, these solutions behaved like a weakly adjusted hydrodynamical run where the multiple jets were driven by the inertial force. Multiple jets were also obtained where the magnetic diffusion was weak at small Ra but large Q. These jets looked similar to the jets at low Q but were produced by magnetic effects as the Lorentz force dominated. Multiple jet solutions are explored in greater detail in Chapter 4.

We also found bursts of convection at low Q for all values of Pm, where solutions behaved as a weakly magnetically adjusted hydrodynamical run. In all cases with bursts the inertial terms dominated. The bursts were lost in the trough of the Ra_c^{MC}/Ra_c^{HD} curve suggesting that when different magnetostrophic modes become important at onset, bursts of convection are not possible. This was discussed by Horn and Aurnou (2022) where they found that increasing magnetic field strength produced both magnetostrophic and geostrophic modes but the magnetostrophic modes become the preferred mode at onset rather than the geostrophic mode. Future work could examine bursts of convection in more detail.

Balances other than a dominant inertial or Lorentz force were also possible. A MAC balance was possible for all values of Pm except $Pm = 5$ when Q was large enough. For all values of Pm except $Pm = 0.01$, a balance between inertial and Lorentz forces was possible when both Q and Ra were sufficiently large. The regimes found in our simulations show similarities in the force hierarchy to the different branches found in spherical dynamo simulations (Schwaiger et al. (2019), Teed and Dormy (2023)). The MAC balance found in our simulations at high Q is similar to the strong field dipolar branch where the dipolar magnetic field is strong and a MAC balance occurs. The inertially dominated regime at low Q has a similar force balance to the fluctuating multipolar branch. However on the fluctuating multipolar branch we usually expect contributions from the Coriolis and buoyancy force. We only found this to be the case close to critical Ra before the system transitioned to a dominant inertial force at all scales. For the parameter space explored, we have not found a regime similar to the weak field dipolar dynamo branch where a VAC balance prevails. This might not be possible to obtain in the annulus model or we might not have studied the correct area of parameter space to obtain solutions involving a VAC balance. This balance may exist at $Pm = 5$ for values of Ra larger

but close to Ra_c^{MC}, which we haven't explored in detail. This is speculated because the weak field dynamo branch where a VAC balance occurs, is known to exist at very low Ra and large Pm. Bistable solutions have been observed in spherical dynamo simulations. Bistability might also occur for some input parameters in our annulus model which has prevented the observation of solutions with a VAC balance. The search for a VAC balance in the annulus model could be investigated in future work.

Chapter 4

Multiple jet solutions in an annulus model

Convecting systems are known to generate strong 'zonal flows' in the azimuthal direction, typically driven by the Reynolds stresses. Zonal flows are most readily observed on the surface of Jupiter, which has a banded structure consisting of alternating prograde and retrograde jets. The depth of these flows has long been the subject of debate although recent evidence suggests they extend only to 3000 kilometres below the surface (Kaspi et al., 2023). A simplified model of (non-magnetic) convection in Jupiter, where zonal flows go deeper than the surface was proposed by Busse (1976b). Convection occurring in planetary cores and atmospheres is strongly affected by magnetic fields generated through dynamo action. It is therefore of interest to consider the effect of magnetic fields on zonal flow and multiple jet generation in planetary interiors.

This chapter expands on work from Chapter 3 where multiple jet solutions in the Busse annulus model with an imposed magnetic field are explored. We know from previous non-magnetic studies (by, e.g., Jones et al. (2003), Rotvig and Jones (2006) and Teed et al. (2012)) that non-linear simulations of the annulus model produce zonal flows which can have a multiple jet structure, determined by the boundary conditions imposed on the annular lids. We focus on solutions with multiple jets and aim to determine where in parameter space multiple jets are found and discuss the impact of a magnetic field on the multiple jet structure. The mathematical setup, numerical method, and various output parameters were discussed in Chapter 2. We start by confirming known multiple jet solutions in the absence of a magnetic field before examining the effect of varying input magnetic field strength and magnetic Prandtl number. Various regimes are identified by considering the kinetic, magnetic and zonal energy and the various forces acting within the system. We also examine how well our results fit with the Rhines scaling theory (Rhines (1975)).

4.1 NON-MAGNETIC CASE

The non-magnetic case has been examined in great detail, where multiple jets are mainly found for $B_f \neq 0$ (Jones et al., 2003; Rotvig and Jones, 2006; Teed et al., 2012). A few isolated cases of multiple jets have been found for $B_f = 0$ in a small window of parameter space close to onset with a suitably large rotation rate (Jones et al., 2003). Figure 4.1a shows a plot of the ratio of zonal to kinetic energy against Ra/Ra_c^{HD}, for different values of B_f with the number of edges of each symbol indicating the time-averaged dominant mode $\hat{m}$. For $B_f = 0$, we find strong zonal flows but no cases of multiple jets. Instead the dominant dynamics are quasi-periodic bursts of convection and zonal flow, in agreement with previous non-magnetic studies. At $B_f = 0.5$, E_Z/E_K is very small close to onset but builds as the driving increases (Figure 4.1a). Multiple jet solutions are also obtained for this value of B_f at the expense of a reduced zonal flow strength compared to the cases with $B_f = 0$. This matches the trend found by Rotvig and Jones (2006) where E_Z/E_K is large when $B_f = 0$ and then decreases for larger B_f. This is expected since B_f increases the likelihood of multiple jets but weakens the zonal flow contribution through additional friction. A 6 jet solution is found at $Ra/Ra_c^{HD} = 3$, transitioning to 5 jets and then to 4 jets with increased driving before then dropping off to a solution without multiple jets. Each transition is associated with a reduction in the contribution of the zonal energy and highlights that the multiple jet phenomenon is restricted to a small window of Ra-space. Figure 4.1b provides further evidence of the nature of the solutions since the $(0, \hat{m})$ is shown to dominate over all other $(l, \hat{m})$ for solutions identified as having multiple jets. Therefore we can be satisfied these are azimuthally axisymmetric jets. The quantity plotted in Figure 4.1b decreases when multiple jets are lost but remains large enough that $l = 0$ still dominates. In this regime the bottom friction is likely not so important because the driving is large and is evidenced by the fact that the blue and red points are located in very similar positions. This is similar to the case where $B_f = 0$, where the ratio decreases at larger Ra but still remains large enough for $(0, \hat{m})$ to dominate.

Typical solutions with and without multiple jets are shown in Figures 4.2 and 4.3, respectively. A banded structure in ψ with 5 bands in the y-direction can be observed in Figure 4.2a, confirming an $\hat{m} = 5$ dominant mode. The $l = 0$ component also dominates which is clear from the azimuthally axisymmetric nature of the flow. The zonal flow displays a multiple jet pattern, where a 6 jet solution is found. In θ we observe small structures and a negative temperature gradient in y attempting to erase the imposed basic state gradient. Solutions with multiple jets are quasi-steady and move across the x-domain. We never observe the jets change direction, although we occasionally see the number of jets found in simulations change as we integrate in time. The case presented in Figure 4.2 is typical of a multiple jet solution, matching previous work (Jones et al. (2003), Rotvig and Jones (2006) and Teed et al. (2012)). In Figure 4.3 we no longer have multiple jets but, otherwise, the solution remains similar to that of Figure 4.2. Axisymmetric flow and large $\bar{U}$ confirm the zonal nature of the solution despite the lack of multiple jets as expected from Figure 4.1b.

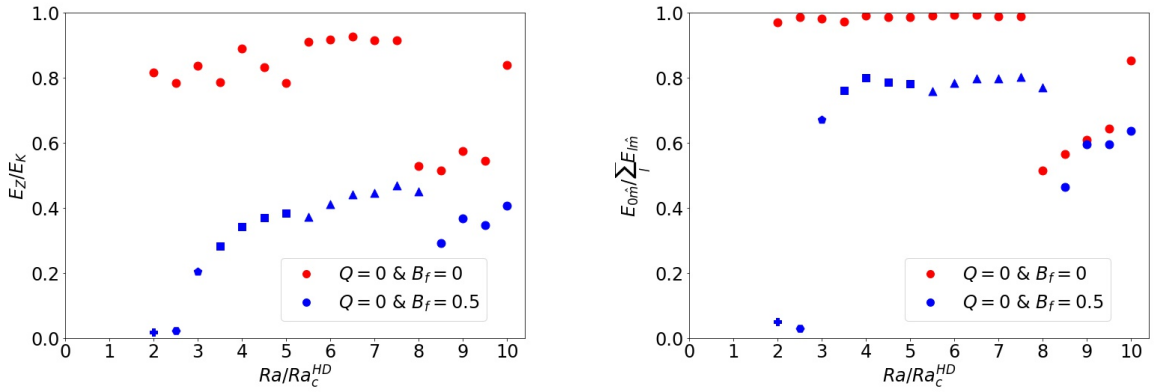

(a) E_Z/E_K against Ra (b) $E_{0\hat{m}}/\sum_l E_{l\hat{m}}$ against Ra

Figure 4.1: Plots of energy against Ra/Ra_c^{HD} for $Pr = 1$, $\eta^* = 5 \times 10^5$, and $Q = 0$. Quantities have been globally averaged in space and time. The number of edges of each symbol represents the dominant time averaged mode $\hat{m}$. Plus symbols represent solutions with $\hat{m} \geq 7$ and circles represent solutions with $\hat{m} \leq 2$.

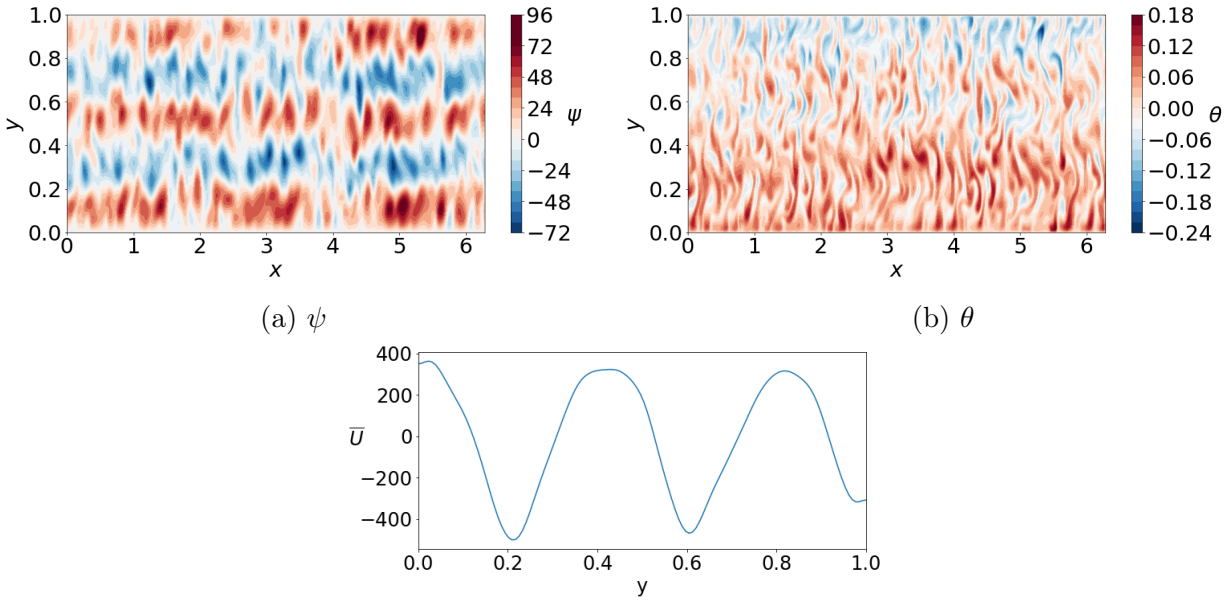

(a) ψ (b) θ

(c) $\bar{U}\,(y)$

Figure 4.2: Snapshots of ψ, θ and zonal flow $\bar{U}$ for $Pr = 1$, $\eta^* = 5 \times 10^5$, $Q = 0$, $B_f = 0.5$, and $Ra/Ra_c^{HD} = 3$.

The curls of forces shown in Figure 4.4 are formed by summing over l and m for each force as given by Equations (2.55)-(2.60), forming globally averaged quantities of each force. Figure 4.4 highlights the dominance of the inertial term in our solutions with a secondary Coriolis force typically in a balance with buoyancy and/or viscous forces. Figure 4.4a shows the global time-averaged curl of each force against Ra/Ra_c^{HD} for $B_f = 0$. As we increase the driving, the inertial force increases at a faster rate than the other forces. The main difference between cases without (Figure 4.4a) and with (Figure 4.4b) bottom friction is increased contributions from the secondary forces in the latter. Indeed, the Coriolis and inertial terms are nearly in balance for low Ra when $B_f \neq 0$. These increased contributions, along with bottom friction, appear

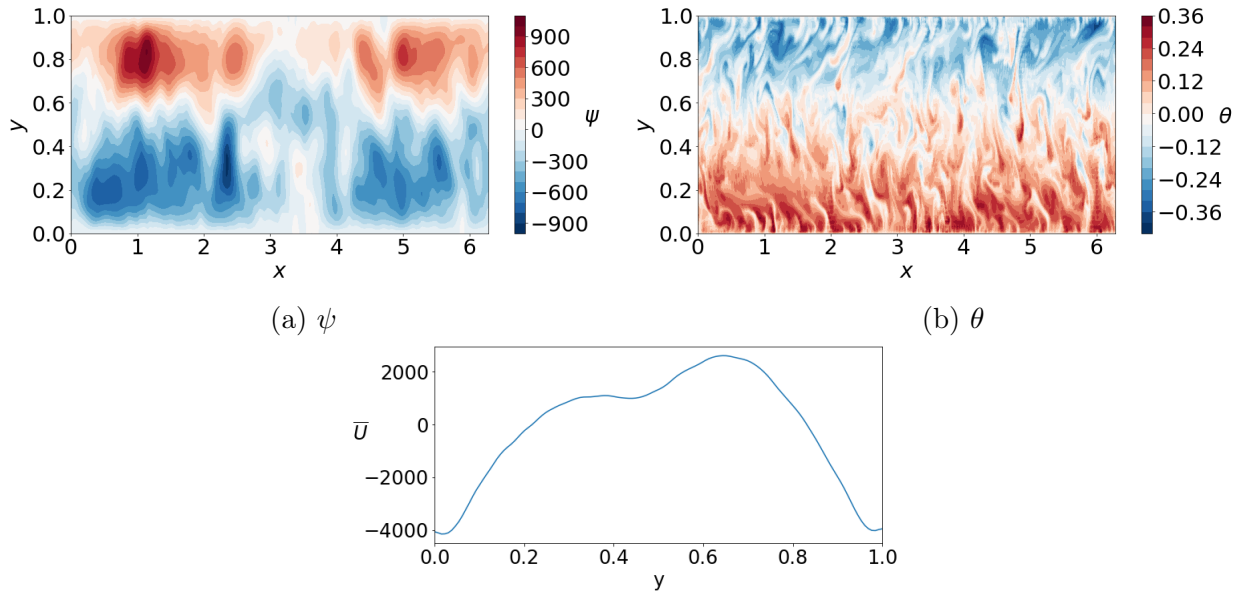

(a) ψ (b) θ

(c) $\bar{U}\,(y)$

Figure 4.3: Snapshots of ψ, θ and zonal flow $\bar{U}$ for $Pr = 1$, $\eta^* = 5 \times 10^5$, $Q = 0$, $B_f = 0.5$, and $Ra/Ra_c^{HD} = 9$.

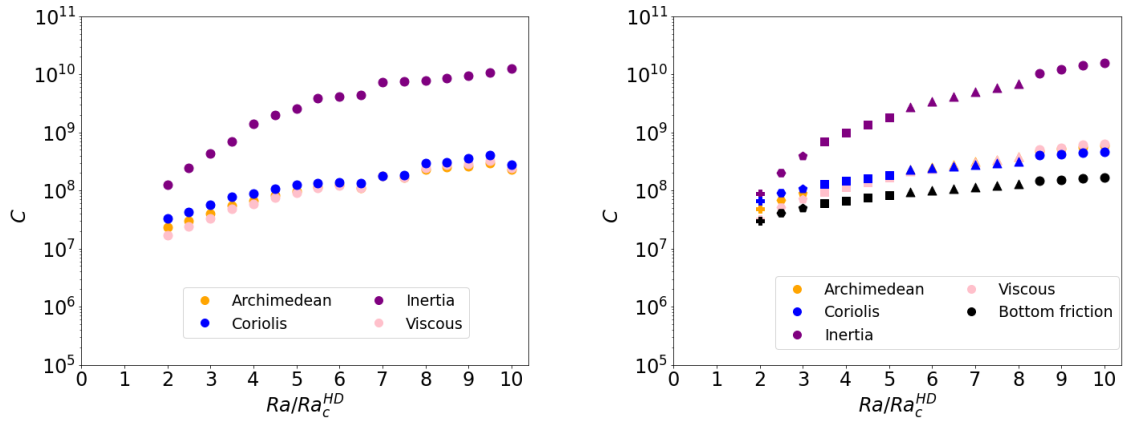

(a) $B_f = 0$ (b) $B_f = 0.5$

Figure 4.4: Curl of each force against Ra/Ra_c^{HD} for $Pr = 1$, $\eta^* = 5\times10^5$, and $Q = 0$. Quantities have been globally averaged in space and time. The number of edges of each symbol represents the dominant time averaged mode $\hat{m}$. Plus symbols represent solutions with $\hat{m} \geq 7$ and circles represent solutions with $\hat{m} \leq 2$.

to be the catalyst for multiple jet solutions. An increase in the driving separates the inertial force from the secondary terms and solutions without multiple jets are preferred, in line with the $B_f = 0$ cases.

4.2 Magnetic case

From previous work and earlier discussion it is clear that multiple jet solutions are more probable with a large rotation rate and bottom friction imposed. Our focus here will therefore be on cases with $B_f \neq 0$; in particular, in Sections 4.2.2 and 4.2.3, we will study $B_f = 0.5$ for

two values of the magnetic Prandtl number: $Pm = 0.5$ and $Pm = 5$. This value of B_f was chosen based on a multiple jet study in the non-magnetic case by Teed et al. (2012). We fix $\eta^* = 5\times10^5$ throughout so we do not expect the magnetic field to have a significant impact until $Q \sim \eta^*$. However, we first briefly examine multiple jets found when $B_f = 0$ with a magnetic field imposed, discussing the main features and how this compares with the non-magnetic case.

4.2.1 No bottom friction

When $B_f = 0$, multiple jets are possible at $Pm = 0.5$ and $Pm = 5$ close to onset (similar to results in the non-magnetic case by Jones et al. (2003)). Figure 4.5 shows an example of such a solution for a weak magnetic field and close to onset. A similar flow structure is found to the multiple jets in the non-magnetic case with ψ featuring a banded structure and a dominant $l = 0$ and $\hat{m} = 3$ mode. The structures in θ are small, g is very weak, and $\bar{U}$ displays a multiple jet structure. In line with the non-magnetic case, very few cases of multiple jets are found for $B_f = 0$. This is particularly true when the field strength is increased. Indeed, at large enough values of Q, no multiple jet solutions are found in the absence of bottom friction, even close to onset. For this reason the remainder of our results focus on $B_f \neq 0$. We also note that, when $B_f = 0$, cases with 'bursts of convection' remain common in this magnetic case. These solutions are thus found in similar regions of parameter space to that in previous non-magnetic results (Jones et al. (2003), Rotvig and Jones (2006), Teed et al. (2012)). Multiple jets and bursts of convection are never found together and bursting is uncommon at $B_f \neq 0$. We find no cases of bursting at $B_f = 0.5$. Since our current study is focused on multiple jet solutions, a thorough examination of the bursting solutions is left to a future study.

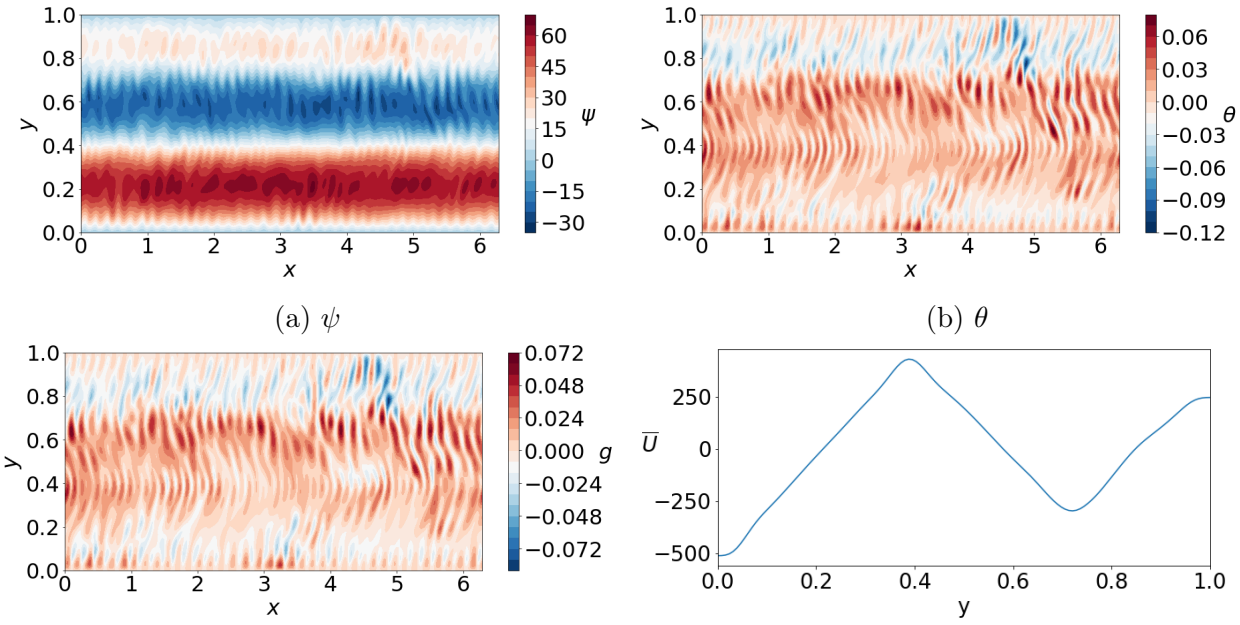

(a) ψ (b) θ

(c) g (d) $\bar{U}\,(y)$

Figure 4.5: Snapshots of ψ, θ, g, and zonal flow $\bar{U}$ for $Pr = 1$, $\eta^* = 5\times10^5$, $Q = 10^3$, $Pm = 0.5$, $B_f = 0$, and $Ra/Ra_c^{HD} = 2$.

4.2.2 WITH BOTTOM FRICTION AND $Pm = 0.5$

We now impose bottom friction, which is known to increase the likelihood of multiple jet solutions. We start by examining a magnetic Prandtl number $Pm = 0.5$, gradually increasing the magnetic field strength and driving to identify regions of parameter space where multiple jets are found.

Figure 4.6 highlights where multiple jet solutions are found and relative strengths of the zonal and magnetic energy for different values of Q and Ra. For $Q = 10^3$, multiple jets are readily found across Ra-space. A dip in E_Z/E_K occurs at 5 times critical, associated with a reduction in the number of jets. For all Ra at $Q = 10^3$ the magnetic field does not play an important role as the ratio E_M/E_K is small, meaning the zonal and total kinetic energy dominate. For this value of Q, rotation remains far more important than the magnetic field (since the Elsasser number, $\Lambda = Q/\eta^* \ll 1$) and the system essentially behaves as a magnetically adjusted version of the hydrodynamical solutions of Section 4.1. It is notable that multiple jets persist for all values of Ra tested for $Q = 10^3$. This is in contrast to the $Q = 0$ case (cf. Figure 4.2a) where multiple jets ceased at ~ 8 times critical. A magnetic field of weak enough strength is therefore conducive to multiple jet production at increased driving.

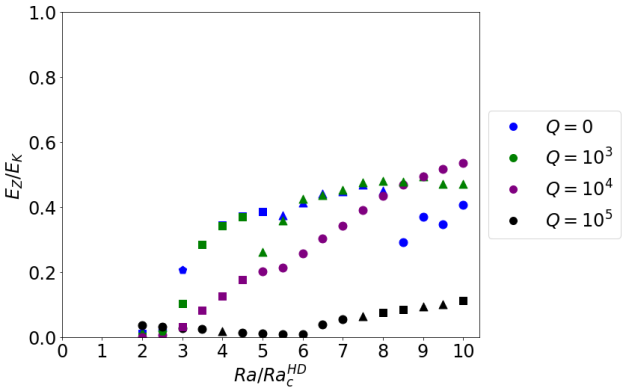

(a) E_Z/E_K against Ra

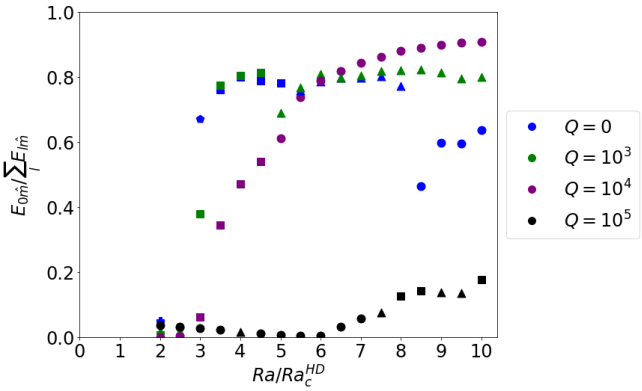

(b) $E_{0\hat{m}}/\sum_l E_{l\hat{m}}$ against Ra

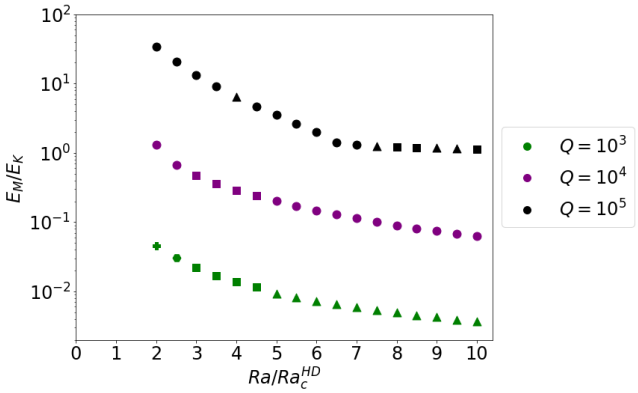

(c) E_M/E_K against Ra

Figure 4.6: Plots of energy against Ra/Ra_c^{HD} for $Pr = 1$, $\eta^* = 5 \times 10^5$, $Pm = 0.5$, $B_f = 0.5$ and varying Q. Quantities have been globally averaged in space and time. The number of edges of each symbol represents the dominant time averaged mode $\hat{m}$. Plus symbols represent solutions with $\hat{m} \geq 7$ and circles represent solutions with $\hat{m} \leq 2$.

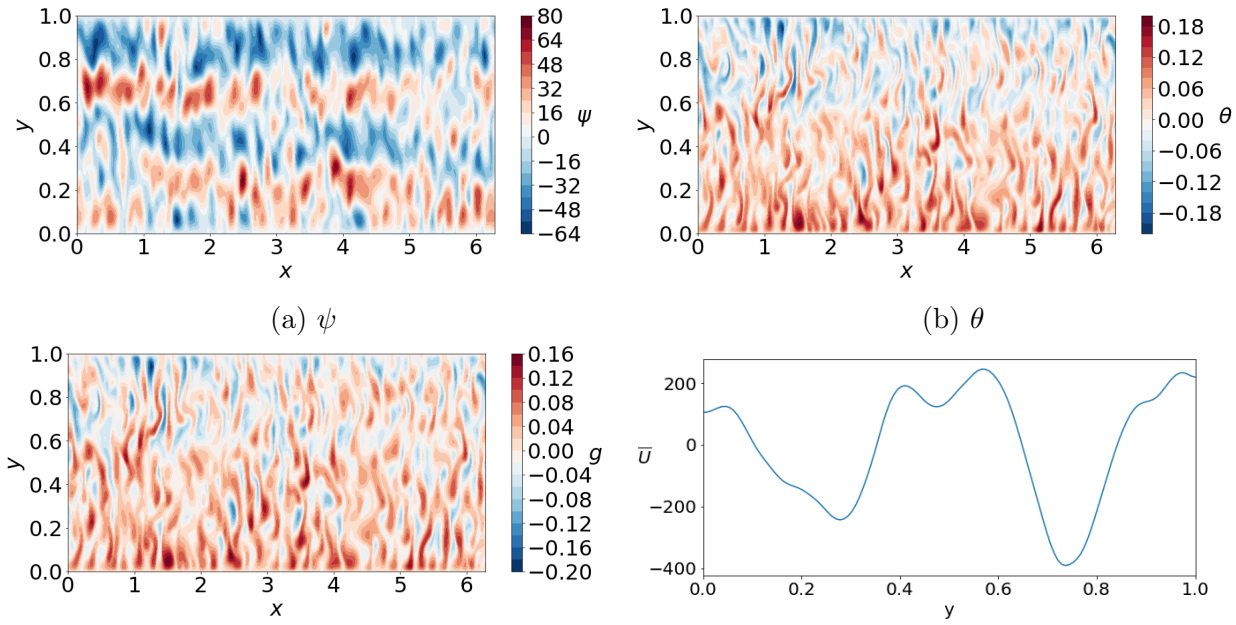

(a) ψ (b) θ

(c) g (d) $\bar{U}\,(y)$

Figure 4.7: Snapshots of ψ, θ, g and zonal flow $\bar{U}$ for $Pr = 1$, $\eta^* = 5 \times 10^5$, $Q = 10^3$, $Pm = 0.5$, $B_f = 0.5$, and $Ra/Ra_c^{HD} = 3$.

At $Q = 10^4$, multiple jet solutions emerge at low driving (albeit with small zonal energy) but soon transition to solutions with $\hat{m} < 3$ as Ra is increased. This suggests there is an optimal value of field strength for production of multiple jets at larger Ra; for the current set of input parameters this optimal value of Q satisfies $0 < Q < 10^4$. The magnetic field has become important as the ratio of E_M/E_K has increased significantly from $Q = 10^3$, reaching an $O\,(1)$ value for some values of Ra. It is clear from Figure 4.6b that solutions for $Q = 10^3$ and $Q = 10^4$ (at least far from onset) are axisymmetric in nature with a strong zonal flow contribution, regardless of value of $\hat{m}$.

The snapshot plots of Figure 4.7 are similar to equivalent plots of multiple jets for the non-magnetic case (cf. Figure 4.2). Again, the flow displays strong axisymmetry in azimuth (Figure 4.7a), the structures in θ and g are small (Figure 4.7b and 4.7c) and the zonal flow shows a multiple jet pattern (Figure 4.7d). The zonal flow is less symmetric than the equivalent non-magnetic case as the position of jets have moved. This suggests the magnetic field is capable of disturbing jet positioning locally at various times. The snapshots of Figure 4.7 are typical of all multiple jet solutions found at $Q = 10^3$ and $Q = 10^4$, although, as we have seen, the precise number of jets is a function of the input control parameters.

At $Q = 10^5$, the behaviour is strikingly different to that seen at other values of Q; this can first be noted through Figure 4.6. The fraction of zonal energy is small for all values of Ra tested although a gradual increase in its value begins at ~ 6 times critical; nevertheless it remains small compared with its values when Q is lower. The value of E_M/E_K is $O(1)$ or greater confirming that the magnetic field has now become dynamically important in the solutions. Figure 4.8 shows a typical solution for $Q = 10^5$ at low Ra. It is immediately clear that the

zonal flow pattern has been lost at these input parameters. The solution in ψ is no longer azimuthally axisymmetric, structures are larger and the zonal flow is very weak.

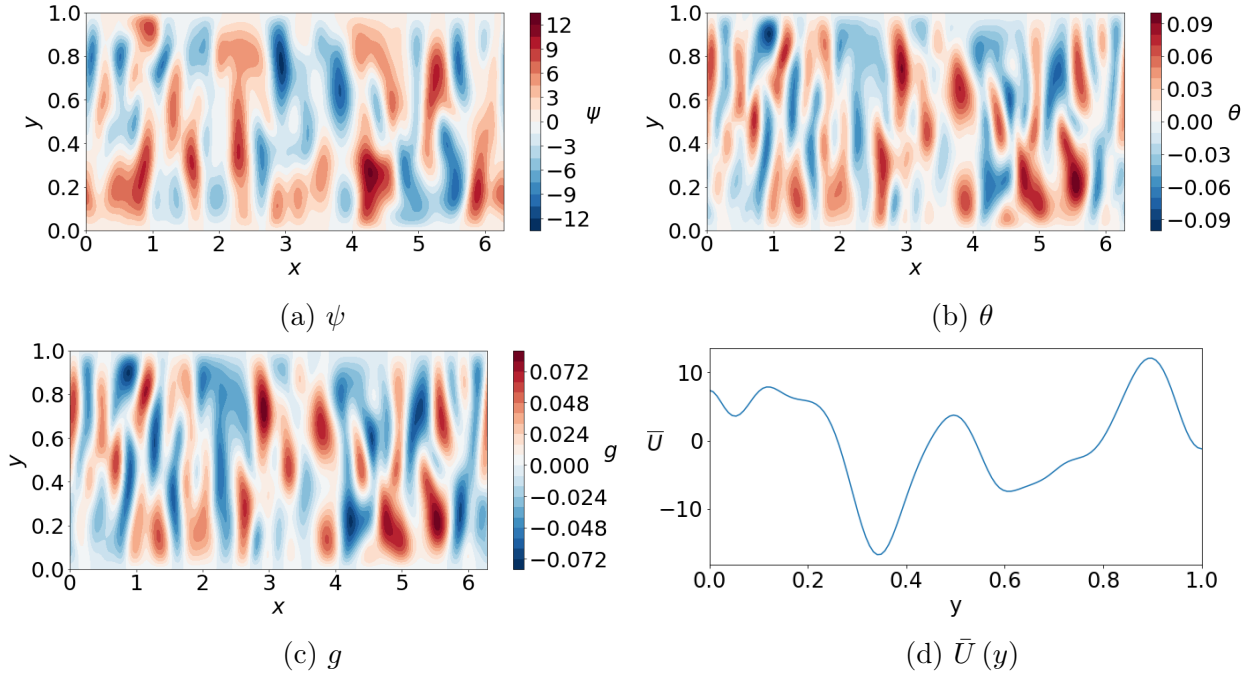

(a) ψ (b) θ

(c) g (d) $\bar{U}\,(y)$

Figure 4.8: Snapshots of ψ, θ, g and zonal flow $\bar{U}$ for $Pr = 1$, $\eta^* = 5 \times 10^5$, $Q = 10^5$, $Pm = 0.5$, $B_f = 0.5$, and $Ra/Ra_c^{HD} = 3$.

The value of $\hat{m}$ (given by the number of edges on the symbols in Figure 4.6) suggests multiple jet solutions may be possible at $Q = 10^5$, once the driving is strong enough. However, Figure 4.6b shows that $l = 0$ no longer dominates indicating that the axisymmetric nature of the solution has been destroyed. Figure 4.9 shows a typical solution for $Q = 10^5$ at larger Ra where $\hat{m} \geq 3$. The zonal flow displays a multiple jet structure but we no longer have azimuthally axisymmetric bands as shown in the snapshot for ψ (Figure 4.9a). Instead we observe a 3-fold symmetry in the x-direction, confirming that the magnetic field is strong enough to break the axisymmetric nature of the flow. Through the snapshots of Figure 4.9, it is clear that this is a different regime to both the multiple jet regimes at lower Q and the regimes at low Ra for $Q = 10^5$.

The effect of magnetic field strength on the zonal flow can be summarised by Figure 4.10 where two values of Ra are considered. It is clear in both cases that increasing the magnetic field strength dampens the zonal flow strength. We find strong zonal flows at $Q = 10^3$ which are almost completely suppressed at $Q = 10^5$. This matches results by Tobias et al. (2007) where the effect of an imposed magnetic field on a β-plane was examined. For the larger value of Ra, the number of jets also reduces with increased field strength.

Figure 4.11 demonstrates different balances of (curls of) forces taking place at each Q tested. Figure 4.11a, for $Q = 10^3$, is remarkably similar to the pattern observed in the non-magnetic case at $B_f = 0.5$ (Figure 4.4b), albeit with the addition of a weak Lorentz force. Very close to onset, the inertial and Coriolis terms are nearly in balance, and the buoyancy is also strong.

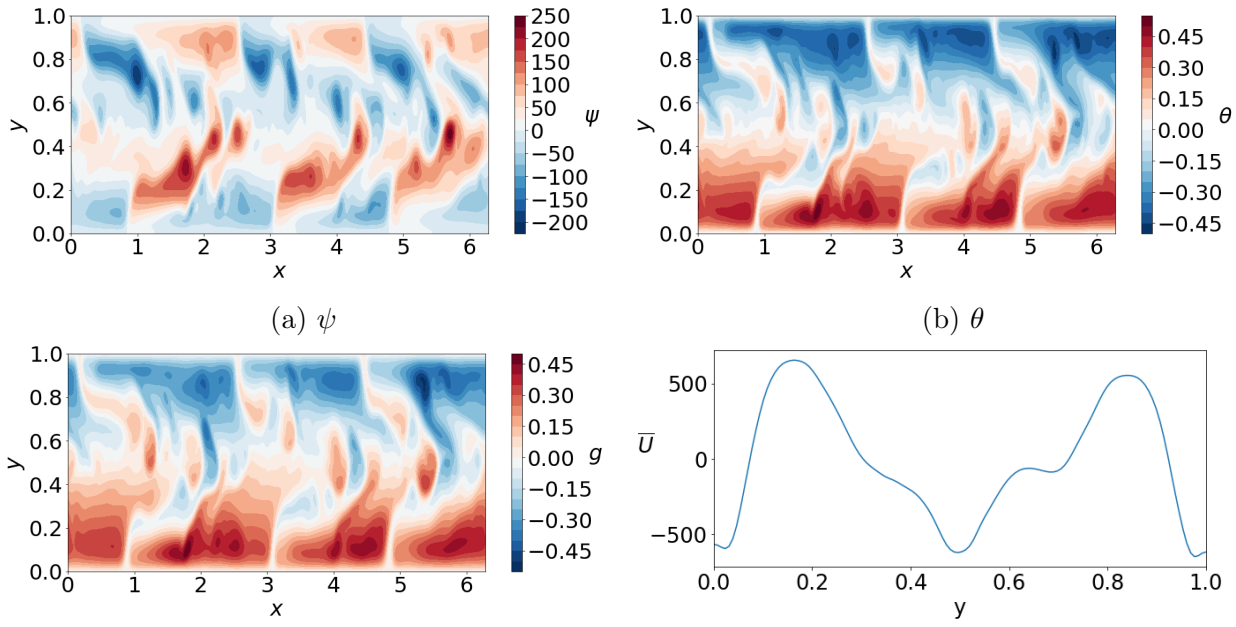

(a) ψ (b) θ

(c) g (d) $\bar{U}\,(y)$

Figure 4.9: Snapshots of ψ, θ, g and zonal flow $\bar{U}$ for $Pr = 1$, $\eta^* = 5 \times 10^5$, $Q = 10^5$, $Pm = 0.5$, $B_f = 0.5$, and $Ra/Ra_c^{HD} = 9$.

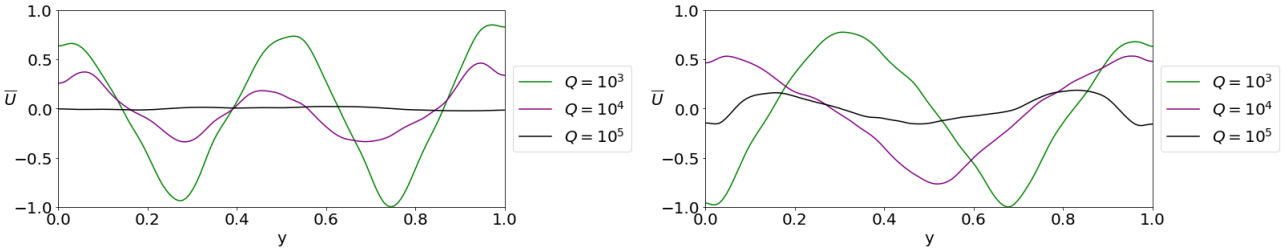

(a) $Ra/Ra_c^{HD} = 4$ (b) $Ra/Ra_c^{HD} = 10$

Figure 4.10: Zonal flow strength for increasing Q at two different values of Ra/Ra_c^{HD} with $Pr = 1$, $\eta^* = 5 \times 10^5$, $Pm = 0.5$, and $B_f = 0.5$. The flow strength has been normalised by the largest value of $\bar{U}$ at each Ra/Ra_c^{HD}.

As Ra is increased, all forces increase with the inertial term increasing at a faster rate and dominating throughout. In all cases the Lorentz term remains very weak but gradually increases relative to Coriolis, buoyancy and viscous terms. At the largest values of Ra tested, the Lorentz term begins to come into a secondary balance with the other forces. This highlights its role in preserving multiple jets at larger values of Ra (in contrast to the non-magnetic case where the force balance is otherwise equivalent). Figure 4.11b shows the (curls of) forces at $Q = 10^4$ where the hierarchy is similar to $Q = 10^3$, but with an increased Lorentz term for all Ra. Once supercriticality is high enough, a secondary balance between Lorentz, buoyancy, and Coriolis (MAC) emerges at moderate Ra where multiple jets occur. At larger Ra the hierarchy transitions such that the Lorentz term becomes the dominant secondary term; it is here that multiple jets are lost (though zonal flows remain). This indicates that, in contrast to $Q = 10^3$, the magnetic field can have a negative effect on multiple jet production, if its Lorentz force becomes strong enough. Nevertheless, with the Lorentz term remaining a secondary contribution

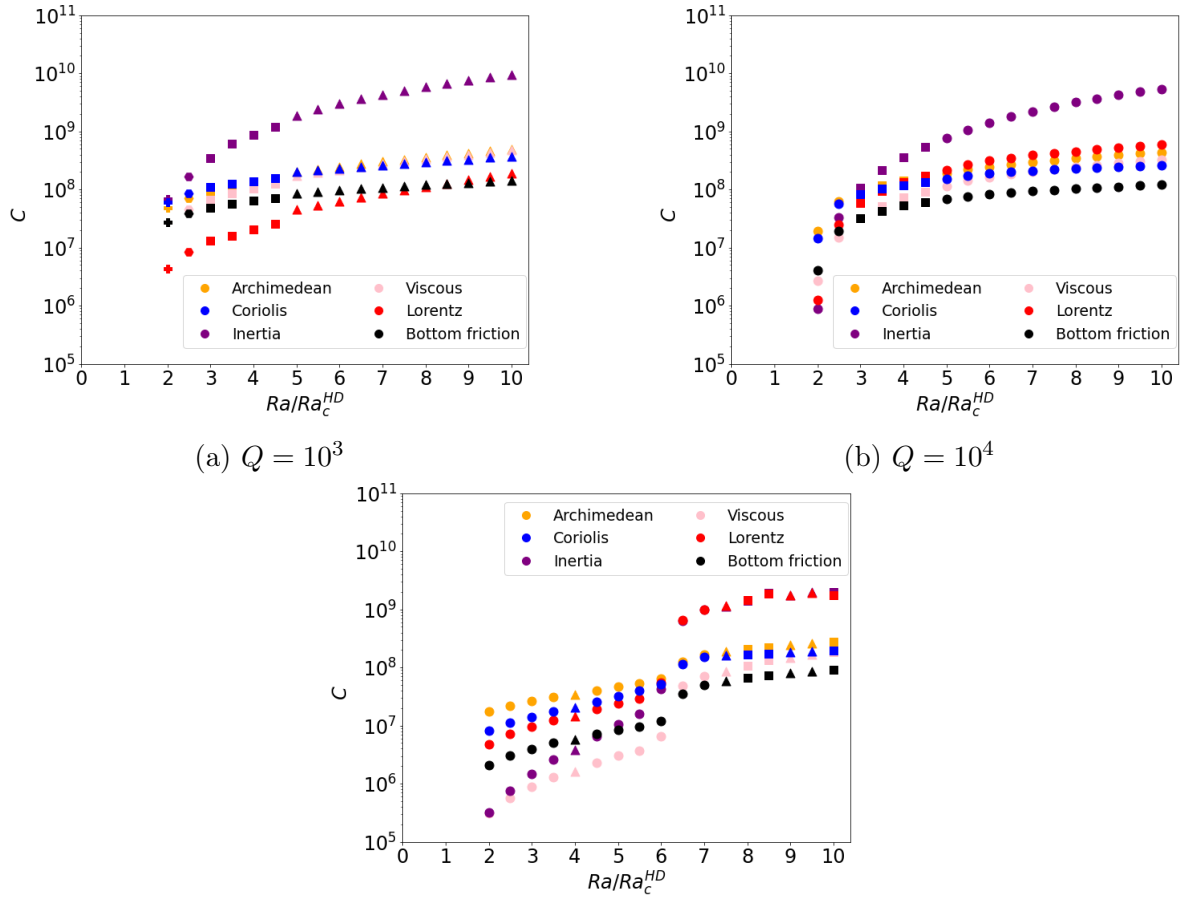

(a) $Q = 10^3$

(b) $Q = 10^4$

(c) $Q = 10^5$

Figure 4.11: Curl of each force against Ra/Ra_c^{HD} for $Pr = 1$, $\eta^* = 5 \times 10^5$, $Pm = 0.5$ and varying Q. Quantities have been globally averaged in space and time. The number of edges of each symbol represents the dominant time averaged mode $\hat{m}$. Plus symbols represent solutions with $\hat{m} \geq 7$ and circles represent solutions with $\hat{m} \leq 2$.

below the inertia, zonal flows remain strong and prevalent. At $Q = 10^5$ (Figure 4.11c) there is a stark change in the hierarchy of (curls of) forces. The dominant position of the inertial force is replaced with a quasi-MAC balance at low and moderate Ra. At $Ra \approx 6.5Ra_c^{HD}$, a sudden change of regime occurs. The Coriolis and buoyancy terms increase entering a secondary balance with the viscous term, and the inertial and Lorentz terms increase drastically, forming the primary balance. This new balance coincides with the previously observed change in $\hat{m}$. There occurs a slight increase in E_Z/E_K (Figure 4.6a) as the inertial enters the primary balance but, ultimately, zonal flows and jets remain weak by the presence of the Lorentz term in the primary balance. This confirms that a strong enough magnetic field is able to suppress the development of zonal flows, as well as multiple jets.

4.2.3 WITH BOTTOM FRICTION AND $Pm = 5$

We now consider a larger value of $Pm = 5$, retaining bottom friction given by $B_f = 0.5$. Figure 4.12a, for $Pm = 5$, can be compared with Figure 4.6a, the equivalent for $Pm = 0.5$. The picture for low Q at $Pm = 5$ is very similar to that at $Pm = 0.5$. Again, at $Q = 10^3$, multiple

jets persist for all Ra explored and at $Q = 10^4$ multiple jets appear at low and moderate Ra before being lost as the driving is increased. At $9.5Ra_c^{HD}$ and $10Ra_c^{HD}$ multiple jets reappear. In both cases, there is a drop in E_Z/E_K coinciding with a reduction in the number of jets, with $Q = 10^3$ transitioning from a 5 jet to 4 jet solution and $Q = 10^4$ transitioning from multiple jets to a solution without multiple jets. This behaviour is similar to $Pm = 0.5$, where a drop in E_Z/E_K occurred coinciding with a decrease in $\hat{m}$ although it is of note that the transition occurs at larger Ra compared to the $Pm = 0.5$ case. The solutions at $Q = 10^3$ are multiple jets, behaving similarly to those found in the non-magnetic case (Figure 4.2) and equivalent magnetic case at Pm=0.5 (Figure 4.7). For both $Q = 10^3$ and $Q = 10^4$, E_M/E_K is small and the solutions behave as magnetically adjusted hydrodynamical solutions with the magnetic field not having a clear discernible impact on the flow.

At $Q = 10^5$, close to onset the behaviour at $Pm = 5$ is similar to $Pm = 0.5$. The ratio E_Z/E_K is very small, E_M/E_K is large and the magnetic field is now strong enough to suppress the development of zonal flows and multiple jets. Solutions at this value of Q are similar to those at $Pm = 0.5$ (e.g. Figure 4.8) although the dominant azimuthal mode l has increased so the structures are smaller. As the driving is increased, the picture at $Pm = 5$ diverges from that at $Pm = 0.5$. The contribution of zonal energy increases steeply leading to the emergence of solutions with strong zonal flows and there is a gradual decrease in E_M/E_K. In this region of parameter space, solutions are similar to those found in previous non-magnetic and magnetic cases where zonal flows are strong but no multiple jets are found (e.g. Figure 4.3). This is in stark contrast to the equivalent region of parameter space at $Pm = 0.5$, where the magnetic field was able to suppress zonal flows and non-axisymmetric flow patterns emerged. Figure 4.12b confirms that, for $Pm = 5$, solutions with zonal flows and bands are produced at all values of Q provided driving is strong enough. This also differs to the $Pm = 5$ case with $B_f = 0$ discussed in Section 3.3.4 where zonal flows occur as multiple jets, close to critical Ra_c^{HD} (Fig. 3.19). The addition of the bottom friction term combined with large magnetic field suppresses multiple jets.

The effect of increasing the magnetic field strength on the zonal flow strength can be summarised through Figure 4.13. At $Ra/Ra_c^{HD} = 4$, the results are similar to $Pm = 0.5$ (cf. Figure 4.10a), where increasing magnetic field strength suppresses zonal flows. However, at $Ra/Ra_c^{HD} = 9$, the increasing magnetic field does not suppress the zonal flow strength significantly but does reduce the jet number.

Figure 4.14, showing contributions from the curl of each force, gives a similar picture to the equivalent figure for $Pm = 0.5$ (cf. Figure 4.11) but the contribution of the Lorentz term is boosted in each plot. At $Q = 10^3$, the inertial term is dominant throughout, similar to the $Pm = 0.5$ case, but with the Lorentz term being the leading secondary term. The inertial term remains an order of magnitude greater than all other terms and hence strong zonal flows and multiple jets exist. The plots for $Q = 10^4$ and $Q = 10^5$ each show the Lorentz term entering the primary balance. It is therefore evident that (compared with $Pm = 0.5$) at $Pm = 5$

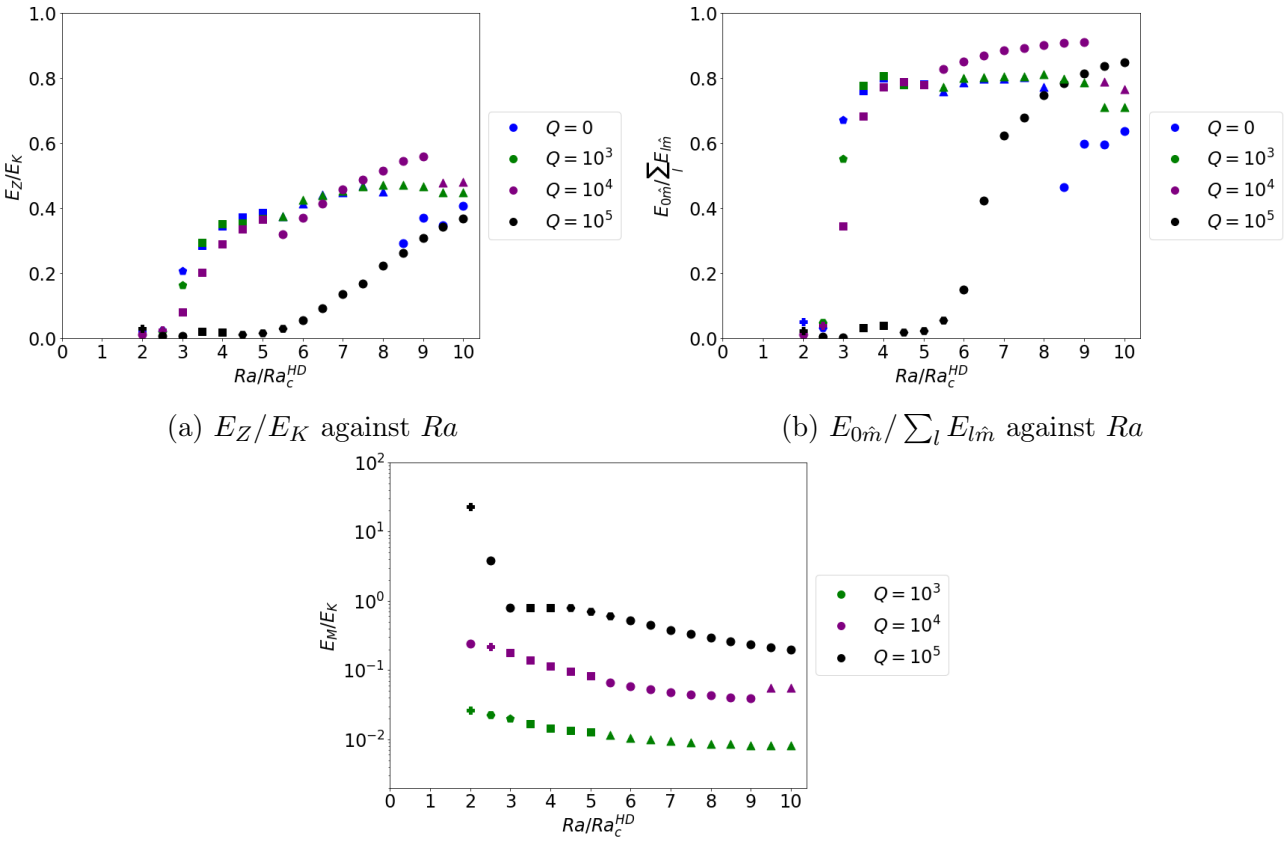

(a) E_Z/E_K against Ra

(b) $E_{0\hat{m}}/\sum_l E_{l\hat{m}}$ against Ra

(c) E_M/E_K against Ra

Figure 4.12: Plots of energy against Ra/Ra_c^{HD} for $Pr = 1$, $\eta^* = 5 \times 10^5$, $Pm = 5$, $B_f = 0.5$ and varying Q. Quantities have been globally averaged in space and time. The number of edges of each symbol represents the dominant time averaged mode $\hat{m}$. Plus symbols represent solutions with $\hat{m} \geq 7$ and circles represent solutions with $\hat{m} \leq 2$.

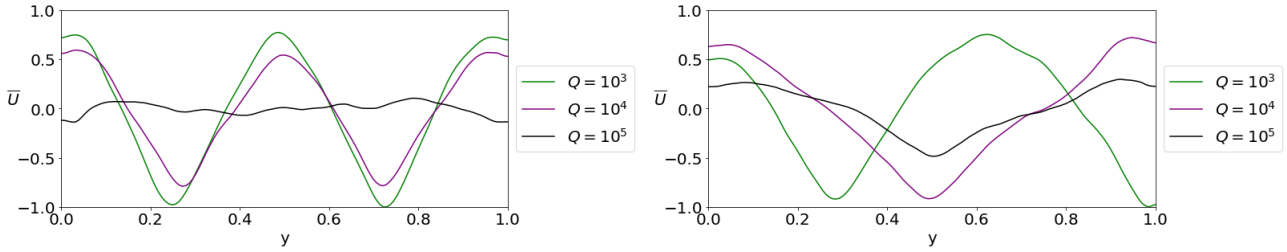

(a) $Ra/Ra_c^{HD} = 4$

(b) $Ra/Ra_c^{HD} = 9$

Figure 4.13: Zonal flow strength for increasing Q at two different values of Ra/Ra_c^{HD} with $Pr = 1$, $\eta^* = 5 \times 10^5$, $Pm = 5$, and $B_f = 0.5$.

the system requires a lower value of Q to transition from an inertially dominated regime to a balance between Lorentz and inertial terms. At $Pm = 0.5$ such a balance resulted in a loss of solutions with zonal flows (cf. Figure 4.11c). Therefore it is somewhat surprising to find that the zonal flows (and in some cases, multiple jets) persist under this balance. Other than the boosted Lorentz force, the main difference in the hierarchy of curls of forces at the different values of Pm is a boosted viscous term. Unlike at $Pm = 0.5$, this strong secondary contribution preserves the axisymmetric nature of the solution so that zonal flows exist even when the Lorentz and inertial terms are in balance. Nevertheless, multiple jet solutions still

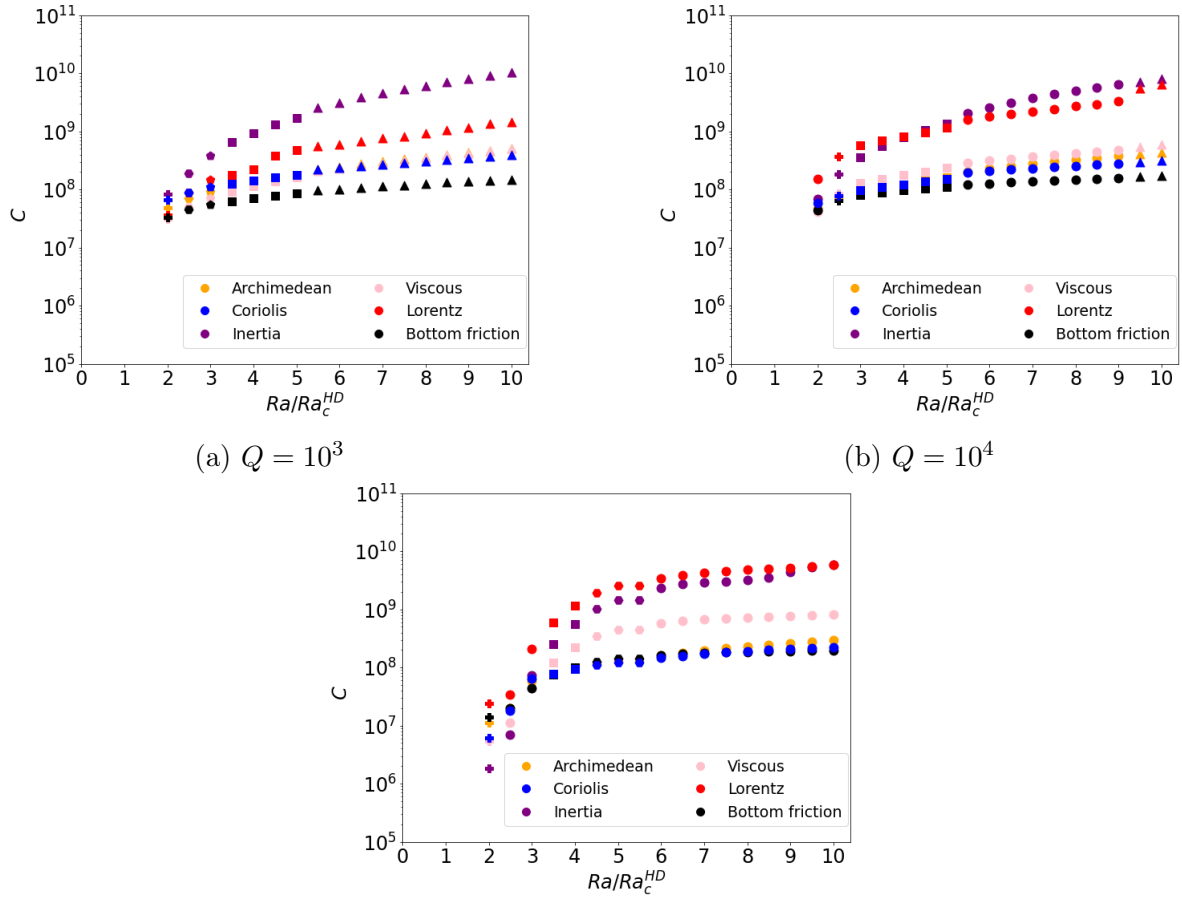

(a) $Q = 10^3$ (b) $Q = 10^4$

(c) $Q = 10^5$

Figure 4.14: Curl of each force against Ra/Ra_c^{HD} for $Pr = 1$, $\eta^* = 5 \times 10^5$, $Pm = 5$ and varying Q. Quantities have been globally averaged in space and time. The number of edges of each symbol represents the dominant time averaged mode $\hat{m}$. Plus symbols represent solutions with $\hat{m} \geq 7$ and circles represent solutions with $\hat{m} \leq 2$.

remain elusive at large magnetic field strengths.

The MAC balance found at $Q = 10^5$ and low Ra in the $Pm = 0.5$ case is also found at $Pm = 5$ but over a much smaller window of Ra-space. It is worth noting that, for simplicity, our study has focused on Rayleigh numbers normalised by the onset value for non-magnetic convection, Ra_c^{HD}. However, at $Pm = 5$, the Rayleigh numbers studied are more supercritical to the onset of *magnetoconvection* compared with $Pm = 0.5$ (since $Ra_c^{MC}(Pm = 5) < Ra_c^{MC}(Pm = 0.5)$). Further exploration at lower Ra may well extend this MAC regime in the $Pm = 5$ case. The stronger effective driving at $Pm = 5$ could also be enabling a zonal flow regime to emerge at larger Ra that is unseen in the lower Pm case.

4.3 RHINES SCALING

By considering a balance between the inertial and Coriolis terms, we can obtain the Rhines scaling theory. A balance between inertial and Coriolis terms gives

$$\begin{aligned} \eta^* \frac{\partial \psi}{\partial x} &\sim \frac{\partial\left(\psi, \nabla^2 \psi\right)}{\partial\left(x, y\right)} \\ \implies \eta^* U &\sim \frac{U^2}{L^2} \\ \implies L_R &\sim \sqrt{\frac{U}{\eta^*}} \end{aligned}$$

where U is a typical flow strength and L_R is the lengthscale of the flow. From this it follows that the dominant wavenumber m_r is given by

$$m_r = c\sqrt{\frac{\eta^*}{U}}, \tag{4.1}$$

for some scaling factor, c, determined to best match simulation data (Rhines, 1975). Rhines suggested that the convective (i.e. radial) speed should be used as the typical flow speed and some studies use this (e.g. Schneider and Liu, 2009). Other studies, both in numerical simulations (Teed et al. (2012) and Heimpel and Aurnou (2007)) and in experimental work (Gillet et al., 2007), have instead defined U to be the zonal speed. In the non-magnetic case Jones et al. (2003) used the convective flow speed whereas Teed et al. (2012) examined both, and found the zonal flow speed to fit best with the scaling theory.

In order to test our results against the theory, we define a convective flow speed and zonal flow speed as

$$\begin{aligned} U_C &= \left(\max\left\{u_y\right\} - \min\left\{u_y\right\}\right)/2, \\ U_Z &= \left(\max\left\{\bar{U}\right\} - \min\left\{\bar{U}\right\}\right)/2, \end{aligned}$$

respectively. These quantities are averaged over time. We wish to consider how our results match with the theory as well as which of U_C and U_Z best fits. The quantities U_C and U_Z are separately used in Equation (4.1) to determine two values of m_r for each simulation.

Figure 4.15 shows plots of the predicted wavenumber m_r from the Rhines scaling theory against the dominant wavenumber $\hat{m}$ obtained from simulations using the convective velocity (Figs 4.15a, 4.15c) and the zonal velocity (Figs 4.15b, 4.15d), where the scaling factor c has been calculated to best match results obtained from simulations. For the Rhines scaling theory to hold, we expect a line of best fit where $m_r \approx \hat{m}$. We have excluded runs at $Q = 10^5$ and any runs where $E_Z/E_K \leq 0.05$ because the theory does not hold for either the convective or zonal velocity. This is explained by the small zonal flows in these runs which result in unrealistically large values of m_r in Equation (4.1). When the convective velocity U_C is used (Figs 4.15a, 4.15c)

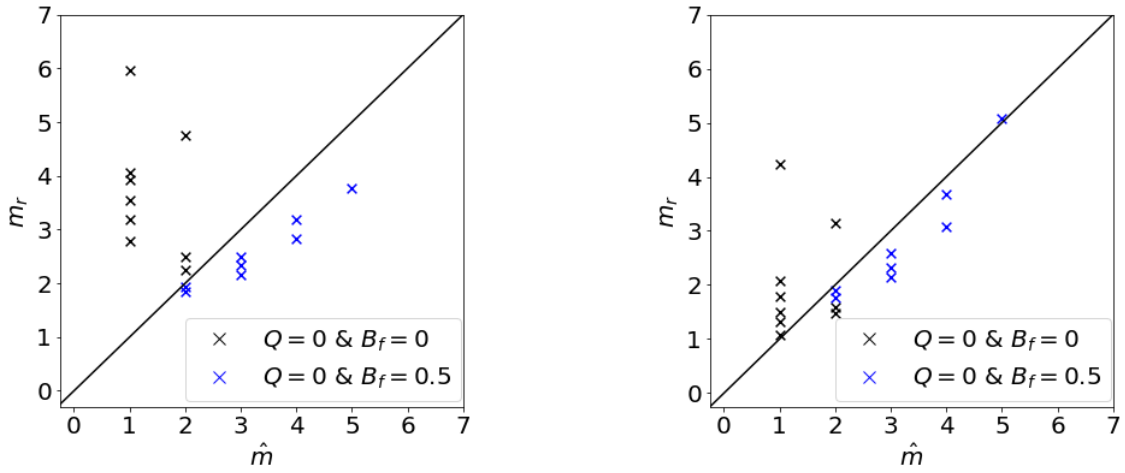

(a) U_C (using $c = 0.1917$)

(b) U_Z (using $c = 0.1562$)

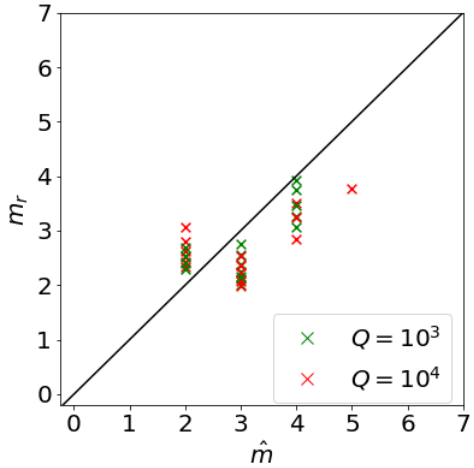

(c) U_C (using $c = 0.1917$)

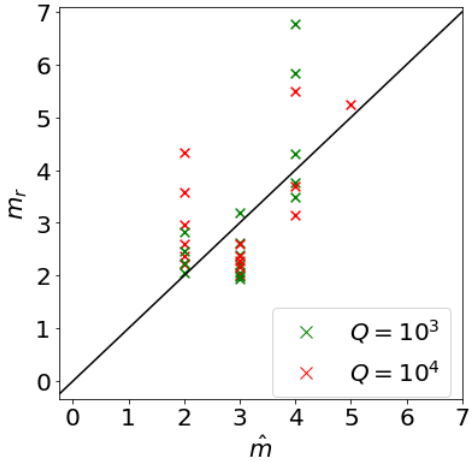

(d) U_Z (using $c = 0.1562$)

Figure 4.15: Plots of the predicted dominant m_r from the scaling theory against the dominant mode $\hat{m}$ from simulations. Non-magnetic results are plotted for both $B_f = 0$ and $B_f = 0.5$ and both values of Pm with $B_f = 0.5$ for $Q = 10^3$ and $Q = 10^4$, all for integer values of Ra/Ra_c^{HD} are plotted. Runs at $Q = 10^5$ and any runs where $E_Z/E_K \leq 0.05$ are excluded.

the theory does not provide a good linear fit between m_r and $\hat{m}$. When the zonal velocity is used (Figs 4.15b, 4.15d), the results indicate a linear fit exists between m_r and $\hat{m}$ especially at lower m_r. The theory arguably becomes less accurate at larger values of $\hat{m}$ but overall when considering a linear fit between m_r and $\hat{m}$, the zonal velocity provides the best fit. This matches the non-magnetic results of Teed et al. (2012) where they found the theory using the zonal flow speed to provide the best fit.

A Wilcoxon Matched-Pairs Test (Wilcoxon, 1945) is performed to assess the statistical significance of this result. This uses a threshold $\alpha = 0.05$ to reject the null hypothesis, where p-values above this threshold indicate statistically significant results. This helps to determine whether the dominant wavenumber m_r obtained from (4.1) differs significantly from the dominant wavenumber $\hat{m}$ obtained from simulations. A p-value of 0.96 is obtained for Fig. 4.15b and a p-value of 0.98 for Fig. 4.15d, indicating there is no significant difference between measurements. For the convective velocity we obtain a p-value of 0.19 for Fig. 4.15a and 0.02 for

Fig. 4.15c.

For runs at $Q = 10^5$, we explore a different scaling by considering a balance between Coriolis and Lorentz terms due to the increased role of the magnetic field. A balance between Coriolis and Lorentz terms gives

$$\begin{aligned} \eta^* \frac{\partial \psi}{\partial x} &\sim \frac{Q}{Pm} \frac{\partial \left(g, \nabla^2 g\right)}{\partial \left(x, y\right)} \\ \implies \eta^* U &\sim \frac{Q}{Pm} \frac{B^2}{L^2} \\ \implies L_{CL} &\sim \sqrt{\frac{QB^2}{\eta^* U Pm}}, \end{aligned}$$

where U is a typical flow strength and B is a typical magnetic field strength. This gives a dominant wavenumber m_{CL} as

$$m_{CL} = c\sqrt{\frac{\eta^* U Pm}{QB^2}}, \tag{4.2}$$

for some scaling factor c. In order to test our results using (4.2) we define two different magnetic field strengths. These are

$$\begin{aligned} B_y &= \left(\max\left\{b_y\right\} - \min\left\{b_y\right\}\right)/2, \\ B_x &= \left(\max\left\{b_x\right\} - \min\left\{b_x\right\}\right)/2, \end{aligned}$$

where B_y is used together with U_C and B_x is used with U_Z. We tested how well m_{CL} correlated to our simulations for which a MAC balance occurs. However, we did not find a good linear fit between $\hat{m}$ in simulations and m_{CL} given by Equation (4.2) using the convective or zonal velocity, indicating that this balance does not provide a prediction for the radial lengthscale (Fig. 4.16).

4.4 SUMMARY

These non-linear simulations of convection in the Busse annulus model show good agreement with previous non-magnetic simulations (Jones et al. (2003), Rotvig and Jones (2006), Teed et al. (2012)). In particular, we found that rigid top and bottom boundary conditions promoted the development of multiple jet solutions but also weakened the zonal flows. Many of the properties of the non-magnetic problem have been studied in detail previously but here we also examined the balances of the (curls of) forces of non-magnetic results. We found that a strong inertial term, with secondary contributions from the remaining terms, occurred for all runs. This is expected for zonal flows driven through the Reynolds stresses. For those simulations which displayed a multiple jet pattern of zonal flows (found typically at low driving with rigid boundaries), the inclusion of bottom friction provides an increased contribution from all secondary forces. Hence multiple jet structures appear to be facilitated in regimes where

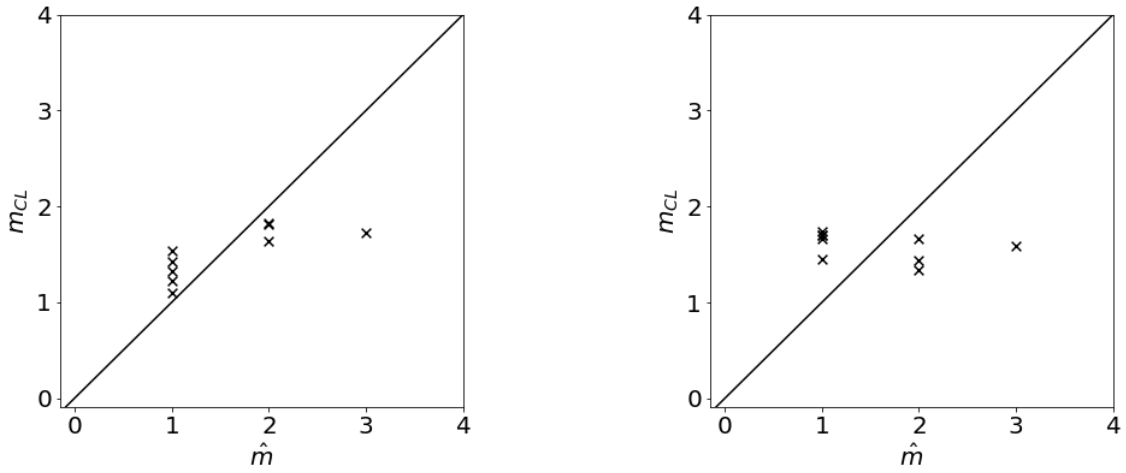

(a) U_C and B_y (using $c = 0.0825$) (b) U_Z and B_x (using $c = 0.0377$)

Figure 4.16: Plots of the predicted dominant m_{CL} from the scaling theory against the dominant mode $\hat{m}$ from simulations.

the inertial force is strong enough to produce zonal flows but secondary forces remain 'only' 1-2 magnitudes weaker. This also provides an explanation as to why multiple jets are found in a small number of cases (at low Ra) where bottom friction is absent since weaker driving leads to weaker Reynolds stresses. Our non-magnetic results agreed well with the Rhines scaling when the zonal velocity was used, in agreement with previous work (Teed et al., 2012).

In this chapter we extended non-magnetic work by imposing an azimuthal magnetic field and examining the effect on multiple jet solutions as the magnetic field strength was varied. Several interesting conclusions can be drawn in the magnetic case. We found zonal flows and solutions with multiple jets are retained under the 'correct' conditions. Typically, this requires a weak enough imposed field strength to either restrain the Lorentz force to be a secondary contributor or to maintain the inertial force in the primary balance alongside the Lorentz force. The remaining secondary forces, especially the viscous force, can also promote the retention of multiple jets. For multiple jets, relatively weak driving is also required (matching the non-magnetic case). Broadly speaking, an increased magnetic field strength reduces the number of jets and can, ultimately, completely suppress the development of multiple jets and zonal flows. However, a weak enough field can preserve multiple jets at larger driving, even compared to the non-magnetic case. The zonal flows of Mason et al. (2022) exhibit similar dependence on magnetic field strength. They find the magnetic field can increase the role of the zonal energy in the total kinetic energy (up to $\approx 30\%$) but stronger imposed field suppresses the zonal flow. However, the flows in their spherical geometry appear to be driven by a thermal or magnetic wind whereas the importance of the inertial force in our work confirms that the flows are formed through Reynolds stresses. The flows in our (magnetic) work also form a far greater proportion of the kinetic energy budget (up to $\approx 50\%$).

We found a MAC balance can be achieved in the annulus model. This was not necessarily expected since the setup of the model is geared towards generation of zonal flows through a

strong inertial force (even at low driving) which must be absent in the MAC balance. The zonal flows (and multiple jets) are suppressed under such a balance. The effect of the magnetic Prandtl number, Pm, is subtle. Two values, an order of magnitude apart, were tested and we found the effect on zonal flow and multiple jet development to be minimal for the low values of imposed magnetic field (i.e. at $Q = 10^3$ and $Q = 10^4$ in our work). The patterns of a lowering of the number of jets and a reduction in the amplitude of the zonal energy as the driving is increased exist, regardless of the value of Pm. At larger field strengths (i.e. at $Q = 10^5$ in our work), where the Elsasser number $\Lambda = Q/\eta^*$ approaches its $O(1)$ optimal value for convective onset (Hori et al., 2014; Soward, 1979), the available regimes depend greatly on Pm. At low driving, regimes are characterised by a MAC balance and weak zonal flow regardless of Pm but, with stronger driving, two different regimes are possible depending on Pm. Zonal flows, jets, and bands are replaced by non-axisymmetric solutions when the magnetic diffusion is large whereas the enhanced role of the viscous term when the magnetic diffusion is weak allows zonal flows to develop. Our results with large magnetic diffusion are in line with the spherical simulations of Mason et al. (2022), where imposing a strong enough magnetic field also suppresses zonal flows (although that work did not vary magnetic diffusion). The magnetic field morphology chosen here acts in the same direction as the zonal flow. A radial magnetic field may have more impact on multiple jets at a smaller value of Q, as it acts in a different direction from the zonal flow.

The Rhines scaling theory (using zonal flow speed) was unable to predict the number of jets if the imposed magnetic field is too large. The theory breaks down in regimes where the Lorentz force enters the primary balance with inertia since the theory is based on the assumption of a balance between only Coriolis and inertial forces.

Chapter 5

Force balances in a spherical dynamo model

Since the first numerical simulation of the geodynamo by Glatzmaier and Roberts (1995) many parameter space studies have been conducted which have identified three main branches of dynamo action. Two of these branches were identified by Christensen and Aubert (2006) where they found one branch of solutions characterised by a dominant dipole field and the other branch was mainly multipolar with a fluctuating dipolar component. For multipolar solutions, all components of the field are of a similar size unlike the dipolar case where the dipolar component is much larger than the others. In all three branches, the Coriolis and buoyancy forces are important. The dipolar branch is controlled by the Coriolis, buoyancy and viscous forces (VAC balance), whilst the multipolar branch is controlled by Coriolis, buoyancy and inertial forces (CIA balance) (Teed and Dormy, 2023). The third branch was identified by Dormy (2016) where solutions have a strong dipolar field and there is a dominant balance between Coriolis, buoyancy and Lorentz forces (MAC balance). The expected force balance in Earth's core is widely believed to be a MAC balance with weak contributions from the viscous and inertial forces (Schwaiger et al., 2019, 2021; Teed and Dormy, 2023). Hence, the strong dipolar branch of solutions is believed to be most relevant to the geodynamo.

With recent advancements in computing power, it has been possible to perform simulations with input parameters closer to the expected parameter values of Earth's core. However, these parameter values are still far from the geophysically relevant parameter values and in some cases these solutions do not display a dominant dipolar field or the expected force balance of Earth. For example the Ekman number of Earth is $O(10^{-15})$, but simulations are only able to reach $O(10^{-7})$ for the most powerful computations (Kageyama et al., 2008; Takahashi et al., 2008). Instead, it has been proposed that simulations of the geodynamo should be carried out at the expected force balance of Earth's core (Aubert et al., 2017; Dormy, 2016). In order to check for the correct force balance, the lengthscale dependence of the forces can be examined in simulations. This concept was first introduced by Aubert et al. (2017) where, over a series of

papers (Aubert, 2019, 2023; Aubert and Gillet, 2021; Aubert et al., 2022), they then attempt to define a path in parameter space where a MAC balance is preserved as the input parameters are moved closer to the values expected in Earth's core. The path in parameter space defined by Aubert et al. (2017) is another name for the distinguished limit first proposed by Dormy (2016).

A systematic study of the lengthscale dependence of forces in dynamo simulations was carried out by Schwaiger et al. (2019). In this analysis, the forces are complicated by the pressure force which always appears with the Coriolis force in the leading order force balance (at least at large scales). However, the pressure gradient is not dynamically important so it is not relevant in the force balance (Hughes and Cattaneo, 2019; Teed and Dormy, 2023). One method of dealing with this is to form an ageostrophic Coriolis force by subtracting the pressure gradient from the Coriolis force. We can then analyse the ageostrophic force in the balance instead and ignore the leading order balance between pressure and Coriolis forces that usually appears in simulations. This approach implicitly assumes that the pressure gradient is only balancing the gradient parts of the Coriolis force. However other forces might also have gradient parts which are in balance with the pressure gradient. Another method is to form solenoidal forces by taking the curl of each force which eliminates the gradient parts of the forces and removes the pressure gradient from the balance. This has been studied most recently by Teed and Dormy (2023) where they examined lengthscale dependence of solenoidal forces. At leading order they recovered the first order balance which usually appears in the forces, and no longer obtained the leading order geostrophic balance. They also found that the small scale balance of the solenoidal forces to be different to the primitive forces as the viscous force enters the small scale balance.

Schwaiger et al. (2021) compared dynamically relevant lengthscales with energetically relevant lengthscales. This was done by extracting the lengthscale at which the two most relevant forces cross each other and comparing these with the peaks in the poloidal kinetic energy spectrum. The crossover points are defined in Section 5.3.1. A correlation was found between inertial and buoyancy force crossover with the poloidal kinetic energy for non-magnetic runs at large enough Ra and a correlation between Lorentz and buoyancy force crossover with the poloidal kinetic energy for magnetically dominated runs. However, they are only able to characterise runs which have a well-defined crossing, and they do not consider runs in the multipolar regime or separate between viscously and magnetically dominated branches of dipolar dynamo action. In this chapter, a triple balance point is introduced and compared with the peaks in the kinetic energy spectra. Unlike crossover analyses that consider only two forces and focus on runs with a well-defined crossing point (Schwaiger et al., 2021), our new method introduces a triple balance point. This approach takes into account the fact that there are usually three main forces controlling the dynamics and allows us to examine all runs regardless of a crossover of forces being present.

This chapter examines force balances in spherical dynamo simulations. Details of the model and methods used are discussed in Chapter 2. We focus on a comparison of the forces and solenoidal

forces in l and m. The hydrodynamical (HD) case is presented first where the forces and curls of forces in l and m are presented for $E = 10^{-4}$ and $E = 10^{-5}$ at different Rayleigh numbers. Then dynamo solutions are presented in the 3 different dynamo regimes where the forces and curls of forces in l and m are examined for $E = 10^{-4}$ and $E = 10^{-5}$. The triple balance point in each regime is analysed and related to the peaks in the kinetic energy spectrum. The position of the three regimes in parameter space are guided by previous studies by Christensen and Aubert (2006), Dormy (2016), Dormy et al. (2018) and Teed and Dormy (2025). For all runs $Pr = 1$ and the aspect ratio is set to $\chi = r_i/r_o = 0.35$. We have a constant temperature difference between boundaries and use no-slip, impenetrable, rigid and electrically insulating conditions.

5.1 Comparison of force spectra

We examine the force spectra for the hydrodynamical case at $E = 10^{-4}$ and for the three main regimes of dynamo action at $E = 10^{-4}$ and $E = 10^{-5}$. The l dependence of forces has been considered previously (Schwaiger et al., 2019; Teed and Dormy, 2023). The l dependence is discussed here and we extend these results by examining the m dependence of forces. It should be noted that the meaning of l and m now changes with respect to the annulus model.

Run	E	Pr	Pm	Ra/Ra_c	Rm	Λ'	f_{dip}
WD	10^{-4}	1	12	2.07	212.862	0.009	0.826
SD	10^{-4}	1	12	2.07	202.147	0.661	0.828
SD	10^{-4}	1	12	10	889.86	2.551	0.555
MP	10^{-4}	1	1	30	285.826	0.112	0.133
WD	10^{-5}	1	5	3	187.415	0.015	0.971
SD	10^{-5}	1	5	4	322.047	0.393	0.765
MP	10^{-5}	1	0.2	100	311.053	0.167	0.201

Table 5.1: Input and output parameters for dynamo solutions presented in Sections 5.1.2 and 5.1.3.

Table 5.1 shows the input and output parameters for the simulations analysed in Sections 5.1.2 and 5.1.3. We include values for the magnetic Reynolds number Rm, the dynamic Elsasser number Λ' and f_{dip}. These parameters were defined in Section 2.2.3.3.The difference in magnetic field strength between the weak field and strong field dipolar case can be seen by comparing values of Λ', which increases by at least an order of magnitude in the strong field case. The parameter f_{dip} is large in the weak field and strong field dipolar regimes but decreases significantly in the multipolar regime, which is to be expected since the field is no longer of a dipolar nature. Some of the runs presented in this chapter have been initialised using state files from existing simulations in Teed and Dormy (2025).

5.1.1 Hydrodynamical solutions at $E = 10^{-4}$

Figure 5.1a shows the forces in l for an HD run at $Ra = 2Ra_c$ where a zeroth order geostrophic balance occurs at all lengthscales. At large scales a first order balance occurs between buoyancy

and ageostrophic Coriolis force which is broken at larger scales by inertia, where this replaces the buoyancy force. Similar behaviour occurs for the lengthscale dependence in m (Fig. 5.1b) although the curves drop off at larger scales compared with l. The ageostrophic Coriolis force can be larger than the Coriolis force, as observed at some scales in Fig. 5.1b. This occurs when geostrophy does not hold, and in such cases, the pressure gradient is balanced by gradient parts of the Coriolis force and gradient parts of the other forces.

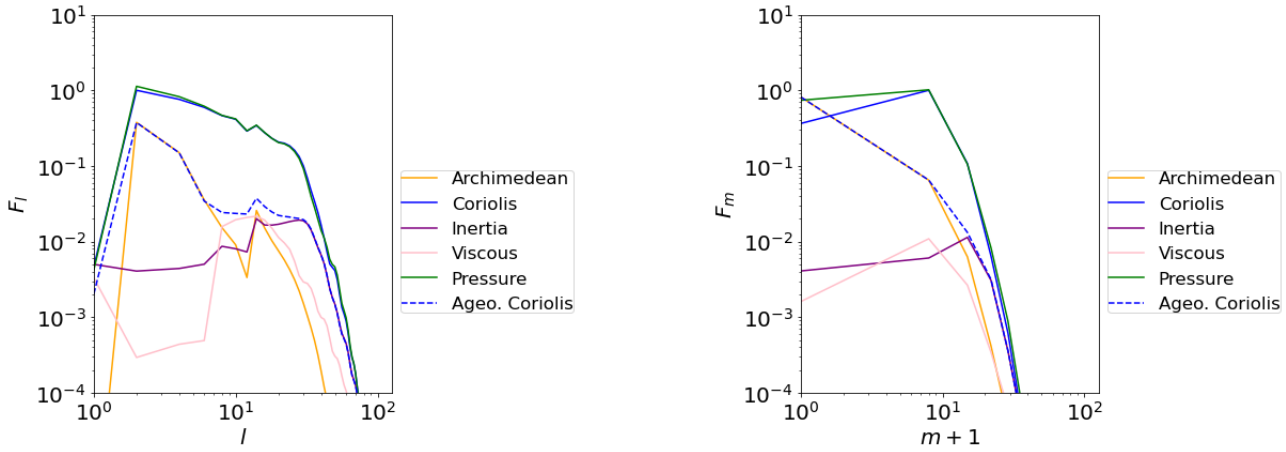

(a) (b)

Figure 5.1: Comparison of forces for a HD run at $E = 10^{-4}$ and $Ra = 2Ra_c$. (a) forces in l (modes with l odd removed), (b) forces in m (every $7m$ plotted). All quantities are time averaged and boundary layers have been removed.

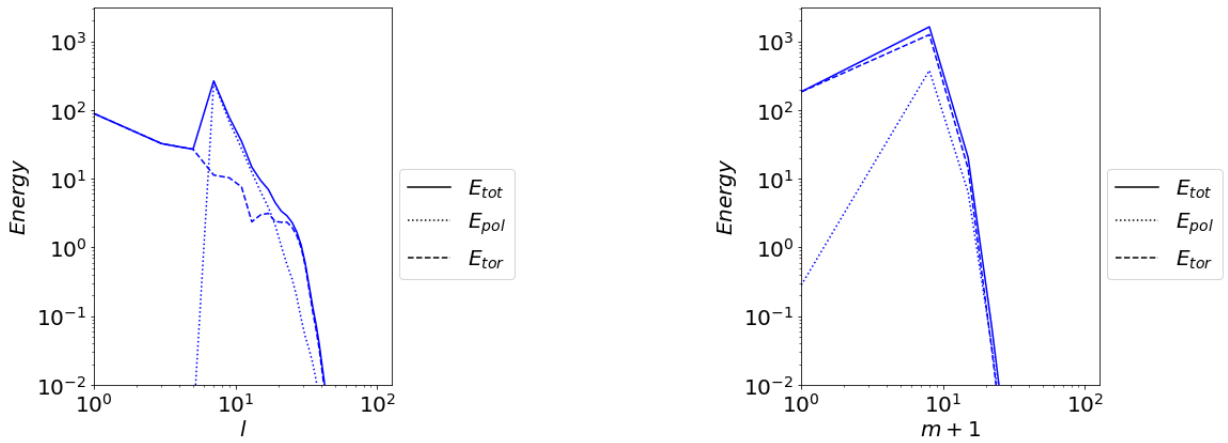

(a) (b)

Figure 5.2: Energy spectrum for a HD run at $E = 10^{-4}$ and $Ra = 2Ra_c$. (a) energy spectrum in l (modes with l odd removed) (b) energy spectrum in m (every $7m$ plotted). All quantities are time averaged.

The run at $Ra = 5Ra_c$ behaves similarly to $Ra = 2Ra_c$ but the system is more supercritical so convection is more developed, causing an increase in the inertial force. The forces in l (Fig. 5.3a) show a zeroth order geostrophic balance at most scales and a first order balance between buoyancy and ageostrophic Coriolis forces at large scales, with the inertial and viscous forces being less important. At small scales the inertia breaks the geostrophic balance as it enters

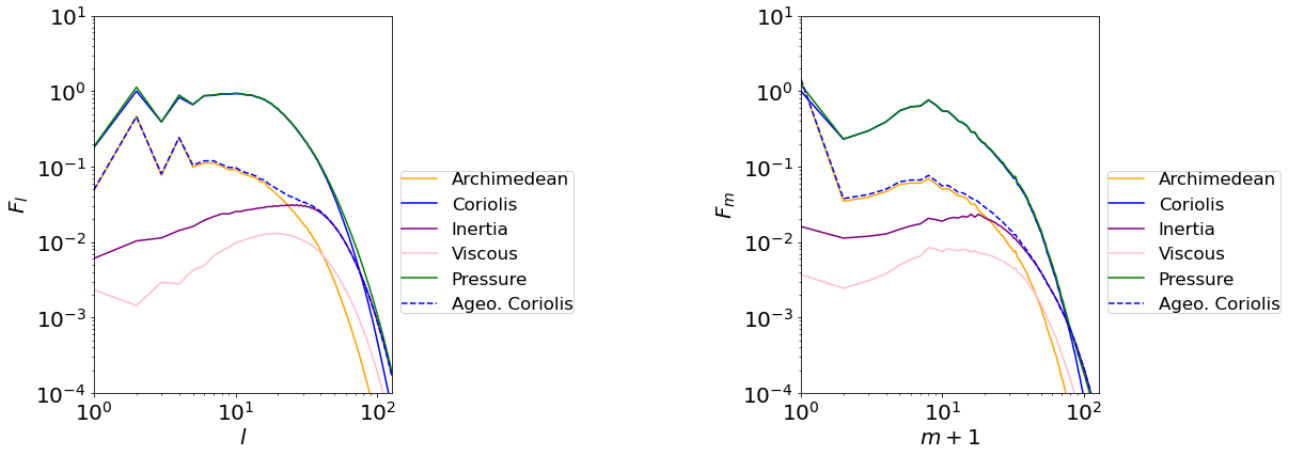

(a) (b)

Figure 5.3: Comparison of forces for a HD run at $E = 10^{-4}$ and $Ra = 5Ra_c$. (a) forces in l, (b) forces in m. All quantities are time averaged and boundary layers have been removed.

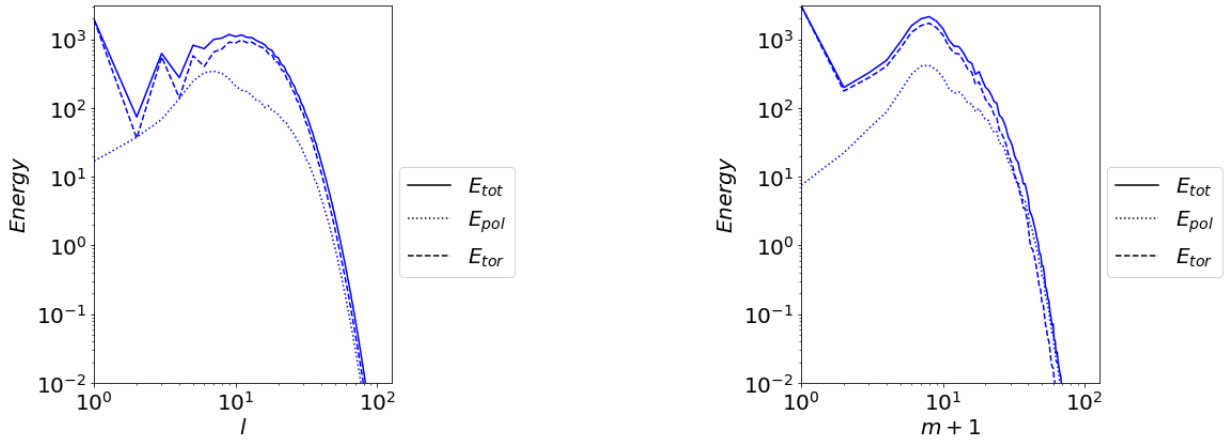

(a) (b)

Figure 5.4: Energy spectrum for a HD run at $E = 10^{-4}$ and $Ra = 5Ra_c$. (a) energy spectrum in l (b) energy spectrum in m. All quantities are time averaged.

the first order balance and replaces the Coriolis force. Similar behaviour for the lengthscale dependence in m is found (Fig. 5.3b). The l and m spectra for the total, toroidal and poloidal kinetic energy are plotted for $Ra = 2Ra_c$ (Fig. 5.2) and $Ra = 5Ra_c$ (Fig. 5.4). At $Ra = 2Ra_c$, in l-space, the total and poloidal energy have similar peaks but the toroidal energy differs. In m-space both toroidal and poloidal parts have a similar peak to the total energy. At $Ra = 5Ra_c$, for both l and m, the toroidal energy spectrum is very similar to the total energy spectrum with peaks occurring at the same values of l and m whereas the peak in the poloidal energy spectrum differs to the total and toroidal kinetic energy. These plots indicate that the toroidal energy dominates for most (or all) scales for all runs. In particular, the toroidal energy is much larger at large scales probably as a result of the development of large scale zonal flows (especially at increased Ra). The position of the peaks in energy are discussed as these will be important in Section 5.3 when they are compared to crossing points and triple balance points. The structured behaviour of the flow is observed in plots of the meridional sections of u_ϕ, where

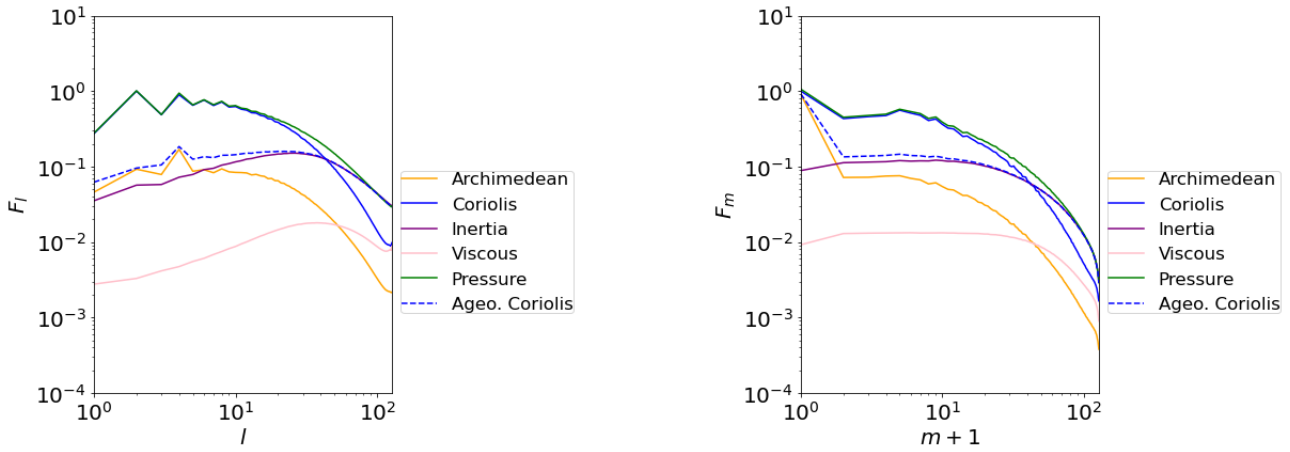

(a) (b)

Figure 5.5: Comparison of forces for a HD run at $E = 10^{-4}$ and $Ra = 30Ra_c$. (a) forces in l, (b) forces in m. All quantities are time averaged and boundary layers have been removed.

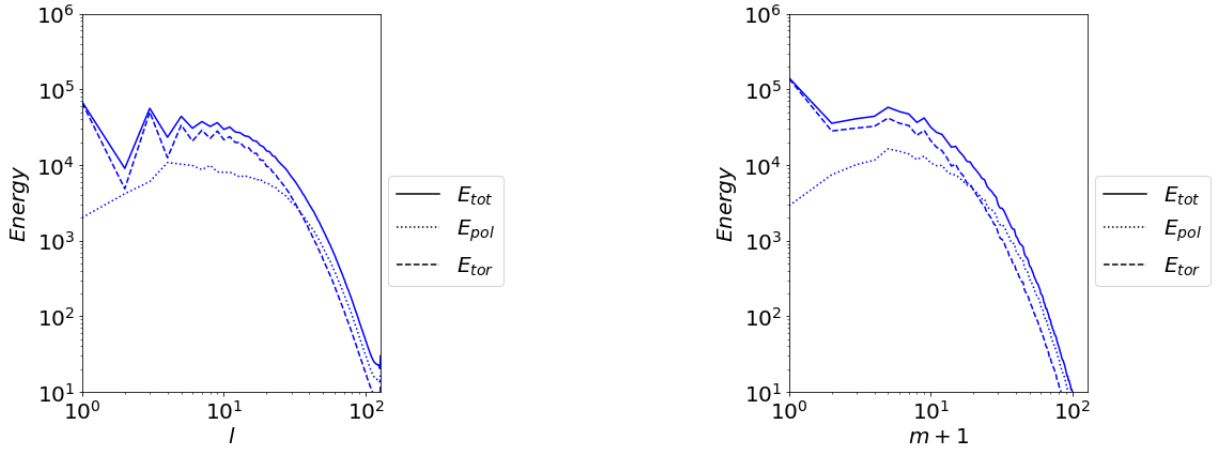

(a) (b)

Figure 5.6: Energy spectrum for a HD run at $E = 10^{-4}$ and $Ra = 30Ra_c$. (a) energy spectrum in l (b) energy spectrum in m. All quantities are time averaged.

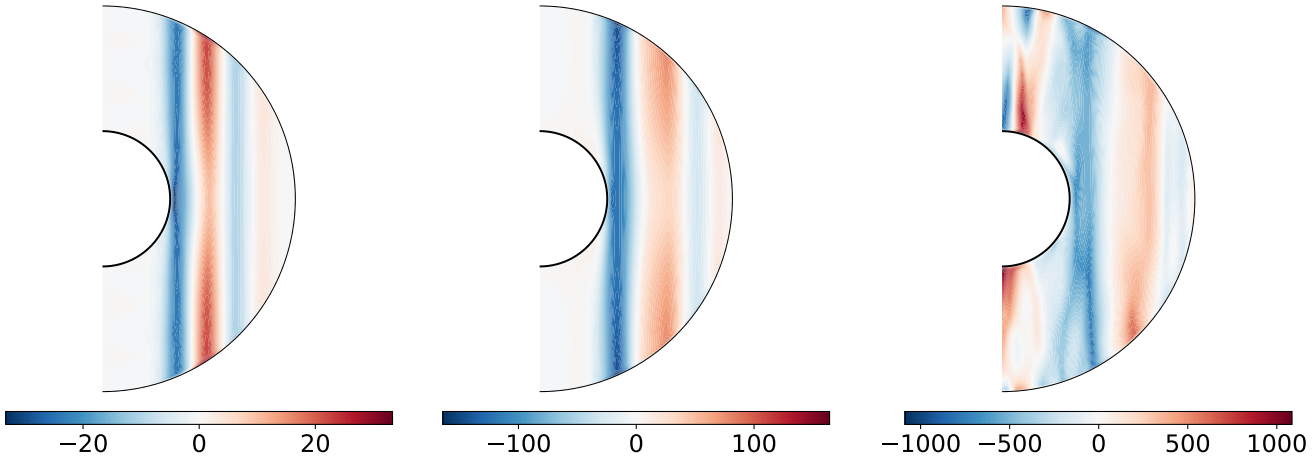

(a) $Ra = 2Rac$ (b) $Ra = 5Rac$ (c) $Ra = 30Rac$

Figure 5.7: Plots of meridional sections of u_ϕ. All plots are ϕ averaged.

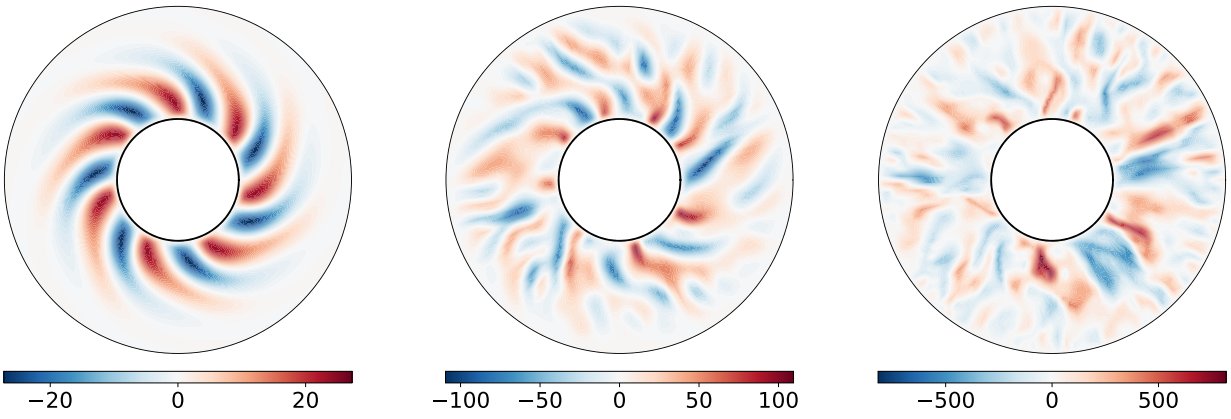

(a) $Ra = 2Rac$ (b) $Ra = 5Rac$ (c) $Ra = 30Rac$

Figure 5.8: Plots of equatorial sections of u_r.

the flow is z-invariant at both $Ra = 2Ra_c$ (Fig 5.7a) and $Ra = 5Ra_c$ (Fig 5.7b). Equatorial sections of u_r also show a highly ordered flow similar to the convective onset mode at $Ra = 2Ra_c$ (Fig. 5.8a). At $Ra = 5Ra_c$ (Fig. 5.8b) the flow is no longer made up of only Taylor columns but the flow retains the z-invariance.

At $Ra = 30Ra_c$ (Fig. 5.5) the inertial force has increased and now enters the first order balance. This is observed in both l and m. The change in behaviour between the runs at low Ra and high Ra is clear from the differences in the hierarchy of forces and the changes in flow patterns. At $Ra = 30Ra_c$ zonal flows are now observed ITC and OTC (Fig. 5.7c) and a wider range of azimuthal modes are excited at this larger supercriticality with the flow becoming more chaotic (Fig. 5.8c). The total and toroidal kinetic energy spectrum are very similar but the poloidal energy spectrum has differing behaviour and peaks at a different l and m to the other components (Fig. 5.6). Overall the plots of the forces in l and m match well qualitatively, where the hierarchy of forces are similar. The main difference between l and m is the point at which the forces decrease and become less important.

5.1.2 DYNAMO SOLUTIONS AT $E = 10^{-4}$

Figure 5.9 shows the forces for a weak field dipolar run. The forces in l and m are similar. A zeroth order geostrophic balance occurs throughout with the viscous, inertial and Lorentz force remaining weak in both cases. The dipolar nature of the field is clear from the spherical surface plot of B_r (Fig. 5.17a). The flow patterns shown in the meridional sections of u_ϕ and equatorial sections of u_r (Figs 5.16a, 5.18a) are similar to those at low Ra in the hydrodynamical case. The flow patterns and hierarchy of forces are similar to the hydrodynamical runs at low Ra, with the inclusion of a weak Lorentz force, so this regime acts like a weakly magnetically adjusted hydrodynamical regime. The energy spectra in l and m (Fig. 5.10) display similar results to the energy spectrum at low Ra for the hydrodynamical case (Fig. 5.2) where the total, toroidal and poloidal kinetic energy spectra peak at the same l and m.

Figure 5.11 shows the forces for the same parameters used in Figure 5.9 but this run has been

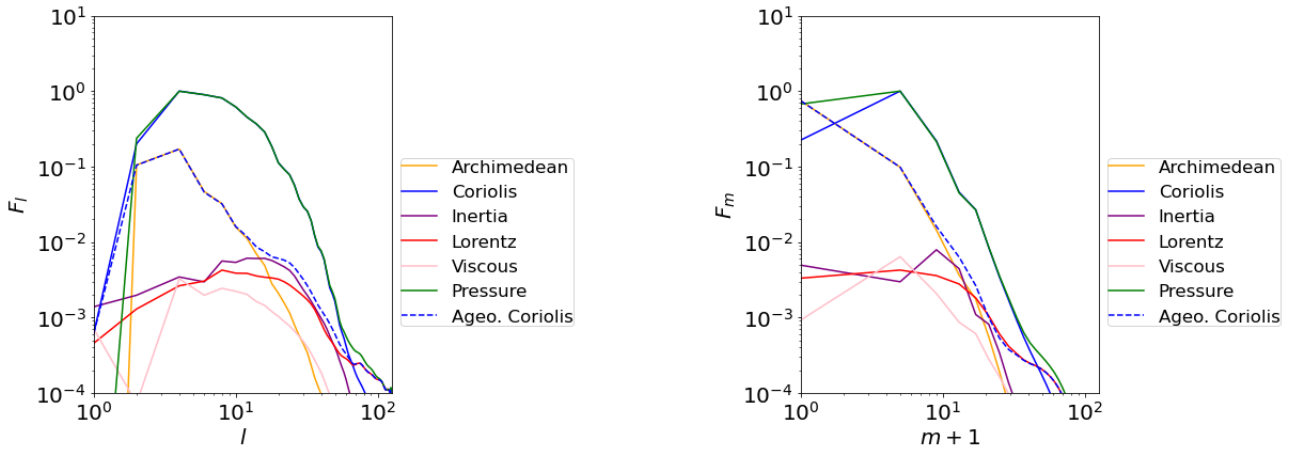

(a) (b)

Figure 5.9: Comparison of forces for weak field dipolar run at $E = 10^{-4}$, $Pm = 12$ and $Ra = 2.07Ra_c$. (a) forces in l (modes with l odd removed), (b) forces in m (every $4m$ plotted). All quantities are time averaged and boundary layers have been removed.

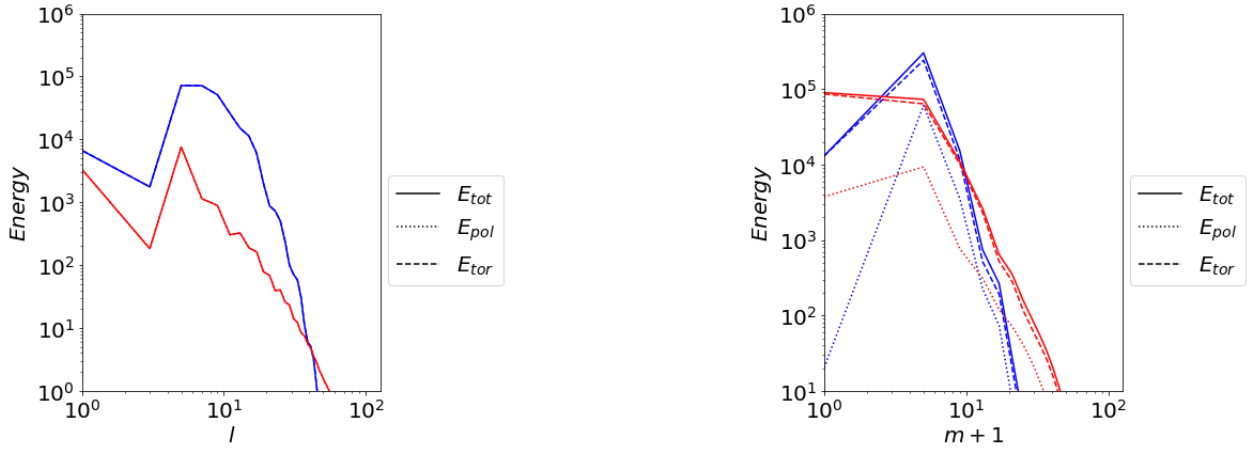

(a) (b)

Figure 5.10: Energy spectrum for weak field dipolar run at $E = 10^{-4}$, $Pm = 12$ and $Ra = 2.07Ra_c$. Blue and red lines represent kinetic and magnetic energy respectively. (a) energy spectrum in l (modes with l odd removed) (b) energy spectrum in m (every $4m$ plotted). All quantities are time averaged.

initialised from the final state of a run on the strong field branch in nearby parameter space to obtain a strong field dipolar solution (Teed and Dormy, 2025). These weak and strong field solutions are bistable. The forces in l and m are very similar (Figs 5.11a and 5.11b) where a zeroth order geostrophic balance occurs at larger scales and at smaller scales the Coriolis force drops off and instead a balance between the pressure gradient and Lorentz force occurs. The buoyancy force is also strong at larger lengthscales but drops off at smaller scales. The viscous and inertial forces are weak across all scales. The energy spectra in l shows that the toroidal part of the kinetic energy is the main contributor to the total energy but the poloidal energy differs with peaks occurring at a different l to the toroidal and total energy (Fig. 5.12a). In m, all three parts display similar behaviour (Fig. 5.12b). Again, the dipolar nature of the field is clear from B_r (Fig. 5.17b) where the field is dipolar but more small scale structures

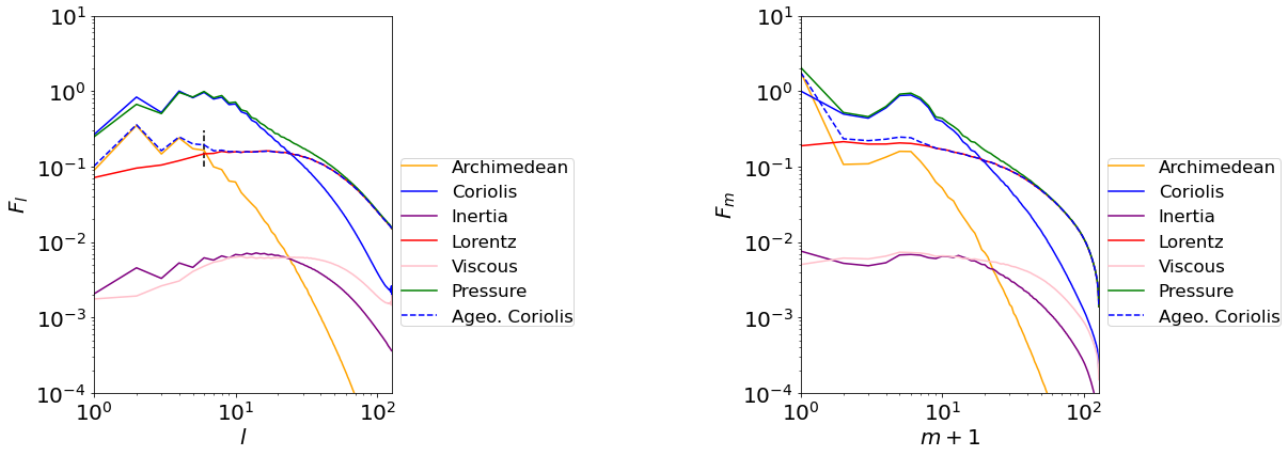

(a) (b)

Figure 5.11: Comparison of forces for strong field dipolar run at $E = 10^{-4}$, $Pm = 12$ and $Ra = 2.07Ra_c$. (a) forces in l, (b) forces in m. All quantities are time averaged and boundary layers have been removed.

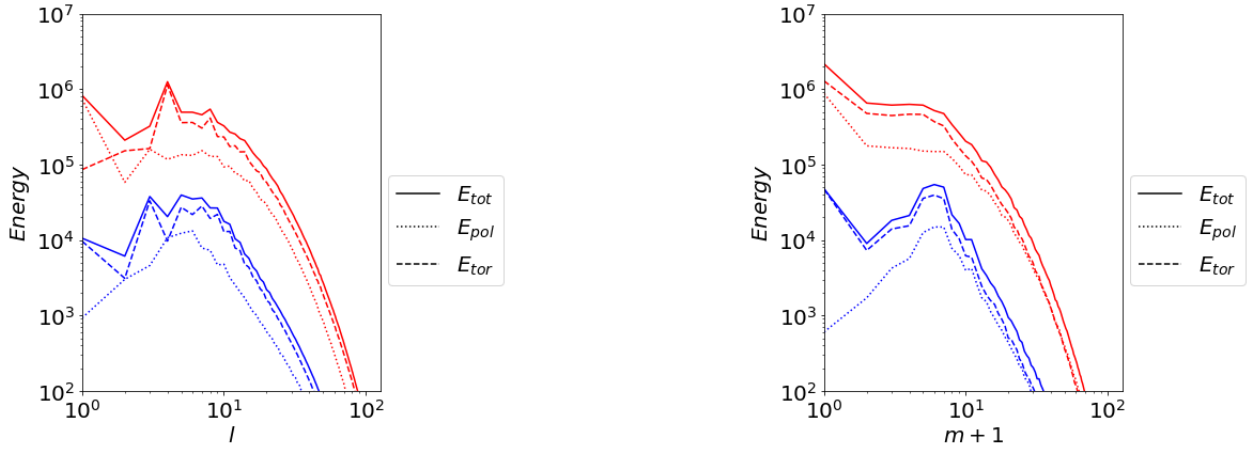

(a) (b)

Figure 5.12: Energy spectrum for strong field dipolar run at $E = 10^{-4}$, $Pm = 12$ and $Ra = 2.07Ra_c$. Blue and red lines represent kinetic and magnetic energy respectively. (a) energy spectrum in l (b) energy spectrum in m. All quantities are time averaged.

appear compared with the weak field dipolar regime. For the strong field dipolar case (Fig. 5.16b), convection is now present inside the tangent cylinder which is not observed for the weak field dipolar case. The likely reason for convection ITC being present in the strong field case and not the weak field case (despite the unchanged value of Ra) is that the magnetic field relaxes the rotational constraint thereby lowering the effective Ra_c. Hence the strong field is more supercritical than the weak field case as the magnetic field is stronger. This is similar to the magnetoconvection study in Chapter 3 where a larger Q usually leads to $Ra_c^{MC} < Ra_c^{HD}$. Outside the tangent cylinder, the flow loses its z-invariance. An increase in the dominant azimuthal wavenumber occurs in the strong dipolar case (Fig 5.18b).

Figure 5.13 shows the forces for another strong field run on the same branch as the run shown in Figure 5.11 but the Rayleigh number has been increased to $Ra = 10Ra_c$. The results are

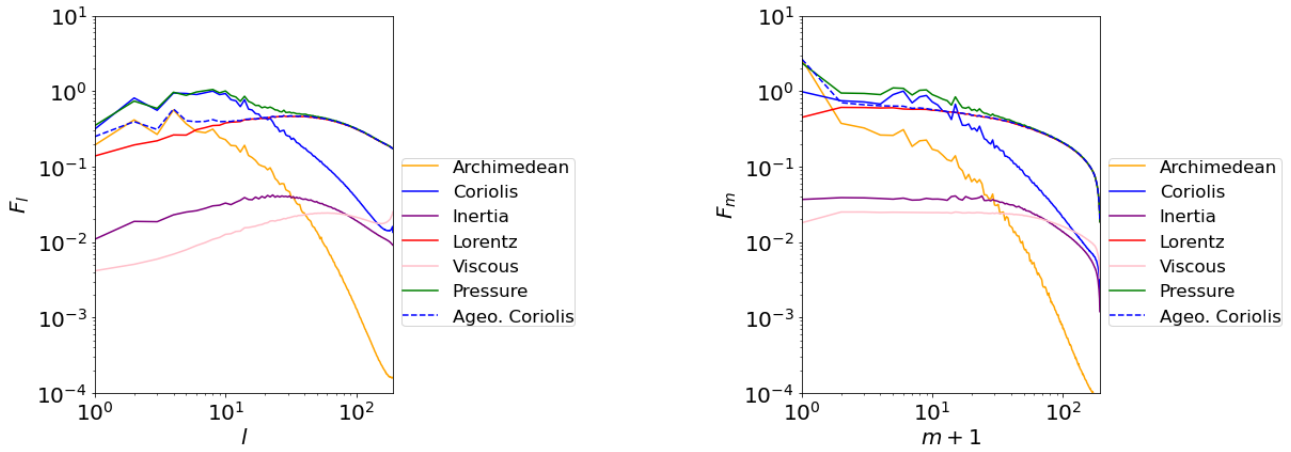

(a) (b)

Figure 5.13: Comparison of forces for strong field dipolar run at $E = 10^{-4}$, $Pm = 12$ and $Ra = 10Ra_c$. (a) forces in l, (b) forces in m. All quantities are time averaged and boundary layers have been removed.

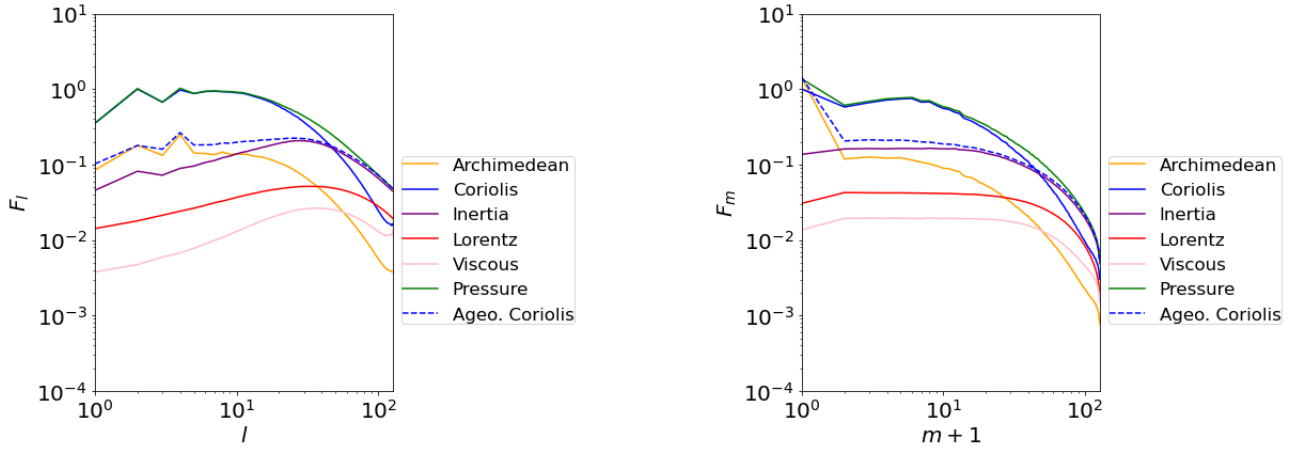

(a) (b)

Figure 5.14: Comparison of forces for multipolar run at $E = 10^{-4}$, $Pm = 1$ and $Ra = 30Ra_c$. (a) forces in l, (b) forces in m. All quantities are time averaged and boundary layers have been removed.

broadly similar to those at $Ra = 2.07Ra_c$ (Fig. 5.11) but the inertial force has increased slightly in both l and m, due to the increase in Ra. This is to be expected as increasing the Rayleigh number creates a more turbulent flow, driven by the non-linear inertial term. The turbulent behaviour can also be observed from the plots of the flow and magnetic field (Figs 5.16c, 5.17c and 5.18c) where more modes are excited so more small scale structures are observed.

Figure 5.14 shows the forces for a fluctuating multipolar run at $E = 10^{-4}$, $Pm = 1$ and $Ra = 30Ra_c$. The hierarchy of forces between l and m are similar. A zeroth order geostrophic balance occurs at large scales followed by a first order balance between buoyancy, inertial and ageostrophic Coriolis forces. The Lorentz and viscous forces remain weak throughout. This balance is similar to the strong field dipolar case but the inertial and Lorentz forces have switched, with the inertial force now controlling the behaviour for this multipolar run. The

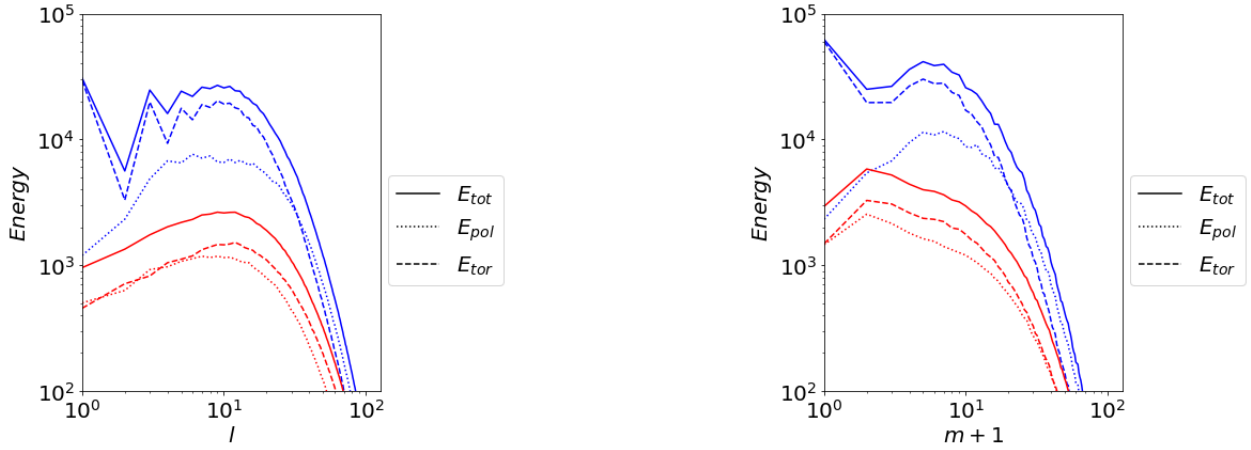

(a) (b)

Figure 5.15: Energy spectrum for fluctuating multipolar run at $E = 10^{-4}$, $Pm = 1$ and $Ra = 30Ra_c$. Blue and red lines represent kinetic and magnetic energy respectively. (a) energy spectrum in l (b) energy spectrum in m. All quantities are time averaged.

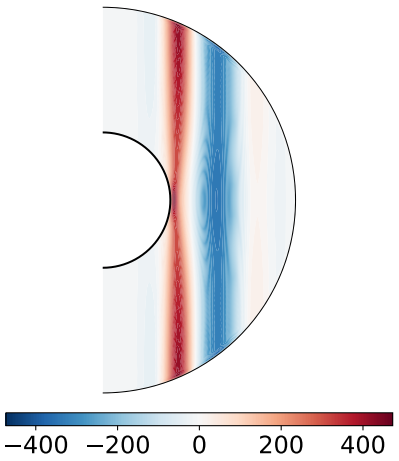

(a) WD at $E = 10^{-4}$, $Ra = 2.07Ra_c$ and $Pm = 12$

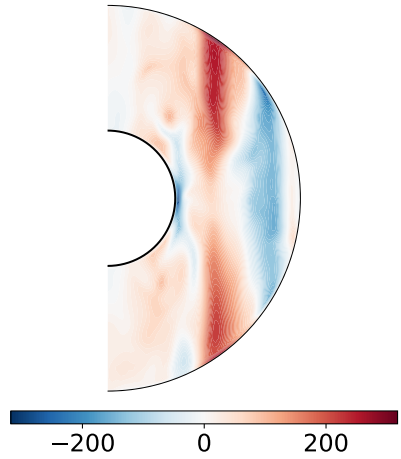

(b) SD at $E = 10^{-4}$, $Ra = 2.07Ra_c$ and $Pm = 12$

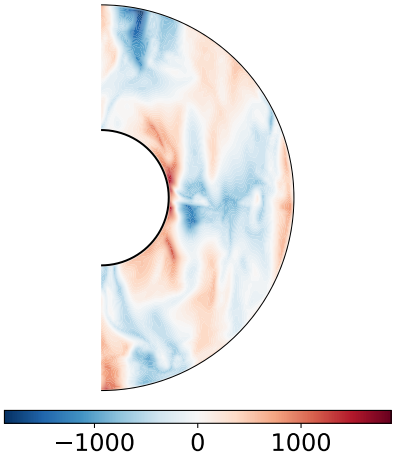

(c) SD at $E = 10^{-4}$, $Ra = 10Ra_c$ and $Pm = 12$

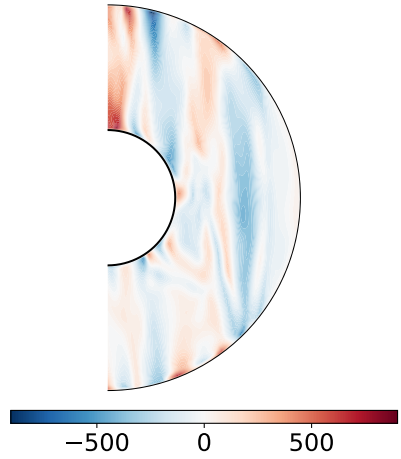

(d) FM at $E = 10^{-4}$, $Ra = 30Ra_c$ and $Pm = 1$

Figure 5.16: Meridional sections of u_ϕ. All plots are ϕ averaged.

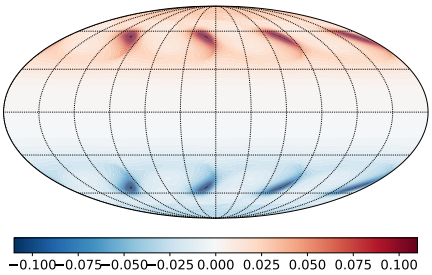

(a) WD at $E-10^{-4}$, $Ra = 2.07Ra_c$ and $Pm = 12$

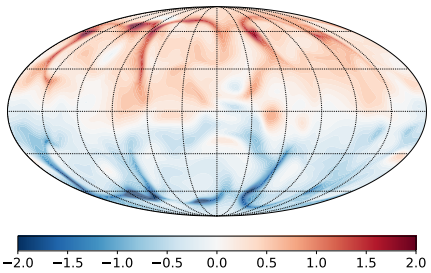

(b) SD at $E = 10^{-4}$, $Ra = 2.07Ra_c$ and $Pm = 12$

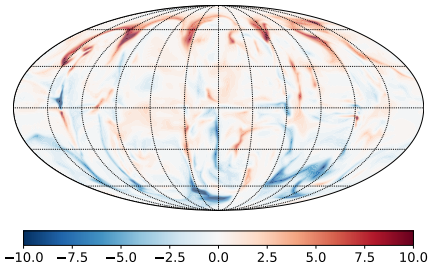

(c) SD at $E = 10^{-4}$, $Ra = 10Ra_c$ and $Pm = 12$

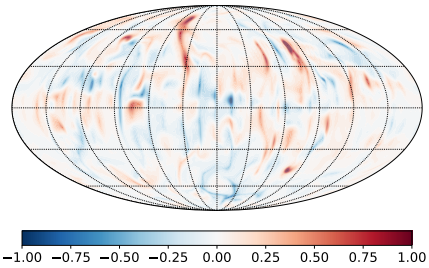

(d) FM at $E = 10^{-4}$, $Ra = 30Ra_c$ and $Pm = 1$

Figure 5.17: Spherical surface plots of B_r at $r = r_o$.

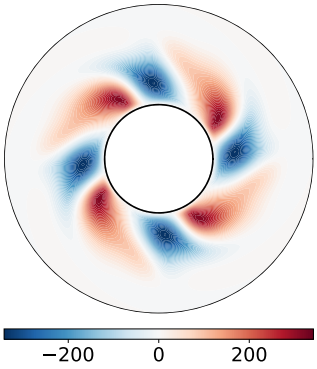

(a) WD at $E = 10^{-4}$, $Ra = 2.07Ra_c$ and $Pm = 12$

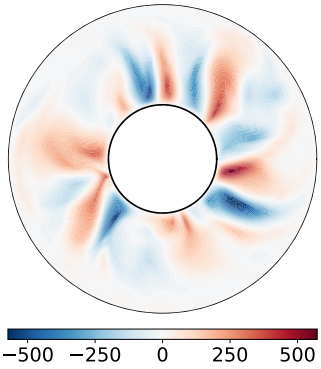

(b) SD at $E = 10^{-4}$, $Ra = 2.07Ra_c$ and $Pm = 12$

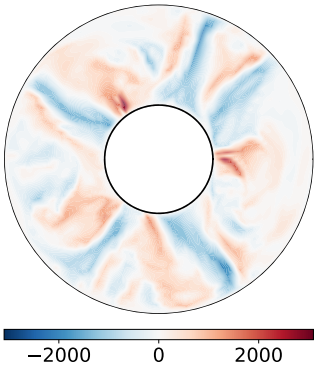

(c) SD at $E = 10^{-4}$, $Ra = 20Ra_c$ and $Pm = 12$

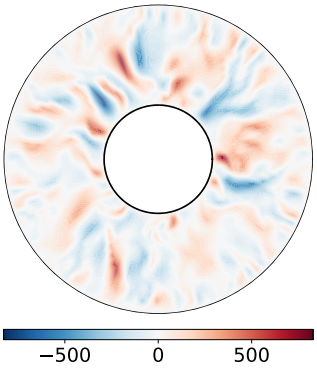

(d) FM at $E = 10^{-4}$, $Ra = 30Ra_c$ and $Pm = 1$

Figure 5.18: Equatorial sections of u_r.

energy spectra show similar results to the strong field dipolar runs and hydrodynamical runs at larger Ra where in l-space the toroidal part of the kinetic energy has similar behaviour to the total energy but the poloidal energy curve has a different shape and peaks at a different

l (Fig. 5.15a). In m-space the poloidal kinetic energy is smaller than the toroidal kinetic energy but both curves have a similar shape to the total energy spectrum (Fig. 5.15b). The magnetic energy is now smaller than the kinetic energy indicating that the magnetic field is much weaker in the multipolar regime (Fig. 5.15) compared to the strong dipolar regime (Fig. 5.12). The multipolar nature of this run can be observed from the spherical surface plot of B_r (Fig. 5.17d) where blue and red patches appear in approximately equal density at both sides of the equator. This multipolar solution is found due to the increase in Rayleigh number combined with decreasing magnetic Prandtl number. The flow patterns found for the fluctuating multipolar run (Figs 5.16d, 5.18d) are similar to the hydrodynamical run at high Ra. This is to be expected as the force balances are similar, with the main difference being the addition of the weak Lorentz force for the dynamo run in the multipolar regime.

5.1.3 DYNAMO SOLUTIONS AT $E = 10^{-5}$

Simulations at $E = 10^{-5}$ are presented, to ensure similar balances persist as the rotation rate is increased. The results match well to those found at $E = 10^{-4}$ where both the hierarchy of l and m are similar and the balances in each regime at $E = 10^{-5}$ match well when comparing to $E = 10^{-4}$.

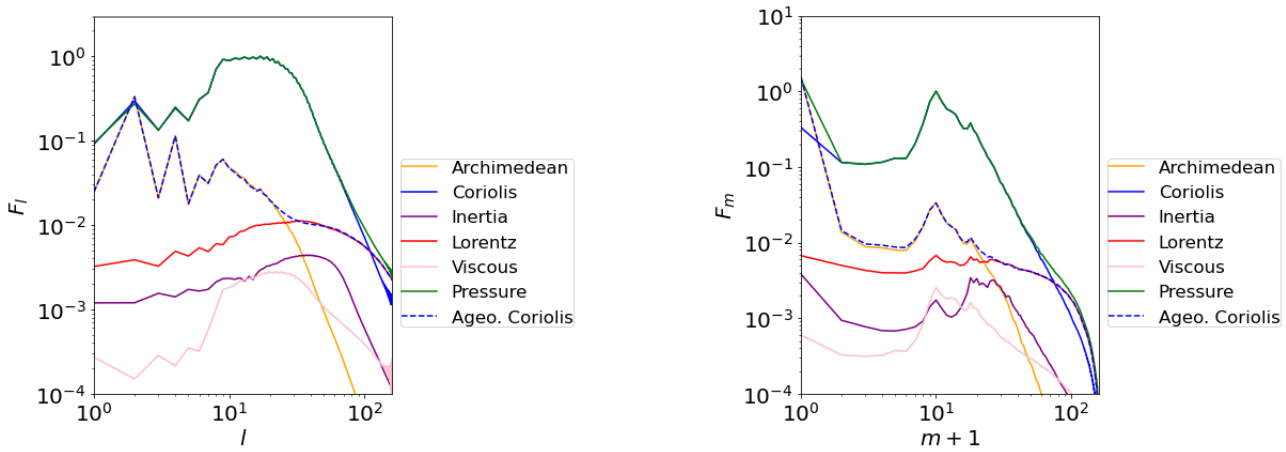

(a) (b)

Figure 5.19: Comparison of forces for weak field dipolar run at $E = 10^{-5}$, $Pm = 5$ and $Ra = 3Ra_c$. (a) forces in l, (b) forces in m. All quantities are time averaged and boundary layers have been removed.

Figure 5.19 shows the forces in l and m for a weak field dipolar case. In both cases a zeroth order geostrophic balance occurs and at first order a balance is found between buoyancy and ageostrophic Coriolis forces at large scales. The Lorentz, inertial and viscous forces remain small. The Lorentz force is larger than the inertial and viscous forces at $E = 10^{-5}$ which was not the case at $E = 10^{-4}$ and is most likely because of the larger Ra/Ra_c. However it still remains small and only enters the main balance at the smallest scales, similar to the case at $E = 10^{-4}$. The results for a strong field dipolar solution show a zeroth order geostrophic balance and at first order a balance between buoyancy, Lorentz and ageostrophic Coriolis forces occurs

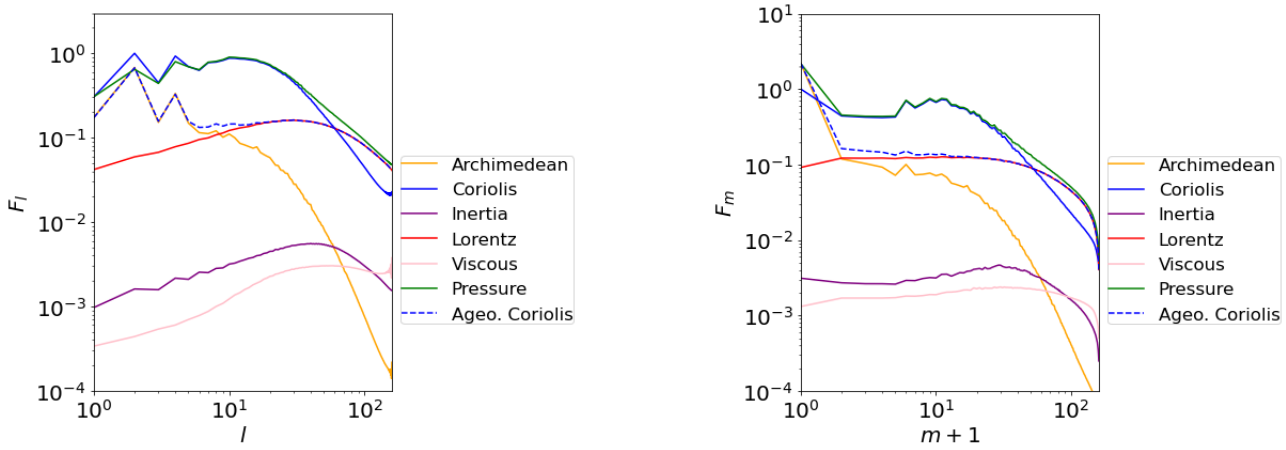

(a) (b)

Figure 5.20: Comparison of forces for strong field dipolar run at $E = 10^{-5}$, $Pm = 5$ and $Ra = 4Ra_c$. (a) forces in l, (b) forces in m. All quantities are time averaged and boundary layers have been removed.

at large scales (Fig. 5.20). The Lorentz force enters the zeroth order balance at small scales. This is similar to the results found at $E = 10^{-4}$. The dipolar magnetic field for both runs is clear from the plots of B_r (Figs 5.23a, 5.23b) where there is a clear divide of red and blue across the equator. The radial velocity for both runs is similar to those at $E = 10^{-4}$ where the flow is similar to the onset state in the sense that convection is still only localised near the TC in the weak dipolar case (Fig. 5.24a). It then becomes more chaotic for the strong dipolar case (Fig. 5.24b). The size of the structures become smaller at $E = 10^{-5}$ compared with $E = 10^{-4}$ and can be seen by comparing Figure 5.16 with Figure 5.22 and Figure 5.18 with Figure 5.24.

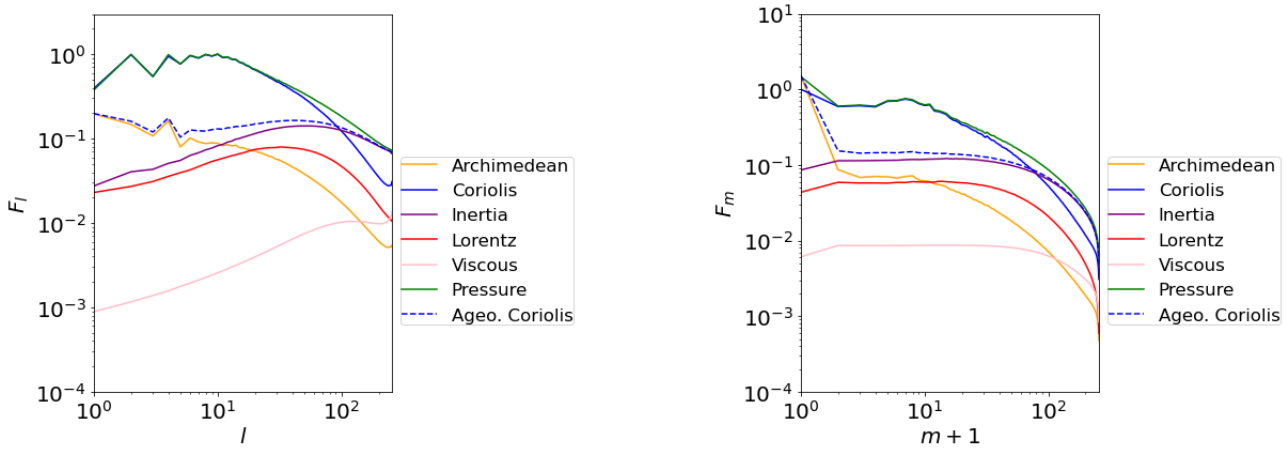

(a) (b)

Figure 5.21: Comparison of forces for a fluctuating multipolar run at $E = 10^{-5}$, $Pm = 0.2$ and $Ra = 100Ra_c$. (a) forces in l, (b) forces in m. All quantities are time averaged and boundary layers have been removed.

The forces for a fluctuating multipolar run are shown in Figure 5.21. The hierarchy of forces in l and m are similar where a zeroth order geostrophic balance occurs followed by a first order balance between buoyancy, ageostrophic Coriolis and inertial forces. These results are

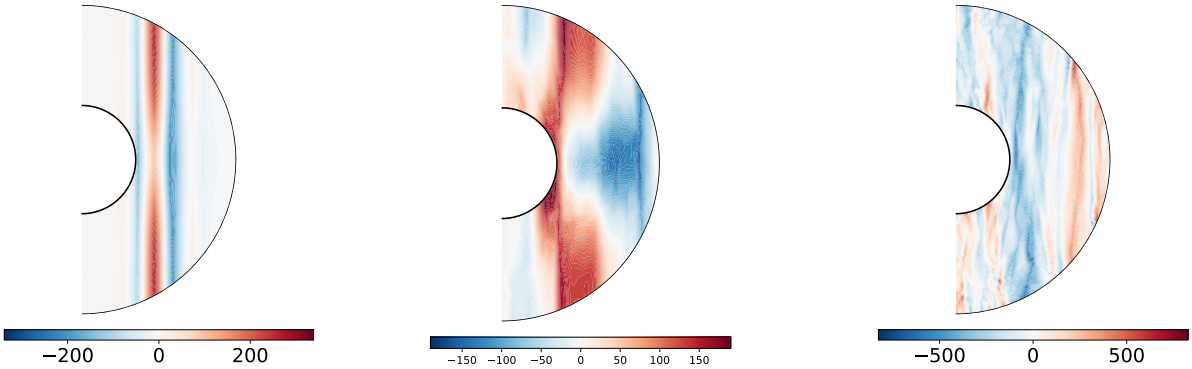

(a) WD at $E = 10^{-5}$, $Ra = 3Ra_c$ and $Pm = 5$ (b) SD at $E = 10^{-5}$, $Ra = 4Ra_c$ and $Pm = 5$ (c) Fm at $E = 10^{-5}$, $Ra = 100Ra_c$ and $Pm = 0.2$

Figure 5.22: Meridional sections of u_ϕ. All plots are ϕ averaged.

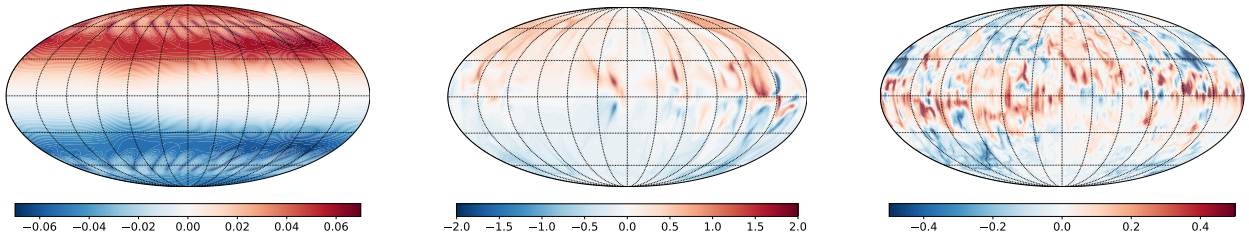

(a) WD at $E = 10^{-5}$, $Ra = 3Ra_c$ and $Pm = 5$ (b) SD at $E = 10^{-5}$, $Ra = 4Ra_c$ and $Pm = 5$ (c) FM at $E = 10^{-5}$, $Ra = 100Ra_c$ and $Pm = 0.2$

Figure 5.23: Spherical surface plots of B_r at $r = r_o$.

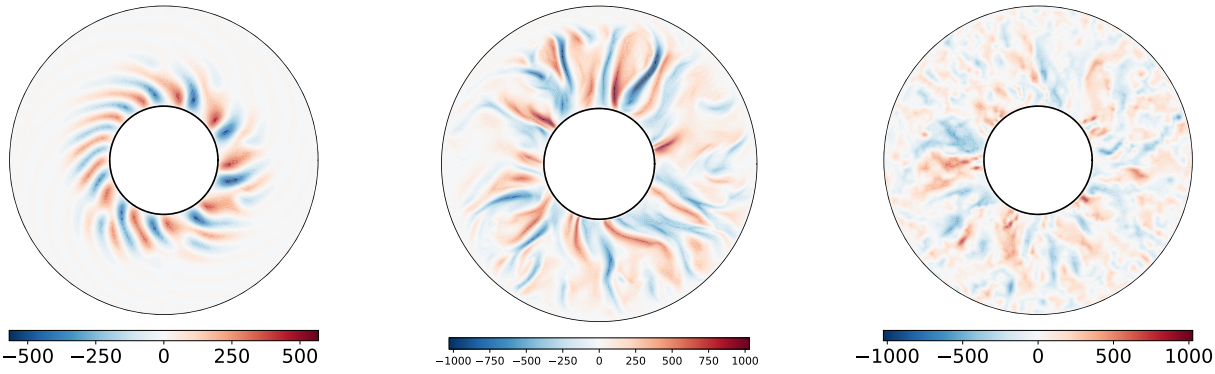

(a) WD at $E = 10^{-5}$, $Ra = 3Ra_c$ and $Pm = 5$ (b) SD at $E = 10^{-5}$, $Ra = 3Ra_c$ and $Pm = 5$ (c) FM at $E = 10^{-5}$, $Ra = 100Ra_c$ and $Pm = 0.2$

Figure 5.24: Equatorial section of u_r.

similar to the fluctuating multipolar case at $E = 10^{-4}$ (Fig. 5.14). Fluctuating multipolar runs are obtained by increasing Ra (at fixed low enough, Pm). As the Ekman number decreases, multipolar runs are harder to obtain. This was discussed in Section 1.5.2 where regime diagrams demonstrated that lowering the Ekman number moves onset of the multipolar regime to larger values of Ra, which makes the fluctuating multipolar regime harder to obtain numerically (Fig. 1.4). Hence, the value of Ra has increased so $Ra = 100Ra_c$ and Pm is decreased to $Pm = 0.2$. The multipolar behaviour of the magnetic field is shown in Figure 5.23c, where red and blue patches appear at both sides of the equator. The azimuthal wavenumber has increased (Fig.

5.24c) compared with the weak and strong field dipolar case (Figs 5.24a, 5.24b).

Overall, the forces in the three main regimes of dynamo action display similar results between $E = 10^{-4}$ and $E = 10^{-5}$. The lengthscale dependence of forces in l were discussed and compared with new results examining the m-dependence of forces. The m-dependence show good agreement with the l-dependence where the hierarchy of forces remain similar. Therefore the forces and their hierarchy are not highly dependent on whether a representation in l or m is used. Hence, either representation (l or m) can be used in further analysis. There are small differences between the force spectra in l and m which are important for further analysis in Section 5.3. The strong field dipolar runs (Figs. 5.11, 5.13) in l-space have scales where certain forces are in balance and cross each other. Figure 5.11a has clear crossing points of Lorentz and buoyancy forces and ageostrophic Coriolis and buoyancy forces. In m-space crossing points for Lorentz and ageostrophic Coriolis forces occur but the crossover of buoyancy and Lorentz forces occurs at $m = 1$ as a result of activity in the $m = 0$ mode, which is not representative in the same way as the crossing in l-space. This is also the case for the multipolar run, where in l-space (Fig. 5.14a) we can obtain crossing points of buoyancy and inertial forces but in m-space the crossing occurs at $m = 1$ (Fig. 5.14b).

5.2 Comparison of curls of forces

The curls of forces in l and m are now examined. As mentioned previously, Teed and Dormy (2023) demonstrated that taking the curl of each force provided a clearer view of the force balances, as this removed the large pressure gradient which does not impact the flow dynamics. Their study showed that taking the curl recovered the relevant force balance at leading order. Here, similar results to their study are presented by discussing the l-dependence of curls of forces, and new results are introduced by examining the m-dependence. The curls of forces in l and m are compared with each other, and the curls of forces are compared to the force balances presented in the previous section.

5.2.1 Hydrodynamical solutions at $E = 10^{-4}$

Figures 5.25 - 5.27 show the curls of forces for the same runs presented in Section 5.1.1. At $Ra = 2Ra_c$ the lengthscale dependence in l (Fig. 5.25a) shows a leading order balance at large scales between Coriolis and buoyancy forces. The viscous force also enters this balance at a wide range of scales to form a VAC balance. In m the hierarchy of forces remain similar to l, but the curves become smaller much sooner in m than in l. Taking the curl has allowed us to retrieve the relevant balance at leading order which was not possible when examining the forces, as the geostrophic balance usually occurred at leading order (Fig. 5.1a).

At $Ra = 5Ra_c$, the lengthscale dependence in l shows a first order balance between Coriolis and buoyancy forces at large scales (Fig. 5.26a) and at smaller scales the inertial and viscous forces break this and these forces now form the first order balance. Similar behaviour is observed for

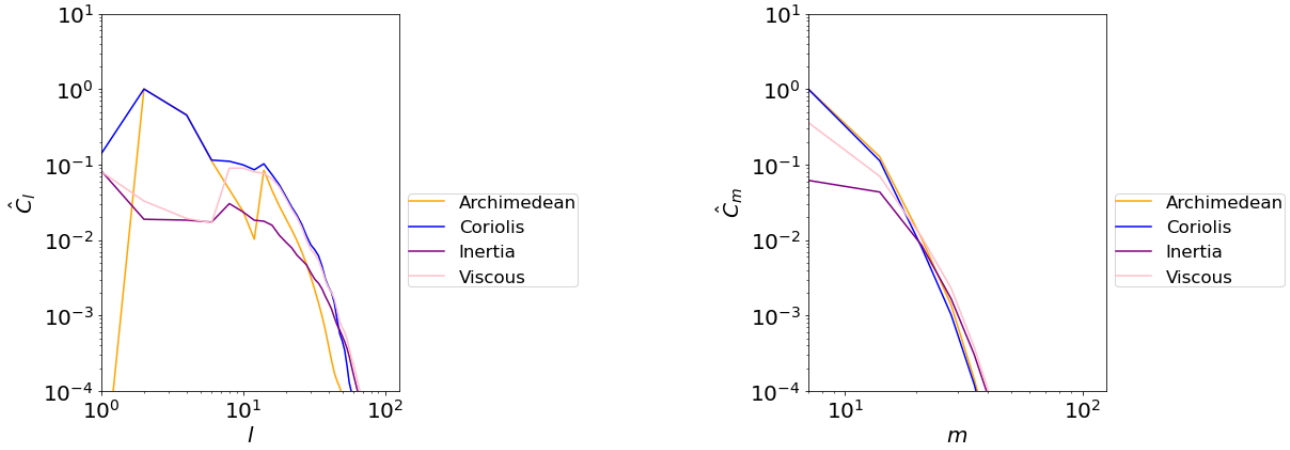

(a) (b)

Figure 5.25: Comparison of curl of forces for a HD run at $E = 10^{-4}$ and $Ra = 2Ra_c$. (a) curl of forces in l (modes with l odd removed), (b) curl of forces in m (every $7m$ plotted). All quantities are time averaged and boundary layers have been removed.

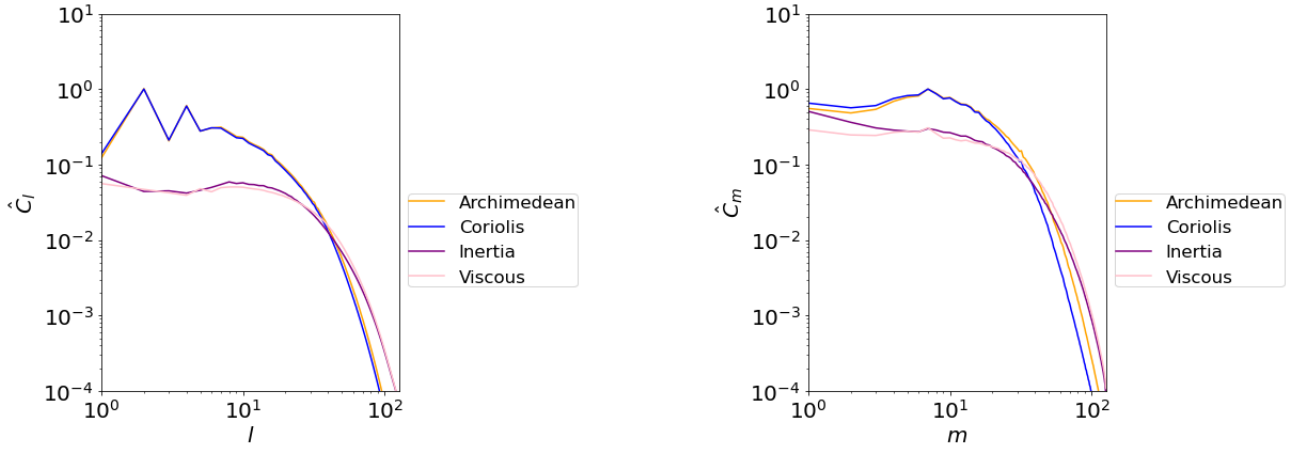

(a) (b)

Figure 5.26: Comparison of curl of forces for a HD run at $E = 10^{-4}$ and $Ra = 5Ra_c$. (a) curl of forces in l, (b) curl of forces in m. All quantities are time averaged and boundary layers have been removed.

the curls in m, where the hierarchy of forces remains similar between l and m but there is an increase in the inertial and viscous terms at large scales and the curl of forces are smoother in m (Fig. 5.26b) than in l (Fig. 5.26a).

At $Ra = 30Ra_c$, the system transitions to an inertially dominated run. In l, the Coriolis and inertial terms are in balance at small scales, with the Coriolis term dropping off at larger scales (Fig. 5.27a). In m a similar balance occurs, but the Coriolis term does not balance the inertia term at any scale and instead the inertial term remains dominant throughout (Fig. 5.27b). In all cases, taking the curl has allowed the relevant balance to be obtained at leading order. This was not possible for the forces as a zeroth order geostrophic balance occurs at least at large scales.

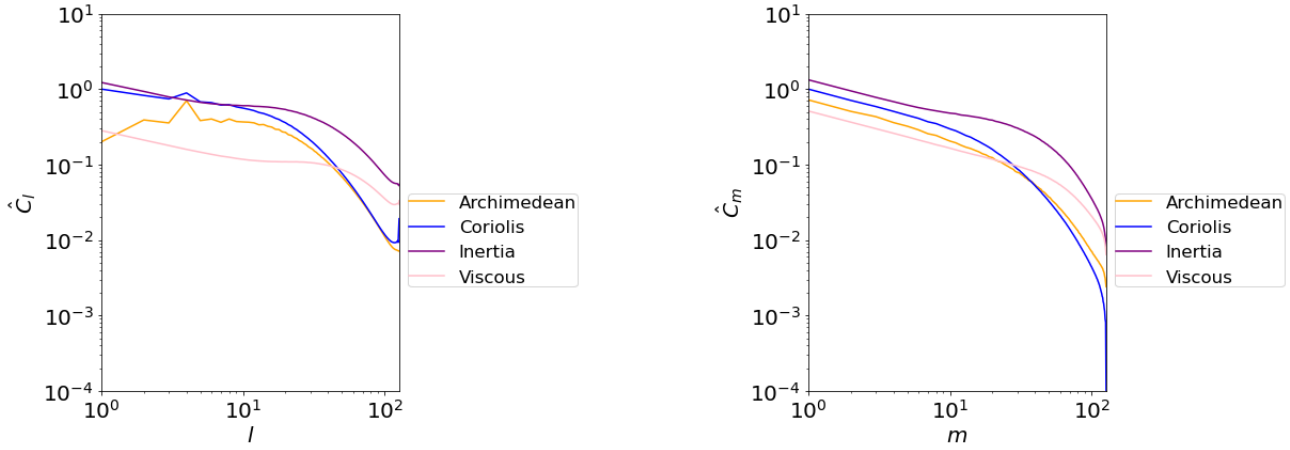

(a) (b)

Figure 5.27: Comparison of curl of forces for a HD run at $E = 10^{-4}$ and $Ra = 30Ra_c$. (a) curl of forces in l, (b) curl of forces in m. All quantities are time averaged and boundary layers have been removed.

5.2.2 DYNAMO SOLUTIONS AT $E = 10^{-4}$

Curls of forces are presented for the same runs discussed in Section 5.1.2. The weak field dipolar case at $Ra = 2.07Ra_c$ shows a first order balance between Coriolis and buoyancy terms in l with the viscous term also entering the balance for a wide range of scales (Fig. 5.28a). In m, the same balance occurs but is only present at large scales before dropping off (Fig. 5.28b). At small scales the main balance is between the Lorentz and viscous terms. This behaviour is similar to the hydrodynamical case at low Ra (albeit with the addition of a weak Lorentz force) and again confirms that the weak field dipolar case behaves like a weakly magnetically adjusted hydrodynamical run. For the strong field dipolar case also at $Ra = 2.07Ra_c$, a triple balance between Coriolis, buoyancy and Lorentz terms occurs in l at large scales and at small scales the buoyancy drops off leaving a balance between Coriolis and Lorentz terms (Fig. 5.29a). In m, the buoyancy contribution is strong but does not reach the same magnitude as the Coriolis and Lorentz terms to be included in the main balance at any scale (Fig. 5.29b). As a result of this, a crossing point between Lorentz and buoyancy terms cannot be defined. This will be discussed in more detail in Section 5.3. A slight increase in the viscous term is also observed in m, and the inertial contribution remains weak throughout.

Figure 5.30 shows the curls of forces for another strong dipolar run where the supercriticality has been increased to $Ra = 10Ra_c$. The curls in l behave similarly to those at $Ra = 2.07Ra_c$ where a MAC balance occurs at large scales and then the buoyancy decreases at smaller scales. An increase in the inertial term occurs, which is to be expected as the Rayleigh number has increased. The lengthscale dependence of the curls in m behave differently to l. Like the run at $2.07Ra_c$, a balance between Coriolis and Lorentz terms occurs with the buoyancy contribution never quite entering the main balance. However, the viscous term is now larger than the buoyancy term and this remains the case throughout, which did not occur at lower Ra (Fig. 5.29b). The viscous and Lorentz terms balance at small scales, similar to lower Ra.

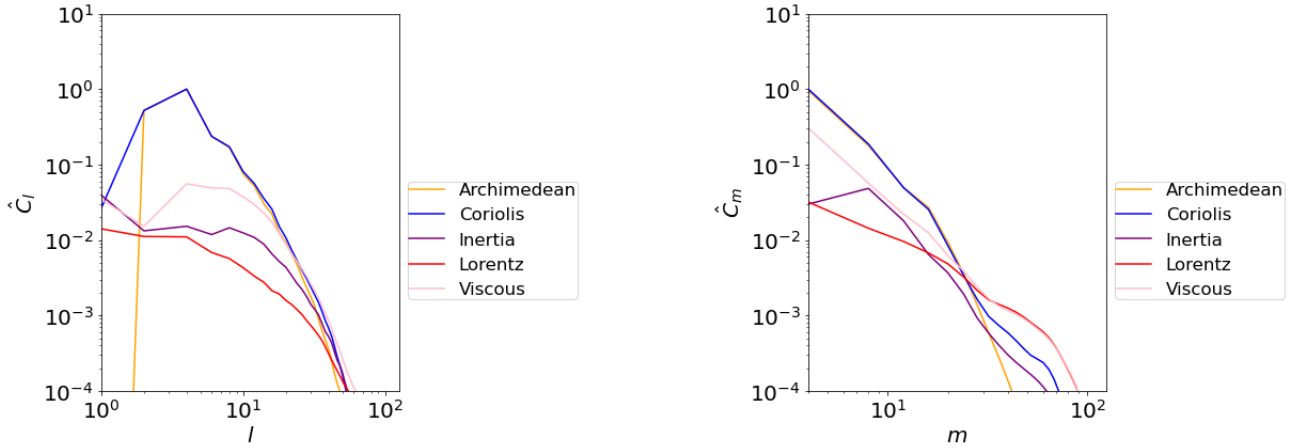

(a) (b)

Figure 5.28: Curl of forces for weak field dipolar case at $E = 10^{-4}$, $Pm = 12$ and $Ra = 2.07Ra_c$. (a) curl of forces in l (modes with l odd removed), (b) curl of forces in m (every $4m$ plotted). All quantities are time averaged and boundary layers have been removed.

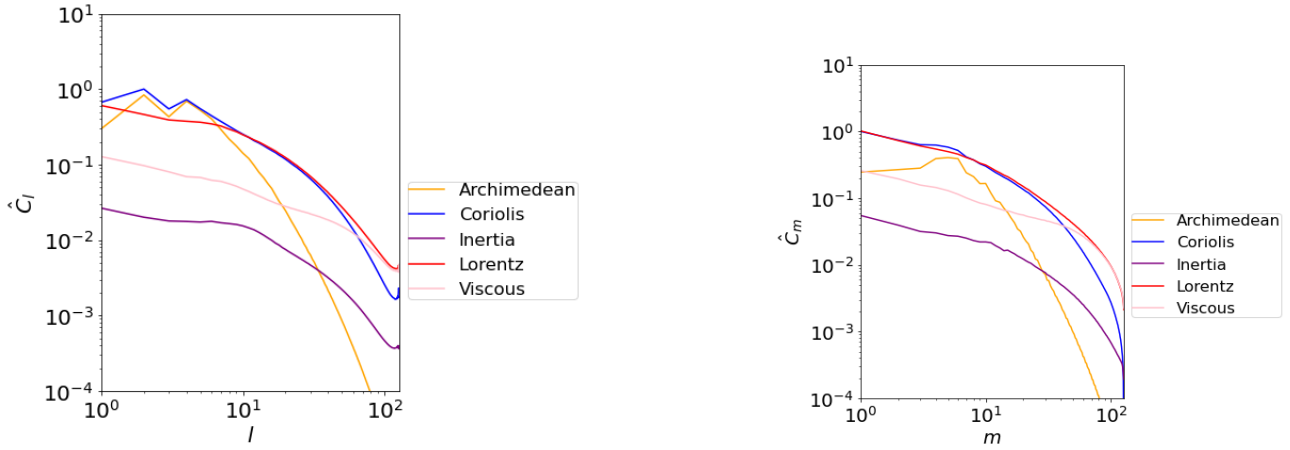

(a) (b)

Figure 5.29: Curl of forces for strong field dipolar case at $E = 10^{-4}$, $Pm = 12$ and $Ra = 2.07Ra_c$. (a) curl of forces in l, (b) curl of forces in m. All quantities are time averaged and boundary layers have been removed.

Figure 5.31 shows the curl of forces for a fluctuating multipolar run at $E = 10^{-4}$, $Pm = 1$ and $Ra = 30Ra_c$. The curls in l show a balance between Coriolis and inertial terms, and the buoyancy force also enters this main balance at some scales. In m, the inertial term is dominant throughout and is balanced by the Coriolis term at large scales. The buoyancy contribution is also strong but never enters the main balance, which is similar to the strong field dipolar runs.

In all cases, both the l and m dependence provide a similar representation of the forces controlling the system. We are able to recover the relevant force balances in the different regimes at leading order, as we have removed the pressure gradient by taking the curl. In the weak field dipolar case we obtain a balance between buoyancy and Coriolis terms, with the viscous term becoming important at a wide range of scales in both l and m. The strong field case displays a MAC balance in l at larger scales with the buoyancy term dropping off at smaller scales.

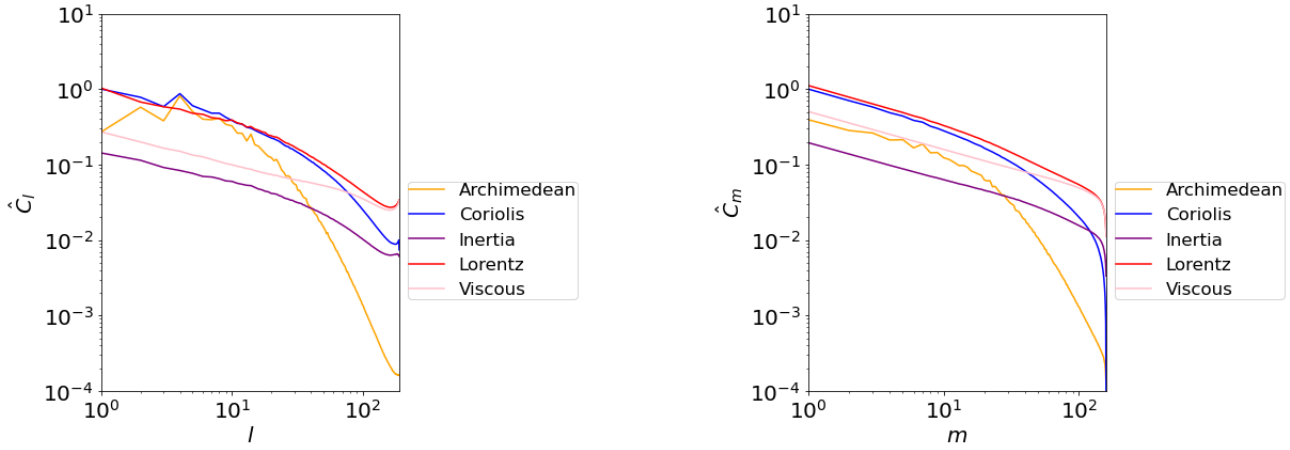

(a) (b)

Figure 5.30: Curl of forces for strong field dipolar case at $E = 10^{-4}$, $Pm = 12$ and $Ra = 10Ra_c$. (a) curl of forces in l, (b) curl of forces in m. All quantities are time averaged and boundary layers have been removed.

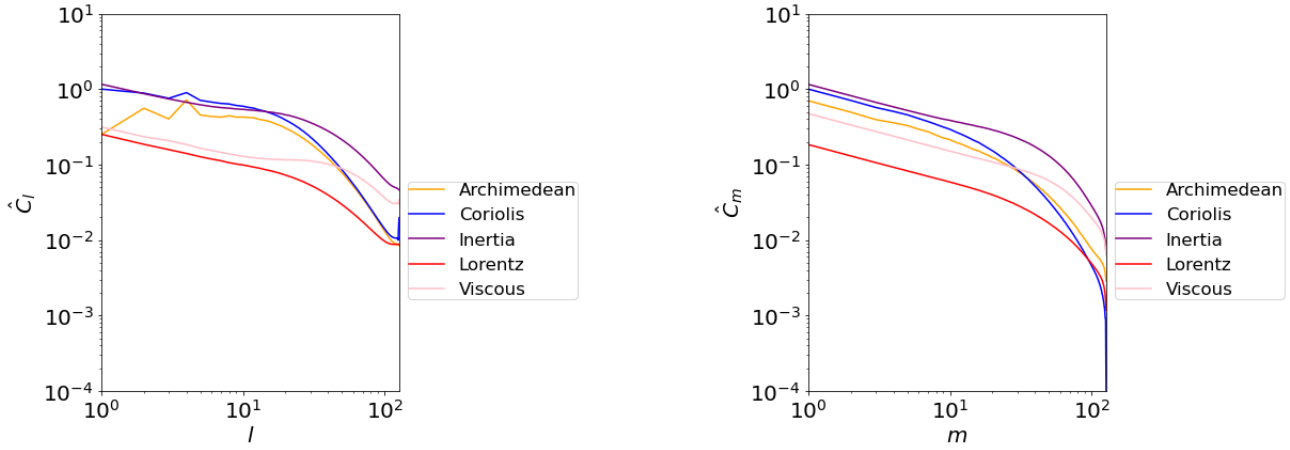

(a) (b)

Figure 5.31: Curl of forces for the multipolar case at $E = 10^{-4}$, $Pm = 1$ and $Ra = 30Ra_c$. (a) curl of forces in l, (b) curl of forces in m. All quantities are time averaged and boundary layers have been removed.

The m-dependence also shows the importance of the Coriolis, buoyancy and Lorentz terms but the buoyancy does not quite enter the main balance with Coriolis and Lorentz terms at any scales. However, both l and m show that the MAC contributions control the dynamics of the flow. The multipolar regime shows similar results where a CIA balance is important in l and m although the buoyancy never enters the main balance with Coriolis and inertial terms in m.

5.2.3 DYNAMO SOLUTIONS AT $E = 10^{-5}$

The curls of forces are presented for the same runs discussed in Section 5.1.3. The weak field dipolar case at $E = 10^{-5}$ (Fig. 5.32) is similar to the run at $E = 10^{-4}$ (Fig. 5.28) although the Lorentz term is larger than the viscous term at $E = 10^{-5}$, most likely due to the larger Ra/Ra_c. The strong field dipolar runs at $E = 10^{-4}$ (Fig. 5.29) and $E = 10^{-5}$ (Fig. 5.33) are also similar

where a MAC balance occurs in l at large scales and transitions to a balance between Coriolis and Lorentz terms at small scales. In m a MAC balance is found, but similarly to $E = 10^{-4}$, the buoyancy contribution never quite enters the main balance with the Lorentz and buoyancy terms.

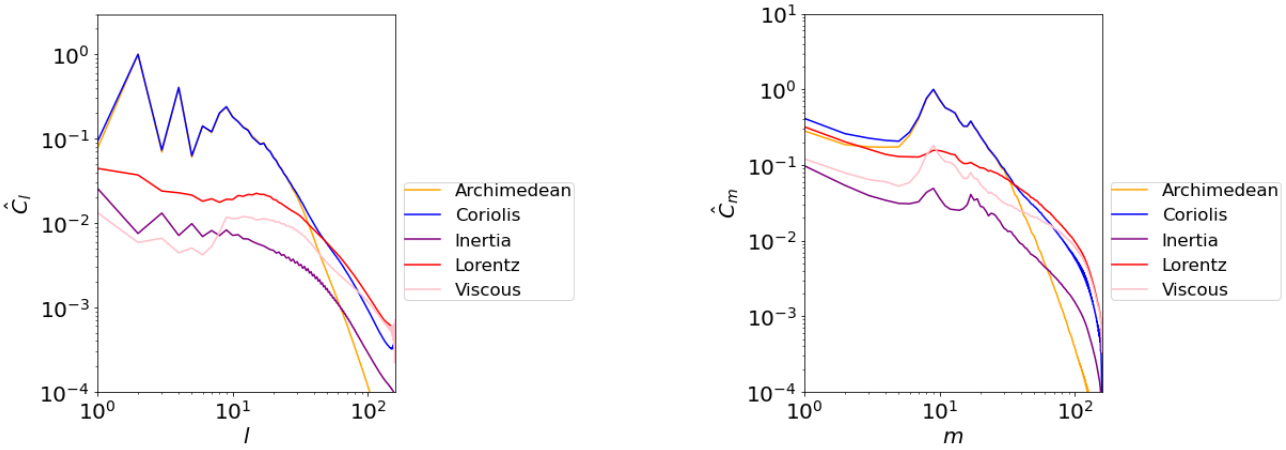

(a) (b)

Figure 5.32: Curl of forces for weak field dipolar run at $E = 10^{-5}$, $Pm = 5$ and $Ra = 3Ra_c$. (a) forces in l, (b) forces in m. All quantities are time averaged and boundary layers have been removed.

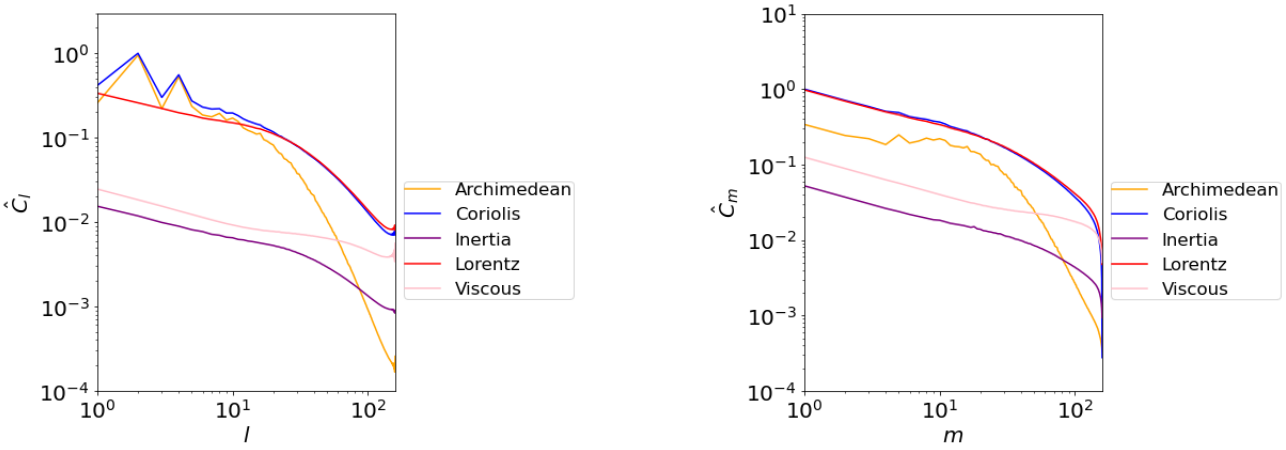

(a) (b)

Figure 5.33: Curl of forces for strong field dipolar run at $E = 10^{-5}$, $Pm = 5$ and $Ra = 4Ra_c$. (a) curl of forces in l, (b) curl of forces in m. All quantities are time averaged and boundary layers have been removed.

For the multipolar case (fig. 5.34), the inertial term is dominant throughout in l and m. In l, the inertial term dominates across all lengthscales and the Coriolis force is also strong but never reaches the same magnitude as the inertial force. This differs to the multipolar run at $E = 10^{-4}$ (Fig. 5.31a) where the inertial force was dominant across all lengthscales but was balanced by the Coriolis force at larger scales. This is due to the stronger driving at $E = 10^{-5}$. In m, the inertial term is strong throughout, and the Coriolis term is also strong but never enters the main balance. Again, like other runs, an increase in the viscous contribution is observed in m compared with l.

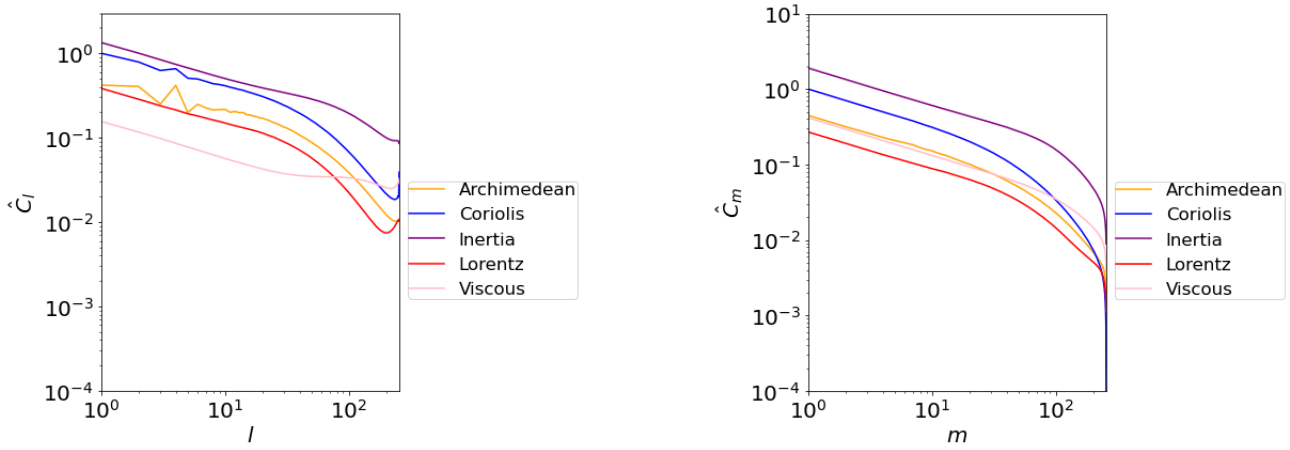

(a) (b)

Figure 5.34: Curl of forces for a multipolar run at $E = 10^{-5}$, $Pm = 0.2$ and $Ra = 100Ra_c$. (a) curl of forces in l, (b) curl of forces in m. All quantities are time averaged and boundary layers have been removed.

There are subtle differences between the curl spectra in l and m which are important for further analysis in the next section. For the strong field dipolar runs (Figs 5.29, 5.30) in l there are scales at which certain curls of forces are in balance and cross each other. For example, Figure 5.29a has a clear crossing point between Lorentz and buoyancy terms and Coriolis and buoyancy terms. However, in m, there are no clear crossing points of Lorentz and buoyancy or Coriolis and buoyancy terms (Fig. 5.29b). The run displays a solution typical of those in a MAC regime but the buoyancy never balances the Coriolis or Lorentz terms at any scale. This tends to be the case when examining the m-dependent curls of forces. Figure 5.31 displays similar results where an inertially dominated solution is obtained and the l dependence shows clear crossovers and balances of Coriolis, inertial and buoyancy terms. In m a combination of Coriolis, inertial and buoyancy terms are also controlling the dynamics. However, there are no clear crossing points of Coriolis, inertial and buoyancy terms or scales at which two or three of these terms are completely in balance.

5.3 Relating flow lengthscales to triple force balances

Studies by Schwaiger et al. (2019, 2021) have related flow lengthscales to force balances by considering the crossover points of relevant forces in simulations. In order to do this, they considered the poloidal kinetic energy spectrum in l and the spectra of forces in l, taking the peak of the poloidal kinetic energy and comparing this with the crossing points of different forces. For magnetically dominated runs they considered the crossover point between Lorentz and buoyancy forces, and in non-magnetic runs with large Ra which are dominated by the inertial force they considered the crossover point between inertia and buoyancy. They were able to relate the dynamically relevant lengthscales (crossover points) to the energetically relevant lengthscales (poloidal energy peaks). They also examined crossover points of viscous and buoyancy forces but were unable to relate these to the energetically relevant lengthscales, most

likely because the boundary layers have been removed in the simulations examined. Only runs which have a clear crossover point of relevant forces were considered and other simulations which do not have clear crossover points were ignored, which leaves open the question of how the dynamic lengthscales are set in such solutions.

Simulations without crossover points are still important and should be considered in the analysis. In our previous analysis we discussed l and m-dependence of forces and curls of forces, where some of our simulations do not contain clear crossover points, especially in m. It should also be noted that Schwaiger et al. (2019, 2021) only consider two of the three relevant forces in each regime. In the non-magnetic runs at large enough Ra, only the inertial and buoyancy forces are considered and for magnetically dominated runs the Lorentz and buoyancy forces are considered when examining the dynamically relevant lengthscales. However, it is clear from the analysis discussed in the previous section and studies by Aubert et al. (2017), Schwaiger et al. (2019) and Teed and Dormy (2023) that the Coriolis term is also important in the main balance and impacts the flow dynamics. Therefore, the triple balance of forces could be considered to obtain a dynamically relevant lengthscale.

We wish to relate both the forces and curls of forces to the flow lengthscales in l and m in our simulations. Clear crossover points of the dominant forces occur in some of the runs discussed in the previous section but not all. In m especially, crossing points do not occur for the majority of runs. Instead, we can construct a triple balance point for the three different regimes of dynamo action. For the strong field dipolar case a balance between Coriolis, Lorentz and buoyancy terms (MAC) is considered, for the multipolar case a balance between Coriolis, inertia and buoyancy (CIA) terms is considered, and for the weak field dipolar case a balance between viscous, Coriolis and buoyancy (VAC) terms is considered. We also include non-magnetic runs to compare with Schwaiger et al. (2021). In this chapter, the work of Schwaiger et al. (2021) is extended in four key ways:

1. Examine the crossover points in m-space.
2. Examine the crossover points of curls of forces in l-space and m-space.
3. Introduce a new dynamically relevant lengthscale by forming a triple balance point which can be compared to energetically relevant lengthscales.
4. Separate runs based on dynamo branch.

Runs at $10^{-5} \leq E \leq 3 \times 10^{-4}$ are considered and are categorised by separating solutions into the three main regimes of dynamo action. Hydrodynamical runs are also separated based on Rayleigh number by considering those with $Ra < 20Ra_c$ and those with $Ra \geq 20Ra_c$. This was chosen by examining the force balances where runs with $Ra < 20Ra_c$ mainly lie in a VAC balance and those with $Ra \geq 20Ra_c$ mainly lie in a CIA balance, allowing us to approximate a distinction between runs in a CIA balance and those in a VAC balance.

5.3.1 CROSSOVERS

We begin by analysing our simulations using the method by Schwaiger et al. (2021) and doing similar for m and for curls of forces. Schwaiger et al. (2021) define the crossover points between the forces in l as

$$l_{MA} = \arg\min_l \left(|F_{M,l} - F_{A,l}|\right) \tag{5.1}$$

$$l_{IA} = \arg\min_l \left(|F_{I,l} - F_{A,l}|\right) \tag{5.2}$$

$$l_{VA} = \arg\min_l \left(|F_{V,l} - F_{A,l}|\right) \tag{5.3}$$

and to obtain a similar method for comparing the crossover points in m we define

$$m_{MA} = \arg\min_m \left(|F_{M,m} - F_{A,m}|\right) \tag{5.4}$$

$$m_{IA} = \arg\min_m \left(|F_{I,m} - F_{A,m}|\right) \tag{5.5}$$

$$m_{VA} = \arg\min_m \left(|F_{V,m} - F_{A,m}|\right), \tag{5.6}$$

where the notation $F_{A,l}$ and $F_{A,m}$ represents the value of the Archimedean force at l and m respectively, and likewise for the other forces. The formulae above are also applied to the curls of forces, but the definitions are not repeated for brevity. An example of an l_{MA} crossover is illustrated on Figure 5.11a. These crossover points are compared with the peaks in the total kinetic energy, poloidal kinetic energy and toroidal kinetic energy spectra in l and m denoted by l_{tot}, l_{pol} and l_{tor} and similar for m. We aim to find a correlation between peaks in the energy and crossover points to allow us to relate dynamically relevant lengthscales to energetically relevant lengthscales. Unlike Schwaiger et al. (2021), we include all of our runs, even those which do not have a well-defined crossover of forces. This means the largest l or m is extracted for runs without a well-defined crossover, as a result of the definitions of Equations (5.1)-(5.6). This occurs since the difference of the two forces being considered in (5.1)-(5.6) will be smallest at the largest l or m. Hence, we expect simulations without crossovers to cluster at the largest l and m in our plots.

For the forces in l, for multipolar runs and hydrodynamical runs at large enough Ra, our plots show that $l_{pol} \approx l_{IA}$ (Fig. 5.35b). Some of these runs also show a correlation with l_{tot} (Fig. 5.35a) and l_{tor} (Fig. 5.35c) but l_{pol} shows the best match. Similarly, for some runs on the strong field branch, there is a correlation between crossings in Lorentz and buoyancy forces and l_{pol} (Fig. 5.35e). Similar to l_{IA}, some of the strong field runs show a correlation between l_{MA} and l_{tot} (Fig. 5.35d) and l_{tor} (Fig. 5.35f) but l_{pol} provides the best match. For runs on the weak field branch and low Ra hydrodynamical runs, there is no correlation between l_{VA} and any of l_{tot}, l_{pol} or l_{tor} (Figs 5.35g, 5.35h, 5.35i). Crossover points of l_{VA} are always at a much larger scale than the peak of the flow. This could be due to removal of the boundary layers in our simulations, causing a reduction in the viscous force. These results match with Schwaiger

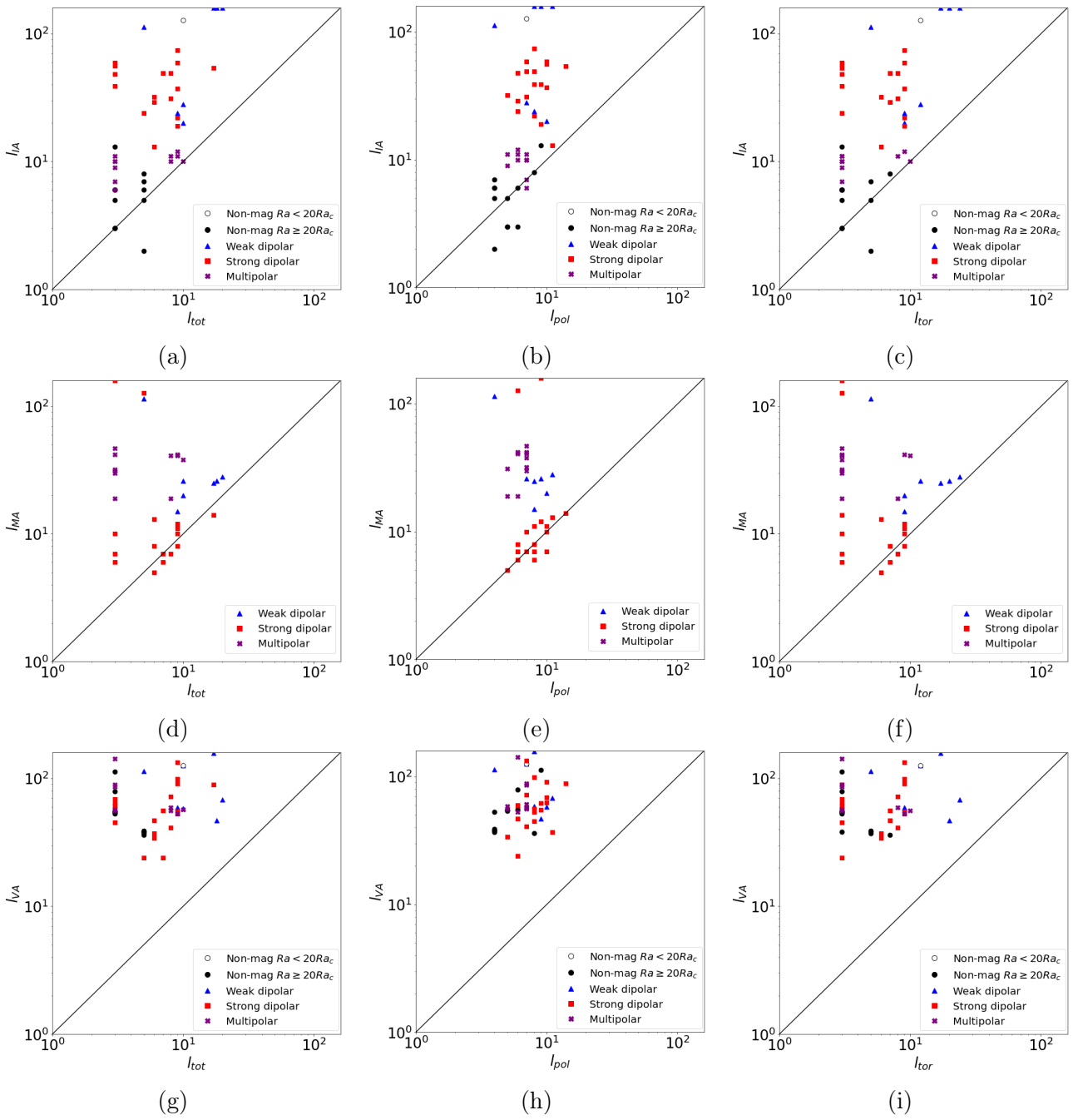

Figure 5.35: Crossover points of forces in l-space as a function of (a-c) IA crossover, (d-f) MA crossover and (g-i) VA crossover. Each column is for a different energetic lengthscale (l_{tot}, l_{pol} and l_{tor}).

et al. (2021) where they found that crossing points between Lorentz and buoyancy forces in magnetically dominated runs and crossing points between inertial and buoyancy forces in non-magnetic runs (at large enough Ra) matched well with l_{pol}. We have extended this work by including runs in the multipolar regime where the inertial force dominates and have found that these follow a similar pattern to the non-magnetic runs at large Ra, demonstrating the weak role of the magnetic field in the multipolar regime. Figures 5.35a, 5.35d and 5.35g are nearly identical to Figures 5.35c, 5.35f and 5.35i respectively, so it is clear that the total kinetic energy spectrum is controlled by the toroidal energy. The poloidal energy spectrum provides a better

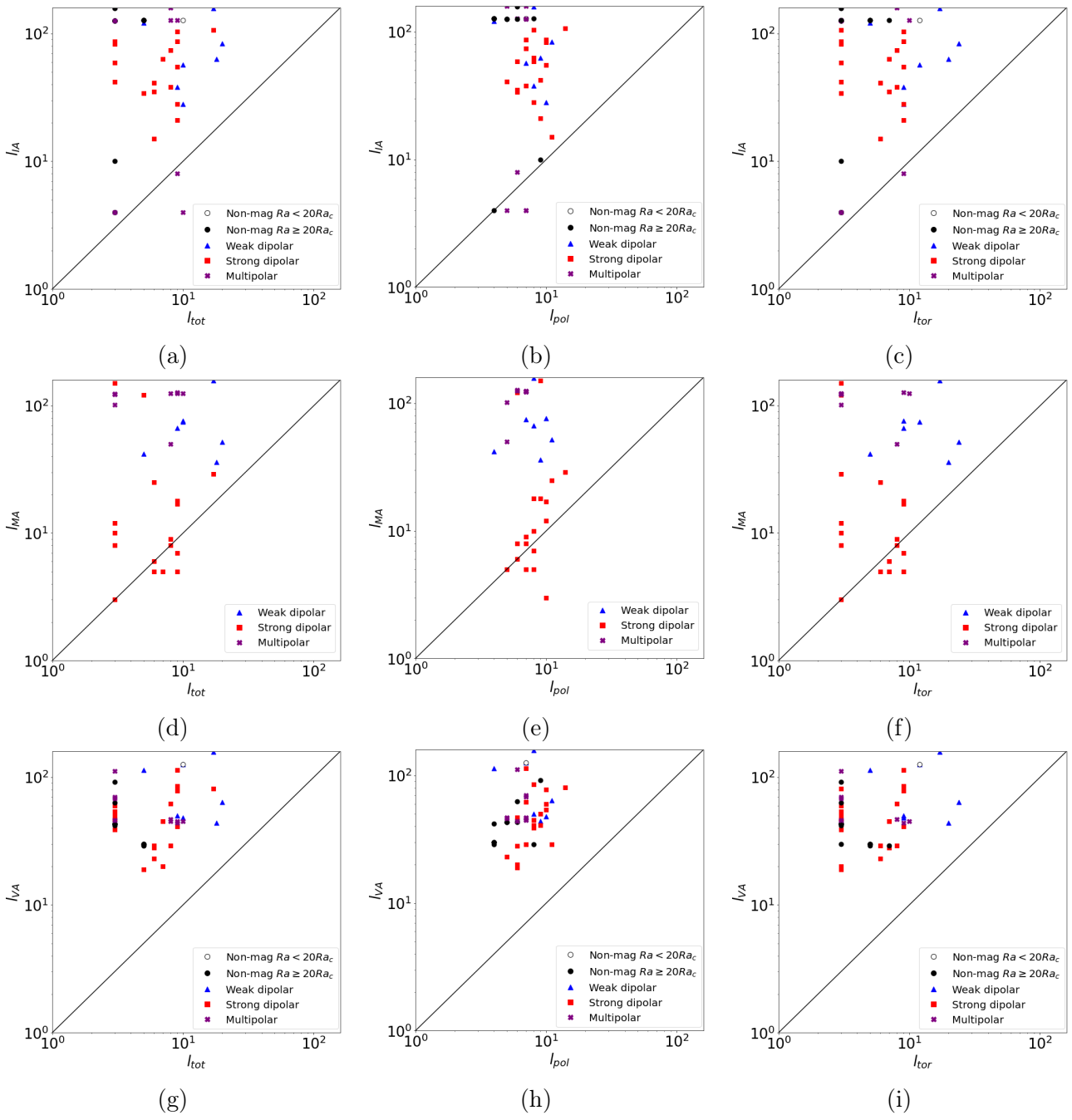

Figure 5.36: Crossover points of curls of forces in l-space as a function of (a-c) IA crossover, (d-f) MA crossover and (g-i) VA crossover. Each column is for a different energetic lengthscale (l_{tot}, l_{pol} and l_{tor}).

correlation between crossing points and peaks in the energy than the total or toroidal energy. This could be caused by the possible development of large scale zonal flows which means the peak of the toroidal energy spectrum no longer represents the scale of convection.

For the curls of forces in l, we find that the crossing points between inertial and buoyancy forces for the multipolar and non-magnetic runs do not correlate well to any of l_{tot}, l_{pol} or l_{tor} (Figs 5.36a, 5.36b, 5.36c) as the crossovers occur at a larger scale than the peak of the flow. For some of the runs in the strong field regime where the Lorentz force is important, we find that $l_{MA} \approx l_{pol}$. However, it is not as accurate as l_{MA} for the forces. For runs in the weak field

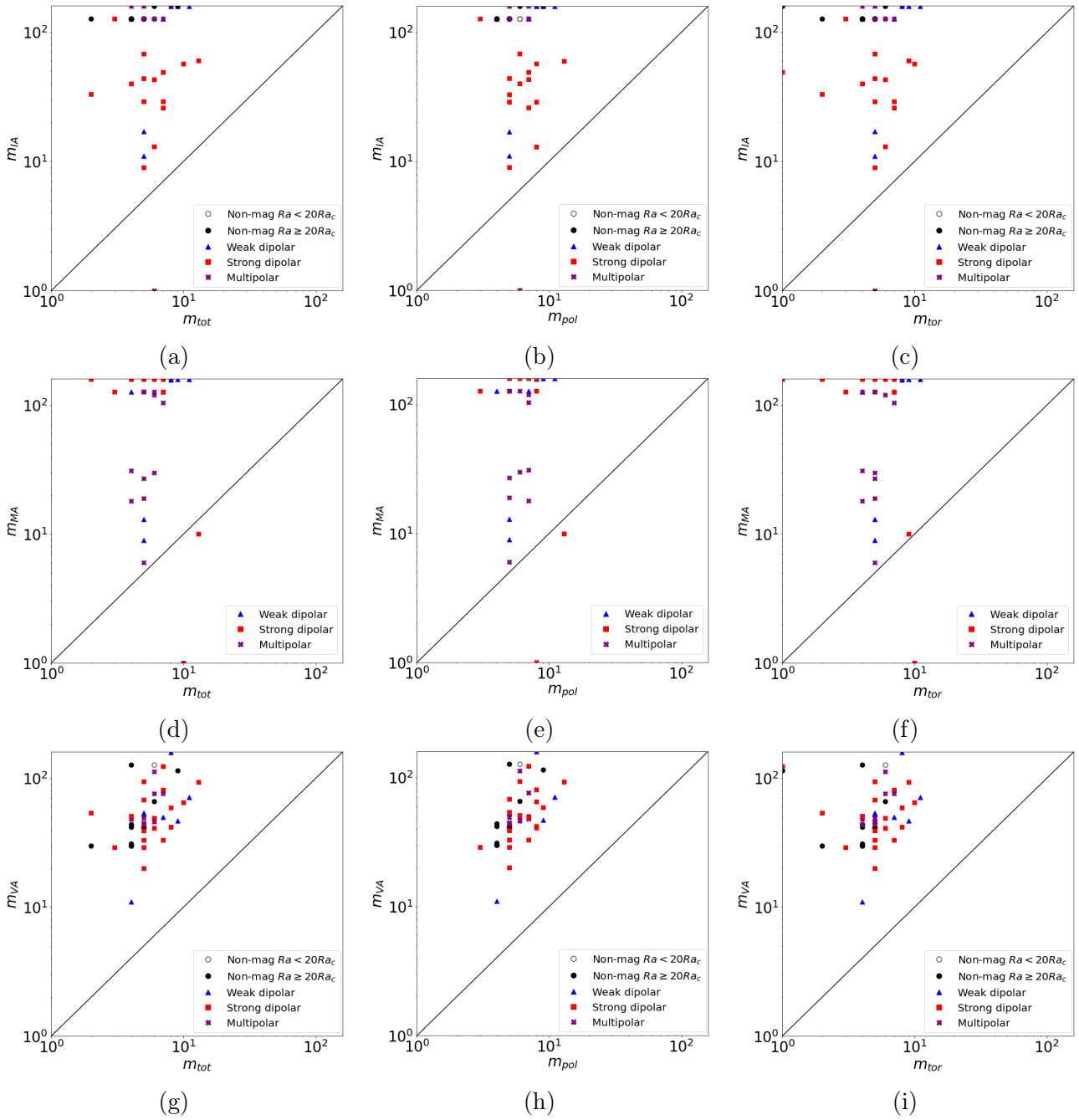

Figure 5.37: Crossover points of forces in m-space as a function of (a-c) IA crossover, (d-f) MA crossover and (g-i) VA crossover. Each column is for a different energetic lengthscale (m_{tot}, m_{pol} and m_{tor}).

regime which have a VAC balance, no correlation is found between l_{VA} and any of l_{tot}, l_{pol} or l_{tor}.

The forces in m show no correlation for any of the crossovers with m_{tot}, m_{pol} or m_{tor}. For m_{IA} (Figs 5.37a - 5.37c) for simulations in the multipolar regime or large Ra hydrodynamical runs, there is no well-defined crossover so all purple points are clustered at the largest m. This is also the case for m_{MA} (Figs. 5.37d - 5.37f) where the majority of strong dipolar runs lie at the largest values of m_{MA}. For the crossover between m_{VA}, we are able to extract well-defined crossovers but these crossovers are at a much larger scale than the flow, similar to l-space. The

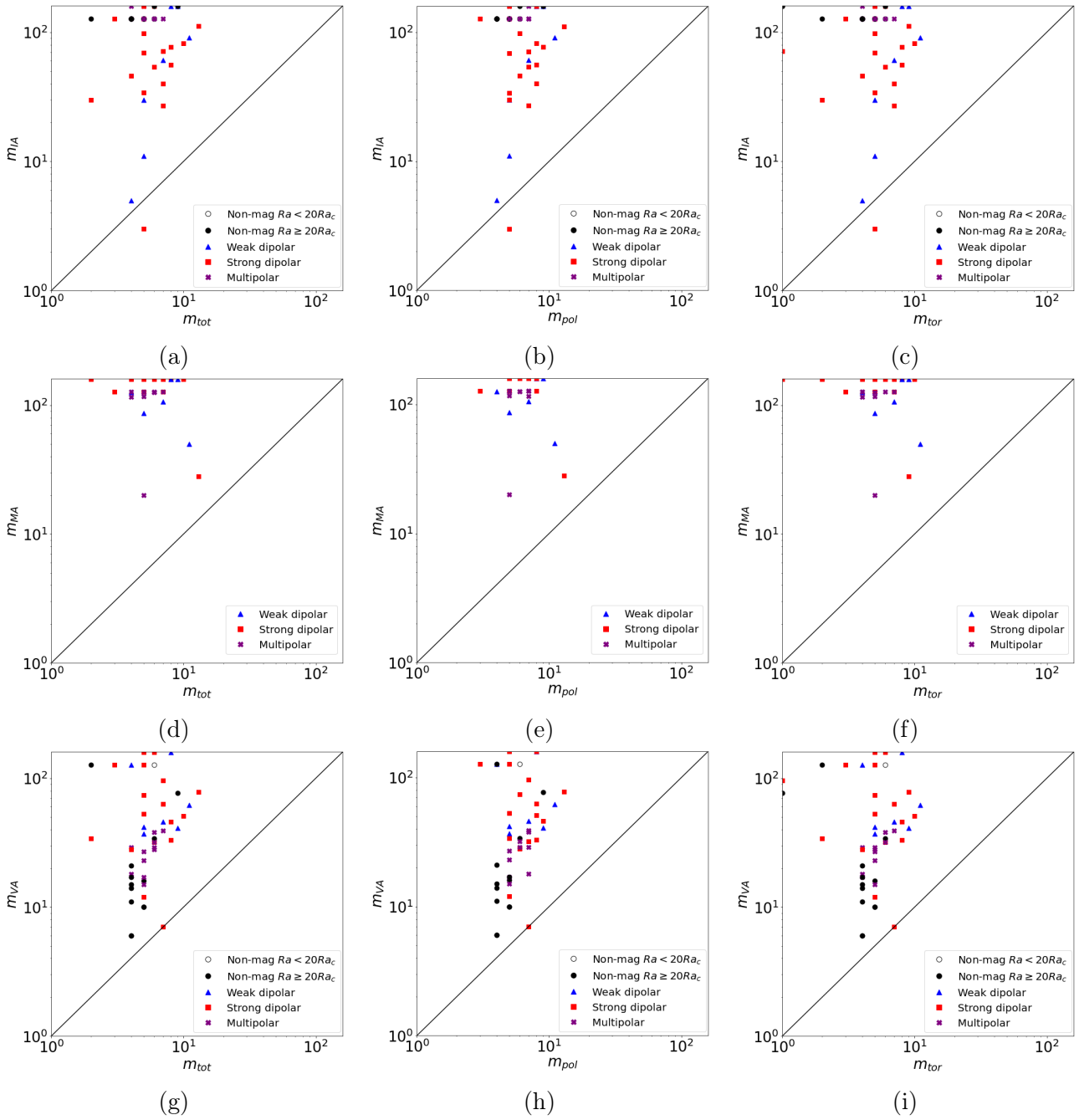

Figure 5.38: Crossover points of curls of forces in m-space as a function of (a-c) IA crossover, (d-f) MA crossover and (g-i) VA crossover. Each column is for a different energetic lengthscale (m_{tot}, m_{pol} and m_{tor}).

curl of forces in m display a similar behaviour. For runs in the multipolar regime or large Ra hydrodynamical runs, there is no clear m_{IA} so points cluster around the largest m (Figs 5.38a - 5.38c). For runs in the strong field regime, we do not obtain a crossover for m_{MA} and again points cluster around the largest m (Figs 5.38d - 5.38f). For m_{VA} we do not find a correlation for any of m_{tot}, m_{pol} or m_{tor} (Figs 5.38g - 5.38i), similar to the other cases examined.

5.3.2 TRIPLE BALANCES

The crossing points of Section 5.3.1 only consider the point at which two of the forces are most in balance, but, as shown in Section 5.2, the three regimes appear to be primarily controlled by a triple balance of forces. Therefore, we define a point where the three relevant forces are most in balance. These are given by

$$l_{MAC} = \arg\min_{l} \left(\frac{|F_{L,l} - F_{A,l}| + |F_{C,l} - F_{A,l}| + |F_{L,l} - F_{C,l}|}{\max\left(F_{L,l}, F_{A,l}, F_{C,l}\right)} \right) \tag{5.7}$$

$$l_{CIA} = \arg\min_{l} \left(\frac{|F_{I,l} - F_{A,l}| + |F_{C,l} - F_{A,l}| + |F_{I,l} - F_{C,l}|}{\max\left(F_{I,l}, F_{A,l}, F_{C,l}\right)} \right) \tag{5.8}$$

$$l_{VAC} = \arg\min_{l} \left(\frac{|F_{V,l} - F_{A,l}| + |F_{C,l} - F_{A,l}| + |F_{V,l} - F_{C,l}|}{\max\left(F_{V,l}, F_{A,l}, F_{C,l}\right)} \right) \tag{5.9}$$

and similarly for m we define

$$m_{MAC} = \arg\min_{m} \left(\frac{|F_{L,m} - F_{A,m}| + |F_{C,m} - F_{A,m}| + |F_{L,m} - F_{C,m}|}{\max\left(F_{L,m}, F_{A,m}, F_{C,m}\right)} \right) \tag{5.10}$$

$$m_{CIA} = \arg\min_{m} \left(\frac{|F_{I,m} - F_{A,m}| + |F_{C,m} - F_{A,m}| + |F_{I,m} - F_{C,m}|}{\max\left(F_{I,m}, F_{A,m}, F_{C,m}\right)} \right) \tag{5.11}$$

$$m_{VAC} = \arg\min_{m} \left(\frac{|F_{V,m} - F_{A,m}| + |F_{C,m} - F_{A,m}| + |F_{V,m} - F_{C,m}|}{\max\left(F_{V,m}, F_{A,m}, F_{C,m}\right)} \right). \tag{5.12}$$

The formulae above are also applied to curls of forces but the definitions are not repeated for brevity. Forming a triple balance point in this way allows us to extract the lengthscale at which the three forces are most in balance. Equation 5.7, extracts the lengthscale at which Lorentz, buoyancy and Coriolis are most in balance. We divide by the maximum of the three relevant forces at each l to obtain the lengthscale where the three forces are most in balance, but also where these forces are large and important to the flow dynamics. If no normalisation was performed, then we are likely to extract the largest values of l or m, where all forces are small in magnitude and are not impacting the main dynamics of the flow. These triple balance points are compared to the peaks in the total kinetic energy, poloidal kinetic energy and toroidal kinetic energy spectra in l and m. To find a triple balance point for the forces, the Coriolis force is replaced with the ageostrophic Coriolis force and the balance between ageostrophic Coriolis, buoyancy and either of viscous, inertia or Lorentz forces is considered. The ageostrophic Coriolis force is considered as this is what has been argued (Schwaiger et al., 2019) to be the dynamically important part of the Coriolis force. These triple balance points are referred to as $l_{MAC_{ag}}$, $l_{C_{ag}IA}$ and $l_{VAC_{ag}}$ and similarly for m. For the curls, the usual (solenoidal) Coriolis force is used in the definition.

For the triple balance of forces in l, multipolar runs and non-magnetic runs at large Ra show

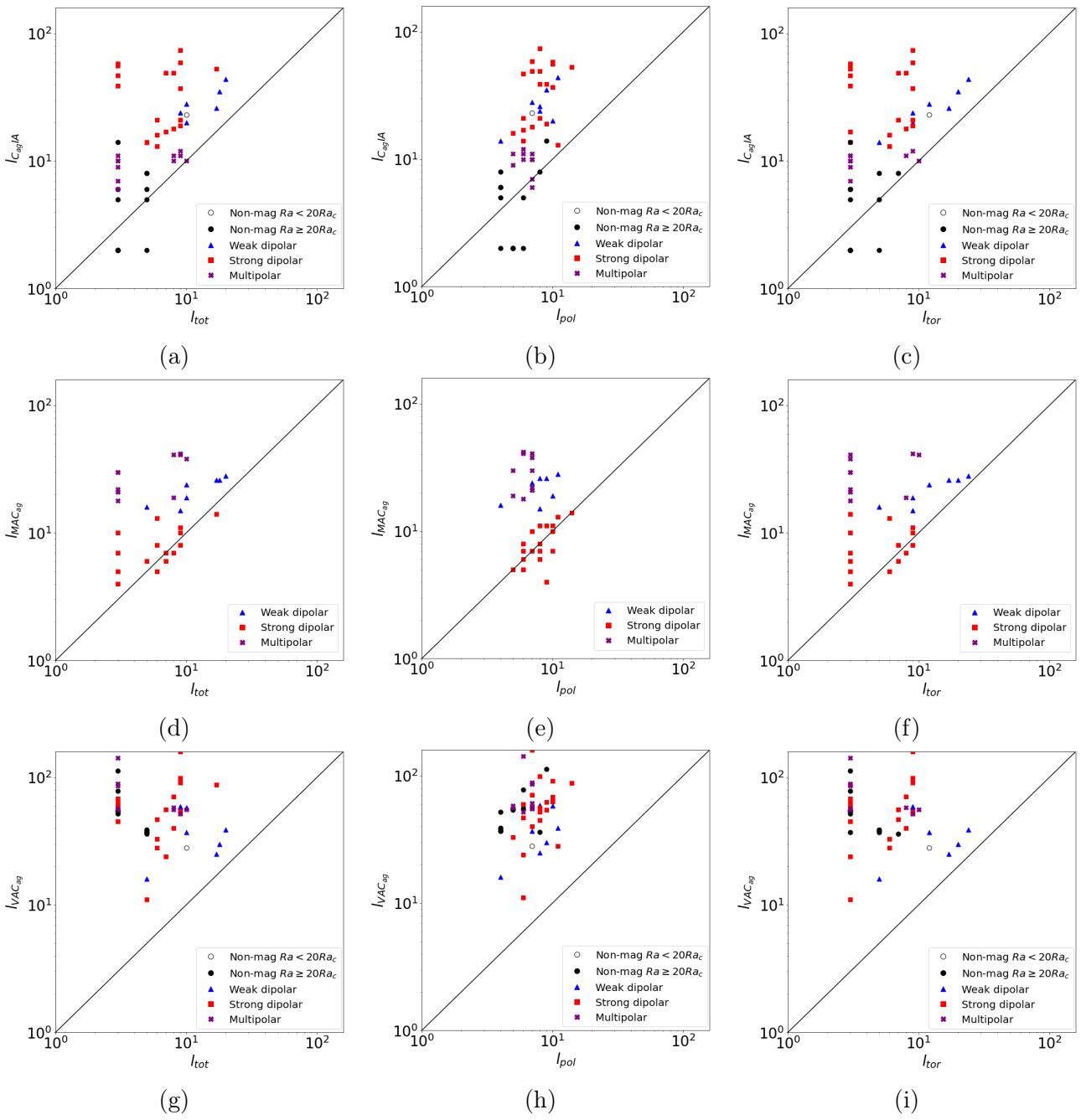

Figure 5.39: Triple balance of forces in l-space as a function of (a-c) $C_{ag}IA$, (d-f) MAC_{ag} and (g-i) VAC_{ag} triple balance point. Each column is for a different energetic lengthscale (l_{tot}, l_{pol} and l_{tor}).

that $l_{C_{ag}IA} \approx l_{pol}$ (Fig. 5.39b). Similarly for runs in the strong field branch where forces are dominated by a MAC balance a correlation is found between $l_{MAC_{ag}}$ and l_{pol} (Fig. 5.39e). The plots involving l_{tot} and l_{tor} for $l_{C_{ag}IA}$ (Figs 5.39a, 5.39c) and $l_{MAC_{ag}}$ (Figs 5.39d, 5.39f) are very similar, again highlighting that the total energy is controlled by the toroidal energy but neither the total nor toroidal energy peaks show a correlation with $l_{C_{ag}IA}$ or $l_{MAC_{ag}}$. There is no correlation between peaks in the energy and the viscous, buoyancy and ageostrophic Coriolis force balance for any of l_{tot}, l_{pol} or l_{tor} (Figs 5.39g - 5.39i). These results are similar to the crossover points where $l_{IA} \approx l_{pol}$ and $l_{MA} \approx l_{pol}$ but the VAC scale did not correlate to any of the peaks in energy.

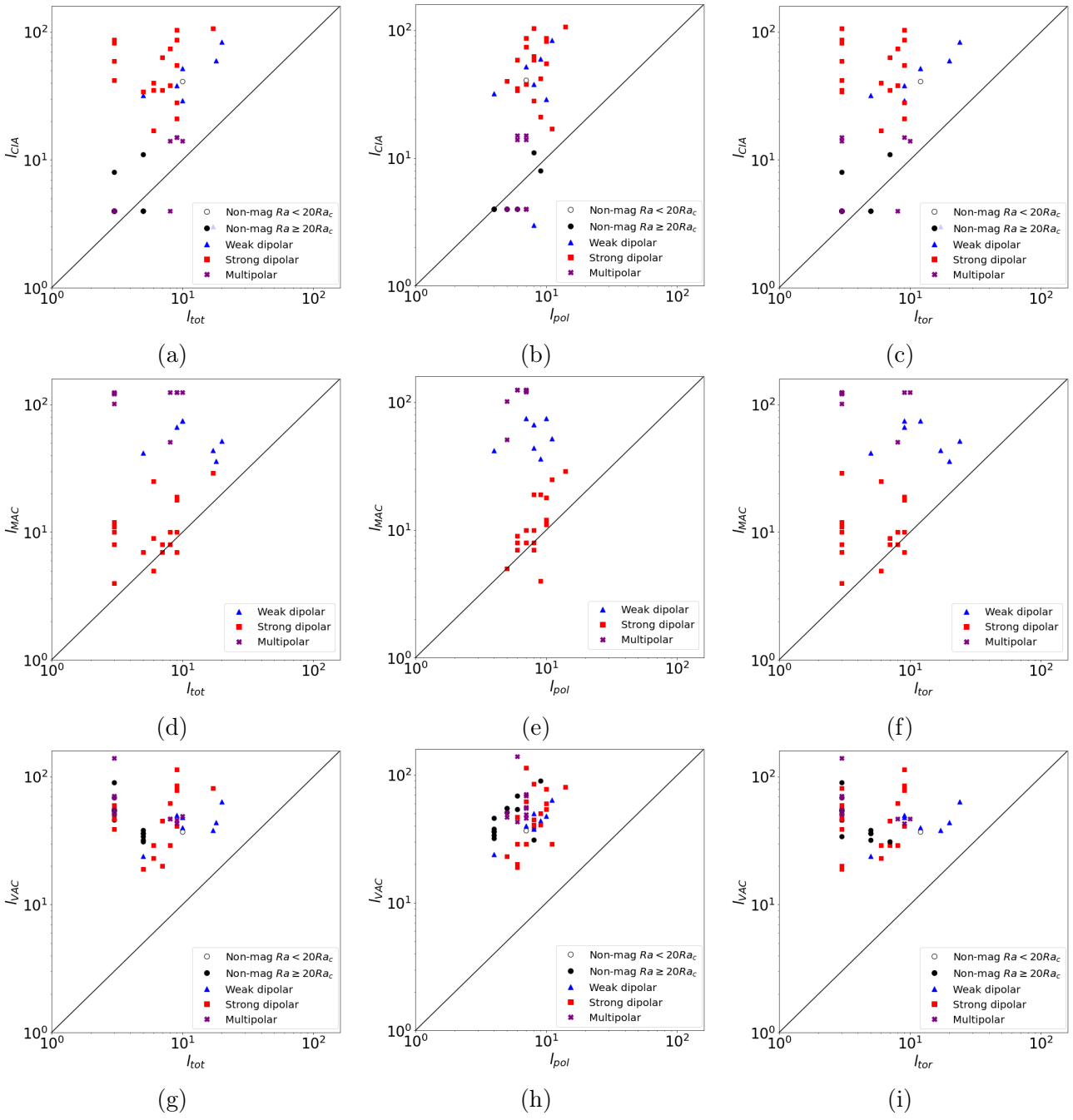

Figure 5.40: Triple balance of curl of forces in l-space as a function of (a-c) CIA, (d-f) MAC and (g-i) VAC triple balance point. Each column is for a different energetic lengthscale (l_{tot}, l_{pol} and l_{tor}).

The curls of forces (Fig. 5.40) show similar results to the forces (Fig. 5.39). The values of l_{pol} are best at relating the peaks in energy to the triple balance point. For l_{CIA}, only some of the multipolar and non-magnetic runs show a correlation with l_{pol} (Fig. 5.40b). This differs from the crossover points of curls of forces where no correlation was found between l_{IA} and l_{pol}. We find a correlation between l_{MAC} and l_{pol} for some of the strong field runs (Fig. 5.40e), similar to the crossover point l_{MA} in the curl of the forces. Both l_{tot} and l_{tor} do not show a correlation with either l_{CIA} (Figs 5.40a, 5.40c) or l_{MAC} (Figs 5.40d, 5.40f). For runs in the weak field regime where viscous forces dominate, the VAC triple balance point cannot be related to any

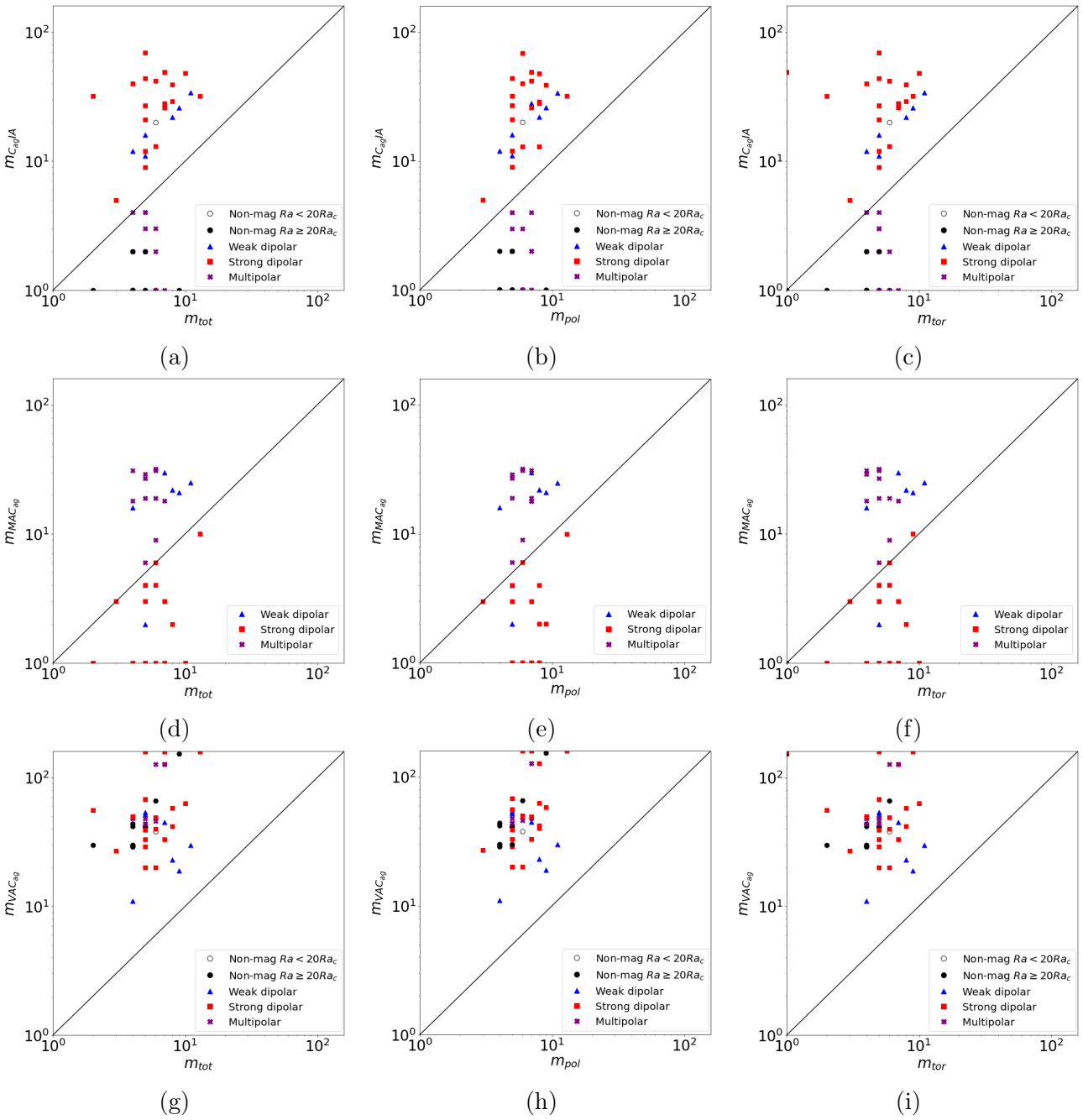

Figure 5.41: Triple balance of forces in m-space as a function of (a-c) $C_{ag}IA$, (d-f) MAC_{ag} and (g-i) VAC_{ag} triple balance point. Each column is for a different energetic lengthscale (m_{tot}, m_{pol} and m_{tor}).

of the energy peaks (Figs 5.40g - 5.40i). This is similar to the results for the forces and the crossover of curls of forces and could be due to the removal of the boundary layers.

For the triple balance point of forces in m no relationship is found between m_{tot}, m_{pol} or m_{tor} and the appropriate triple balance point for any of the regimes. For $m_{C_{ag}IA}$, the triple balance point for most runs occurs at a small m compared to the peak of the flow (Figs 5.41a - 5.41c). Similar results are found for $m_{MAC_{ag}}$ where the triple balance point for most runs occurs at a small m compared with the peak of the flow (Figs 5.41d - 5.41f). Although no correlation is found between the triple balance points and peaks in the flow, we are able to obtain a triple

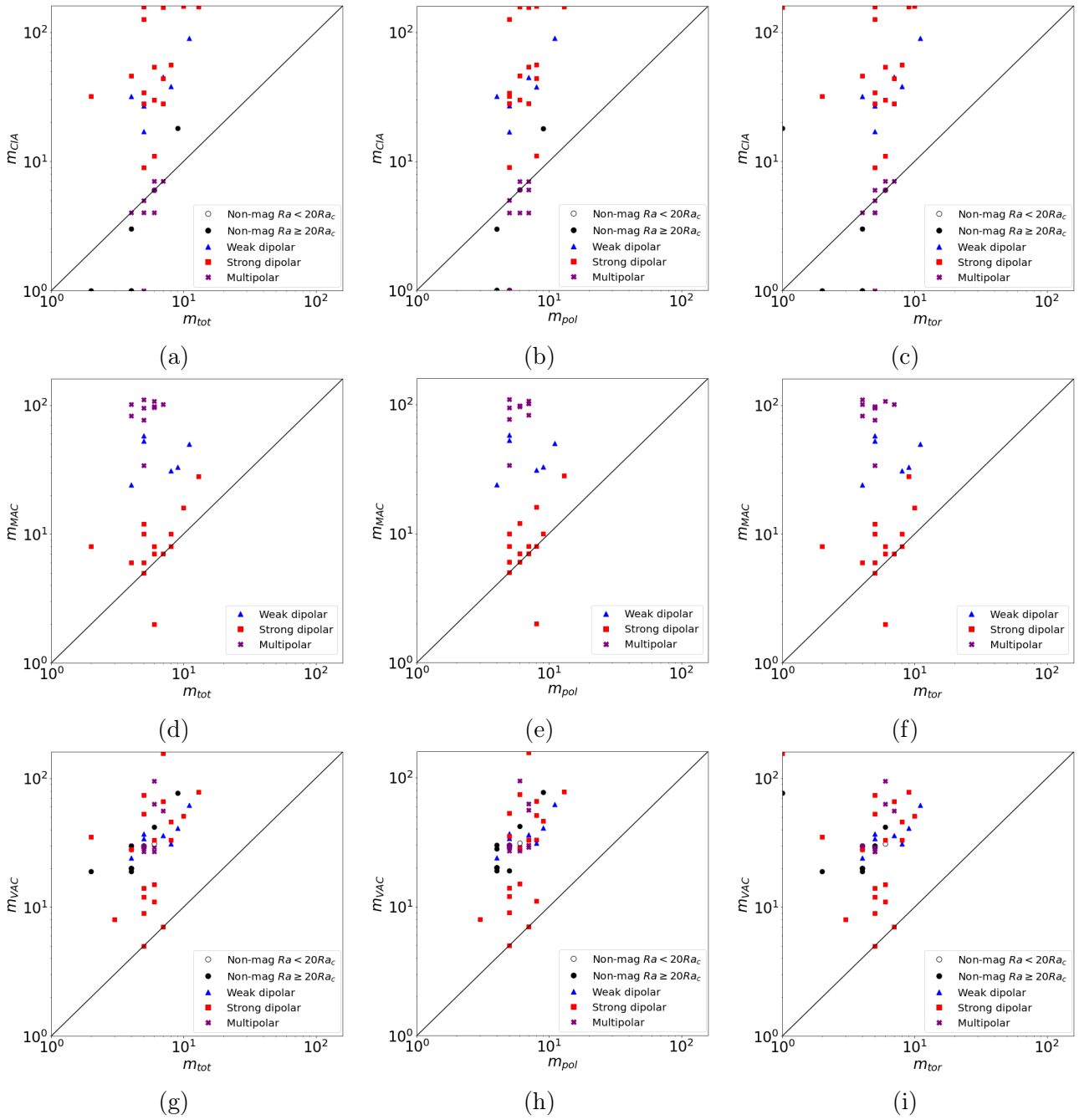

Figure 5.42: Triple balance of curls of forces in m-space as a function of (a-c) CIA, (d-f) MAC and (g-i) VAC triple balance point. Each column is for a different energetic lengthscale (m_{tot}, m_{pol} and m_{tor}).

balance point unlike the crossovers, where in most cases in m space the crossover points are not well-defined. Once again no relationship is found between $m_{VAC_{ag}}$ and any of m_{tot}, m_{pol} or m_{tor} (Figs 5.41g - 5.41i).

For the curls of forces in m-space, a correlation is obtained between triple balance points of the curls and peaks in the flow. Multipolar runs and hydrodynamical runs at large enough Ra show that $m_{CIA} \approx m_{pol}$ in some cases (Fig. 5.42b). We also find that m_{tot} and m_{tor} show some correlation with m_{CIA} for multipolar and hydrodynamical runs (Figs 5.42a, 5.42c). Similarly, for most runs in the strong field regime $m_{MAC} \approx m_{pol}$ (Fig. 5.42e), and m_{tot} and m_{tor} (Figs.

5.42d, 5.42f) also show correlation with m_{MAC} for some runs in the strong field regime. This differs to the crossovers in m space where no correlation is found between the crossover points and peaks in the flow, as most runs do not have a well-defined crossover of relevant forces. For m_{VAC} no relationship is found between this and any of m_{tot}, m_{pol} or m_{tor} (Figs 5.42h - 5.42g), similar to all other cases involving the viscous force.

5.4 SUMMARY

This analysis shows that the l-dependence and m-dependence of forces show good agreement, where both display a similar hierarchy of forces. Similarly, the l-dependence of curls of forces matches well with the m-dependence and offer a cleaner way of accessing the dynamical balances controlling the behaviour of the system (Teed and Dormy, 2023). The dynamo solutions presented demonstrated that decreasing the Ekman number still produced the relevant force balance in each regime of dynamo action, although the multipolar regime was harder to reach at lower Ekman number as stronger driving is required. For this reason, fewer multipolar runs are found. Hence, the correlation of l_{CIA} with l_{pol} shows less agreement than the correlation of l_{MAC} with l_{pol} and similarly for m.

Crossover points of relevant forces and curls of forces were discussed using the method followed by Schwaiger et al. (2021). In most cases for the l-dependence of forces the crossing points of Lorentz and buoyancy forces in the strong field dipolar regime were successfully related to the poloidal kinetic energy peak. Similarly, the crossing points of inertial and buoyancy forces in the multipolar regime and hydrodynamical runs at large Ra correlated well with the poloidal kinetic energy peaks in l-space. However, no relationship was found between crossover points for the curls of forces in l and the polodial kinetic energy peak, as the crossing points occur at much smaller scales than the poloidal energy peak or the crossover points do not exist. In m-space, the forces and curls of forces showed no correlation to the poloidal kinetic energy peak because most do not have crossing points of the relevant forces.

The triple balance points demonstrated an alternative approach for forming dynamically relevant lengthscales and, unlike the crossovers, we were able to extract a triple balance point for every run regardless of whether crossover points occurred or not. Separating runs by their branch (weak field or strong field) of dynamo action helped to confirm that weak field runs are not in a MAC balance. For forces in l-space, the MAC triple balance point for the strong field dipolar runs correlated well to the poloidal kinetic energy peak, as did the CIA triple balance point for multipolar runs and hydrodynamical runs at large driving, but in m-space we were unable to relate the triple balance point of forces to the kinetic energy peaks. For the curls of forces, the MAC triple balance point for strong field dipolar runs was successfully matched to the poloidal kinetic energy peak for both l-space and m-space. This was also the case for the CIA triple balance point for multipolar runs and hydrodynamical runs at large Ra. In this work the branch of dynamo action clearly determines whether or not the MAC triple balance point sets the poloidal scale, whereas work by Schwaiger et al. (2021) uses the ratio of magnetic

Forces or Curls	l **or** m	**Balance**	p**-value**	**Summary**
Forces	l-space	Crossover	• 0.76 • 0.008 • 0.07	• Good agreement between l_{IA} and l_{pol} for HD runs at large Ra. • Good agreement between l_{IA} and l_{pol} for multipolar runs. • Good agreement between l_{MA} and l_{pol} for strong field runs.
Forces	m-space	Crossover		No correlation between m_{pol} and m_{MA} or m_{IA} for any regime.
Forces	l-space	Triple balance	• 0.82 • 0.008 • 0.69	• Some agreement between $l_{C_{ag}IA}$ and l_{pol} for HD runs at large Ra. • Some agreement between $l_{C_{ag}IA}$ and l_{pol} for multipolar runs. • Good agreement $l_{MAC_{ag}}$ and l_{pol} for strong field runs.
Forces	m-space	Triple balance		No correlation between m_{pol} and $m_{MAC_{ag}}$ or $m_{C_{ag}IA}$ for any regime.
Curls	l-space	Crossover	• 0.01	• Good agreement between l_{MA} and l_{pol} for strong field runs.
Curls	m-space	Crossover		No correlation between m_{pol} and m_{MA} or m_{IA} for any regime.
Curls	l-space	Triple balance	• 0.26 • 0.7 • 0.004	• Good agreement between l_{CIA} and l_{pol} for HD runs at large Ra. • Some agreement between l_{CIA} and l_{pol} for multipolar runs. • Good agreement between l_{MAC} and l_{pol} for strong field runs.
Curls	m-space	Triple balance	• 0.04 • 0.02 • 0.7	• Some agreement between m_{CIA} and m_{pol} for HD runs at large Ra. • Some agreement between m_{CIA} and m_{pol} for multipolar runs. • Good agreement between m_{MAC} and m_{pol} for strong field runs.

Table 5.2: Summary of results discussed in Section 5.3 where crossovers and triple balances are compared to l_{pol} and m_{pol} only.

to kinetic energy which can act as a proxy to the weak and strong field branches. The VAC triple balance point for the weak field dipolar runs and hydrodynamical runs at low Ra show no correlation with the poloidal kinetic energy peak. This is possibly caused by the removal of the boundary layers in the calculation of the forces and curls of forces, which causes a reduction in the viscous force. Further analysis would be required to confirm this (see discussion of future work in Chapter 7). The VAC balance may be found in the hydrodynamical case at Ra closer to onset which has not been explored.

The analysis in this chapter demonstrates that the poloidal kinetic energy is most appropriate for defining the energetic lengthscale. Table 5.2 summarises the results presented in Section 5.3 in order to highlight the key findings based on the poloidal kinetic energy. A Wilcoxon Matched-Pairs Test (Wilcoxon, 1945) is again performed here to obtain a p-value for cases that indicate a linear fit. This helps to determine whether the peak in poloidal energy differs significantly from crossover or triple balance points in the cases where we cannot reject the null hypothesis of the test. Note this test uses a threshold $\alpha = 0.05$ to reject the null hypothesis, where p-values above this threshold indicate statistically significant results. For certain regimes the triple balance point between curls of forces determines the convective lengthscale. This method worked for the strong field dipolar regime and strongly driven regimes (i.e. the multipolar regime and large Ra hydrodynamical states). These results reinforce that using the curls of forces offers a better way to understand the forces controlling the flow dynamics.

Chapter 6

Force balances inside and outside the tangent cylinder

The linear theory of non-magnetic convection in a rotating sphere, as proposed by Busse (1970), suggests that convection onsets at a higher Rayleigh number inside the tangent cylinder (ITC) compared to outside the tangent cylinder (OTC). This was later confirmed through numerical simulations by Dormy et al. (2004). The differences in convection modes ITC and OTC was shown by Busse (1976a). Experimental investigations by Aurnou et al. (2003) and Aujogue et al. (2018) have also demonstrated differences in convection ITC and OTC. Most recently Gastine and Aurnou (2023) performed spherical shell simulations to analyse heat transport properties ITC and OTC. They found that although convection ITC onsets at a higher Ra than OTC, once it does so it becomes more turbulent and is able to transport heat more efficiently as Ra is increased further. Despite this, studies of force balances in dynamo simulations often emphasise globally averaged quantities or the lengthscale dependence of these quantities across the entire spherical shell. In this chapter, we investigate the lengthscale dependence of forces and curls of forces ITC and OTC. A detailed description of the methods used is discussed in Section 2.2.3.5. The dissection of the domain at the TC occurs along a cylindrical surface. The only coordinate in spherical geometry that does not cross this surface is the ϕ coordinate. Hence the m-dependence of quantities can be naturally split and compared ITC and OTC. Chapter 5 examined the m-dependence of forces and curls of forces across the entire shell, comparing these to the global l-dependence, and demonstrated that both displayed a similar hierarchy of (curls of) forces. When discussing the lengthscale dependence of forces and curls of forces across the entire shell we will refer to these as the global m-dependence.

The behaviour of forces and curls of forces ITC and OTC in hydrodynamical simulations at $E = 10^{-4}$ for varying Ra are examined. Then, forces and curls of forces ITC and OTC for the main branches of dynamo action at $E = 10^{-4}$ and $E = 10^{-5}$ are discussed. Finally, transitions between the different branches of dynamo action are analysed. Firstly from weak field dipolar to multipolar and then from strong field dipolar to multipolar, with the aim of identifying

differences between the forces ITC and OTC that may influence the transition between regimes.

6.1 COMPARISON OF FORCE DENSITY SPECTRA

In this section, the force density spectra globally, ITC and OTC are examined. We discuss similarities and differences between the behaviour ITC and OTC, examining how the solutions ITC and OTC change for the main regimes of dynamo action. The simulations presented are the same as those discussed in Chapter 5. However, the alternative method discussed in Section 2.2.3 is used for computing the m-dependence of forces and curls of forces. The global hierarchy of forces in Chapter 5 match those discussed in Section 5.1, confirming the alternative method for extracting the forces provides the correct results. Some of the runs presented in this chapter have been initialised using state files from existing simulations in Teed and Dormy (2025). In the cases presented below, the spectra for the force density is formed, given by Equations (2.113) - (2.115).

6.1.1 HYDRODYNAMICAL SOLUTIONS AT $E = 10^{-4}$

At $Ra = 2Ra_c$ a zeroth order geostrophic balance occurs across the total spherical shell with a first order balance between buoyancy and ageostrophic Coriolis forces. The viscous and inertial forces remain small. The behaviour OTC is very similar to the total shell (Fig. 6.1b). Changes are observed ITC where a decrease in inertial and viscous forces occur (Fig. 6.1c). The behaviour is mainly controlled OTC as the forces in this region are similar to the total spherical shell. Convection is underdeveloped ITC at this low supercriticality which is why the contribution of forces are lower. At $Ra = 5Ra_c$ a zeroth order geostrophic balance occurs at all scales, similar to $Ra = 2Ra_c$ (Fig. 6.2). The inertial force has increased as the strength of convection is larger. Similar to $Ra = 2Ra_c$, the behaviour OTC (Fig. 6.2b) matches the global behaviour (Fig. 6.2a) and the inertial force decreases ITC (Fig. 6.2c).

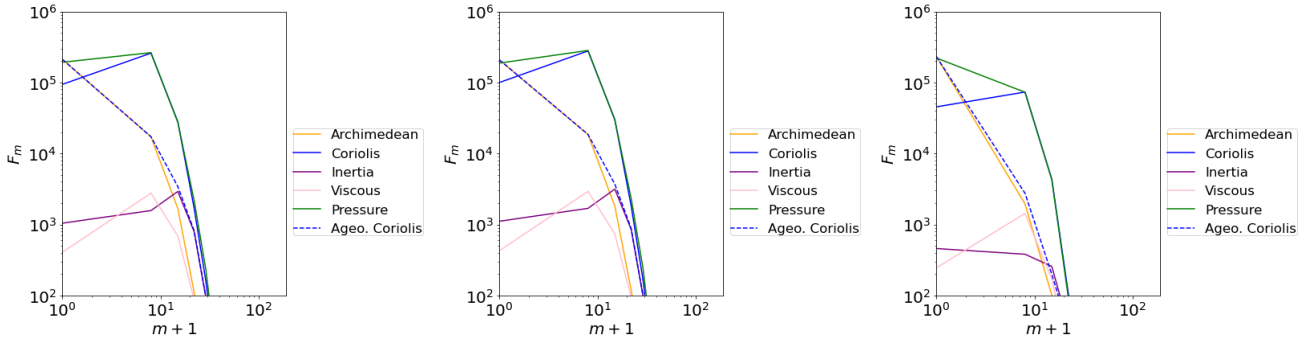

(a) Total (b) OTC (c) ITC

Figure 6.1: Force density spectra. Hydrodynamical run at $E = 10^{-4}$ and $Ra = 2Ra_c$. All quantities are time averaged and boundary layers have been removed. Only every $7m$ mode is plotted.

At $Ra = 30Ra_c$ (Fig. 6.3), the solution becomes inertially dominated as an increase in the inertial force is observed across all regions. A zeroth order geostrophic balance occurs followed

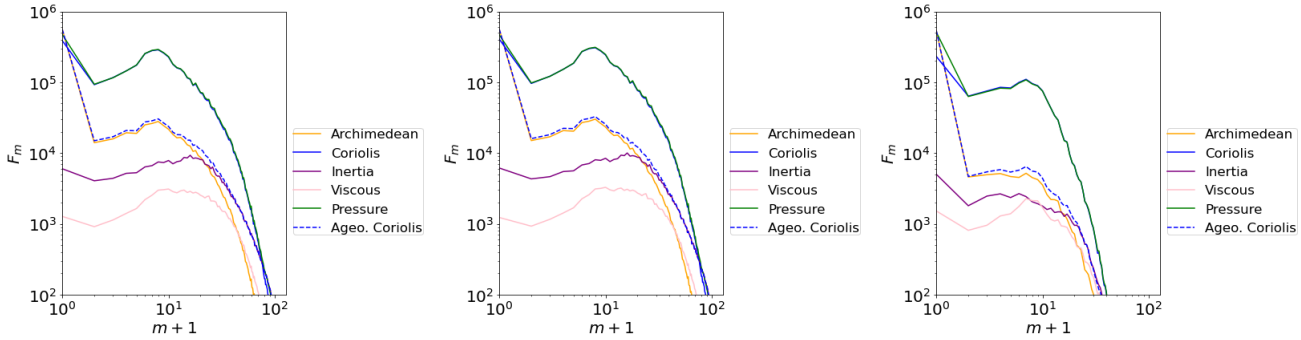

(a) Total (b) OTC (c) ITC

Figure 6.2: Force density spectra. Hydrodynamical run at $E = 10^{-4}$ and $Ra = 5Ra_c$. All quantities are time averaged and boundary layers have been removed.

by a strong inertial force OTC and ITC (Figs 6.3b, 6.3c). The inertial force is slightly larger ITC which is likely because at this level of supercriticality, convection ITC has begun in earnest and, since it quickly becomes more efficient than OTC Gastine and Aurnou (2023), it is effectively in a more supercritical state than OTC. The viscous force remains weak throughout, both ITC and OTC. Again, similar to the runs at lower Ra, the behaviour OTC is similar to the behaviour across the entire shell. The hierarchy of forces for each case match those in Section 5.1.1. Overall, for all values of Ra examined, we do not find significant differences in behaviour ITC and OTC.

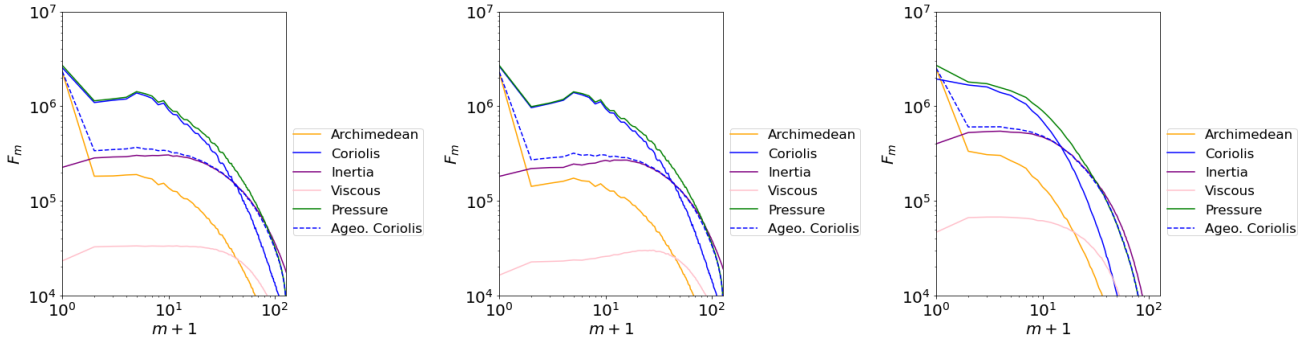

(a) Total (b) OTC (c) ITC

Figure 6.3: Force density spectra. Hydrodynamical run at $E = 10^{-4}$ and $Ra = 30Ra_c$. All quantities are time averaged and boundary layers have been removed.

6.1.2 DYNAMO SOLUTIONS AT $E = 10^{-4}$

The behaviour of the weak dipolar run at $Ra = 2.07Ra_c$ and $Pm = 12$ is very similar to the hydrodynamical run at low Ra, but a weak Lorentz force is now included and the magnitudes of all quantities have increased. The lengthscale dependence OTC (Fig. 6.4b) is similar to the global lengthscale dependence (Fig. 6.4), as was observed in the hydrodynamical case at low Ra. The inertial force decreases ITC (Fig. 6.4c), similar to the hydrodynamical run, and a slight decrease in the Lorentz force is observed in this region. The weaker Lorentz force ITC could be due to weaker convection ITC so the dynamo mechanism is less supercritical. For the strong dipolar case at $Ra = 2.07Ra_c$ and $Pm = 12$ a zeroth order geostrophic balance occurs

at large scales and at small scales there is a balance between Lorentz and pressure forces, which is observed globally, OTC and ITC (Figs 6.5a-6.5c). A notable reduction in the large scale geostrophic balance ITC is observed to the point where a balance between pressure, Coriolis and Lorentz forces (magnetostrophic) almost forms. The inertial and viscous force remain weak across all regions of the shell and the hierarchy OTC matches the hierarchy across the total shell. The buoyancy force balances the Lorentz force OTC at some scales but ITC this decreases in magnitude at larger scales compared with OTC.

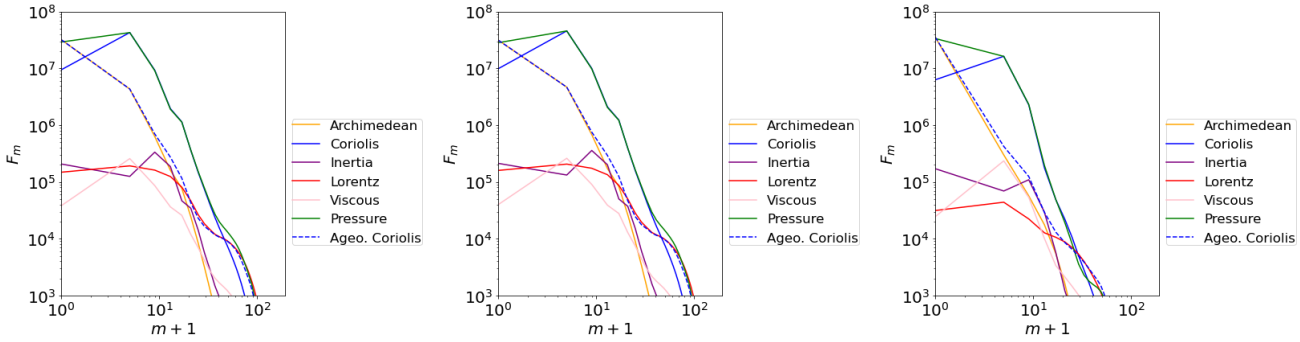

(a) Total (b) OTC (c) ITC

Figure 6.4: Force density spectra. Dynamo solution for a weak field dipolar run at $E = 10^{-4}$, $Ra = 2.07Ra_c$ and $Pm = 12$. All quantities are time averaged and boundary layers have been removed. Only every $4m$ mode is plotted.

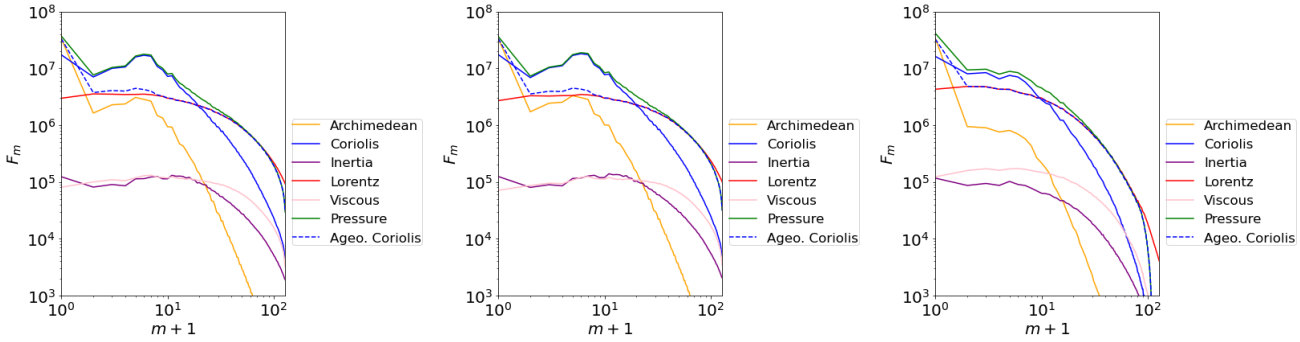

(a) Total (b) OTC (c) ITC

Figure 6.5: Force density spectra. Dynamo solution for a strong field dipolar run at $E = 10^{-4}$, $Ra = 2.07Ra_c$ and $Pm = 12$. All quantities are time averaged and boundary layers have been removed.

For another strong field run at larger Ra (Fig. 6.6), a zeroth order geostrophic balance occurs at large scales and at small scales a balance between Lorentz and pressure occurs OTC (Fig. 6.6b). However, ITC at zeroth order, a fully formed magnetostrophic balance is found at large scales, in contrast with the strong field dipolar run at lower Ra (Fig. 6.5c). This magnetostrophic balance transitions to a balance between Lorentz and pressure forces at small scales (Fig. 6.6c). The buoyancy force decreases at a larger scale ITC (Fig. 6.6c) compared to OTC (Fig. 6.6b), similar to the other strong field dipolar solution at lower Ra (Fig. 6.5). The strong Lorentz force ITC is expected as we have a strong field dipolar solution.

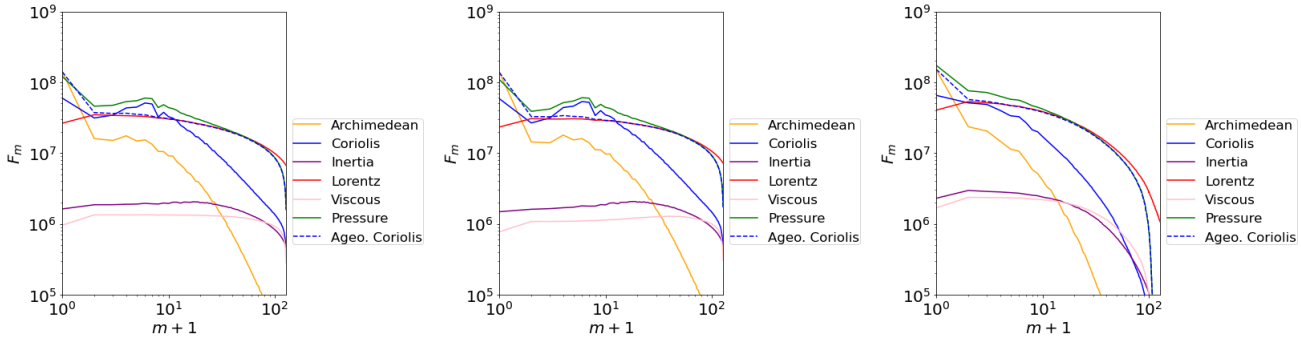

(a) Total (b) OTC (c) ITC

Figure 6.6: Force density spectra. Dynamo solution for a strong field dipolar run at $E = 10^{-4}$, $Ra = 10Ra_c$ and $Pm = 12$. All quantities are time averaged and boundary layers have been removed.

Figure 6.7 shows a multipolar run at $Pm = 1$ and $Ra = 30Ra_c$. The global force density shows a zeroth order geostrophic balance with a first order balance between inertial and buoyancy forces and weak Lorentz and viscous forces (Fig. 6.7). The hierarchy of forces OTC (Fig. 6.7b) is similar to the total force density (Fig. 6.7a) but a slight decrease in the inertial force is observed. The force density ITC shows an increase in inertial and buoyancy forces and is likely due to convection being more efficient ITC compared to OTC at this level of supercriticality (Gastine and Aurnou, 2023). The buoyancy force decreases at a larger scale (Fig. 6.7c), compared with OTC. The Lorentz and viscous force are in balance ITC but both remain weak.

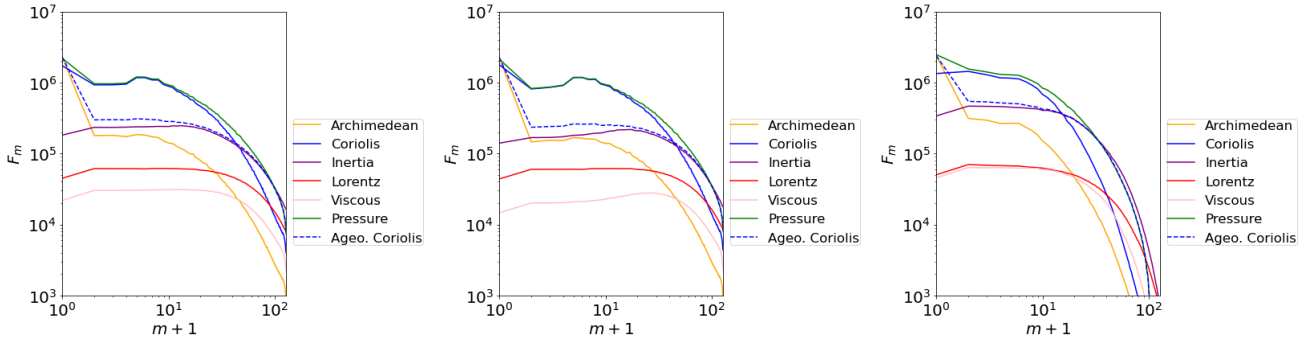

(a) Total (b) OTC (c) ITC

Figure 6.7: Force density spectra. Dynamo solution for a fluctuating multipolar at $E = 10^{-4}$, $Ra = 30Ra_c$ and $Pm = 1$. All quantities are time averaged and boundary layers have been removed.

6.1.3 DYNAMO SOLUTIONS AT $E = 10^{-5}$

Simulations at $E = 10^{-5}$ are now examined for the three main branches of dynamo action to ensure that similar results persist as the rotation rate is increased. The results for the weak field dipolar case are similar to $E = 10^{-4}$, where the force density OTC (Fig. 6.8b) matches the total force density (Fig. 6.8a). A zeroth order geostrophic balance occurs with other forces remaining weak. The buoyancy force has decreased ITC (Fig. 6.8c) and the peak in this force which occurs in the total force density and the force density OTC is less prominent ITC. The

viscous and inertial forces remain weak ITC and OTC. For the strong field case, the forces OTC (Fig. 6.9b) match the total shell (Fig. 6.9a). A leading order balance occurs between the pressure gradient and Coriolis force, followed by a balance between buoyancy and Lorentz forces with the viscous and inertial forces remaining weak. The buoyancy force has decreased ITC (Fig. 6.9c). The multipolar run (Fig. 6.10) shows similar results to the multipolar run at $E = 10^{-4}$ (Fig. 6.7). The behaviour OTC (Fig. 6.10b) is similar to the total force density (Fig. 6.10a) but a slight decrease in the buoyancy and viscous forces occur. The inertial force is strong in both cases, but it is larger ITC (Fig. 6.10c).

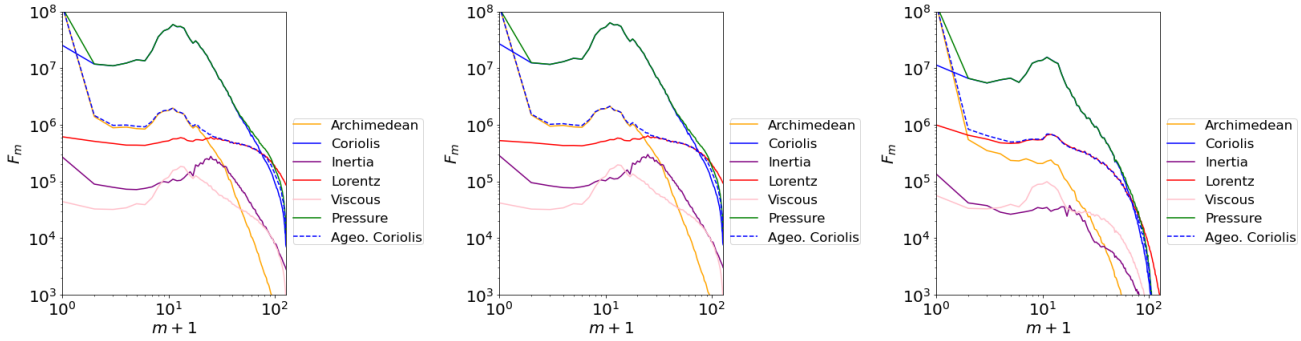

(a) Total (b) OTC (c) ITC

Figure 6.8: Force density spectra. Dynamo solution for weak field dipolar run at $E = 10^{-5}$, $Ra = 3Ra_c$ and $Pm = 5$. All quantities are time averaged and boundary layers have been removed.

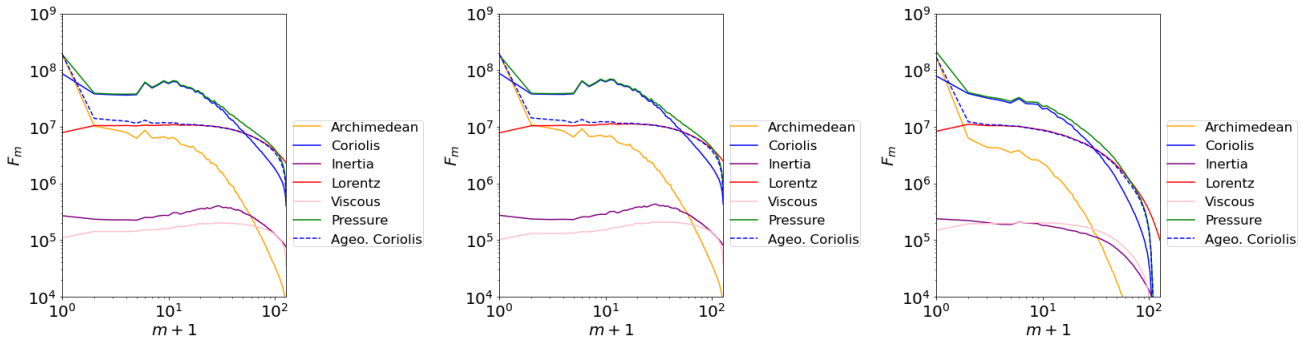

(a) Total (b) OTC (c) ITC

Figure 6.9: Force density spectra. Dynamo solution for strong field dipolar run at $E = 10^{-5}$, $Ra = 4Ra_c$ and $Pm = 5$. All quantities are time averaged and boundary layers have been removed.

The results at $E = 10^{-5}$ are similar to those discussed at $E = 10^{-4}$. The hydrodynamical cases and dynamo solutions at $E = 10^{-4}$ and $E = 10^{-5}$ show no significant difference in the regions ITC and OTC. The most notable differences are the increased inertial force ITC compared with OTC for the multipolar runs and hydrodynamical runs at large Ra (i.e. $Ra = 30Ra_c$) and there is a tendency for the forces to decrease at a larger scale ITC compared with OTC. In particular, the buoyancy drops off at a much larger scale ITC than OTC. For all cases examined, the behaviour of the forces OTC matches the behaviour across the total shell, which tells us that the behaviour OTC is primarily controlling the dynamics of the flow.

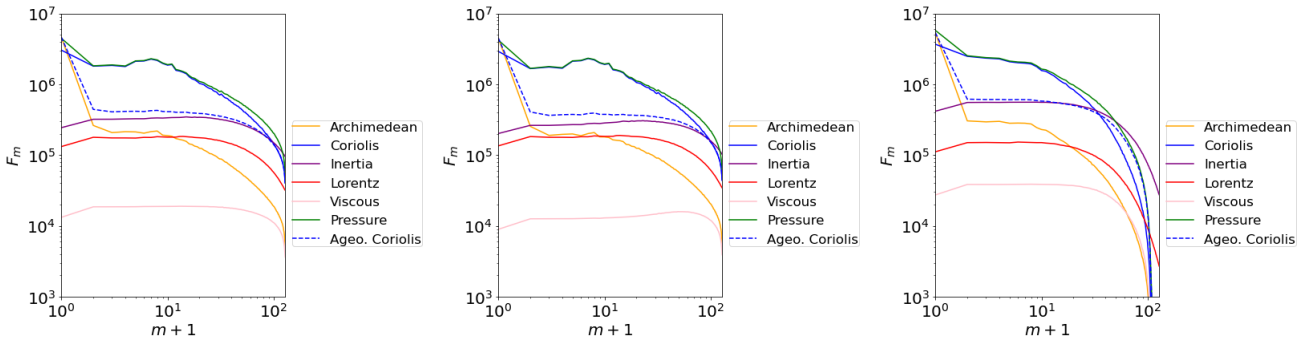

(a) Total (b) OTC (c) ITC

Figure 6.10: Force density spectra. Dynamo solution for fluctuating multipolar run at $E = 10^{-5}$, $Ra = 100Ra_c$ and $Pm = 0.2$. All quantities are time averaged and boundary layers have been removed.

6.2 Comparison of curl of force density spectra

The curl of forces are examined for hydrodynamical runs at $E = 10^{-4}$ and for dynamo solutions at $E = 10^{-4}$ and $E = 10^{-5}$. The similarities and differences between the behaviour ITC and OTC are discussed. We expect to recover the first order balance occurring in the force density spectra in Section 6.1 at leading order in the curl spectra, as the pressure gradient has been removed. The curl density spectra presented in this section match the hierarchy of curls of forces discussed in Section 5.2, confirming that the alternative method, which is discussed in Section 2.2.3 where the m-dependence is computed by moving from a spherical to cylindrical grid, provides the correct results.

6.2.1 Hydrodynamical solutions at $E = 10^{-4}$

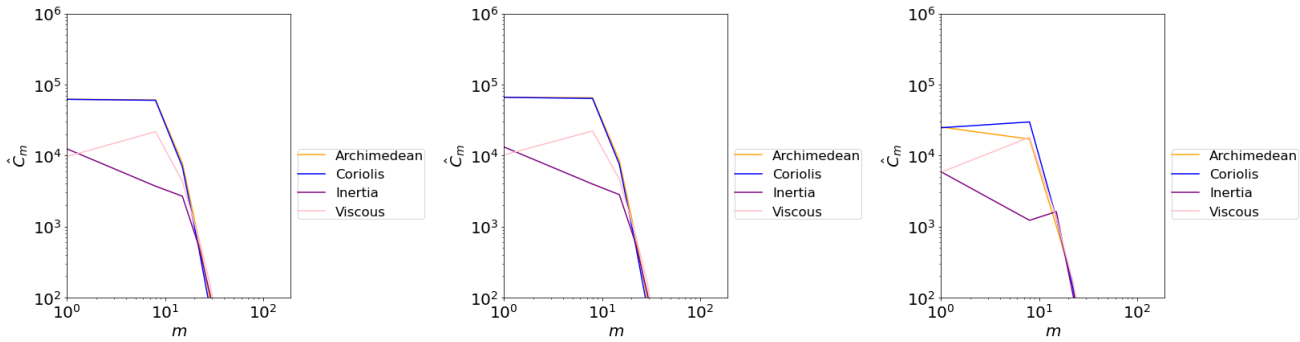

(a) Total (b) OTC (c) ITC

Figure 6.11: Curl density spectra. Hydrodynamical run at $E = 10^{-4}$ and $Ra = 2Ra_c$. All quantities are time averaged and boundary layers have been removed. Only every $7m$ mode is plotted.

At low Ra (Fig. 6.11) a balance between Coriolis and buoyancy forces occurs. Similar to the force density spectra, the behaviour OTC (Fig. 6.11b) is similar to the total shell (Fig. 6.11a). The Coriolis and buoyancy forces are still in balance ITC but have decreased in magnitude, and are balanced by the viscous force at some scales, including near the peak in the spectra

(Fig. 6.11c). At $Ra = 5Ra_c$, a balance between Coriolis and buoyancy forces occurs across the total shell (Fig. 6.12a) with similar behaviour occurring OTC (Fig. 6.12b). A slight increase in the viscous force is observed ITC (Fig. 6.12c). At $Ra = 30Ra_c$, we no longer obtain a balance between Coriolis and buoyancy forces. Instead the inertial force dominates OTC (Fig. 6.13b) and ITC (Fig. 6.13c). OTC the inertial force dominates at all scales with the Coriolis force also strong but never entering the main balance. ITC the inertial force remains strong but is balanced at large scales by the Coriolis force, despite the fact that in the forces, ITC showed the biggest increase in inertia.

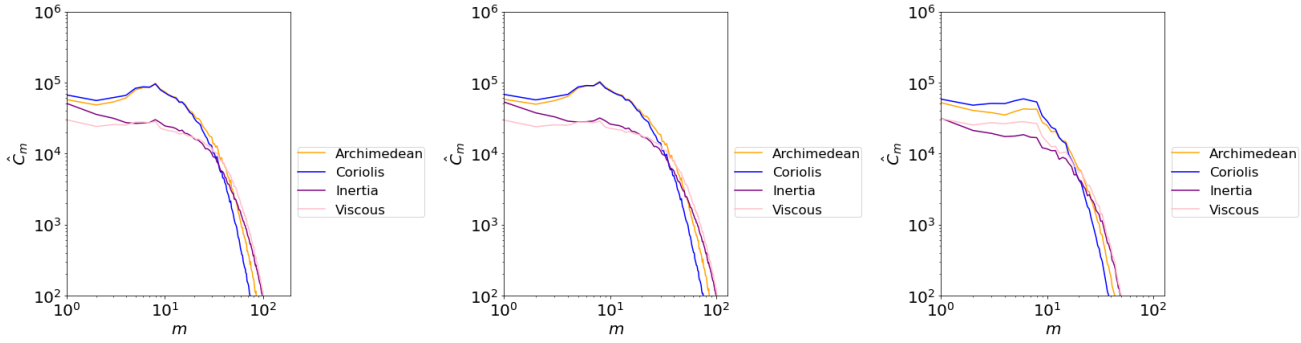

(a) Total (b) OTC (c) ITC

Figure 6.12: Curl density spectra. Hydrodynamical run at $E = 10^{-4}$ and $Ra = 5Ra_c$. All quantities are time averaged and boundary layers have been removed.

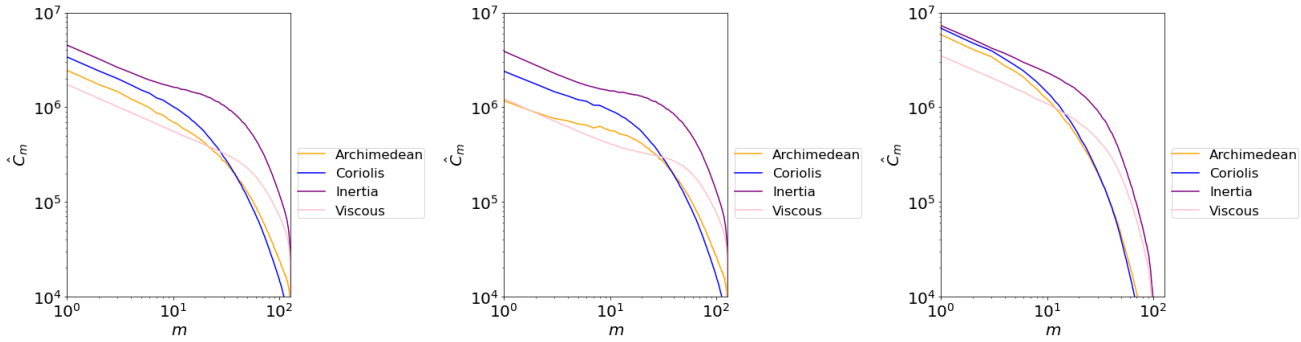

(a) Total (b) OTC (c) ITC

Figure 6.13: Curl density spectra. Hydrodynamical run at $E = 10^{-4}$ and $Ra = 30Ra_c$. All quantities are time averaged and boundary layers have been removed.

6.2.2 DYNAMO SOLUTIONS AT $E = 10^{-4}$

The weak field dipolar run at $E = 10^{-4}$ and $Ra = 2.07Ra_c$ (Fig. 6.14) behaves similarly to the hydrodynamical case at low Ra (Fig. 6.11) with the addition of a weak Lorentz force. For the strong field dipolar run at $E = 10^{-4}$ and $Ra = 2.07Ra_c$ (Fig. 6.15) the behaviour changes. The behaviour of the curl of forces OTC (Fig. 6.15b) matches those across the total shell (Fig. 6.15a). A balance between Coriolis and Lorentz terms is obtained OTC which is balanced by the buoyancy term at some scales. A balance between Coriolis and Lorentz terms is still found ITC (Fig. 6.15c) but this is never balanced by the buoyancy term at any scale. Instead, a second order balance occurs between buoyancy and viscous forces ITC. For the other strong

field dipolar solution at $Ra = 10Ra_c$ the behaviour OTC (Fig. 6.16b) and ITC (Fig. 6.16c) both match the total curl density (Fig. 6.16a) where a leading order balance between Coriolis and Lorentz terms is now found at both sides of the TC, with a second order balance between buoyancy and viscous terms.

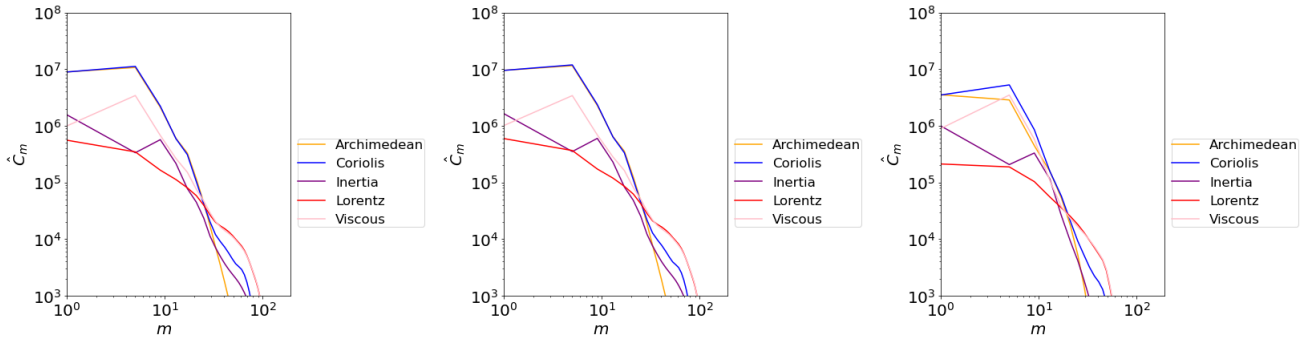

(a) Total (b) OTC (c) ITC

Figure 6.14: Curl density spectra. Dynamo solution for weak field dipolar run at $E = 10^{-4}$, $Ra = 2.07Ra_c$ and $Pm = 12$. All quantities are time averaged and boundary layers have been removed. Only every $4m$ mode is plotted.

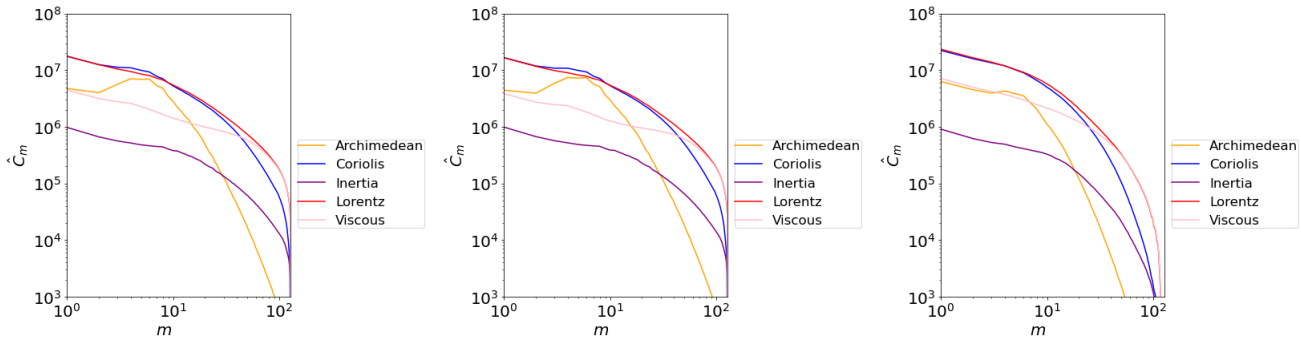

(a) Total (b) OTC (c) ITC

Figure 6.15: Curl density spectra. Dynamo solution for strong field dipolar run at $E = 10^{-4}$, $Ra = 2.07Ra_c$ and $Pm = 12$. All quantities are time averaged and boundary layers have been removed.

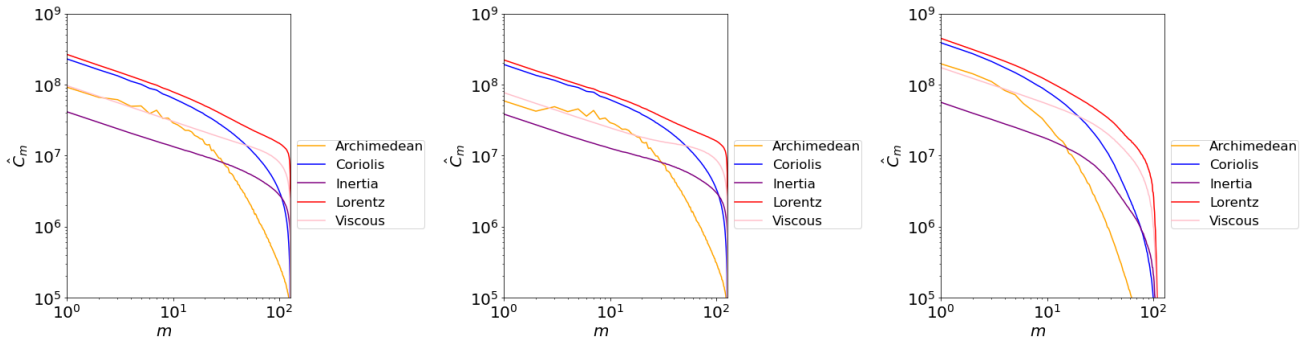

(a) Total (b) OTC (c) ITC

Figure 6.16: Curl density spectra. Dynamo solution for strong field dipolar run at $E = 10^{-4}$, $Ra = 10Ra_c$ and $Pm = 12$. All quantities are time averaged and boundary layers have been removed.

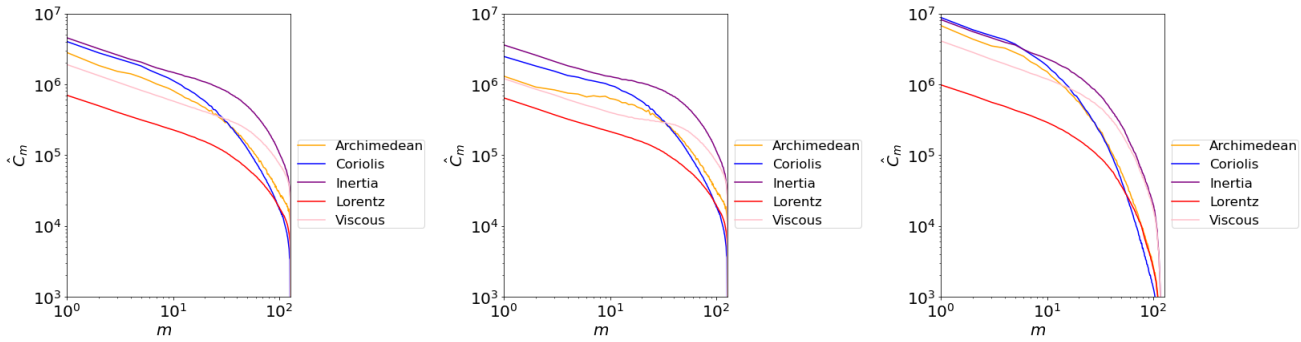

(a) Total (b) OTC (c) ITC

Figure 6.17: Curl density spectra. Dynamo solution for fluctuating multipolar run at $E = 10^{-4}$, $Ra = 30Ra_c$ and $Pm = 1$. All quantities are time averaged and boundary layers have been removed.

For the multipolar run at $E = 10^{-4}$, the balance ITC (Fig. 6.17c) matches the total curl density (Fig. 6.17a) although the force density is larger ITC. At large scales there is a balance between Coriolis and inertial forces with the Coriolis force dropping out at smaller scales. The buoyancy is also strong but never enters the main balance. The behaviour OTC (Fig. 6.17b) is similar to the region ITC. However OTC the inertial term dominates throughout and although the Coriolis term is also strong, it does not balance the inertial force at any scale. This is unlike the region ITC where both terms are in balance at large scales.

6.2.3 DYNAMO SOLUTIONS AT $E = 10^{-5}$

The behaviour OTC for the weak field dipolar run at $E = 10^{-5}$ (Fig. 6.18b) matches the total curl density (Fig. 6.18a) where for the peak scales the Coriolis and buoyancy terms balance and for the largest scales a MAC balance occurs. The small scales show a balance between Lorentz and Coriolis terms. In the region ITC (Fig. 6.18c) the Coriolis and Lorentz terms are in balance for almost all lengthscales. A balance between buoyancy and viscous forces occurs at second order. Although this solution lies on the weak field branch it is clear, especially from the balance ITC, that the Lorentz term has become more important as it enters the main balance at some scales. Figure 6.19 shows a strong field dipolar solution where the behaviour OTC (Fig. 6.19b) matches the behaviour across the total shell (Fig. 6.19a). In all cases a leading order balance occurs between Coriolis and Lorentz terms at all scales. The buoyancy term is also large but never enters the main balance.

For the multipolar run all three regions display a dominant inertial force but some subtle differences occur at second order. Similar to the multipolar run at $E = 10^{-4}$ and the hydrodynamical run at large Ra, the behaviour OTC (Fig. 6.20b) differs slightly to the behaviour across the total shell (Fig. 6.20a). Across the total shell, the inertial term dominates at all scales, and a large Coriolis term is also found but never enters the leading order balance. The buoyancy term is also relatively important and viscous and Lorentz terms remain weak. In the region OTC, inertial and Coriolis terms remain important but a decrease in the buoyancy term occurs and

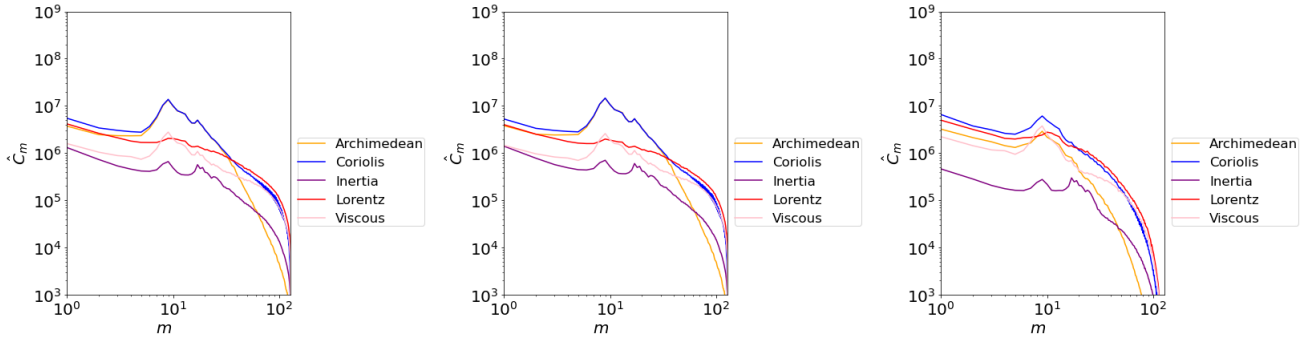

(a) Total (b) OTC (c) ITC

Figure 6.18: Curl density spectra. Dynamo solution for weak field dipolar run at $E = 10^{-5}$, $Ra = 3Ra_c$ and $Pm = 5$. All quantities are time averaged and boundary layers have been removed.

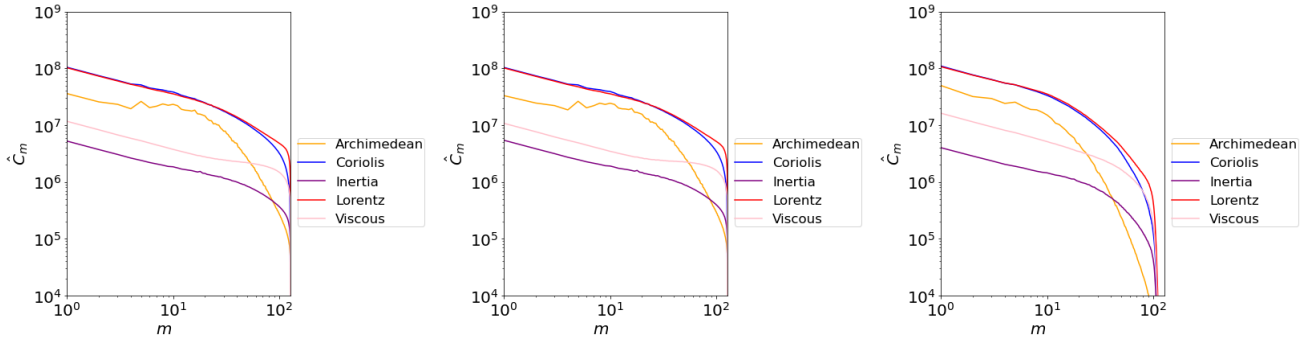

(a) Total (b) OTC (c) ITC

Figure 6.19: Curl density spectra. Dynamo solution for strong field dipolar run at $E = 10^{-5}$, $Ra = 4Ra_c$ and $Pm = 5$. All quantities are time averaged and boundary layers have been removed.

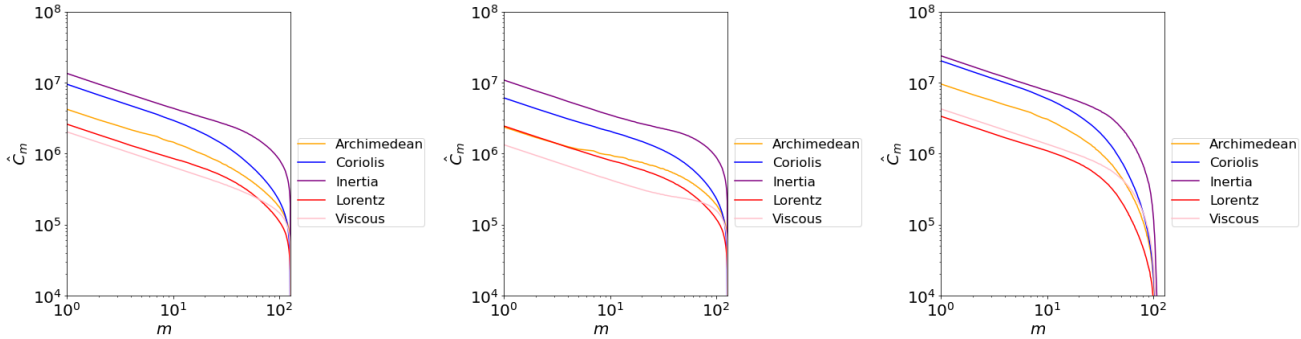

(a) Total (b) OTC (c) ITC

Figure 6.20: Curl density spectra. Dynamo solution for fluctuating multipolar run at $E = 10^{-5}$, $Ra = 100Ra_c$ and $Pm = 0.2$. All quantities are time averaged and boundary layers have been removed.

now balances the Lorentz force. The viscous term remains unimportant. The region ITC (Fig. 6.20c) shows an increase magnitude of inertial and Coriolis terms and are nearly in balance but the inertial term remains most important. The buoyancy term is relatively important, similar to the region OTC but the Lorentz term becomes less important ITC.

Although small differences are obtained in the regions ITC and OTC, the main balance expected in the three main regimes of dynamo action appear both ITC and OTC. The biggest differences occur in the multipolar regime where both regions remain inertially dominated with small changes in the hierarchy of terms at second order.

6.3 TRANSITIONS BETWEEN DIFFERENT REGIMES OF DYNAMO ACTION

In this section, the transition between different branches of solutions is explored. Two cases are examined: from weak field dipolar to multipolar, and from strong field dipolar to multipolar. We start from input parameters of a known multipolar solution and give the initial state as either a weak dipolar state or a strong dipolar state. Previous analysis demonstrated that taking the curl reproduced the expected force balance, without being complicated by the pressure gradient at zeroth order. Therefore, when looking at these solutions, only the curls of forces are presented. To determine the dipolarity of the solution, we examine the dipolarity of the field f_{dip} and the Gauss coefficients. The parameter $f_{dip} \in [0, 1]$ measures the dipolarity of the magnetic field with a value close to 1 being dipolar and a value close to 0 being multipolar. The magnetic energy E_M is also presented. These output parameters were discussed in Section 2.2.3.3.

6.3.1 FROM WEAK FIELD DIPOLAR TO MULTIPOLAR

A solution is tracked as it transitions from weak field dipolar to multipolar. The input parameters are $E = 10^{-4}$, $Pr = 1$, $Pm = 1$ and $Ra = 30Ra_c$ and the run has been initialised from the output state of a weak field dipolar solution with input parameters $E = 10^{-4}$, $Pr = 1$, $Pm = 1$ and $Ra = 20Ra_c$. We provide snapshots of the curl density spectra, meridional sections of u_ϕ and spherical surface plots of B_r that are representative of the changes as it transitions from the weak field dipolar regime to the multipolar regime.

The time series plots of E_M, f_{dip} and the Gauss coefficients show the solution changing from a dipolar to a multipolar solution. At the beginning, $f_{dip} \approx 0.8$ and as the simulation moves forward in time f_{dip} decreases significantly. The multipolar nature of the solution is also clear from the Gauss coefficients where, at the start, g_{10} which is the dipole component dominates and as the solution reaches the multipolar state both g_{10} and g_{20} fluctuate around zero. From the outset the inertial force is in the main balance (Fig. 6.22) combined with Lorentz, buoyancy and Coriolis terms, occurring in the regions ITC (Fig. 6.22c) and OTC (Fig. 6.22b). At $\times_2$, the magnetic energy has decreased significantly but f_{dip} still remains relatively large. The curls of forces change from those at $\times_1$, where the inertial term now dominates and the Lorentz term has decreased significantly across the total shell. The buoyancy and Coriolis terms remain large but do not balance with the dominant inertial term at any scale (Fig. 6.23a). This is also the case OTC (Fig. 6.23b). The behaviour ITC is still dominated by the inertial term but this is balanced by Coriolis and buoyancy terms at large scales (Fig. 6.23c). Eventually the solution settles to a multipolar state which can be observed in the time series of f_{dip} and Gauss

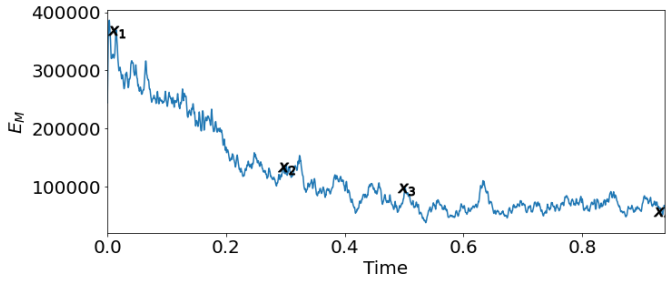

(a) Time series of E_M

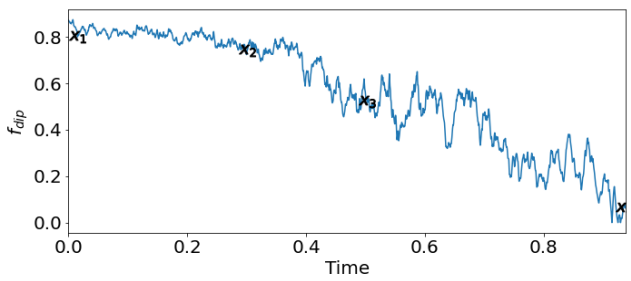

(b) Time series of f_{dip}

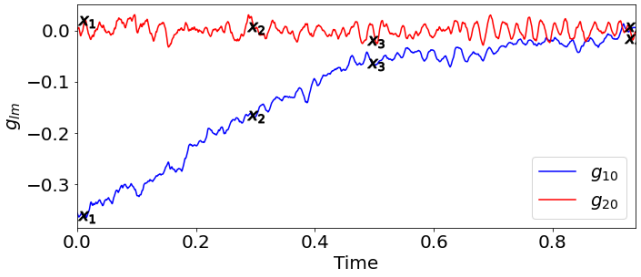

(c) Time series of Gauss coefficients

Figure 6.21: Time series of magnetic energy, dipolarity and Gauss coefficents. Transition from weak field dipolar to multipolar regime with input parameters $E = 10^{-4}$, $Pr = 1$, $Pm = 1$ and $Ra = 30Ra_c$. Curls of forces are shown below at points marked with a cross.

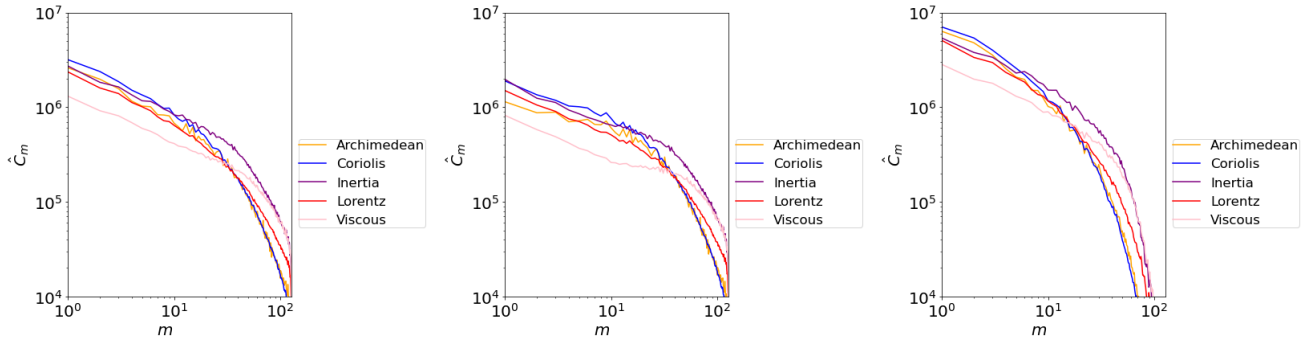

(a) Total (b) OTC (c) ITC

Figure 6.22: Curl density spectra at $\times_1$ marked on Fig. 6.21 for weak field dipolar to multipolar transition.

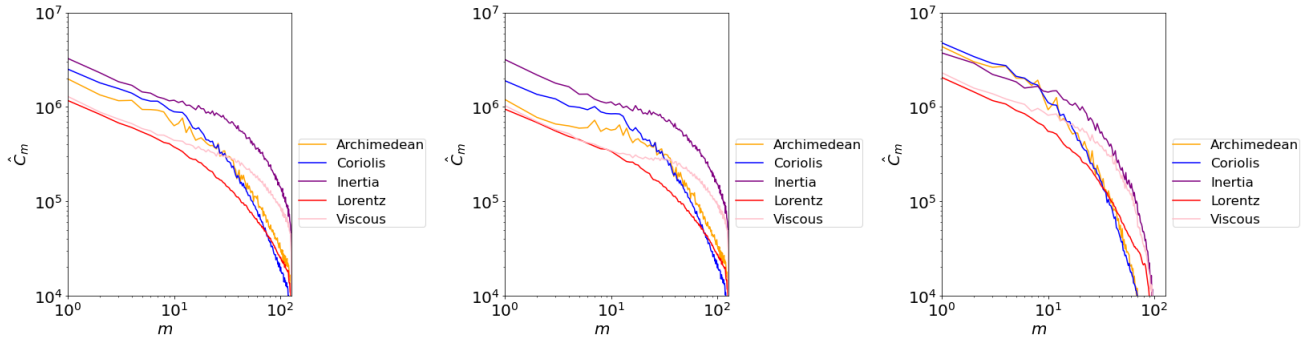

(a) Total (b) OTC (c) ITC

Figure 6.23: Curl density spectra at $\times_2$ marked on Fig. 6.21 for weak field dipolar to multipolar transition.

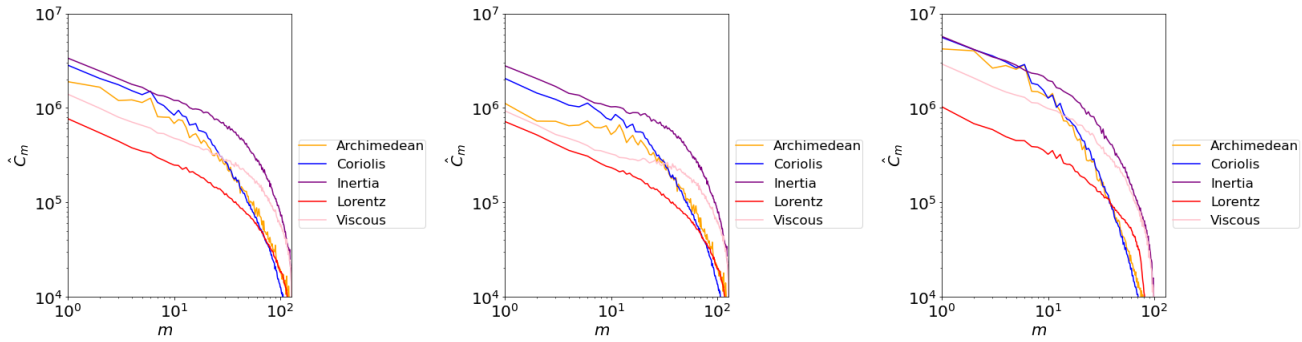

(a) Total (b) OTC (c) ITC

Figure 6.24: Curl density spectra at $\times_3$ marked on Fig. 6.21 for weak field dipolar to multipolar transition.

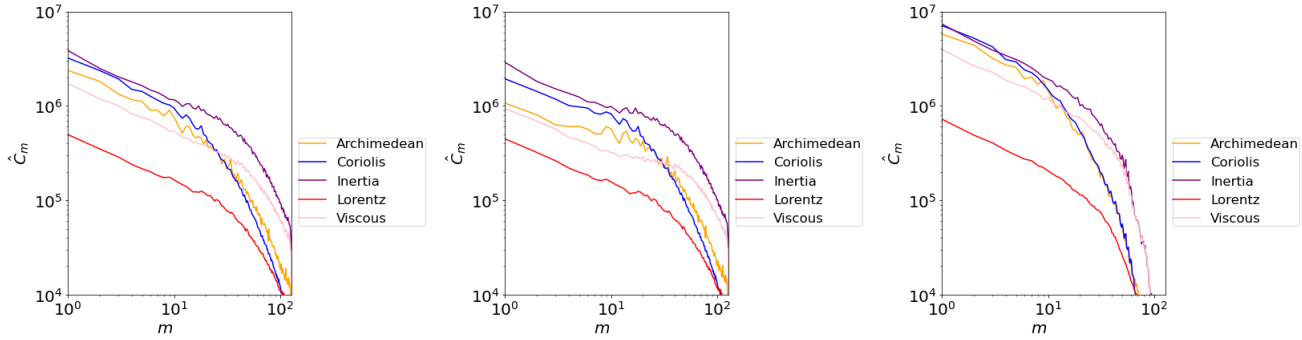

(a) Total (b) OTC (c) ITC

Figure 6.25: Curl density spectra at $\times_4$ marked on Fig. 6.21 for weak field dipolar to multipolar transition.

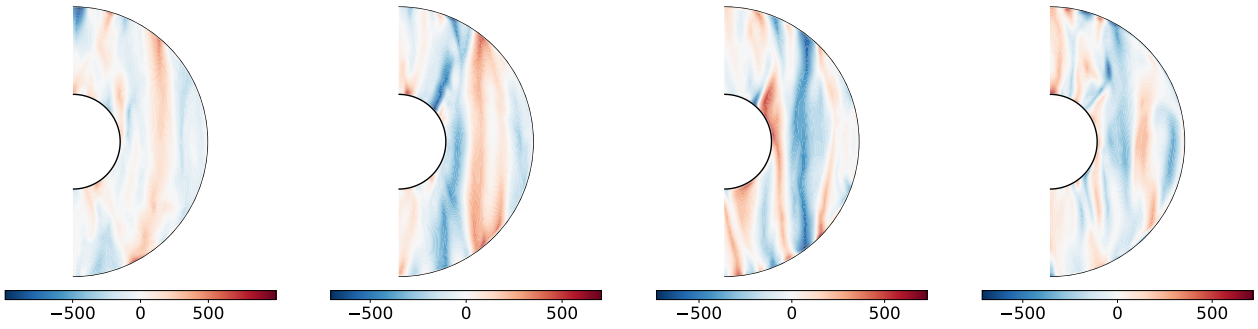

(a) $\times_1$ (b) $\times_2$ (c) $\times_3$ (d) $\times_4$

Figure 6.26: Meridional sections of u_ϕ for weak field dipolar to multipolar transition. All plots are ϕ averaged. Points $\times_1$, $\times_2$, $\times_3$ and $\times_4$ correspond to the points marked on Fig. 6.21.

coefficients (Figs 6.21b, 6.21c). At $\times_3$ and $\times_4$, the curls of forces are inertially dominated both ITC and OTC with a weak Lorentz term (Figs 6.24, 6.25). Overall, no significant differences in the curl of forces ITC and OTC are found. However, the Lorentz term reduces more rapidly and the inertial term increases more rapidly ITC before OTC catches up. In both regions the system is in an inertially dominated regime which persists as the simulation moves forward in time.

The flow patterns and magnetic field at $\times_1$ (Figs 6.26a, 6.27a) match those of a weak field

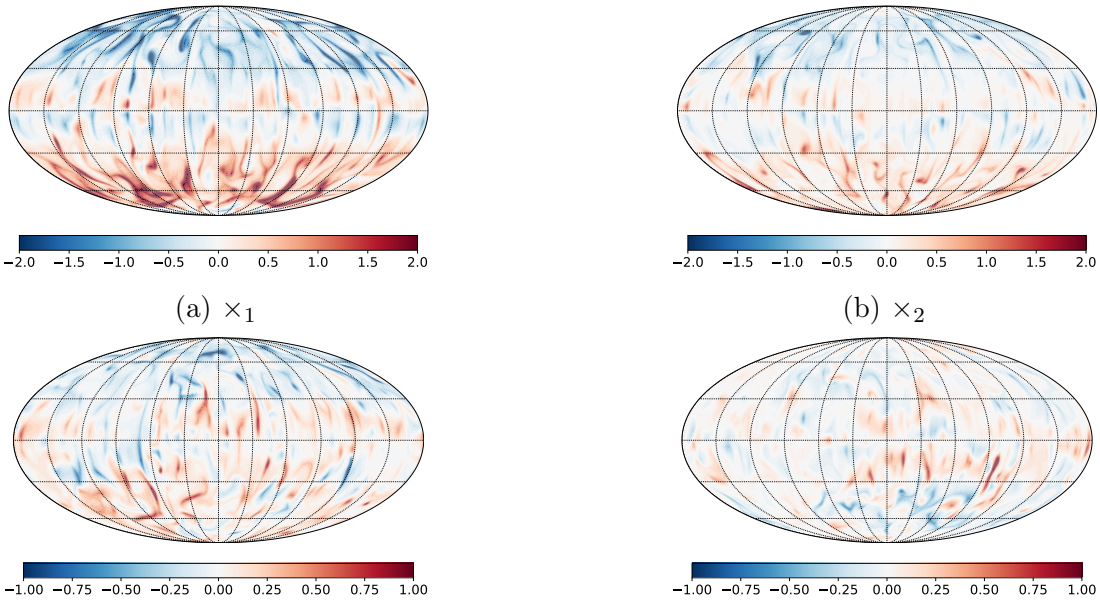

(a) $\times_1$ (b) $\times_2$

(c) $\times_3$ (d) $\times_4$

Figure 6.27: Spherical surface of B_r at $r = r_o$ for weak field dipolar to multipolar transition. Points $\times_1$, $\times_2$, $\times_3$ and $\times_4$ correspond to the points marked on Fig. 6.21.

dipolar solution discussed in Chapter 5 (e.g. Figs 5.16a, 5.17a). As the simulation is integrated forward in time, the solution transitions from a dipolar field to a multipolar field, as shown in the snapshots of the field in Figures 6.27a - 6.27d. The simulation reaches a state similar to the multipolar regime discussed in Chapter 5 (Figs 5.16d, 5.17d).

6.3.2 FROM STRONG FIELD DIPOLAR TO MULTIPOLAR

The transition from a strong field dipolar solution to a multipolar solution is analysed. The input parameters are $E = 10^{-4}$, $Pr = 1$, $Pm = 1$ and $Ra = 30Ra_c$ and the run has been initialised from the output state of a strong field dipolar solution at $E = 10^{-4}$, $Pr = 1$, $Pm = 12$ and $Ra = 20Ra_c$. Similarly to the previous case examined, snapshots are provided of the curl density spectra, meridional sections of u_ϕ and spherical surface plots of B_r that are representative of the changes as the solution transitions from the strong field dipolar regime to the multipolar regime.

The time series plots of E_M, f_{dip} and the Gauss coefficients show the solution changing from a dipolar to a multipolar solution. At the beginning, $f_{dip} \approx 0.6$ and as the simulation moves forward in time, an increase to $f_{dip} \approx 0.8$ occurs before decreasing significantly. The multipolar nature of the solution is also clear from the Gauss coefficients where, at the start, g_{10} dominates and as the solution reaches the multipolar state both g_{10} and g_{20} fluctuate around zero.

Initially a strong field dipolar solution is obtained (Fig. 6.29) as a MAC balance occurs. The inertial term is also stronger than has been observed previously in strong field solutions but this is unsurprising given the input parameters of the solution. The behaviour OTC (Fig. 6.29b) is similar to the behaviour across the entire shell (Fig. 6.29a). At $\times_2$, the value of

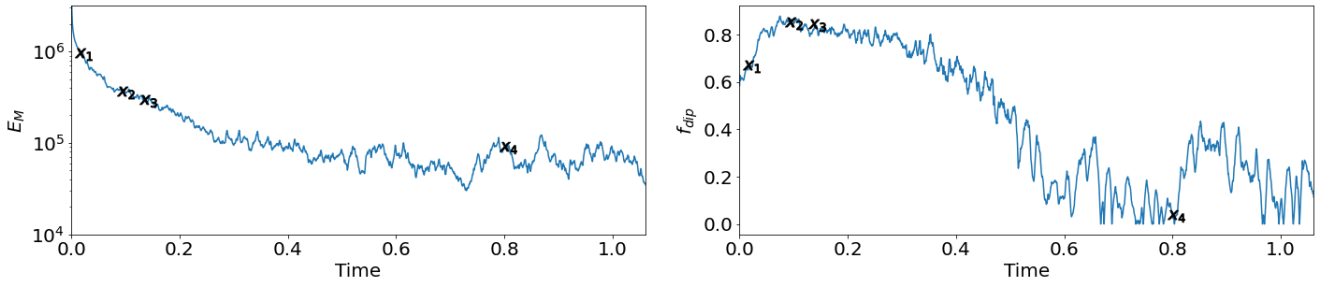

(a) Time series of E_M (b) Time series of f_{dip}

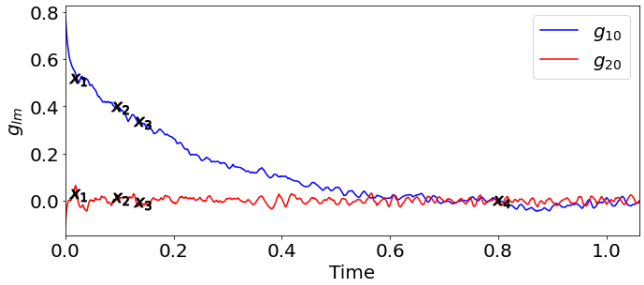

(c) Time series of Gauss coefficients

Figure 6.28: Time series of magnetic energy, dipolarity and Gauss coefficents. Transition from strong field dipolar to multipolar regime with input parameters $E = 10^{-4}$, $Pr = 1$, $Pm = 1$ and $Ra = 30Ra_c$. Curls of forces are shown below at points marked with a cross.

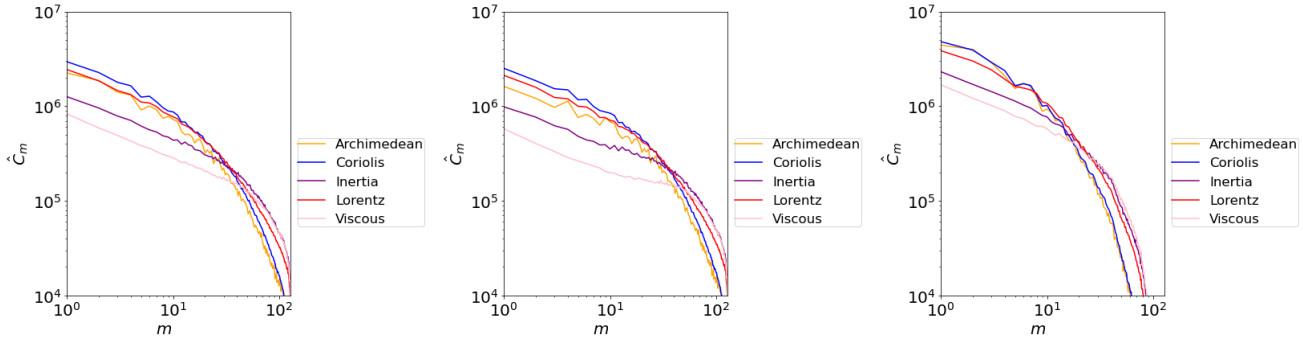

(a) Total (b) OTC (c) ITC

Figure 6.29: Curl density spectra at $\times_1$ marked on Fig. 6.28 for strong field dipolar to multipolar transition.

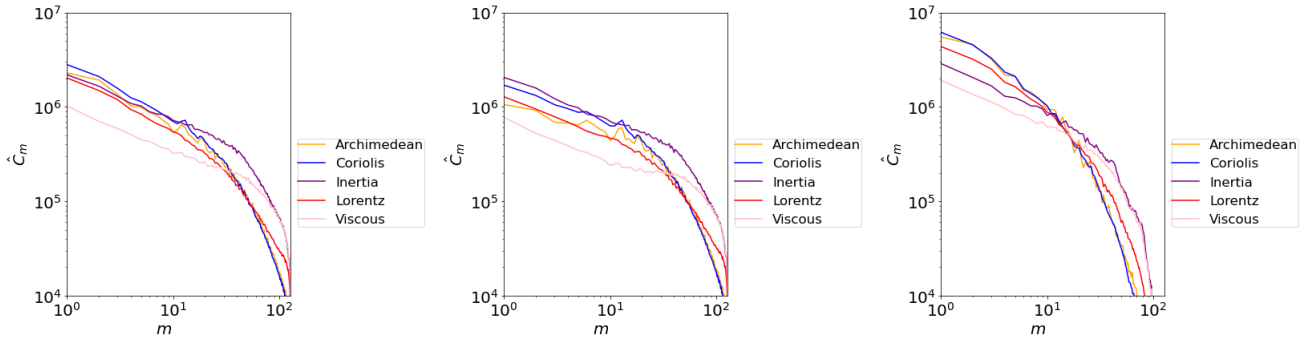

(a) Total (b) OTC (c) ITC

Figure 6.30: Curl density spectra at $\times_2$ marked on Fig. 6.28 for strong field dipolar to multipolar transition.

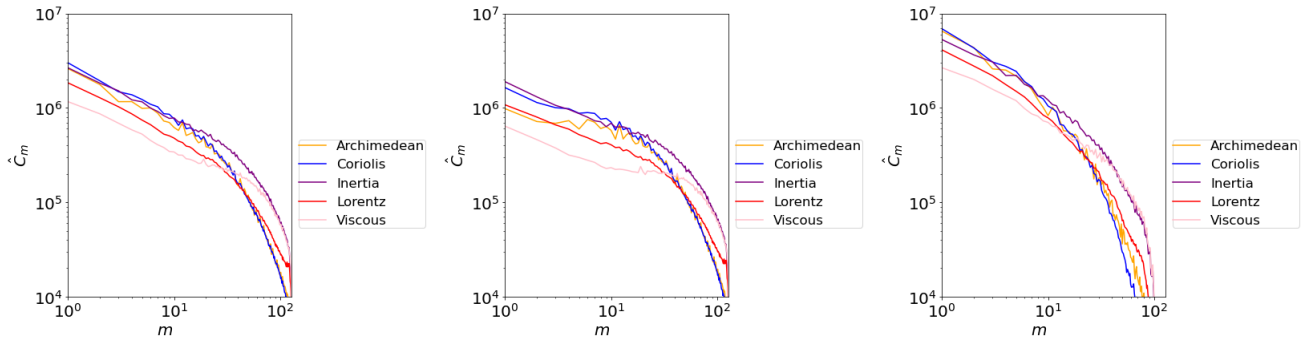

(a) Total (b) OTC (c) ITC

Figure 6.31: Curl density spectra at $\times_3$ marked on Fig. 6.28 for strong field dipolar to multipolar transition.

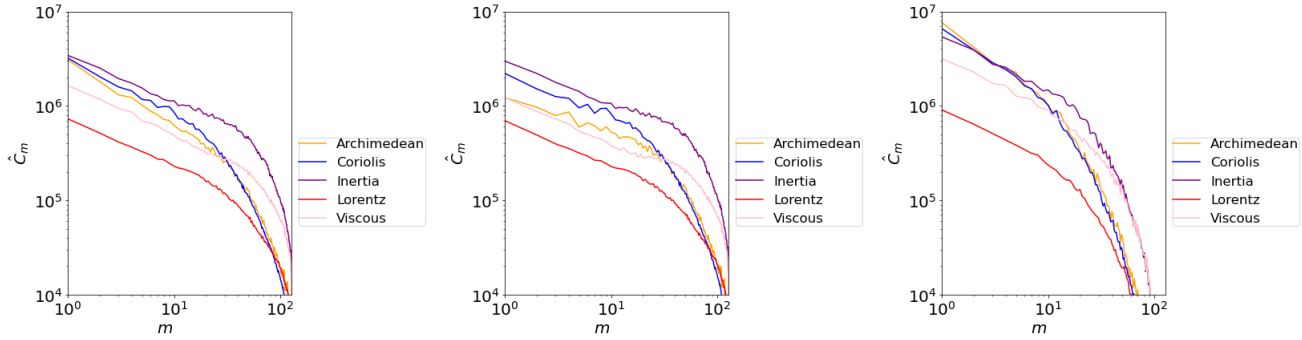

(a) Total (b) OTC (c) ITC

Figure 6.32: Curl density spectra at $\times_4$ marked on Fig. 6.28 for strong field dipolar to multipolar transition.

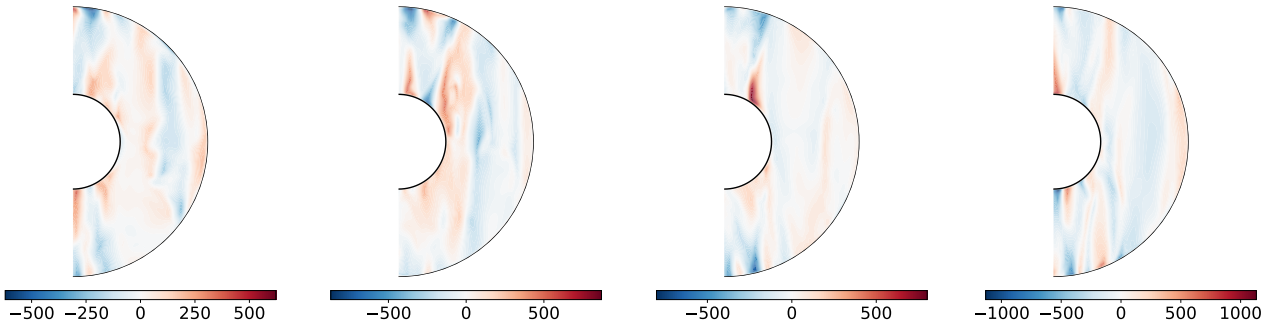

(a) $\times_1$ (b) $\times_2$ (c) $\times_3$ (d) $\times_4$

Figure 6.33: Meridional sections of u_ϕ for strong field dipolar to multipolar transition. All plots are ϕ averaged. Points $\times_1$, $\times_2$, $\times_3$ and $\times_4$ correspond to the points marked on Fig. 6.28.

f_{dip} increases slightly but both the magnetic energy and g_{10} decrease. This suggests that the total energy in the non-axial dipole components must be significantly reduced between $\times_1$ and $\times_2$. The system is possibly first adapting to the change in Pm so is reconfiguring to a weak dipolar branch solution, given the increase in f_{dip}, before moving to the multipolar branch. At this point, a change in the forces controlling the dynamics of the flow is observed. The global behaviour of the curl spectra is unclear (Fig. 6.30a) as all terms except the viscous term are impacting the flow, at least at the largest scales. ITC a MAC balance is still observed at the

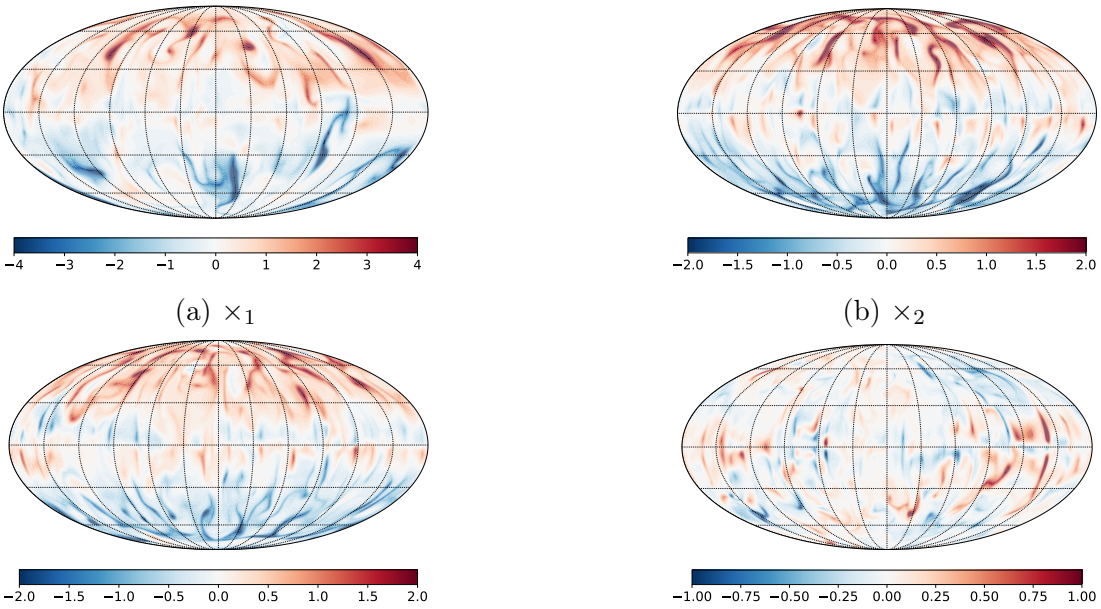

(a) $\times_1$ (b) $\times_2$

(c) $\times_3$ (d) $\times_4$

Figure 6.34: Spherical surface of B_r at $r = r_o$ for strong field dipolar to multipolar transition. Points $\times_1$, $\times_2$, $\times_3$ and $\times_4$ correspond to the points marked on Fig. 6.28.

largest scales (Fig. 6.30c) but OTC the flow is in an inertially dominated regime as the inertial term is in the main balance with the Coriolis force (Fig. 6.30b). At $\times_3$ the system transitions to an inertially dominant regime ITC (Fig. 6.31c) and the behaviour across the total shell (Fig. 6.31a) now resembles the forces in the multipolar regime. At $\times_4$, the system is now clearly in the multipolar regime, where the forces OTC and ITC (Fig. 6.32b, 6.32c) resemble the global behaviour (Fig. 6.32a) and are also similar to those shown in Figure 6.25 as expected.

The behaviour of the different states can also be observed from the flow patterns and magnetic field. Meridional sections of u_ϕ at $\times_1$ and $\times_2$ (Figs 6.33a, 6.33b) show similar flow patterns to strong field dipolar runs discussed in Chapter 5 (e.g. Fig. 5.16c). The magnetic field at these points is dipolar (Figs 6.34a, 6.34b), although the field has decreased in strength slightly at $\times_2$, which is expected given the decrease in g_{10}. At $\times_3$ where the behaviour ITC and OTC is inertially dominated, the flow patterns start to change before reaching the multipolar state at $\times_4$ where the flow pattern and magnetic field (Figs 6.33d, 6.34d) are similar to those discussed in Chapter 5 (e.g. Figs 5.16d, 5.17d) and match the same solution reached in Figures 6.26d and 6.27d.

6.4 SUMMARY

In this chapter, the force balances ITC and OTC have been analysed for a small number of simulations. Forces and curls of forces for hydrodynamical solutions at $E = 10^{-4}$ and dynamo solutions at $E = 10^{-4}$ and $E = 10^{-5}$ were discussed. The behaviour ITC and OTC was very similar with both regions showing the balance expected for the given dynamo regime. The terms tended to drop off at a larger scale ITC than OTC and was most apparent in the

buoyancy term. The biggest difference was observed for the multipolar run at $E = 10^{-5}$ where the hierarchy of curl of forces changed. In that case the inertial term dominated ITC and OTC but at lower order the buoyancy and viscous forces increased ITC compared with OTC. This could be due to convection becoming more efficient ITC compared to OTC at large enough Ra (Gastine and Aurnou, 2023).

The transition from a weak field dipolar solution to a multipolar solution did not show differing behaviour ITC and OTC. The inertial term became important in the balance near the beginning and became more dominant as the simulation moved forward in time. This was the case ITC and OTC. This transition only involved altering a single control parameter (Ra). Hence, the transition between the input state and final state may be relatively smooth as a result. However, our analysis from a strong field dipolar to a multipolar solution showed that it is possible to find differences in behaviour ITC and OTC. The solution started from a MAC balance both ITC and OTC. Early in the transition between regimes, the MAC balance persisted ITC but OTC the inertial term entered the main balance and the Lorentz force decreased. This change in behaviour OTC provoked the change in balance globally from a MAC balance to a CIA balance.

Although only one case where significant differences occur ITC and OTC has been found, a way to compute forces and curls of forces in different regions of the spherical shell has been demonstrated which has shown that it is possible for different balances to occur ITC and OTC. We have only examined this for a small number of simulations and analysis of other simulations could be carried out to find differences in behaviour ITC and OTC.

Chapter 7

Conclusion

This chapter concludes the work carried out in this thesis, which has centred on understanding the forces controlling the dynamics of the flow in planetary interiors. Chapters 3 and 4 focused on magnetoconvection in the Busse annulus model, highlighting the force balances responsible for the emergence of multiple jets, bursts of convection, and other solutions. The magnetic field strength and magnetic diffusivity were varied to assess how this influenced multiple jet formation. Chapters 5 and 6 shifted the focus to spherical shell dynamo simulations, where the l and m dependence of forces and curls of forces were examined. Dynamically relevant lengthscales were discussed by forming a triple balance point. These were compared to energetically relevant lengthscales by considering the peak in kinetic energy. The force balances both inside (ITC) and outside the tangent cylinder (OTC) were analysed, identifying transitions between different dynamo regimes and demonstrating how local changes in force balances can drive changes in the system globally.

Our non-linear simulations of convection in the Busse annulus model show good agreement with previous non-magnetic studies (Jones et al., 2003; Rotvig and Jones, 2006; Teed et al., 2012), particularly regarding the emergence of multiple jets and bursts of convection. This thesis extended non-magnetic work by imposing a magnetic field on the system. We were able to identify different force balance regimes, some of which are similar to those observed in dynamo simulations. Solutions dominated by the inertial term were found, similar to the inertially dominated multipolar regime in spherical shell simulations. However, on the fluctuating multipolar branch in dynamo simulations, contributions from the Coriolis and buoyancy terms are usually expected. In the annulus model, this was only found close to critical Ra before the system transitioned to a dominant inertial force at all scales. This could either be due to the different boundary conditions used in the two models, or could be caused by the annular geometry failing to account for an effect due to spherical geometry. Alternatively, the correct region of parameter space to obtain this balance may not have been found. A MAC balance can also be achieved under certain conditions, similar to the MAC balance in the strong dipolar regime. To obtain this balance low Ra and small Pm was required. This balance was not expected, as

the model is geared towards generation of zonal flows through a strong inertial force (even at low driving), which must be absent in the MAC balance.

In the annulus model we studied in detail the effects of an imposed toroidal magnetic field on the production of multiple jets. Recent work has shown that the multiple jets found on the surface of Jupiter extend roughly 3000 kilometres below the surface (Kaspi et al., 2023). Although a simplified model is used in this thesis, the analysis demonstrated that increasing magnetic field strength suppressed multiple jets. This confirms that jets found on Jupiter's surface, where a toroidal field is absent, will likely not penetrate into the metallic hydrogen region where the toroidal field is strong. The mechanism that creates multiple jets seen on Jupiter's surface is a feature of non-magnetic convection and models of the Jovian dynamo struggle to produce multiple jet structures in combination with a strong dipolar magnetic field (e.g., Duarte et al., 2013; Jones, 2014) without invoking the use of a stably-stratified layer (Gastine and Wicht, 2021; Moore et al., 2022). Work in this thesis has shown that it is possible to obtain multiple jets in the presence of a toroidal magnetic field without the need for a stably-stratified layer. However, whether this remains the case when the model is subject to a strong 'poloidal-like' field (as appropriate for the molecular region of Jupiter) and under a wider parameter survey, remains to be seen. Nevertheless, magnetic fields may still have an observable effect on surface features even if they do not contribute to the generation of multiple jets (Hori et al., 2023). The results presented also suggest that zonal flows and multiple jets driven by Reynolds stresses may not be a feature of Earth's core where, like Jupiter, the expected balance of forces is 'MAC'. However, a magnetic or thermal wind driven by, for example, spatially heterogeneous heat flux on the core-mantle boundary, provides an alternative zonal flow generation mechanism within Earth's core (Zhang and Gubbins, 1996). The effects of an imposed magnetic field of different strengths on such a flow would need to be studied using a different set-up to the model discussed here, which assumes fixed temperature conditions. Finally, the magnetic field strengths found to preserve, and even promote, zonal flow and jet production in the annulus model are likely not relevant to many known natural dynamos, which have strong dipolar fields under a 'MAC balance'. However, they may be relevant to weak field spherical dynamos found numerically at low driving (Dormy et al., 2018), or to dynamos of a non-dipolar nature.

Work in the annulus model could be extended in various ways. For simplicity, only a single value of the rotation rate was considered. Although the value chosen was appropriate for the rapidly rotating regimes of planetary atmospheres and Earth's core, it should be varied to confirm existing results more widely. A second widely observed phenomenon of non-magnetic convection in the annulus model is the development of bursts of convection, interrupted by periods of strong zonal flows (Jones et al., 2003; Rotvig and Jones, 2006; Teed et al., 2012). Such behaviour has been observed in this thesis, but a detailed study has been left for future work. The annulus model with an imposed magnetic field is known to admit various MHD waves (Hori et al., 2014) including the slow magnetic Rossby waves that are thought to be important in Earth's core and planetary atmospheres (Hori et al., 2018). The model may therefore be

appropriate for studying the non-linear behaviour of such waves in a simplified setting. In this work an imposed azimuthal (i.e. *toroidal*) magnetic field has been chosen. Other options of field morphology are possible but this configuration was focused on both for mathematical simplicity and because of the strong toroidal fields expected to be found in Earth's core and planetary atmospheres where magnetic field generation occurs.

In the spherical shell model, the l-dependence and m-dependence of forces showed good agreement where both showed a similar hierarchy of forces and both were representative of the forces controlling the flow dynamics. Similarly, the l-dependence of curls of forces matched well with the equivalent m-dependence and curls offered a cleaner way of representing the forces controlling the behaviour of the system (Teed and Dormy, 2023). Spherical shell simulations discussed weak field dipolar, strong field dipolar, multipolar and hydrodynamical solutions (Teed and Dormy, 2025). The dynamo solutions presented, demonstrated that decreasing the Ekman number still produced the relevant force balances in each regime of dynamo action, although the multipolar regime was harder to reach at lower Ekman number as stronger driving was required. We were able to extract a dynamically relevant lengthscale from these simulations by forming a triple balance point of (curls of) forces. This work extended and refined that of Schwaiger et al. (2021) where they examined only horizontal lengthscales (i.e. l-space), only the forces themselves and did not distinguish between the distinct branches of dynamo action. Results in this thesis showed that for certain regimes the triple balance point between curls of forces determined the convective lengthscale. This method worked for the strong field dipolar regime, multipolar regime, and the large Ra hydrodynamical states. A method for examining the force balances ITC and OTC has also been demonstrated. The behaviour ITC and OTC were very similar, with both regions showing the balance of forces expected for the given dynamo regime. Analysis of a transition from a strong field dipolar to a multipolar solution showed that it was possible to find differences in behaviour of the force hierarchy ITC and OTC. The solution started from a MAC balance at leading order with contributions from the inertial term, both ITC and OTC. Early in the transition between regimes, the MAC balance persisted at large scales ITC but OTC the inertial term entered the main balance and the Lorentz force decreased. This change in behaviour OTC provoked the change in balance globally from a MAC balance to a CIA balance.

The spherical shell simulations could also be extended in future work. In this study, triple balance points were computed and compared with the peaks in kinetic energy. For weak field dipolar runs exhibiting a VAC balance, no relationship was obtained between the dynamically relevant lengthscales and the kinetic energy peak. This may be due to the absence of boundary layers in these simulations. To confirm this, further analysis would be required to assess whether the inclusion of boundary layers allows dynamically relevant lengthscales in weak field regimes to align more closely with energetically relevant lengthscales. Simulations at $E = 10^{-4}$ and $E = 10^{-5}$ were examined. Further studies could apply the methods developed in this thesis as one way to determine strong field or multipolar regimes at lower E. Only a small set of simulations

were analysed for the behaviour of forces ITC and OTC, but these were able to demonstrate differing behaviour between the different domains. In particular, changes were observed in force balances when transitioning from the strong field dipolar branch to the multipolar branch. However, this transition is not likely to be relevant for the geodynamo as the inertia plays too large a role in multipolar simulations. Instead the weak to strong field transition could be examined as this may be more applicable to the geodynamo, since it is likely that this is the route the geodynamo took after onsetting on the weak field branch. In this work, the aspect ratio between the inner and outer core was fixed. However, Earth's inner core is known to be expanding. If the weak to strong field transition is to be modelled more realistically, a different aspect ratio to the one used in current simulations may be required to reflect the early growth of Earth's inner core as the geodynamo transitioned from the weak field to the strong field branch. It has also been suggested that reversals of the dipole may be triggered by differing behaviour either side of the tangent cylinder (e.g., Rotvig, 2009), meaning that the regime briefly changes to multipolar in one part of the domain, which, after a delay, also affects the rest of the solution. Then, when the dipole solution recovers, it may do so in the reversed configuration. Results presented here have shown that for a period of time it is possible to have the force balance for the strong field branch in one part of the domain and the balance for the multipolar branch in another part of the domain. Although the transition found in this study is not realistic as it requires an order of magnitude change in Pm, it does suggest that with further investigation it may be possible to find similar behaviour without varying Pm.

The two models discussed in this thesis differ significantly, both in geometry and setup. The annulus model employs a cylindrical geometry with an imposed magnetic field, whereas the spherical shell model uses a spherical geometry and allows for self-sustained dynamo action. Due to its simplified setup, the annulus model allows a broader exploration of parameter space than is feasible in spherical geometry. Despite its simplicity, this work has shown that the annulus model can reproduce force balances similar to those observed in key dynamo regimes of spherical shell models. In particular, regimes dominated by CIA and MAC balances were identified, analogous to the multipolar and strong field dipolar branches, respectively. This suggests that the annulus model could serve as a valuable tool for guiding parameter studies in numerically demanding spherical dynamo simulations. By identifying regions of parameter space that provide the desired force balance, such as that expected in Earth's core, the annulus model could help to optimise parametric studies in spherical simulations. The methods developed which related triple balance points to energetic lengthscales could also be used to aid identification of different dynamo regimes. The impact of magnetic fields on the development of multiple jets and zonal flows has also been examined. Since reproducing multiple jets remains a challenge in spherical geometry, the annulus model may provide a foundation for investigating the conditions required for their formation in more complex systems, both in terms of parameters and force balances required.

Bibliography

Aubert, J. (2019). Approaching earth's core conditions in high-resolution geodynamo simulations. *Geophysical Journal International 219*(Supplement_1), S137–S151.

Aubert, J. (2023). State and evolution of the geodynamo from numerical models reaching the physical conditions of earth's core. *Geophysical Journal International 235*(1), 468–487.

Aubert, J., T. Gastine, and A. Fournier (2017). Spherical convective dynamos in the rapidly rotating asymptotic regime. *Journal of Fluid Mechanics 813*, 558–593.

Aubert, J. and N. Gillet (2021). The interplay of fast waves and slow convection in geodynamo simulations nearing earth's core conditions. *Geophysical Journal International 225*(3), 1854–1873.

Aubert, J., P. W. Livermore, C. C. Finlay, A. Fournier, and N. Gillet (2022). A taxonomy of simulated geomagnetic jerks. *Geophysical Journal International 231*(1), 650–672.

Aujogue, K., A. Pothérat, B. Sreenivasan, and F. Debray (2018). Experimental study of the convection in a rotating tangent cylinder. *Journal of Fluid Mechanics 843*, 355–381.

Aurnou, J., S. Andreadis, L. Zhu, and P. Olson (2003). Experiments on convection in earth's core tangent cylinder. *Earth and Planetary Science Letters 212*(1-2), 119–134.

Backus, G. (1958). A class of self-sustaining dissipative spherical dynamos. *Annals of Physics 4*(4), 372–447.

Batchelor, G. K. (2000). *An introduction to fluid dynamics*. Cambridge university press.

Boussinesq, J. (1903). *Théorie analytique de la chaleur: mise en harmonie avec la thermodynamique et avec la théorie mécanique de la lumière*, Volume 2. Gauthier-Villars.

Brummell, N. H. and J. Hart (1993). High rayleigh number β-convection. *Geophysical & Astrophysical Fluid Dynamics 68*(1-4), 85–114.

Bullard, E. C. and H. Gellman (1954). Homogeneous dynamos and terrestrial magnetism. *Philosophical Transactions of the Royal Society of London. Series A, Mathematical and Physical Sciences 247*(928), 213–278.

Busse, F. H. (1970). Thermal instabilities in rapidly rotating systems. *Journal of Fluid Mechanics 44*(3), 441–460.

Busse, F. H. (1976a). Generation of planetary magnetism by convection. *Physics of the Earth and Planetary Interiors 12*(4), 350–358.

Busse, F. H. (1976b). A simple model of convection in the jovian atmosphere. *Icarus 29*(2), 255–260.

Busse, F. H. and P. Cuong (1977). Convection in rapidly rotating spherical fluid shells. *Geophysical & Astrophysical Fluid Dynamics 8*(1), 17–41.

Busse, F. H. and F. Finocchi (1993). The onset of thermal convection in a rotating cylindrical annulus in the presence of a magnetic field. *Physics of the earth and planetary interiors 80*(1-2), 13–23.

Busse, F. H. and A. Or (1986). Convection in a rotating cylindrical annulus: thermal rossby waves. *Journal of Fluid Mechanics 166*, 173–187.

Cao, H., R. K. Yadav, and J. M. Aurnou (2018). Geomagnetic polar minima do not arise from steady meridional circulation. *Proceedings of the National Academy of Sciences 115*(44), 11186–11191.

Cardin, P. and P. Olson (1995). The influence of toroidal magnetic field on thermal convection in the core. *Earth and Planetary Science Letters 132*(1-4), 167–181.

Chandrasekhar, S. (1961). *Hydrodynamic and hydromagnetic stability*. Clarendon Press.

Childress, S. and A. Soward (1972). Convection-driven hydromagnetic dynamo. *Physical Review Letters 29*(13), 837.

Christensen, U., P. Olson, and G. Glatzmaier (1999). Numerical modelling of the geodynamo: a systematic parameter study. *Geophysical Journal International 138*(2), 393–409.

Christensen, U. R. and J. Aubert (2006). Scaling properties of convection-driven dynamos in rotating spherical shells and application to planetary magnetic fields. *Geophysical Journal International 166*(1), 97–114.

Christensen, U. R., J. Aubert, P. Cardin, E. Dormy, S. Gibbons, G. Glatzmaier, E. Grote, Y. Honkura, C. Jones, M. Kono, et al. (2001). A numerical dynamo benchmark. *Physics of the Earth and Planetary Interiors 128*(1-4), 25–34.

Cowling, T. G. (1933). The magnetic field of sunspots. *Monthly Notices of the Royal Astronomical Society, Vol. 94, p. 39-48 94*, 39–48.

Davidson, P. A. (2017). *Introduction to magnetohydrodynamics*, Volume 55. Cambridge university press.

Dormy, E. (2016). Strong-field spherical dynamos. *Journal of Fluid Mechanics 789*, 500–513.

Dormy, E. (2025). Rapidly rotating magnetohydrodynamics and the geodynamo. *Annual Review of Fluid Mechanics 57*.

Dormy, E., L. Oruba, and L. Petitdemange (2018). Three branches of dynamo action. *Fluid Dynamics Research 50*(1), 011415.

Dormy, E., A. Soward, C. Jones, D. Jault, and P. Cardin (2004). The onset of thermal convection in rotating spherical shells. *Journal of Fluid Mechanics 501*, 43–70.

Duarte, L. D., T. Gastine, and J. Wicht (2013). Anelastic dynamo models with variable electrical conductivity: An application to gas giants. *Physics of the Earth and Planetary Interiors 222*, 22–34.

Elsasser, W. M. (1946a). Induction effects in terrestrial magnetism part i. theory. *Physical Review 69*(3-4), 106.

Elsasser, W. M. (1946b). Induction effects in terrestrial magnetism part ii. the secular variation. *Physical Review 70*(3-4), 202.

Elsasser, W. M. (1947). Induction effects in terrestrial magnetism. part iii. electric modes. *Physical Review 72*(9), 821.

Gastine, T. and J. M. Aurnou (2023). Latitudinal regionalization of rotating spherical shell convection. *Journal of Fluid Mechanics 954*, R1.

Gastine, T. and J. Wicht (2021). Stable stratification promotes multiple zonal jets in a turbulent jovian dynamo model. *Icarus 368*, 114514.

Gauss, C. F. (1839). *Allgemeine theorie des erdmagnetismus*.

Gilbert, W. (1600). *De Magnete*.

Gillet, N., D. Brito, D. Jault, and H. Nataf (2007). Experimental and numerical studies of convection in a rapidly rotating spherical shell. *Journal of Fluid Mechanics 580*, 83–121.

Gillet, N. and C. Jones (2006). The quasi-geostrophic model for rapidly rotating spherical convection outside the tangent cylinder. *Journal of Fluid Mechanics 554*, 343–369.

Glatzmaier, G. A. and P. H. Roberts (1995). A three-dimensional convective dynamo solution with rotating and finitely conducting inner core and mantle. *Physics of the Earth and Planetary Interiors 91*(1-3), 63–75.

Greenspan, H. P. (1968). *The theory of rotating fluids*, Volume 327. Cambridge University Press Cambridge.

Grote, E. and F. H. Busse (2001). Dynamics of convection and dynamos in rotating spherical fluid shells. *Fluid Dynamics Research 28*(5), 349.

Gubbins, D. (1973). Numerical solutions of the kinematic dynamo problem. *Philosophical Transactions of the Royal Society of London. Series A, Mathematical and Physical Sciences 274*(1241), 493–521.

Guervilly, C. and E. Dormy (2025). The cross-over from viscous to inertial lengthscales in rapidly-rotating convection. *Geophysical Research Letters 52*(7), e2024GL111593.

Heimpel, M. and J. Aurnou (2007). Turbulent convection in rapidly rotating spherical shells: A model for equatorial and high latitude jets on jupiter and saturn. *Icarus 187*(2), 540–557.

Heimpel, M., J. Aurnou, and J. Wicht (2005). Simulation of equatorial and high-latitude jets on jupiter in a deep convection model. *Nature 438*(7065), 193–196.

Herzenberg, A. (1958). Geomagnetic dynamos. *Philosophical Transactions of the Royal Society of London. Series A, Mathematical and Physical Sciences 250*(986), 543–583.

Hori, K., C. A. Jones, A. Antuñano, L. N. Fletcher, and S. M. Tobias (2023). Jupiter's cloud-level variability triggered by torsional oscillations in the interior. *Nature Astronomy*, 1–11.

Hori, K., S.-i. Takehiro, and H. Shimizu (2014). Waves and linear stability of magnetoconvection in a rotating cylindrical annulus. *Physics of the Earth and Planetary Interiors 236*, 16–35.

Hori, K., R. Teed, and C. Jones (2018). The dynamics of magnetic rossby waves in spherical dynamo simulations: a signature of strong-field dynamos? *Physics of the Earth and Planetary Interiors 276*, 68–85.

Horn, S. and J. M. Aurnou (2022). The elbert range of magnetostrophic convection. i. linear theory. *Proceedings of the Royal Society A 478*(2264), 20220313.

Hughes, D. W. and F. Cattaneo (2019). Force balance in convectively driven dynamos with no inertia. *Journal of Fluid Mechanics 879*, 793–807.

Hunter, E. and R. J. Teed (2024). Multiple jets in a rotating annulus model with an imposed azimuthal magnetic field. *Geophysical & Astrophysical Fluid Dynamics 118*(5-6), 441–466.

Hutcheson, K. A. and D. R. Fearn (1995). The nonlinear evolution of magnetic instabilities in a rapidly rotating annulus. *Journal of Fluid Mechanics 291*, 343–368.

Jeffreys, H. (1926). The rigidity of the earth's central core. *Geophysical Supplements to the Monthly Notices of the Royal Astronomical Society 1*(7), 371–383.

Jones, C. (2007). Thermal and compositional convection in the outer core. *Core Dynamics 8*, 131–185.

Jones, C. (2014). A dynamo model of jupiter's magnetic field. *Icarus 241*, 148–159.

Jones, C., J. Rotvig, and A. Abdulrahman (2003). Multiple jets and zonal flow on jupiter. *Geophysical research letters 30*(14).

Kageyama, A., T. Miyagoshi, and T. Sato (2008). Formation of current coils in geodynamo simulations. *Nature 454*(7208), 1106–1109.

Kageyama, A. and T. Sato (1997). Generation mechanism of a dipole field by a magnetohydrodynamic dynamo. *Physical review E 55*(4), 4617.

Kaspi, Y., E. Galanti, R. Park, K. Duer, N. Gavriel, D. Durante, L. Iess, M. Parisi, D. Buccino, T. Guillot, et al. (2023). Observational evidence for cylindrically oriented zonal flows on jupiter. *Nature Astronomy 7*(12), 1463–1472.

Klesman, A. (2020). The Sky This Week from September 4 to 11 — astronomy.com. `https://www.astronomy.com/observing/the-sky-this-week-see-stormy-jupiter-and-neptune-at-opposition/`. [Accessed 09-07-2025].

Kuang, W. and J. Bloxham (1997). An earth-like numerical dynamo model. *Nature 389*(6649), 371–374.

Kurt, E., F. H. Busse, and W. Pesch (2004). Hydromagnetic convection in a rotating annulus with an azimuthal magnetic field. *Theoretical and Computational Fluid Dynamics 18*, 251–263.

Kutzner, C. and U. Christensen (2000). Effects of driving mechanisms in geodynamo models. *Geophysical Research Letters 27*(1), 29–32.

Larmor, J. (1919). How could a rotating body such as the sun become a magnet? *Report for the British Association for the Advancement of Science,*, 159–160.

Lehmann, I. (1936). P, publ. bur. centr. seism. internat. *Serie. A 14*, 87–115.

Lilley, F. (1970). On kinematic dynamos. *Proceedings of the Royal Society of London. A. Mathematical and Physical Sciences 316*(1525), 153–167.

Lowes, F. (1974). Spatial power spectrum of the main geomagnetic field, and extrapolation to the core. *Geophysical Journal International 36*(3), 717–730.

Mason, S. J., C. Guervilly, and G. R. Sarson (2022). Magnetoconvection in a rotating spherical shell in the presence of a uniform axial magnetic field. *Geophysical & Astrophysical Fluid Dynamics 116*(5-6), 458–498.

Moffatt, H. K. (1978). Field generation in electrically conducting fluids. *Cambridge University Press, Cambridge, London, New York, Melbourne 2*, 5–1.

Moore, K., A. Barik, S. Stanley, D. Stevenson, N. Nettelmann, R. Helled, T. Guillot, B. Militzer, and S. Bolton (2022). Dynamo simulations of jupiter's magnetic field: The role of stable stratification and a dilute core. *Journal of Geophysical Research: Planets 127*(11), e2022JE007479.

Morin, J., E. Dormy, M. Schrinner, and J.-F. Donati (2011). Weak-and strong-field dynamos: from the earth to the stars. *Monthly Notices of the Royal Astronomical Society: Letters 418*(1), L133–L137.

Naskar, S., C. Davies, J. Mound, and A. Clarke (2025). Force balances in spherical shell rotating convection. *Journal of Fluid Mechanics 1009*, A70.

Oldham, R. D. (1906). The constitution of the interior of the earth, as revealed by earthquakes. *Quarterly Journal of the Geological Society 62*(1-4), 456–475.

Or, A. and F. H. Busse (1987). Convection in a rotating cylindrical annulus. part 2. transitions to asymmetric and vacillating flow. *Journal of Fluid Mechanics 174*, 313–326.

Oruba, L. and E. Dormy (2014). Transition between viscous dipolar and inertial multipolar dynamos. *Geophysical Research Letters 41*(20), 7115–7120.

Petitdemange, L. (2018). Systematic parameter study of dynamo bifurcations in geodynamo simulations. *Physics of the Earth and Planetary Interiors 277*, 113–132.

Proudman, J. (1916). On the motion of solids in a liquid possessing vorticity. *Proceedings of the Royal Society of London. Series A, Containing Papers of a Mathematical and Physical Character 92*(642), 408–424.

Rayleigh, L. (1916). Lix. on convection currents in a horizontal layer of fluid, when the higher temperature is on the under side. *The London, Edinburgh, and Dublin Philosophical Magazine and Journal of Science 32*(192), 529–546.

Rhines, P. B. (1975). Waves and turbulence on a beta-plane. *Journal of Fluid Mechanics 69*(3), 417–443.

Roberts, P. (1978). Magnetoconvection in a rapidly rotating fluid. *Rotating Fluids in Geophysics (ed. PH Roberts & AM Soward)*, 421–435.

Roberts, P. H. (1988). Future of geodynamo theory. *Geophysical & Astrophysical Fluid Dynamics 44*(1-4), 3–31.

Roberts, P. H. and E. M. King (2013). On the genesis of the earth's magnetism. *Reports on Progress in Physics 76*(9), 096801.

Rotvig, J. (2009). An investigation of reversing numerical dynamos driven by either differential or volumetric heating. *Physics of the Earth and Planetary Interiors 176*(1-2), 69–82.

Rotvig, J. and C. A. Jones (2006). Multiple jets and bursting in the rapidly rotating convecting two-dimensional annulus model with nearly plane-parallel boundaries. *Journal of Fluid Mechanics 567*, 117–140.

Schnaubelt, M. and F. H. Busse (1992). Convection in a rotating cylindrical annulus part 3. vacillating and spatially modulated flows. *Journal of Fluid Mechanics 245*, 155–173.

Schneider, T. and J. Liu (2009). Formation of jets and equatorial superrotation on jupiter. *Journal of the Atmospheric Sciences 66*(3), 579–601.

Schwaiger, T., T. Gastine, and J. Aubert (2019). Force balance in numerical geodynamo simulations: a systematic study. *Geophysical Journal International 219*(Supplement_1), S101–S114.

Schwaiger, T., T. Gastine, and J. Aubert (2021). Relating force balances and flow length scales in geodynamo simulations. *Geophysical Journal International 224*(3), 1890–1904.

Simitev, R. and F. Busse (2003). Patterns of convection in rotating spherical shells. *New Journal of Physics 5*(1), 97.

Simitev, R. D. and F. H. Busse (2009). Bistability and hysteresis of dipolar dynamos generated by turbulent convection in rotating spherical shells. *Europhysics Letters 85*(1), 19001.

Soderlund, K. M., A. Sheyko, E. M. King, and J. M. Aurnou (2015). The competition between lorentz and coriolis forces in planetary dynamos. *Progress in Earth and Planetary Science 2*, 1–10.

Soward, A. (1974). A convection-driven dynamo i. the weak field case. *Philosophical Transactions of the Royal Society of London. Series A, Mathematical and Physical Sciences 275*(1256), 611–646.

Soward, A. (1979). Convection driven dynamos. *Physics of the Earth and Planetary Interiors 20*(2-4), 134–151.

Sreenivasan, B. and C. A. Jones (2005). Structure and dynamics of the polar vortex in the earth's core. *Geophysical research letters 32*(20).

Takahashi, F., M. Matsushima, and Y. Honkura (2008). Scale variability in convection-driven mhd dynamos at low ekman number. *Physics of the Earth and Planetary Interiors 167*(3-4), 168–178.

Taylor, G. I. (1922). The motion of a sphere in a rotating liquid. *Proceedings of the Royal Society of London. Series A, Containing Papers of a Mathematical and Physical Character 102*(715), 180–189.

Teed, R. J. and E. Dormy (2023). Solenoidal force balances in numerical dynamos. *Journal of Fluid Mechanics 964*, A26.

Teed, R. J. and E. Dormy (2025). Scaling of strong-field spherical dynamos. *Geophysical Research Letters 52*(20), e2025GL118078.

Teed, R. J., C. A. Jones, and R. Hollerbach (2012). On the necessary conditions for bursts of convection within the rapidly rotating cylindrical annulus. *Physics of fluids 24*(6).

Teed, R. J., C. A. Jones, and S. M. Tobias (2015). The transition to earth-like torsional oscillations in magnetoconvection simulations. *Earth and Planetary Science Letters 419*, 22–31.

Tobias, S. M., P. H. Diamond, and D. W. Hughes (2007). β-plane magnetohydrodynamic turbulence in the solar tachocline. *The Astrophysical Journal 667*(1), L113.

Weiss, N. O. and M. Proctor (2014). *Magnetoconvection*. Cambridge University Press.

Wilcoxon, F. (1945). Individual comparisons by ranking methods. *Biometrics bulletin 1*(6), 80–83.

Willis, A. P., B. Sreenivasan, and D. Gubbins (2007). Thermal core–mantle interaction: exploring regimes for 'locked'dynamo action. *Physics of the Earth and Planetary Interiors 165*(1-2), 83–92.

Yadav, R. K., T. Gastine, U. R. Christensen, S. J. Wolk, and K. Poppenhaeger (2016). Approaching a realistic force balance in geodynamo simulations. *Proceedings of the National Academy of Sciences 113*(43), 12065–12070.

Zhang, K. and D. Gubbins (1996). Convection in a rotating spherical fluid shell with an inhomogeneous temperature boundary condition at finite prandtl number. *Physics of Fluids 8*(5), 1141–1148.

Zhang, K.-K. and F. H. Busse (1989). Convection driven magnetohydrodynamic dynamos in rotating spherical shells. *Geophysical & Astrophysical Fluid Dynamics 49*(1-4), 97–116.

Zhang, K.-K. and F. H. Busse (1990). Generation of magnetic fields by convection in a rotating spherical fluid shell of infinite prandtl number. *Physics of the earth and planetary interiors 59*(3), 208–222.